# Molecular determinants of immune receptor signalling




**João Ferreira Fernandes**
Lincoln College

Supervisors: Simon J. Davis, Richard J. Cornall

Thesis submitted for the degree of Doctor of Philosophy

Hilary Term 2023

## Declaration of Authorship

I hereby declare that, except where specific reference is made, the contents of this work are original and have not been submitted in whole or in part for consideration for another degree or qualification in this, or any other, university. This document is my own work and contains nothing which is the outcome of work done in collaboration with others, except as specified in the text or in the listed instances:

**Chapter 3**

- HM79b Fab-Halo purification was assisted by Nicole Ashman.
- 2D imaging experiments were conducted with assistance from Caitlin O'Brien-Ball, James McColl, and Gregory Chant.
- 3D imaging experiments were conducted with Sam Daly, who was responsible for image reconstruction and nearest-neighbour analysis.
- The cross K-function analysis was conducted by Bin Fu.

**Chapter 4**

- SPR experiments were conducted with assistance from Martin Fellermeyer.

**Chapter 5**

- The initial BCR purification was conducted with help from Mai Vuong.
- Cryo-EM imaging and data processing were exclusively done by Lukas Sušac (Goethe University Frankfurt).

**Chapter 6**

- 22E7 Fab-Halo purification (incl. SDS-PAGE) was conducted by Mai Vuong.
- Cryo-EM imaging and data processing were exclusively done by Lukas Sušac (Goethe University Frankfurt).

## COVID-19 Impact Statement

The COVID-19 global pandemic disrupted experimental work for this degree. Departmental closures and limited access after reopening hindered laboratory-based work, which was almost exclusively the work to be conducted at this time. The department was closed from the end of March 2020 to June 2020 (inclusive), where no experimental work could be conducted. For the 15 months from the department reopening in July 2020 to November 2021, restrictions to the number of people in the lab were applicable to varying degrees. This introduced great limitations on the capacity to conduct experiments throughout this period, and severely impacted the work described in this thesis.

## Acknowledgements

I would first like to thank my supervisors, Simon and Richard, for allowing me to join their labs and for their guidance since. I was encouraged to take on many different projects and opportunities - I have learnt a lot as a result, and I am very thankful for that. I would extend this thank you to our collaborators, David Klenerman, Steven Lee, and Robert Tampé, and to all the members of their labs who either contributed directly to the work in this thesis or provided helpful discussions along the way. Thank you also to the facilities at the WIMM for their excellent help.

No doctorate is an individual achievement, especially in the age of the global COVID-19 pandemic. I must therefore extend my thanks to those who helped me at the bench and elsewhere.

This work exists only through the support of the Davis lab (and our many coffee breaks). I would like to thank Mafalda and Sumana, who could not be greater examples in science, and ones I will strive to emulate. I cannot wait to see what great supervisors you will be and the many interesting projects that will follow. To Mafalda especially, who has advised me throughout, *obrigado*. To Mai, who provided a guiding example in experimental rigour, and whose indefatigability is legendary, a big thank you – part of how I think about science has come from your example and I will carry that on for a long time. To Martin, who, as a great student, colleague and (I am sure he will dispute this) friend, worked tirelessly alongside me during the lockdowns, and whose support was invaluable. For your many years of help and for your supporting nature, thank you. To Oliver, who always provided a friendly ear, even when I was talking too much. To Matt, who has grown into a tireless student always ready to ruin a coffee break with work, thank you. To Rob, Carmelita, Francis, and Toby, who at different times were calming influences and supportive labmates. To Heather, who diligently taught me much at the start, and who patiently stood by as I failed to cast polyacrylamide gel after gel, thank you. And to Alex, who sets a high bar himself.

To Nicole and Ed, who were first my teachers, then my colleagues, and ultimately my great friends – an enormous thank you. To Nicole, who provided innumerable runs and advice over the years, and many coffees during the writing of this thesis, who with unshakeable principle never fails to let me know when I am wrong, thank you. To Ed, who taught me a lot – thank you for all the discussions, all the help, and for never failing to be able to have fun at your own expense, to great effect. I do not need to wish you success for the future, as it will surely come, and I cannot wait to hear all about the great science that will come from your future efforts.

For Caitlin and Kamal, many pages of acknowledgements would not be sufficient, so I will be brief: for always being there for me; for the singing car rides to Cambridge, and for the many epic visits to Holywell Manor; for the walks in Barton; for your friendship, I am forever grateful.

To Elisa, and her unvacillating support since our time in London, *obrigado*. To Zainab, who made her way from London to Oxford and had to continue to listen to my never-ending chats – thank you for your friendship over the years. To Mario, Noémie and Madalena, whose friendship goes back to a time when I would never have thought I would write something like this, and who helped me get here in more ways than perhaps they realise - *grazie, merci*, *obrigado*.

*E finalmente, não posso deixar de agradecer à minha família, sem a qual nada disto seria possível*. *Pelo apoio, de Lisboa a Oxford – muito obrigado.*

## Abstract

Immunoreceptors play a key role in leukocyte function. Despite the important role of these receptors, the mechanisms by which non-catalytic tyrosine-based receptor signalling is initiated in response to their ligands is still controversial. To fully understand the molecular mechanisms driving receptor signalling, previous work has focused on determining the structure of these receptors prior to and following ligand binding, as well as the organisation of the receptors on resting cells, often with contradictory conclusions. Among these, the B-cell receptor (BCR) plays a central role in the activation of antigen-specific B cells and the production of targeted antibody responses. In this study, a new super-resolution imaging technique is used to characterise the three-dimensional distribution of the BCR in resting B cells, in the context of the often-overlooked complex architecture of the cell membrane. B-cell responsiveness to membrane antigens was also tested for antigens on supported lipid bilayers (SLBs), and the impact of antigen molecular height in BCR signalling was assessed. Moreover, purification of fully assembled BCR complexes in the presence or absence of antigen molecules ligated *in situ* provided material for preliminary cryo-electron microscopy (cryo-EM) analysis of individual BCR molecules. Similarly, complexes of the high-affinity IgE immune receptor, FcεRI, were also purified in the presence or absence of their ligand for future structure determination using cryo-EM. Together, these results provided initial observations that seek to define the molecular mechanisms driving both immunoreceptor assembly and signalling.

# Abbreviations

| | |
|---|---|
| **ADCC** | Antibody-dependent cellular cytotoxicity |
| **AF** | Alexa Fluor |
| **AID** | Activation-induced cytidine deaminase |
| **Akt** | Protein kinase B |
| **ANOVA** | Analysis of variance |
| **AP-1** | Activator protein 1 |
| **B220** | B-cell isoform of 220kDa |
| **BAFF** | B-cell activating factor |
| **BCAP** | B-cell adaptor for PI3K |
| **BCR** | B-cell receptor |
| **BiFC** | Bifluorescence complementation |
| **BLNK** | B-cell linker |
| **BSA** | Bovine serum albumin |
| **Btk** | Bruton's tyrosine kinase |
| **C3/C5** | Complement C3/C5 |
| **CD** | Cluster of differentiation |
| **CH** | Constant heavy |
| **CHO** | Chinese hamster ovary |
| **CLL** | Chronic lymphocytic leukaemia |
| **CLP** | Common lymphoid progenitor |
| **CLR** | C-type lectin receptor |
| **CR** | Complement receptor |
| **CSR** | Class-switch recombination |
| **DAG** | diacylglycerol |
| **DAMP** | Damage-associated molecular pattern |
| **(c)DC** | (classical) Dendritic cell |
| **DDM** | n-dodecyl-β-D-maltopyranoside |
| **DMEM** | Dulbecco's Modified Eagle Medium |
| **DMSO** | Dimethyl sulfoxide |
| **dSTORM** | Direct stochastic optical reconstruction microscopy |
| **EDTA** | Ethylenediaminetetraacetic acid |
| **EM** | Electron microscopy |
| **eOD-GT** | Engineered outer domain (of HIV-1 gp120), germline-targeting |
| **ER** | Endoplasmic reticulum |
| **EtBr** | Ethidium bromide |
| **Fab** | Fragment, antigen-binding |
| **Fc** | Crystallisable fragment |
| **FcγR** | Fc gamma receptor |
| **FcεRI** | High-affinity IgE receptor |
| **FCS** | Foetal calf serum |
| **(p)FCS** | (Point) fluorescence correlation spectroscopy |
| **FDC** | Follicular dendritic cell |
| **FO** | Follicular |
| **FRET** | Förster resonance energy transfer |

| | |
|---|---|
| **FSEC** | Fluorescence size-exclusion chromatography |
| **GC** | Germinal centre |
| **GDN** | Glyco-diosgenin |
| **Grb2** | Growth-factor receptor-bound protein 2 |
| **HBS** | HEPES-buffered saline |
| **HEL** | Hen egg lysozyme |
| **HILO** | Highly inclined illumination |
| **ICAM-1** | Intercellular adhesion molecule 1 |
| **IFN** | Interferon |
| **Ig** | Immunoglobulin |
| **IGKV** | Immunoglobulin kappa variable segment |
| **IGLV** | Immunoglobulin lambda variable segment |
| **IL** | Interleukin |
| **$IP_3$** | Inositol 1,4,5-trisphosphate |
| **IPTG** | Isopropyl β-D-1 thiogalactopyranoside |
| **IRF** | Interferon regulatory factor |
| **ITAM** | Immunoreceptor tyrosine-based activation motif |
| **ITIM** | Immunoreceptor tyrosine-based inhibition motif |
| **$K_D$** | Dissociation constant |
| **$k_{off}$** | Dissociation rate |
| **$k_{on}$** | Association rate |
| **KS** | Kinetic-segregation |
| **LAT** | Linker for activation of T cells |
| **LB** | Lysogeny broth |
| **LMNG** | Lauryl maltose neopentyl glycol |
| **LTR** | Long terminal repeat |
| **MAC** | Membrane attack complex |
| **MAPK** | Mitogen-activated protein kinase |
| **MHC** | Major histocompatibility complex |
| **mIg** | Membrane immunoglobulin |
| **mRNA** | Messenger ribonucleic acid |
| **MZ** | Marginal zone |
| **NiNTA** | Nickel-nitrilotriacetic acid |
| **NF-κB** | Nuclear factor kappa-light-chain enhancer of activated B cells |
| **NFAT** | Nuclear factor of activated T cells |
| **NLR** | NOD-like receptor |
| **NTAL** | Non-T-cell activation linker |
| **PAMP** | Pathogen-associated molecular pattern |
| **PBS** | Phosphate-buffered saline |
| **PCR** | Polymerase chain reaction |
| **PE** | Phycoerythin |
| **PFA** | Paraformaldehyde |
| **PI3K** | Phosphoinositide 3-kinase |
| **PKC** | Protein kinase C |
| **PLA** | Proximity-ligation assay |
| **$PLA_2$** | Phospholipase A2 |
| **PLC** | Phospholipase C |

| | |
|---|---|
| **PLL** | Poly-L-lysine |
| **pMHC** | Peptide-MHC complex |
| **PRR** | Pattern recognition receptor |
| **RAG** | Recombination activating gene |
| **RLR** | RIG-like receptor |
| **RPMI** | Roswell Park Memorial Institute medium |
| **RPTP** | Receptor-type protein tyrosine phosphatase |
| **SCS** | Subcapsular sinus |
| **SD** | Standard deviation |
| **SDS-PAGE** | Sodium dodecyl sulfate-polyacrylamide gel electrophoresis |
| **SEC** | Size-exclusion chromatography |
| **SH** | Src-homology domain |
| **SHP** | SH2-containing phosphatase |
| **SLB** | Supported lipid bilayer |
| **SFFV** | Spleen focus forming virus |
| **SFK** | Src-family kinase |
| **SLO** | Secondary lymphoid organ |
| **SLP76** | SH2-domain-containing leukocyte protein of 76 kDa |
| **SMLFM** | Single-molecule light-field microscopy |
| **SpA** | Staphylococcal (IgG-binding) protein A |
| **SPR** | Surface plasmon resonance |
| **STED** | Stimulated emission depletion |
| **SUV** | Small unilamellar vesicle |
| **TCR** | T-cell receptor |
| **TD** | T-cell-dependent |
| **TdT** | Terminal deoxynucleotidyl transferase |
| **TI** | T-cell-independent |
| **TIRF(M)** | Total internal reflection fluorescence (microscopy) |
| **TLR** | Toll-like receptor |
| **UV** | Ultraviolet |
| **VCAM-1** | Vascular cell adhesion protein 1 |
| **WPRE** | Woodchuck hepatitis virus post-transcriptional regulatory element |

# Table of Contents


**Chapter 1. Introduction ..... 1**

**1.1 The immune system: an overview ..... 1**
- **1.1.1. Immunity ..... 1**
- **1.1.2. Innate immunity ..... 1**
- **1.1.3. Adaptive immunity ..... 4**
- **1.1.4. Interdependence of innate and adaptive immunity ..... 8**

**1.2. B cells ..... 10**
- **1.2.1. B-cell development and maturation ..... 10**
- **1.2.2. Naïve B-cell subsets ..... 13**
- **1.2.3. Antigen presentation to B cells ..... 14**
- **1.2.4. B-cell activation ..... 15**
- **1.2.5. The germinal centre reaction: an overview ..... 16**
- **1.2.6. Antibody production ..... 17**
- **1.2.7. B-cell memory ..... 18**

**1.3. Immunoglobulins ..... 18**
- **1.3.1 Immunoglobulin structure and isotypes ..... 18**
- **1.3.2 The BCR complex ..... 21**
- **1.3.3 Antibodies ..... 23**

**1.4. BCR signalling ..... 24**
- **1.4.1. Overview of initial events in BCR signalling ..... 24**
- **1.4.2. Tyrosine kinases and phosphatases in BCR signalling ..... 25**
- **1.4.3. Membrane-distal BCR signalling ..... 27**
- **1.4.4. Accessory surface proteins in BCR signalling ..... 30**

**1.5. Models of BCR signalling ..... 31**
- **1.5.1. Cross-linking model ..... 31**
- **1.5.2. Conformational-change oligomerisation model ..... 34**
- **1.5.3. Dissociation-activation model ..... 35**
- **1.5.4. Collision-coupling model ..... 36**
- **1.5.5. Kinetic-segregation model ..... 37**
- **1.5.6. Organisation of the resting BCR complex ..... 39**

**1.6. FcεRI signalling ..... 41**
- **1.6.1. IgE-mediated immunity ..... 41**
- **1.6.2. FcεRI structure and function ..... 42**
- **1.6.3. Events in FcεRI signalling ..... 43**
- **1.6.4. Mechanisms of FcεRI signalling ..... 45**

**1.7 Aims of this thesis ..... 47**

**Chapter 2. Materials and Methods ..... 48**

**2.1 Cell culture ..... 48**

**2.2 Molecular biology ..... 50**
- **2.2.1. DNA cloning ..... 50**
- **2.2.2. Plasmid preparation ..... 52**
- **2.2.3. Lentiviral transduction ..... 53**

**2.3 Flow cytometry ..... 54**
- **2.3.1. Labelling cells ..... 54**
- **2.3.2. Antibodies used ..... 55**

**2.4 Production of soluble proteins ..... 56**
- **2.4.1 Protein design and purification overview ..... 56**
- **2.4.2 Bacterial protein production ..... 56**
- **2.4.3 Mammalian protein production ..... 57**

**2.4.4 Affinity chromatography – His purification** ..... 57
**2.4.5 Affinity chromatography – CTag purification** ..... 58
**2.4.6 Affinity chromatography – Twin-StrepTag purification** ..... 59
**2.4.7 Size-exclusion chromatography (SEC)** ..... 60
**2.4.8 SDS-PAGE and protein storage** ..... 60
**2.4.9 Fluorescent labelling of soluble proteins** ..... 61

**2.5 Data processing and presentation** ..... **62**

**Chapter 3. The stoichiometry of the BCR complex in resting cells** ..... **64**

**3.1 Introduction** ..... **64**

**3.2 Methods** ..... **66**
**3.2.1. Isolation of primary mouse B cells** ..... 66
**3.2.2. Generation of imaging probes** ..... 66
**3.2.3. QuantiBrite quantification of receptor expression** ..... 66
**3.2.4. Cell labelling for dSTORM** ..... 67
**3.2.5. dSTORM sample preparation** ..... 67
**3.2.6. TIRF/dSTORM imaging** ..... 68
**3.2.7. SMLFM/dSTORM imaging** ..... 68
**3.2.8. Image reconstruction** ..... 69
**3.2.9. Cross K-function analysis** ..... 70

**3.3 Results** ..... **71**
**3.3.1. Reagents for super-resolution imaging of B-cell surface proteins** ..... 71
**3.3.2. Initial 2D TIRF/dSTORM experiments** ..... 75
**3.3.3. 3D SMLFM/dSTORM experiments** ..... 77
**3.3.4. Cross K-function analysis of BCR organisation** ..... 85

**3.4 Discussion** ..... **89**

**Chapter 4. Increased antigen molecular height impairs BCR triggering** ..... **94**

**4.1 Introduction** ..... **94**

**4.2 Methods** ..... **97**
**4.2.1. Isolation of primary mouse B cells** ..... 97
**4.2.2. Generation of model antigen molecules** ..... 97
**4.2.3. Surface plasmon resonance** ..... 97
**4.2.4. Supported lipid bilayer generation and functionalisation** ..... 98
**4.2.5. Point fluorescence correlation spectroscopy** ..... 100
**4.2.6. Calcium signalling experiments** ..... 102

**4.3 Results** ..... **103**
**4.3.1. Soluble proteins for the study of antigen height** ..... 103
**4.3.2. Generating HEL-bearing supported lipid bilayers** ..... 112
**4.3.3. BCR triggering in response to HEL proteins of varying molecular height** ..... 116

**4.4 Discussion** ..... **120**

**Chapter 5. Purification of a complete human BCR complex for structural studies** ..... **125**

**5.1 Introduction** ..... **125**

**5.2 Methods** ..... **128**
**5.2.1 Transduction of CHO-S cell lines** ..... 128
**5.2.2 Saturation test for BCR binders** ..... 128
**5.2.3 Surface complex labelling** ..... 129
**5.2.4 Membrane complex purification** ..... 130
**5.2.5 Optimisation of solubilisation conditions** ..... 132
**5.2.6 FSEC and SDS-PAGE** ..... 133

5.2.7. Cryo-EM data collection and processing ... 133
5.3 Results ... 134
5.3.1 Generating a system for BCR complex expression ... 134
5.3.2 Purification of soluble proteins for receptor extraction ... 137
5.3.3 Initial BCR complex purification ... 142
5.3.4 Optimisation of receptor purification ... 144
5.3.5 Purification of a BCR-antigen complex ... 150
5.3.6 Cryo-EM imaging of the ligated BCR complex ... 155
5.4 Discussion ... 158
Chapter 6. Purification of a complete human FcεRI complex for structural studies ... 161
6.1 Introduction ... 161
6.2 Methods ... 164
6.2.1. CHO-S cell line and soluble protein generation ... 164
6.2.2. Optimisation of receptor solubilisation ... 164
6.2.3. Membrane complex purification ... 164
6.2.4. SDS-PAGE and FSEC ... 165
6.2.5. Cryo-EM data collection and processing ... 165
6.2.6. Rendering representations of previous crystal structures ... 165
6.3 Results ... 166
6.3.1 Generating a system for FcεRI purification ... 166
6.3.2 Purification of the SpyCatcher-bound FcεRI complex ... 171
6.3.3 Purification of the ligated FcεRI complex ... 176
6.3.4. Preliminary cryo-EM imaging of the ligated FcεRI complex ... 179
6.3.5 Purification of a Fab-bound FcεRI complex ... 181
6.4 Discussion ... 186
Chapter 7. General Discussion ... 190
7.1 Overview of the results ... 190
7.2 The stoichiometry of the resting BCR ... 192
7.3 Increased molecular height impairs BCR sensitivity to low-affinity antigens ... 196
7.4 Purified BCR complexes for cryo-EM structure determination ... 200
7.5 Purified FcεRI complexes for cryo-EM structure determination ... 204
7.5.1 Extraction of ligated FcεRI complexes and preliminary cryo-EM analysis ... 205
7.5.2 Differential states of unbound and bound FcεRI ... 205
7.6 Summary of observations and their implications for signalling ... 210
7.7 Concluding remarks ... 211
Appendices ... 213
Appendix A. Supplementary Figures ... 213
Appendix B. Sequences of proteins used in this work ... 215
References ... 224

## List of Figures


| | | |
|---|---|---|
| **Figure 1.1.** | Schematic of B-cell development | 12 |
| **Figure 1.2.** | Diagram of the mammalian immunoglobulin isotypes | 20 |
| **Figure 1.3.** | Schematic representing the key features of the (IgM) BCR complex | 22 |
| **Figure 1.4.** | Events in BCR signalling | 29 |
| **Figure 1.5.** | Alternative models of BCR signalling | 33 |
| **Figure 1.6.** | The kinetic-segregation (KS) model of receptor signalling | 39 |
| **Figure 1.7.** | Events in FcεRI signalling | 44 |
| **Figure 3.1.** | Purification of HM79b Fab-Halo | 73 |
| **Figure 3.2.** | Purification of 30F11 Fab-Halo | 74 |
| **Figure 3.3.** | Saturation of receptor labelling on primary B cells | 76 |
| **Figure 3.4.** | Reconstructed 2D TIRF/dSTORM images of primary B cells | 77 |
| **Figure 3.5.** | Example raw data from SMLFM/dSTORM | 79 |
| **Figure 3.6.** | Primary B cells imaged in a single illumination volume using SMLFM | 80 |
| **Figure 3.7.** | Membrane protrusions are preserved in fixed B cells | 81 |
| **Figure 3.8.** | Quantification of receptor expression on primary C57BL/6J B cells | 83 |
| **Figure 3.9.** | Quantification of 3D localisations from SMLFM/dSTORM imaging | 84 |
| **Figure 3.10.** | Principles of K-function analysis | 85 |
| **Figure 3.11.** | Cross K-function analysis of BCR distribution in the presence and absence of crosslinking | 87 |
| **Figure 3.12.** | Nearest-neighbour representation of localisations in BCR-labelled cells | 88 |
| **Figure 3.13.** | Impact of membrane folding on cross-K function analysis | 92 |
| **Figure 4.1.** | Design of HEL fusion proteins | 103 |
| **Figure 4.2.** | Purification of HSpyC-HEL proteins | 105 |
| **Figure 4.3.** | Purification of HEL-Halo-CD43 proteins | 107 |
| **Figure 4.4.** | Purification of HyHEL10 Fab | 108 |
| **Figure 4.5.** | Representative sensorgrams for HyHEL10 Fab binding to immobilised HEL | 110 |
| **Figure 4.6.** | SPR-determined affinities of HEL fusion proteins | 111 |
| **Figure 4.7.** | Example autocorrelation curves from confocal imaging of functionalised HEL bilayers | 113 |
| **Figure 4.8.** | Characterising protein density and diffusion on HEL bilayers | 115 |
| **Figure 4.9.** | Example stills from confocal microscopy videos of MD4 B cells Interacting with bilayer surfaces | 117 |
| **Figure 4.10.** | Primary MD4 B cell triggering in response to HEL bilayers | 119 |
| **Figure 5.1.** | Generation of a mammalian system for $VRC01_{GL}$ IgM BCR expression | 135 |
| **Figure 5.2.** | Schematic representing two approaches for BCR purification | 137 |
| **Figure 5.3.** | Purification of the 6His-SpyC3-CTag protein | 138 |
| **Figure 5.4.** | Characterising SpyCatcher labelling of CHO-S $VRC01_{GL}$ cells | 139 |
| **Figure 5.5.** | Purification of polatuzumab Fab fragment | 141 |
| **Figure 5.6.** | Initial SpyCatcher extraction of BCR complexes via GDN/HPC4 purification | 143 |
| **Figure 5.7.** | Optimisation of BCR solubilisation | 145 |
| **Figure 5.8.** | Purification of 6His-SpyCatcher3-TwinStrep | 146 |
| **Figure 5.9.** | Comparison of BCR purification protocols by SEC | 147 |
| **Figure 5.10.** | SpyCatcher extraction of BCR complexes using LMNG/StrepTag purification | 149 |
| **Figure 5.11.** | Purification of monomeric eOD-GT8 | 151 |
| **Figure 5.12.** | eOD-GT8 extraction of BCR complexes using LMNG/StrepTag purification with detergent exchange | 153 |
| **Figure 5.13.** | Comparison of SEC profiles for complexes isolated using different | |

soluble proteins and eluted in different detergents 154
**Figure 5.14** Reference-free 2D classification of eOD-GT8-bound IgM BCR complexes 155
**Figure 5.15** Selected 2D class averages 156
**Figure 6.1.** Diagram depicting purification strategies for FcεRI extraction 166
**Figure 6.2.** Generation of CHO-S FcεRI cells 168
**Figure 6.3.** Purification of the Fcε(C225A) fragment 170
**Figure 6.4.** Solubilisation of the FcεRI complex under different conditions 171
**Figure 6.5.** Purification of SpyCatcher-bound FcεRI (without detergent exchange) 173
**Figure 6.6.** Purification of SpyCatcher-bound FcεRI (with detergent exchange) 174
**Figure 6.7.** Comparison of SEC profiles for differently purified FcεRI complexes 175
**Figure 6.8.** Purification of Fcε-bound FcεRI (with detergent exchange) 177
**Figure 6.9.** Comparison of SEC profiles of unligated and ligated FcεRI complexes 178
**Figure 6.10.** 2D class averages of particles selected from micrographs of grids containing vitrified Fcε-bound FcεRI 179
**Figure 6.11.** Selected 2D class averages 180
**Figure 6.12.** Diagrammatic depiction of 22E7-based purification of FcεRI 181
**Figure 6.13.** Purification of the 22E7 Fab-Halo fragment 183
**Figure 6.14.** Purification of 22E7-bound FcεRI (with detergent exchange) 184
**Figure 6.15.** Comparison of SEC profiles for unligated FcεRI complexes 185
**Supp. Fig. 1** HEL capture on nickelated SPR sensor chips 213

# Chapter 1. Introduction

## 1.1 The immune system: an overview

### 1.1.1. Immunity

Most metazoan organisms rely on the complex architecture of distinct tissues to regulate specific functions essential to life[1]. The finely-tuned conditions required for multicellular life provide a unique opportunity for other opportunistic or mutualistic organisms to find suitable environments for growth[2,3]. As such, mechanisms exist for the detection and disposal of other (*nonself*) opportunistic or tissue-damaging organisms, albeit without affecting the varied host tissues[4]. Initially, the distinction between *self* and *nonself* was mediated by evolutionarily conserved receptors recognising broad classes of pathogen-specific molecules[4] (Section 1.1.2). In jawed vertebrates, more complex complementary mechanisms evolved, driving the emergence of a broad molecular toolkit capable of specifically recognising target molecules arising from *nonself* or altered *self*[5] (Section 1.1.3). In mammals, these two arms of the immune system cooperate extensively, creating a targeted defence against foreign molecules without targeting host tissue[6].

### 1.1.2. Innate immunity

Innate immunity is predicated on the recognition of molecular cues by germline-encoded receptors, known as pattern recognition receptors (PRRs)[7]. PRRs bind to conserved motifs from molecular components of foreign particles and cells, or to molecules arising from tissue damage. These ligands are known as pathogen-

associated or damage-associated molecular patterns (PAMPs or DAMPs, respectively)[7]. Toll-like receptors (TLRs) comprise a class of membrane-bound PRR which detects a variety of ligands derived from viral, bacterial, and fungal sources which are not commonly present in the vertebrate host[8]. Similarly, C-type lectin receptors (CLRs) are surface-bound or soluble PRRs responsible for recognising sugar moieties that permit recognition of bacterial, viral, fungal and helminth surfaces, with varying specificity[9]. Cytosolic receptors, including NOD-like receptors (NLRs), RIG-I-like receptors (RLRs) and other cytosolic sensors, provide recognition of viral or mycobacterial components, predominantly nucleic acids[10]. These receptors all share similar functions, activating pro-inflammatory signalling pathways in the cell, namely through the transcription of target genes mediated by the NF-κB and IRF classes of transcription factors[11]. While expression of some of these receptors is constrained to specialised immune cells, others are ubiquitous in mammalian cells, and can coordinate both cell-intrinsic factors and propagate signals to neighbouring cells. A key example is the production of type I interferon molecules in infected cells, which can mediate the expression of interferon-mediated genes which suppress infection in nearby cells in a paracrine manner without the involvement of immune cells[12]. The recognition of molecules which are absent in healthy tissue is not constrained to infection or PRRs, and can serve important physiological functions – for example, the receptors recognising *eat me* signals, which are indispensable in the clearance of apoptotic vesicles in healthy tissue or necrotic debris[13].

Soluble components of the innate immune system play an essential role in pathogen control and mediate cellular innate immune responses. These include both soluble PRRs, such as pentraxins, and the complement system, among others[14]. Complement

activation pathways rely on sequences of enzymatic actions that lead to the cleavage of complement proteins (including C3 and C5), producing both inflammatory factors and chemically reactive fragments which can label nearby cellular surfaces (opsonins)[15]. Complement can direct cytotoxicity via the formation of macromolecular attack complexes (MACs), forming pores that disrupt cellular integrity, or via engagement of effector cells through opsonins and other fragments[15].

Cell-mediated mechanisms are key effectors in innate immunity. The most primitive factors, used in more evolutionarily ancient animals, are phagocytosis and the targeted release of granules containing proteolytic agents against stimulants[4]. Phagocytosis involves the engulfment of large particles by specialised cells and their subsequent degradation[16], a function that is already present in the amoebocytes of sponges of the *Parazoa* sub-kingdom[4]. Precursors of granulocytes, in turn, were present in the *Protostomia* clade[4]. In vertebrates, these evolutionarily ancient functions are predominantly performed by cells of the myeloid lineage[4].

Neutrophils are myeloid cells which act as both phagocytes and granulocytes. In response to PRR signalling, these cells can phagocytose bacteria, and release a variety of cytotoxic and antimicrobial molecules, including reactive oxygen species, proteases, antimicrobial peptides, among others[17]. Other granulocytes, including eosinophils, basophils, and mast cells, can also release granules containing proteases and other effector molecules, most commonly in response to antibodies (Section 1.3.3)[18].

Mononuclear phagocytes[19] are a distinct class of myeloid cells with essential functions in innate immunity. These cells can phagocytose pathogens and particles in response

to PRR signalling, as well as through activation of receptors engaging complement fragments and antibodies on opsonised surfaces[16]. Macrophages, tissue-resident cells, are not only involved in pathogen engulfment and degradation, but also play a key role in homeostatic functions and the clearance of apoptotic debris[20]. Conventional dendritic cells (cDCs), derived from common DC progenitor cells[19], also act as phagocytes, and play a key role in the initiation of the immune response and the activation of T lymphocytes[21] (Section 1.1.4). Lastly, monocytes are circulating myeloid cells which can be recruited into inflamed tissues upon infection or damage, differentiating into monocyte-derived cells with functions similar to those of macrophages and cDCs[19,22]. Mononuclear phagocytes play an important role beyond phagocytosis in the activation of the adaptive immune system, by presenting intact or processed proteins to lymphocytes[21,23], as expanded below (Section 1.1.4).

### 1.1.3. Adaptive immunity

The metazoan adaptive immune system evolved in jawed vertebrates, and some jawless fish have a similar yet distinct system[5]. Unlike the innate immune system, its recognition of *nonself* molecules relies on receptors that are not germline-encoded. In jawed vertebrates, adaptive immune cells are derived from the lymphoid lineage[5].

These cells can be subcategorised into two cell types: T and B cells. Both these cell types differentiate from the common lymphoid progenitor (CLP) cell but have important phenotypic differences[24]. Broadly speaking, each cell type expresses a class of hypervariable receptor encoding antigen-recognition capacity. In T cells, the T-cell receptor (TCR) detects and responds to restricted classes of molecules expressed on the membranes of target cells[25]. B cells express a different class of receptor, the B-cell

receptor (BCR), which can react to many classes of biomolecules, present both in solution and on surfaces[26]. In both cases, parts of their structure are shared across the same class of receptor, and it is the variability of the antigen-binding domains (known as variable regions) that allows selective recognition of target molecules[25,26].

**T cells**

T cells are lymphocytes characterised by the expression of T-cell receptors (TCRs). These transmembrane receptors are composed of a disulphide-bonded heterodimer of two TCR chains, which is noncovalently associated with three dimers: CD3εγ, CD3εδ and CD3$\zeta_2$[27]. The TCR chains confer antigen specificity to the receptor, while the associated CD3 chains are responsible for signal transduction upon antigen binding[28]. T cells can be subcategorised by the differential expression of two classes of TCR molecules, which are derived from distinct sets of gene segments[28].

αβ T cells comprise ~95% of total T cells and express receptors containing paired TCRα and TCRβ chains[29]. Overwhelmingly, these receptors recognise small peptide fragments presented in the context of MHC molecules on cell surfaces[25]. MHC class I molecules present peptides derived from the cellular protein repertoire, and are expressed by all nucleated cells for recognition by CD8-expressing T cells[29]. MHC class II molecules, on the other hand, present peptides derived from internalised protein antigens. These molecules play a key role in lymphocyte activation, and their expression is restricted to DCs, macrophages and B cells[29]. MHC-II-peptide complexes are recognised by CD4-expressing T cells[29]. αβTCR molecules do not respond to protein antigens only, and some can recognise lipid antigens incorporated into MHC-like molecules[30]. Conversely, γδ T cells, which represent <5% of the total T cell

population, express TCRγ and TCRδ, and this antigen-binding heterodimer is not constrained to the recognition of peptide-MHC molecules[29].

By sampling peptide antigens derived from all proteins expressed *in cellulo*, $CD8^+$ T cells act as surveyors of the intracellular milieu, which is largely inaccessible to humoral immune factors[31]. Therefore, they play a key role in the defence against intracellular pathogens and transformed cells, where modifications from *self* may arise from mutations in intracellular proteins[31]. Their cytotoxic functions, mediated via degranulation of lytic vesicles and induction of apoptosis, are essential in the clearance of infected and transformed cells[32]. Conversely, $CD4^+$ T cells play a key role in providing activatory factors to other cell types, including B cells[33].

T-cell development in the thymus involves a series of intermediate differentiation steps where receptor expression can be tested to validate productive gene rearrangement events[34]. T cells undergo positive selection to generate clones expressing functional, MHC-reactive TCRs but also negative selection to delete clones displaying heightened reactivity to peptides derived from self-antigens[34]. These central mechanisms are essential for the maintenance of immune tolerance, and match in part those involved in B-cell development (Section 1.2.1).

**B cells**

B cells are the primary focus of the work in this thesis and will be extensively described in Section 1.2. Briefly, B cells are lymphocytes expressing functionally rearranged immunoglobulin genes. In humans and mice, B-cell development occurs in the bone marrow, where a series of differentiation steps gives rise to mature B cells expressing

fully rearranged B-cell receptors[35] (Section 1.2.1). Membrane-bound BCRs are composed of two disulphide-bonded pairs of heavy and light immunoglobulin chains, noncovalently associated with a disulphide-linked heterodimer composed of CD79A and CD79B[36] (Section 1.3). The paired variable regions derived from the heavy and light chain provide the antigen-binding paratope[37]. Clonal activation of B cells, partly driven by BCR signalling, induces the production of a soluble form of the antigen-binding immunoglobulin, the antibody[38]. Antibodies are humoral factors which play a key role in the recognition of foreign or mutant molecules, functioning both to neutralise antigen function and mediate antigen clearance through opsonisation of target molecules or surfaces[38]. Unlike T cells, B cells can also undergo extensive modification of their antigen receptors in response to antigen, adapting randomly generated receptors to the target antigen during the immune response[39]. These concepts will be further explained in Section 1.2.

**Antigen receptor diversity**

The antigen receptor diversity needed to recognise an enormous range of possible foreign antigens is created by gene rearrangements resulting in the stochastic assembly of functional genes encoding antigen receptor variable regions[40,41]. This mechanism allows for the generation of extensive diversity derived from the random combination of several germline-encoded gene segments[42]. This unique feature of the adaptive immune system provides great adaptability to emerging antigens but must be tempered by selection processes that delete or disable both non-functional receptors and those with reactivity to *self* molecules[24].

Rearranged immunoglobulin genes are formed by V(D)J recombination. This is driven by RAG recombinases (RAG1 and RAG2), which bind asymmetrically to two distinct recombination signal sequences (RSSs) on two gene segments , looping and excising the intervening DNA sequence.[42] The joining of V gene segments to J segments (VJ recombination) forms the basis of TCRα and immunoglobulin light chain (IGKV and IGLV) variable region generation[42]. For TCRβ and immunoglobulin variable heavy chain generation, recombination of D and J segments precedes the junction of V to DJ segments (VDJ recombination)[42]. Another source of immunoglobulin diversity arises from the repair of the DNA hairpins generated by RAG recombination. The opening of these hairpins by the enzyme Artemis, and the resolution of the resulting break by nonhomologous end joining driven by the terminal deoxynucleotidyl transferase (TdT) enzyme, leads to the addition of extra nucleotides to the gene sequence[43]. This is known as junctional diversity, as it generates variation at the sites of segment joining[44]. Together, these mechanisms generate vast antigen receptor clonal diversity. αβTCR diversity is expected to be in the range of $\sim 10^{12}$ clones[25]. For the BCR, immunoglobulin M clonal diversity ranges from $10^{10}$-$10^{11}$ clones per individual[45]. In the latter case, this variation cannot fully be ascribed to these 'somatic diversification'[46] mechanisms, as BCR clones can mutate and adapt after maturation, as explained below (Section 1.2.4).

### 1.1.4. Interdependence of innate and adaptive immunity

Despite their separate descriptions here, the innate and adaptive immune system do not exist as two independent arms – their functions are highly cooperative[6]. Phagocytosis is in part mediated by antibody opsonisation of target surfaces, and degranulation by mast cells and basophils in response to allergens and helminths is

triggered by antibodies[38] (Section 1.6). Antibody opsonisation also plays a central role in complement deposition and directs antibody-dependent cellular cytotoxicity (ADCC) by innate lymphoid cells (primarily natural killer cells) and by other adaptive immune cells[38].

Innate antigen-presenting cells, in particular dendritic cells, play a key role in lymphocyte activation. Activation of naïve T cells relies on the engagement of specific clones by antigen-presenting cells, responsible for licensing subsequent T-cell activation upon TCR re-engagement[31]. Dendritic cell maturation involves the integration of a variety of signals, including PRR and cytokine signalling, which lead to phenotypic modifications that are essential for downstream T-cell activation[47]. T cells encountering pMHC complexes on dendritic cells are thereby provided with selected signals that shape their subsequent response, including soluble factors such as cytokines and receptor signalling driven by membrane-bound ligands on the DC surface[48]. The transfer of innate signals to adaptive cells[48] is typified by the upregulation of costimulatory molecules downstream of TLR signalling in maturing DCs, which can provide further activatory signals to DC-engaged T cells[49]. Upregulation of MHC class II proteins and costimulatory molecules upon maturation is also essential in the activation of $CD4^+$ T cells[21]. $CD4^+$ T-cell activation and licensing by DCs plays an essential role in B-cell activation[39], as will be further explained in Section 1.2.4. DCs also play a key role in $CD8^+$ T cell responses, as some DC subsets can cross-present antigen, that is, present peptides derived from internalised pathogens on MHC class I molecules, an essential event in activating $CD8^+$ T cell clones via cognate pMHC complexes which would otherwise only be present in infected cells[31]. Antigen presentation to B cells does not rely solely on leukocytes, but dendritic cells and

macrophages can also play a role in directly presenting intact antigen[23], as will be explored in Section 1.2.3. Innate cells also integrate signals from PRR signalling via the secretion of soluble factors, including cytokines and chemokines, which drive lymphocyte differentiation[21] and migration to sites of infection or secondary lymphoid organs[50]. As such, the two arms of the immune system interact, from the broad recognition of pathogens and damage to the antigen-specific adaptive response[6].

## 1.2. B cells

### 1.2.1. B-cell development and maturation

B cells are specialised lymphocytes which develop in the bone marrow in humans and mice. B-cell development relies on membrane-bound and soluble factors provided by the stromal cell niches in the bone marrow, of which interleukin 7 (IL-7) is a predominant factor[51]. Their multistep differentiation involves the sequential expression and rearrangement of all chains of the BCR complex, ensuring the generation of clonal cells expressing functional, signalling-competent receptors[52]. This is depicted in Figure 1.1[53].

Pre-pro-B cells are the first product of CLP differentiation into the B-cell lineage, and these cells already express B220, a key B-cell marker[54]. These cells differentiate into pro-B cells, early precursors of the B-cell lineage. Pro-B cells express the CD79 heterodimer on their surface before rearrangement of the immunoglobulin genes, stabilising this signalling complex through association with calnexin[55]. Expression of CD79 is essential for progression in the B-cell developmental pathway, as *Cd79b-/-* mice exhibit blocked B-cell development at this step[56]. Pro-B cells express RAG

recombinase, and immunoglobulin DJ heavy chain rearrangement occurs at the pro-B cell stage[57]. Upon differentiation to the large pre-B cell stage, V-DJ heavy chain recombination occurs[57], leading to the formation of a fully recombined heavy chain variable gene. In pre-B cells in which this rearrangement has been successful, heavy chains containing the rearranged variable region and the immunoglobulin M (IgM) constant regions can now be expressed[35]. This immunoglobulin heavy chain associates with the CD79 heterodimer and two other protein subunits, VpreB and $\lambda_5$, which together form a surrogate light chain[58]. This allows surface expression of an immunoglobulin complex in the absence of a rearranged light chain – an assembly called the pre-B-cell receptor (pre-BCR)[58]. Pre-BCR signalling is essential for the differentiation of large-pre-B cell into the small-pre-B cell state but may occur in the absence of surrogate light chains in cases where early light chain rearrangement occurs[35]. Expression of the pre-BCR suppresses VDJ recombination, ensuring that upon productive gene rearrangement other gene segments will not form extra immunoglobulin chains. This forms the basis of allelic exclusion and ensures that each B cell expresses a unique pair of immunoglobulin chains[35].

Small-pre-B cells re-express RAG recombinases, and no longer express the surrogate light chain[35]. As such, small-pre-B cells do not express pre-BCRs or surface immunoglobulin. Upon successful VJ recombination, light chain expression can occur, permitting the correct folding and surface expression of the BCR complex, and driving allelic exclusion by stopping further recombination[35]. These cells differentiate into the immature B cell stage, where a functional immunoglobulin is now expressed[52]. Immature B cells are subject to central tolerance mechanisms which ensure that functional receptors without marked self-reactivity are selected. The absence of basal

levels of receptor signalling (known as tonic signalling), leads to apoptotic cell death, while strong signals also lead to apoptosis or a re-entry into the small pre-B cell stage, allowing rearrangement of a new light chain and avoiding autoreactivity[59].

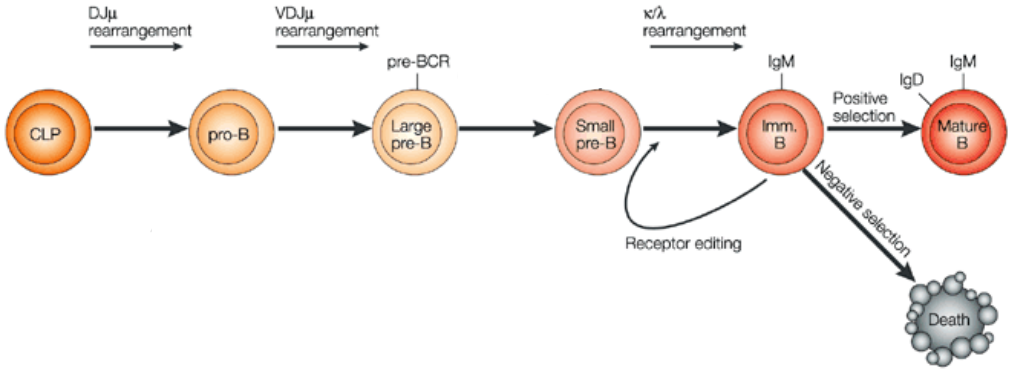



**Figure 1.1 | Schematic of B-cell development**. Differentiation stages from the common lymphoid progenitor (CLP) to mature B cells. Rearrangement events and selection outcomes also shown. Adapted from Engel and Murre (ref. 53).

Maturation of immature B cells occurs predominantly in the periphery, and in these final developmental stages (known as transitional B cells) peripheral tolerance occurs[52]. In transitional B cells, positive selection results in apoptosis of B cells generating impaired tonic BCR signals[35]. Conversely, strong BCR signalling in these intermediate steps can also lead to apoptosis, driving the deletion of self-reactive clones[59]. Some self-reactive B cells are not deleted but are maintained in a quiescent state known as anergy, incapable of further antigen-driven responses under normal conditions[52].

Importantly, peripheral selection also relies on factors beyond BCR signalling. For example, the cytokine BAFF promotes B-cell survival through engagement of its

receptor BAFF-R[60]. At physiological levels, the competition for BAFF fine-tunes BCR-dependent signals and restricts the number of cells maturing, and increased BAFF availability leads to the development of autoimmunity[61]. BCR signalling may directly help control BAFF-R signalling in immature B cells by inducing downregulation of BAFF-R expression in autoreactive B cells compared to those exhibiting normal tonic signalling[60]. In conclusion, B-cell development requires a series of differentiation steps that rely on the expression of fully rearranged immunoglobulins, selected to encode receptors that are signalling-competent without reacting strongly to endogenous stimuli[52].

### 1.2.2. Naïve B-cell subsets

The majority of immature and transitional B cells maturing in the periphery differentiate into two distinct classes of B2 B cell - follicular (FO) B cells, and marginal zone (MZ) B cells. FO B cells (>70% of splenic B cells[62]) occupy highly dense B-cell follicle structures in the secondary lymphoid organs (SLOs), while MZ B cells (~15% of splenic B cells[62]) are mostly present in the marginal zone between the splenic white and red pulps[63]. Follicular B cells are the archetypal B2 B-cell subset, expressing BCRs which do not react to self-molecules, and taking part in T-cell-dependent B-cell responses[63] (further elaborated in Sections 1.2.3-1.2.5). Conversely, MZ B cells express BCR molecules which can bind to a broad range of self-molecules with low affinity[63]. MZ B cells play a central role in the production of low-affinity, polyreactive IgM antibodies, termed natural antibodies, which facilitate the clearance of novel pathogens and *self*-derived debris[63]. In line with this, transgenic expression of autoreactive BCRs may lead to MZ B cell differentiation, circumventing the need for

other factors[64]. MZ B cells can be activated by TLR signalling which, coupled with their broad BCR reactivity, initiates the induction of a rapid, innate-like humoral response[63]. In contrast to B2 B cells, B1 B cells have a distinct ontogeny and function[62]. B1 B cells, tissue-resident lymphocytes, express BCRs with reactivity against self-antigens, including modified lipid molecules, and against broadly shared antigens of pathogenic origin[65]. They produce antibodies without the need for receptor stimulation, contributing to the natural antibody repertoire[62].

### 1.2.3. Antigen presentation to B cells

The context in which B cells encounter antigens is central to their activation. B-cell antigens, unlike TCR ligands, are not restricted to a class of molecule and do not have to be present on cell membranes[66]. B cells can therefore respond to soluble proteins or membrane-bound targets[66]. While some naïve B cells reside in tissues (Section 1.2.2), most follicular B cells circulate through the body, entering the secondary lymphoid organs (SLOs), and transiently occupying specialised areas termed B-cell follicles[23].

Soluble proteins derived from blood or transported in lymph from sites of infection are transported to SLOs, where they can be recognised by cognate B cells[66]. Small soluble proteins entering lymph nodes have been shown to freely diffuse from their initial entry point in the subcapsular sinus (SCS) directly into the follicles and activate B cells[67]. Conversely, large antigens do not diffuse into the B-cell follicles[23]. These include immune complexes, assemblies of antigen bound to antibodies and deposited complement[23,68]. Immune complexes can be captured by macrophages lining the subcapsular sinus via complement interactions with target receptors (mainly CR3 in macrophages), and can be transported by non-cognate naïve B cells travelling into the

follicle, which express complement receptor 2 (CR2)[69]. In the follicle, B-cell migration is directed to the follicular dendritic cell (FDC) network, where complement-containing antigen assemblies are transferred to the FDC surface via binding to complement receptors CR2 and CR1[69]. These interactions are likely also facilitated by antibody binding to the IgG receptor FcγRIIb, expressed by all cell types mentioned[23]. FDCs are stromal cells which play a crucial role in B-cell activation, as antigen can be maintained on the FDC surface for extended periods of time via continuous endocytic recycling[70]. Recently, it has been suggested that protease activity is low in B-cell follicles, but not elsewhere in the lymph node, permitting the maintenance of intact antigen in this area specifically[71]. Macrophages and FDCs have been shown to play central roles in antigen presentation, but dendritic cells can also present antigen to B cells outside the B-cell follicle[72]. As such, while B cells can respond to antigen in solution, antigen molecules are also presented to B cells in the context of a cell surface.

### 1.2.4. B-cell activation

The activation of naïve B cells plays a central part in the generation of adaptive humoral immunity. B-cell activation often requires cellular signals provided by $CD4^+$ T cells, but in some circumstances, B-cell activation and immunoglobulin generation can occur in the absence of T-cell help.

Successful B-cell activation in the absence of T-cell help is predicated on the induction of TLR signalling by type 1 (TI-1) antigens, such as lipopolysaccharide, which drive the induction of a polyclonal response, as they do not engage the B-cell receptor[73]. Type 2 (TI-2) antigens are highly repetitive, polyvalent protein or polysaccharide motifs, which can engage cognate BCRs[73]. TI responses are therefore predominantly driven by

the TLR-expressing, polyreactive B1 and MZ B cell populations, which upon stimulation with these antigens and/or PAMPs can differentiate into short-lived antibody-producing cells to secrete cross-reactive, low affinity natural antibodies[62,63,65].

Conversely, FO B-cell activation relies predominantly on T-cell-dependent B-cell activation[39]. This involves a two-step response, whereby BCR signalling and subsequent antigen internalisation are complemented with signals derived from helper T cells. Upon antigen binding, the BCR complex induces a signalling cascade responsible for the induction of B-cell transcriptional changes[74] (Section 1.3). The BCR complex also undergoes clathrin-mediated internalisation upon antigen binding, leading to antigen uptake and processing[75]. Peptides derived from internalised antigens are presented to cognate $CD4^+$ T cells, and B-T cell interactions mediated by productive TCR signalling provide a series of important factors for B-cell activation[76]. CD40 signalling is initiated in response to interactions with CD40L on the T-cell surface, and potentiates transcriptional changes driving B-cell activation and proliferation[77]. The targeted release of cytokines by B-cell-engaged T cells, such as interleukins IL-4 and IL-21, also contribute to B-cell activation[78]. T-cell-derived signals are particularly important in the induction of the germinal centre response, which plays a central role in antibody evolution and selection[79].

### 1.2.5. The germinal centre reaction: an overview

The germinal centre is a complex multicellular structure driving the emergence of higher-affinity immunoglobulin variants[79]. Briefly, upon B-T cell engagement in the SLOs, productive B-cell activation can result in B-cell differentiation into short-lived,

antibody-producing plasmablasts[80] (Section 1.2.6). However, some activated B cells undergo a transcriptional program that leads to a hyperproliferative state[79]. These dividing germinal centre (GC) B cells express AID, a cytidine deaminase which can introduce point mutations to the assembled immunoglobulin genes (a process known as somatic hypermutation)[81]. The risks in expressing a highly mutagenic protein in GC B cells are partly mitigated by mechanisms directing the enzyme to immunoglobulin variable region sequences[81]. GC B cells are highly susceptible to apoptosis in the absence of T-cell help[82], and GC B cells expressing variants of the original receptor must compete for antigen to process and present[79]. As B cells expressing immunoglobulins binding the target antigen with higher affinity are more likely to successfully internalise and process antigen, they are more likely to receive T-cell-derived stimuli[76]. This iterative process leads to cycles of mutation and selection, allowing for the development of higher-affinity antibodies against target antigens (this process is known as affinity maturation)[79].

### 1.2.6. Antibody production

B cells are ultimately responsible for the production of antibodies, soluble variants of the membrane-bound immunoglobulin forming part of their BCR (Section 1.3). B cells can differentiate into antibody-producing cells, which can secrete soluble immunoglobulins[80]. In T-cell-independent B-cell responses, as well as those arising from TD responses prior to GC formation, short-lived plasmablasts can be generated to quickly produce antibodies in response to pathogens prior to affinity maturation[80,83]. In turn, GC B cells that successfully mature in the germinal centre can differentiate into plasma cells, long-lived cells which secrete high-affinity antibodies[80].

It is thought that the longevity of these cells is associated with their residence in specific niches in the bone marrow[84], and they form a key component of B-cell memory.

### 1.2.7. B-cell memory

Upon antigen exposure, the maintenance of a pool of memory lymphocytes plays a key role in long-term immunity. This is advantageous in that retaining clones generated in response to a pathogen allows for a more rapid response to be mounted upon re-challenge[85]. As described above, some antibody-secreting plasma cells are maintained in the bone marrow, secreting high-affinity antibodies after antigenic challenge[80]. However, antigen-experienced B cells can also differentiate into long-lived memory B cells, capable of responding to antigen upon rechallenge[86]. Memory B cells can be present in the circulation or reside in SLOs, but interestingly can also reside at sites of antigen encounter, until a second antigen encounter reactivates these clones[87]. Memory B cells can differentiate from GC B cells, maintaining high-affinity, antigen-specific clones in the B-cell repertoire[86]. However, activated B cells can differentiate into memory B cells without entering the GC reaction[88]. It has been suggested that these cells may form a reservoir of clones which have not been refined to bind to a specific variant of the antigen, retaining cross-reactivity to similar antigens which may exist or arise in future through pathogen evolution[88].

## 1.3. Immunoglobulins

### 1.3.1 Immunoglobulin structure and isotypes

The activation of antigen-specific B-cell clones, partly driven by their BCR specificity, is the mechanism by which cognate immunoglobulins are selected, affinity matured,

and produced as soluble proteins in response to antigenic stimulus[39]. The BCR is therefore the surface molecule responsible for sampling antigen, while antibodies are secreted effector molecules[39]. The two forms of immunoglobulins are produced as a result of the production of two alternative mRNA transcripts encoding the heavy chain[89].

Both types of immunoglobulins can be expressed as distinct isotypes, immunoglobulin variants containing the same variable regions but different constant domains (Fig. 1.2). Immunoglobulins can be classed as one of nine isotypes: IgM, IgD, four IgG classes (IgG1-IgG4), two IgA isotypes (IgA1 and IgA2) and IgE[90]. All immunoglobulins contain disulphide-bonded heavy and light chain pairs which form a covalently linked homodimer. Both heavy chains are disulphide-bonded, and each heavy chain is disulphide-linked to a single light chain, which can be classified as a κ or λ light chain depending on the constant light domain used[40].

Both secreted and membrane immunoglobulins share two functional regions. The first are Fab domains, composed invariably of the light chain in association with the variable heavy and the first constant Ig domain of the heavy chain (CH1)[40]. There are two Fab domains per molecule, and these are the minimal antigen-binding unit[40]. The second is the Fc region, composed of the remaining domains of the heavy chain. In human IgD, IgG, and IgA immunoglobulins, the constant heavy region contains an Fc domain composed of two Ig domains and a proline-rich, flexible hinge region which provides flexibility and rotational freedom to the Fab arms[91]. Conversely, IgM and IgE immunoglobulins do not possess hinge regions, instead containing an extra immunoglobulin domain in the Fc region[91]. Notably, IgD is quite variable across

vertebrate species, and murine IgD differs from the human isotype in that it contains a single Ig domain in its Fc region[92].

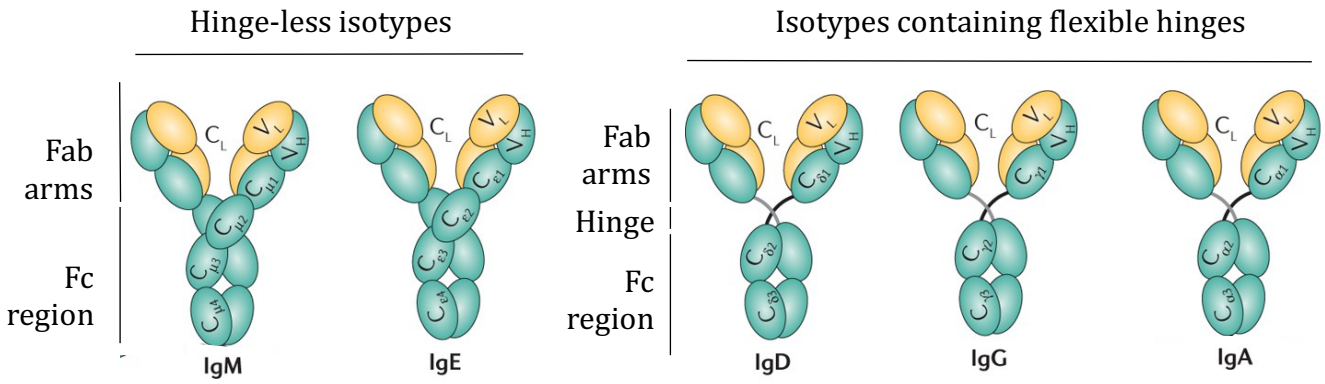



**Figure 1.2 | Diagram of the mammalian immunoglobulin isotypes.** Depiction of the five classes of immunoglobulin isotypes in mammals, with annotated individual Ig domains. Shown are the monomeric units of each isotype. Adapted from Duarte (ref. 91).

The majority of mature, naïve B cells express both IgM and IgD BCRs of the same specificity. These two isotypes are expressed as splice variants of the same genetic sequence and can therefore be co-expressed[93]. In FO B cells, the IgD BCR is overexpressed compared to IgM, while in MZ B cells and B1 B cells IgM expression is more prevalent[92]. Expression of IgG, IgA and IgE BCRs requires the excision of intervening DNA containing other constant region sequences, in a process known as class-switch recombination (CSR)[93]. CSR relies on the expression of the mutagenic enzyme AID (Section 1.2.5), which is directed to transcriptionally active switch (S) regions preceding constant domain sequences[93]. DNA breaks introduced to resolve these mutations, and their subsequence resolution, lead to the joining of the sequences of the previously active and the newly transcribed switch regions, excising the previously used constant domain sequences[94]. Cytokine-derived signals specifically activate transcription of different constant domain genes, and in this manner soluble

factors derived from T cells and other cell types can modulate the production of specific immunoglobulin isotypes with functions more appropriate to a given immune stimulus. For example, IL-4 can skew class-switching to IgG1 or IgE, while IFN-γ can induce CSR to IgG2a[95]. The germline organisation of the constant domain genes controls the possible isotype switching that can occur since, depending on the current isotype, DNA sequences for other constant domains may have already been excised from the genome[93].

In T-cell-dependent responses, T-cell-induced CD40 and IL-4 signalling induces AID expression, promoting both CSR and somatic hypermutation[93]. However, T-cell-independent stimuli, namely concurrent BCR and TLR signalling, can also transiently activate AID and induce CSR[93,96]. As such, the induction of different immunoglobulin isotypes does not always rely on $CD4^+$ T cell help.

### 1.3.2 The BCR complex

The membrane-bound immunoglobulin (mIg) is present on the B-cell surface as part of the BCR complex. This complex is composed of membrane-spanning mIg, which is noncovalently associated with a heterodimeric complex (Figure 1.3). This heterodimer is composed of two proteins, CD79A and CD79B (also known as Igα and Igβ, respectively)[36]. These are transmembrane proteins containing extracellular domains composed of membrane-proximal connecting peptides and a single Ig domain[97–99]. These two molecules are covalently linked via a disulphide bond formed by cysteines in their extracellular domains[100]. CD79A and CD79B each have an immunoreceptor tyrosine-based activation motif (ITAM) on their cytoplasmic sequence[58]. ITAM sequences comprise two tandem sequences (YxxL/I) separated by six to eight

residues[101] (Section 1.4.1). The mIg complex and the CD79 heterodimer associate in a 1:1 stoichiometry, as initially shown using biochemical data[36] and Förster resonance energy transfer (FRET) studies[102].

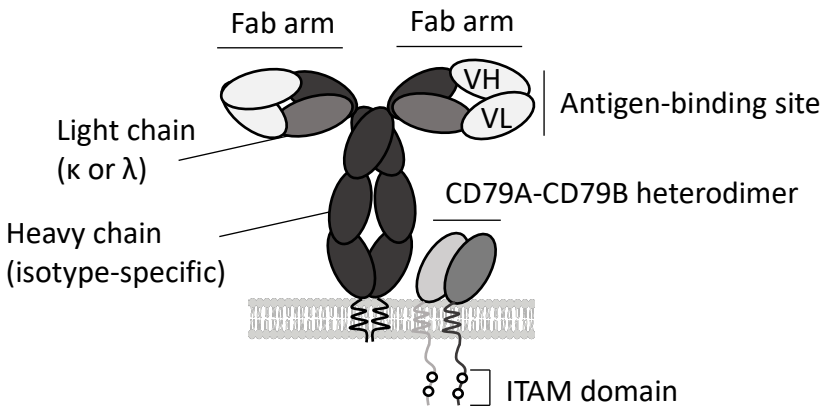



**Figure 1.3 | Schematic representing the key features of the (IgM) BCR complex.**

This assembly occurs in all BCR isotypes and is essential for correct receptor folding for almost all isotypes[103]. It is thought that in the absence of any of the four chains of the receptor, the complex is retained in the endoplasmic reticulum[104,105], with CD79A incorporation forming the last step in this assembly[105]. This process, which relies on the release of the complex from the ER chaperone calnexin upon CD79A binding[106], ensures only correctly folded BCR complexes are expressed on the cell surface. A possible exception is IgG (specifically IgG2b), which may be expressed on the cell surface in the absence of CD79A expression[103].

As described in Section 1.3.1, the Fab domains of the BCR complex are responsible for antigen binding, mediated by the variable regions[40]. In turn, the constant heavy chain of the membrane-bound immunoglobulins contain the Fc region, membrane-proximal

connecting peptides, transmembrane domains and cytoplasmic tails[107]. The heavy chain cytoplasmic tails vary depending on the isotype, containing a short sequence (KVK) in the case of IgM and IgD[92,107]. The longer tails of IgG, IgA and IgE BCRs may mediate interactions with cytoplasmic proteins[108]. IgG can recruit effector molecules directly to its cytoplasmic tails[109], affecting signalling outcomes *in vivo*[110,111]. However, in fully assembled BCR complexes, activatory signals are transduced through tyrosine phosphorylation of ITAM sequences in the CD79A and CD79B cytoplasmic tails[58]. The molecular structure of this complex, recently described in three studies[97–99], will play an important role in the experiments contained in this thesis.

### 1.3.3 Antibodies

Secreted immunoglobulins are produced by antibody-secreting cells, including plasmablasts and plasma cells[80]. Antibodies are key effector molecules in adaptive immunity[68]. While IgD, IgG and IgE antibodies are predominantly found in the monomeric state, IgM and IgA molecules can form higher-valency structures[91]. IgM pentamers can form in association with the soluble J chain protein[112], while both IgA isotypes can form dimeric molecules in association with the J chain and another chain, the secretory component[113].

Antibodies can serve an important role through neutralisation, where target molecules are impaired in their function due to antibody binding[38]. Antibodies also play an important role through the opsonisation of target surfaces. For example, IgM and IgG antibodies bound to target membranes can activate complement deposition onto these surfaces[114]. Importantly, Fc-mediated antibody functions rely on engagement of Fc receptors. Fcγ receptor (FcγR) binding to IgG molecules can produce both positive and

negative regulation of phagocytosis and other cellular functions[115]. Another example is the engagement of IgE by the FcεRI receptor on mast cells, which initiates degranulation in response to helminths and allergens[116,117], and will be further explored in Section 1.6. There are differences between the binding of human and mouse Fc receptors to the soluble immunoglobulins produced by each species[115], which are summarised in Supplementary Table 1 (Appendix A).

## 1.4. BCR signalling

### 1.4.1. Overview of initial events in BCR signalling

Upon antigen binding, the initial event in BCR signalling is the phosphorylation of the ITAM motifs in the CD79A or CD79B cytoplasmic tails[58]. The introduction of a phosphate group to the tyrosine residues in these sequences is mediated by Src-family kinases (SFKs)[118]. These molecules are acylated on residues in their SH4 domains, through which they are incorporated into the inner leaflet of the plasma membrane[119]. Upon antigen binding, active SFKs phosphorylate the receptor via their kinase domains[118]. Phosphorylated ITAM domains are recognised by the kinase Syk, in an interaction mediated by its two SH2 domains[120]. Binding to phosphorylated ITAMs results in both Syk phosphorylation by SFKs as well as auto-phosphorylation[118]. Phosphorylated, active Syk plays a central role in BCR signalling by phosphorylating downstream targets, leading to the activation of several signalling cascades[121] (Section 1.4.3). Syk may also play a role in signal amplification through transphosphorylation of other BCR molecules when bound to the receptor[122]. Control of BCR signalling is exerted by tyrosine phosphatases, in part through signal termination by the removal

of signalling-induced phosphate groups[123]. This balance of kinase and phosphatase activity, therefore, controls the dynamics of BCR signalling.

### 1.4.2. Tyrosine kinases and phosphatases in BCR signalling

**SFKs**

B cells express several Src-family kinases, including Lyn, Fyn and Blk, among others[124]. Knockout mice lacking expression of any given SFK do not show defects in B-cell development, with triple knockout of Lyn, Fyn and Blk arresting development at the pre-B cell stage, suggestive of impaired pre-BCR signalling[124]. However, Lyn is thought to be particularly important in BCR signalling[120], as Lyn-deficient B cells display poor survival post-development[125]. However, transgenic expression of the SFKs Fyn and Lck in Lyn-deficient B cells restores BCR phosphorylation, suggesting a redundant role among the different SFKs[126].

SFKs, including Lyn, diffuse on the inner leaflet of the plasma membrane, and rely on phosphorylation of a tyrosine residue in their kinase domain for their function[118]. They can be present in an autoinhibitory state resulting from the presence of a phosphorylated tyrosine that interacts with the Lyn SH2 domain, preventing access to the kinase domain[127]. In murine and human Lyn, this inhibitory tyrosine is located at Y508[118]. Phosphorylation of this residue by the kinase Csk and its removal by phosphatases, including CD45 and CD148[128] (see below), lead to an 'inhibited' and a 'primed' state, respectively[118]. The activation loop of SFKs can be phosphorylated in 'primed' molecules, leading to enhanced kinase activity[127]. This transition to the active state of Lyn is modulated by trans-autophosphorylation at Y397, which can in turn be removed by tyrosine phosphatases, including CD45[127].

Despite the key role of Lyn in BCR signalling, other SFKs have been found to play a role in initial ITAM phosphorylation[118]. It has been proposed that differential use of Lyn and Fyn kinases by distinct isotypes may play a role in differential signalling outcomes[129].

**Tyrosine phosphatases**

Tyrosine phosphatases play a crucial role in the modulation of BCR signalling. This occurs not just through their role in removing inhibitory tyrosine residues from SFKs, but by their control of signalling dynamics through the removal of tyrosine phosphorylation in Lyn, CD79A, CD79B and Syk[130–132]. An important class of tyrosine phosphatases are receptor-type protein tyrosine phosphatases (RPTPs), which in B cells includes CD45 and CD148[128,133]. These are membrane-spanning proteins containing large ectodomains and cytoplasmic tyrosine phosphatase domains[134].

CD45 is expressed on all leukocytes[123], and its ectodomain invariably contains four modular protein domains and a membrane-distal mucin-like region[135]. Different isoforms of CD45 are expressed across cell types, controlled by alternative splicing, producing variations in the length of the N-terminal mucin-like region[135]. B cells express predominantly the B220 isoform of CD45, the largest, most heavily glycosylated form of the molecule[136]. In B cells, CD45 plays a key role in modulating Lyn function, as explained above, by both promoting its primed state and dephosphorylating the tyrosine in its activation loop[137]. It has been suggested that CD45-knockout B cells display enhanced BCR signalling in the resting state[138] and are hyperactive in response to antigen[138,139]. This has been attributed to the loss of the

inhibition of active Lyn mediated by CD45, while Lyn priming can still be mediated by other phosphatases, particularly CD148[130]. It has been claimed that CD45 can directly dephosphorylate the ITAM domains of CD79A and CD79B, as observed *in vitro*[131].

CD148 is a membrane-spanning RPTP, containing a large ectodomain composed of eight to ten fibronectin domains[134], and an intracellular phosphatase domain[123]. CD148 has been predominantly implicated in potentiating BCR signalling through the removal of the inhibitory Lyn Y508 phosphorylation[130]. CD148 is also thought to play a role in dephosphorylation of active SFKs[140], although this may be a less important function compared to its activatory role[128]. As no early developmental block is seen in CD45- or CD148-deficient B cells, but is present in double-knockout cells, it is likely that there is a redundancy of both phosphatases in pre-BCR signalling[128].

Other tyrosine phosphatases are also involved in early BCR signalling. Examples include SHP1 and SHP2, cytoplasmic phosphatases which can be recruited by inhibitory receptors (Section 1.4.4) to the cell membrane, where they can dephosphorylate tyrosine residues on key proteins involved in BCR signalling[141]. SHP1 and SHP2 are thought to directly inhibit BCR signalling through dephosphorylation of CD79A and CD79B, as well as through dephosphorylation of Syk and other downstream effectors[132]. This is also evident in the observation that B-cell-specific abrogation of SHP1 expression in mice leads to B-cell hyper-responsiveness and autoimmunity[142].

### 1.4.3. Membrane-distal BCR signalling

ITAM phosphorylation and subsequent Syk activation are a central node in BCR signalling. Phosphorylated Syk initiates signalling through the phosphorylation of a

variety of target molecules, leading to transcriptional activation of genes modulating survival and proliferation[121] (Figure 1.4). Of particular importance is the phosphorylation of the adaptor molecule BLNK (also known as SLP65), to which several downstream effectors are recruited via SH2 domain engagement[143]. Among these is Bruton's tyrosine kinase (Btk), which enhances phosphorylation of other downstream molecules[144].

Phospholipase C γ2 (PLCγ2) is a key molecule phosphorylated by Syk and Btk, which produces the signalling molecules $IP_3$ and DAG[145]. $IP_3$ signalling leads to the release of intracellular calcium stores from the ER, increasing cytoplasmic calcium concentrations which in turn induces the nuclear translocation of the transcription factor NFAT[146]. Increased calcium and DAG production concomitantly contribute to the activation of protein kinase Cβ (PKCβ), which in turn activates MAP kinase (MAPK) signalling and induces the activation and nuclear translocation of NF-κB[144]. MAPK signalling in B cells contributes to both NFAT and AP-1 nuclear translocation[147].

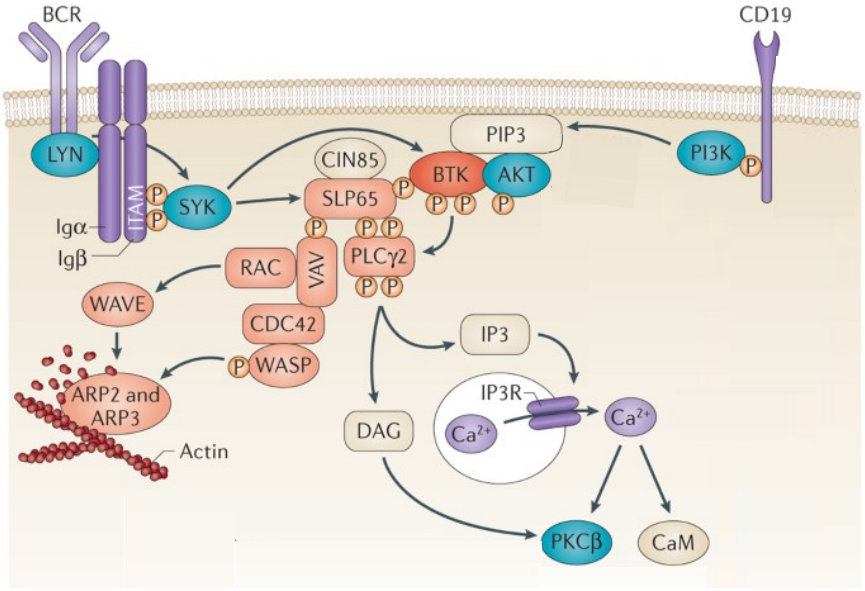



**Figure 1.4 | Events in BCR signalling.** ITAM phosphorylation by Lyn kinase drives recruitment of Syk, which phosphorylates and activates a variety of downstream targets. Of particular importance is the phosphorylation of the adaptor molecule SLP65 (BLNK), which recruits several other effector molecules, including Vav and PLCγ2. Transcriptional activation downstream of these events drives B-cell activation. CD19 also promotes these events via induction of PI3K signalling. Adapted from Hendriks and colleagues (ref. 144)

Although other factors are activated downstream of these signalling pathways, these transcriptional regulators are the key examples of receptor-mediated factors that control lymphocyte transcription of proteins involved in proliferation, survival and activation[148,149]. Other factors are recruited to BLNK upon Syk phosphorylation which potentiate B cell activation. Vav phosphorylation leads to reorganisation of the actin cytoskeleton[150], promoting the spreading response observed for B cells encountering membrane antigen[151] and facilitating BCR endocytosis and antigen uptake[152]. Grb2, another SH2-containing protein recruited to BLNK, further enhances MAPK signalling[153]. Finally, phosphoinositide 3-kinase (PI3K) signalling, which plays a key role in B-cell survival[154], is initiated by BCAP upon its phosphorylation by Syk and Btk[155]. In short, BCR-derived signals drive both morphological and transcriptional

modification through Syk phosphorylation, directing B-cell behaviour in response to antigen.

### 1.4.4. Accessory surface proteins in BCR signalling

Signalling downstream of the BCR is modulated by several surface proteins. Among these, CD19 is an essential modulator of BCR signalling. CD19 is associated with the tetraspanin CD81, and upon phosphorylation by active Lyn induces PI3K signalling, which through AKT phosphorylation produces signals directing B-cell survival[156]. CD19 does not possess a known ligand but can be found associated with the complement receptor CR2. It is therefore suggested that complement-tagged antigen co-ligates the BCR and CR2, bringing CD19 to sites of receptor phosphorylation and enhancing receptor signalling[156]. In line with this, tagging antigen with the CR2 ligand C3d enhances antigen-specific BCR signalling[157].

In contrast, engagement of some ligand molecules by receptors on the B-cell surface leads to downregulation of BCR signalling. In particular, CD22 and the antibody receptor FcγRIIb are expressed on the B-cell surface, and contain cytoplasmic immunoreceptor tyrosine-based inhibitory motifs (ITIMs)[141]. ITIM sequences in these two molecules can be phosphorylated by Lyn at sites of BCR signalling[141], promoting the recruitment of SHP phosphatases which in turn dephosphorylate BCR molecules[158,159]. FcγRIIb modulates BCR signalling in response to IgG molecules present in immune complexes[141]. In contrast, CD22 is thought to play a central role in tolerance to membrane self-antigens through binding of sialic acids on self-proteins on opposing membranes, promoting immune tolerance[160].

## 1.5. Models of BCR signalling

The signalling molecules involved in BCR signalling after antigen binding are well characterised (Section 1.4). However, the mechanisms through which antigen encounter leads to intracellular phosphorylation events initiating signalling are unclear[161]. Several models of receptor signalling have been proposed, which are described below.

### 1.5.1. Cross-linking model

The best-established model of BCR signalling is the cross-linking model, in which physical aggregation of receptors by multivalent antigens leads to signalling[162]. Early studies observed that anti-immunoglobulin antibodies and bivalent F(ab')2 fragments, but not monovalent Fab fragments, could induce lymphocyte proliferation[163,164]. Other studies have since suggested that multivalent antigen can induce BCR signalling, whereas monovalent antigen cannot[165–167]. While bivalent antigens induce BCR signalling *in vitro*, the BCR displays higher responsiveness to higher-valency antigens, as predicted by this model[166]. Multivalent antigens have been shown to bring receptors into close proximity, as assessed by FRET assays[102].

Moreover, BCR clustering may play a key role in the aberrant BCR signalling driving some B-cell malignancies. Some BCR clones in transformed B cells derived from chronic lymphocytic leukaemia (CLL) have been suggested to cluster via a homotypic interaction dependant on Fab self-recognition[168,169]. In CLL B cells, receptor clustering is associated with increased phosphorylated Syk, consistent with receptor self-association producing BCR signalling[170]. Constrained BCR diffusion, a marker of receptor clustering, is also observed in other B-cell malignancies, as is the association

of phosphorylation events and BCR clusters[171]. As such, BCR clustering may have an important role in the dysfunctional BCR signalling in transformed B cells.

The strongest arguments in favour of the cross-linking model in BCR signalling come from the effects that cross-linking induces *in vivo.* TI-2 B-cell responses rely on repetitive epitopes to induce strong BCR signalling, suggesting a role for multivalent binding in receptor signalling[73,172]. Another example of the potent BCR triggering induced by cross-linking is pan-specific BCR activation induced by superantigens. Superantigens such as the bacterial protein SpA can induce BCR cross-linking through repetitive binding to invariable epitopes in the immunoglobulin Fab arms, leading to extensive BCR signalling and subsequently cell death[173]. The well-noted enhanced signalling observed as a result of increased antigen valency plays a significant role in B-cell activation *in vivo*, with important consequences for vaccination strategies[174].

It is worth noting that several studies have reported BCR signalling in response to soluble monomeric antigen, in contrast to the studies cited above[175–178]. However, the main challenge to the cross-linking model has come from many studies describing BCR triggering in response to membrane-bound, monomeric antigen[139,167,179–181], which cannot be explained by the cross-linking model. In response to membrane antigens, distinct puncta of BCR accumulation (known as BCR microclusters) are formed as the B cell spreads over the target surface[139,179–181], ultimately contracting and accumulating antigen in a central cluster within the immunological synapse[181], as described for T cells[182]. These events occur even in response to monomeric antigen[139,167,179–181] and, as such, other models were introduced to explain the responsiveness to monomeric antigen in certain contexts.

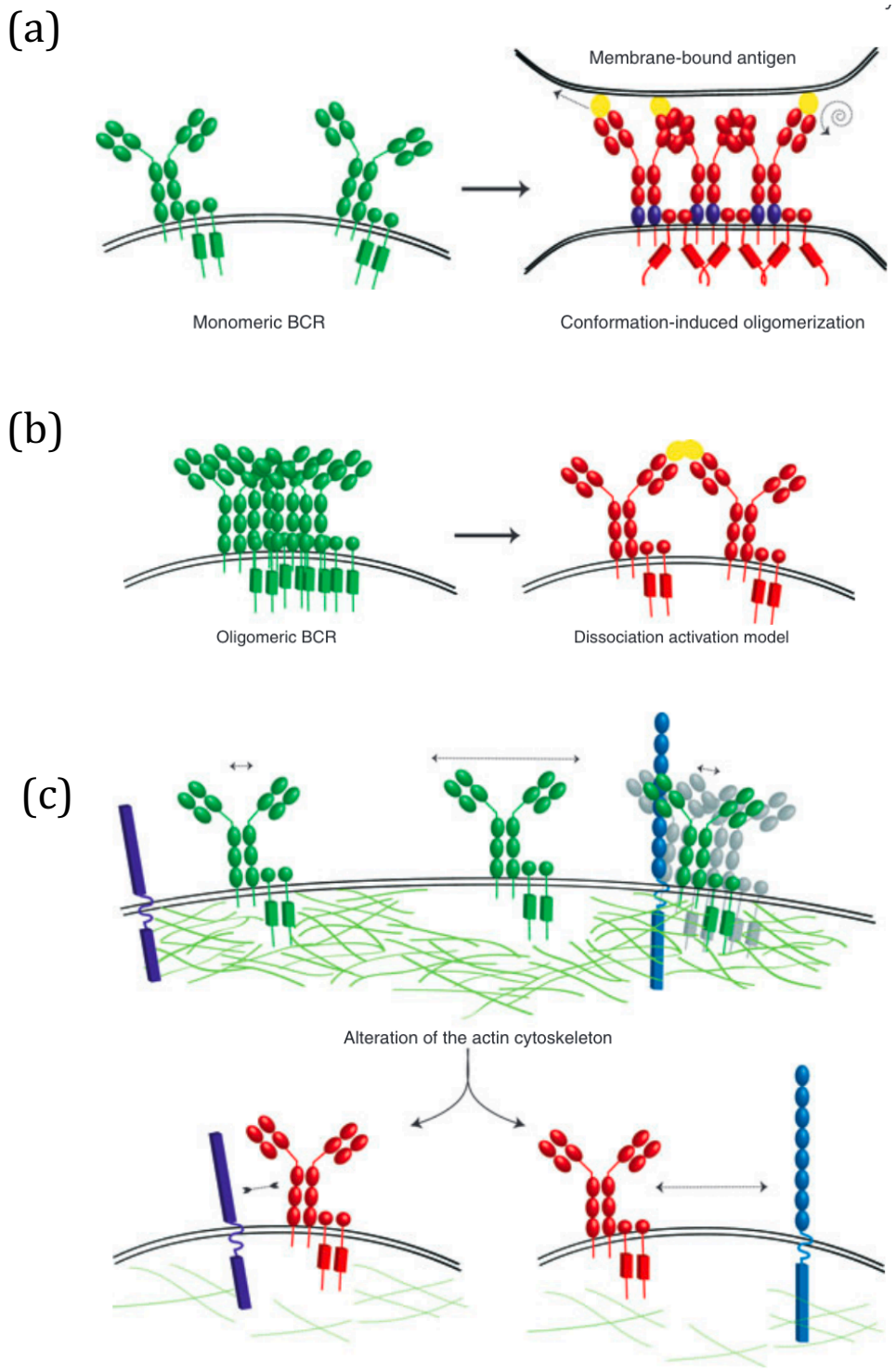



**Figure 1.5 | Alternative models of BCR signalling.** Proposed models to complement or replace the cross-linking model. **(a)** depicts the conformation-induced model, **(b)** depicts the dissociation-activation model, and **(c)** depicts the collision-coupling model. Green molecules represent inactive BCRs, red molecules represent activated BCRs. Purple and blue molecules represent activatory and inhibitory receptors, respectively. Adapted from Treanor (ref. 161).

### 1.5.2. Conformational-change oligomerisation model

The necessity to explain signalling induced by monovalent antigens presented to B cells on membrane surfaces led to the development of a model where antigen binding reconfigures receptor structure into a signalling-permissive conformation (Figure 1.5a)[26]. In this model, antigen binding modifies receptor conformation, exposing a previously occluded epitope which can then mediate receptor clustering, propagating signals in a similar manner to the cross-linking model[26]. Therefore, in this model, the BCR complex is predominantly monomeric in the resting state, clustering upon antigen-induced conformational changes. FRET studies had initially suggested that the BCR is distributed as a monomer on the cell surface[102], but this remains controversial (see Section 1.5.6).

As argued by Liu and colleagues, the well-known absence of conformational rearrangements within Fab fragments upon antigen binding in solution places constraints on the mechanisms by which antigen binding could cause allosteric changes to the BCR[26]. The conformational-change-induced oligomerisation model therefore relies on the induction of force by antigen in order to modify BCR complex organisation[183]. It has been demonstrated that force is induced on the BCR complex during antigen binding using atomic force microscopy, and that this event is essential for antigen internalisation[184]. It has been suggested that force exertion is increased in GC B cells compared to naïve B cells, relating to their differential ability to internalise antigen[185]. It has also been suggested that force exerted on the BCR complex is correlated to microcluster formation and signalling, and force thresholds may vary between BCR isotypes[186]. However, the direct mechanism by which force would modify BCR conformation has not been explored.

The modification of BCR conformation under force has been suggested to impact the stoichiometry of the complex by exposing a clustering motif in the membrane-proximal Cμ4 domain of IgM, which is inaccessible in the resting state. IgM displays intermolecular interactions in the structure of pentameric IgM, suggesting there are residues within the Fc region of the molecule that could mediate such interactions[112]. It has been demonstrated that antigen binding slows BCR diffusion, and that impaired diffusion dynamics rely on the presence of the Cμ4 domain of the IgM BCR[167]. The expression of a truncated receptor containing an ectodomain comprising only the Cμ4 domain spontaneously clustered on the cell surface in the absence of the other Fc region domains, suggesting the involved epitope may be occluded by the orientation of the other domains in resting receptors[167]. Similar effects were observed for the membrane-proximal Cγ3 domain of the IgG BCR, suggesting this may be a universal mechanism present in different isotypes[167]. It has been suggested that the binding of antigen on artificial lipid membranes may rearrange the Fab arms with respect to the Cμ2 domain, as confirmed by FRET experiments, and that this modification could be translated to the membrane-proximal domains of the mIg[187].

### 1.5.3. Dissociation-activation model

An entirely orthogonal signalling model has also been proposed to explain BCR signalling to both soluble and membrane antigens. The dissociation-activation model proposes that the BCR is an oligomeric unit on the resting B-cell surface, a conformation in which signalling is not permissible. Upon antigen binding, BCR clusters dissociate into signalling-competent monomeric units, initiating BCR triggering (Figure 1.5b)[188].

This model was predicated on solution data suggesting that detergent-solubilised BCR complexes extracted from resting cells could be found in oligomeric units[36]. This observation was further corroborated by studies conducted using bifluorescence complementation (BiFC) assays, which suggested transgenically expressed IgM and IgD BCRs are oligomeric on the surface of insect and B cell lines[189]. The opening of BCR clusters upon antigen binding was also visualised using proximity-ligation assays (PLA), and found to require phosphorylation by Syk kinase[190]. Other studies using PLA-based techniques have been used to support this result[178,191], and have suggested that monomeric soluble antigen can induce BCR signalling by disrupting the autoinhibitory geometry in BCR clusters[178]. There are limitations to these methods, in that BiFC assays are known to artificially create clusters by irreversible binding, as previously argued[161]. The presence of BCR clusters on the B-cell surface has been suggested by studies using super-resolution microscopy and will be reviewed in Section 1.5.6.

### 1.5.4. Collision-coupling model

The observation that BCR accumulation into small domains occurs upon interactions with an antigen-bearing membrane (Section 1.5.1) was followed by studies of whether such domains were present in the resting state. Super-resolution imaging studies have suggested that IgM and IgD BCRs in resting cells are found in distinct clusters in regions of actin polymerisation[192,193]. Within these clusters, BCR molecules display constrained diffusion, and may be spatially separated from kinase and co-receptor molecules[192,193]. Disruption of the actin cytoskeleton using latrunculin A led to BCR triggering, suggesting receptor release from these constrained sites allows interactions between the BCR and positive modulators of receptor signalling[192,193]. Similarly, it has been suggested that both the BCR and CD19 are co-localised in clusters

with the inhibitory molecule CD22 in the resting state[194]. The collision-coupling model therefore predicts that modifications to the actin cytoskeleton liberate constrained BCR molecules from co-association with inhibitory molecules and permit interactions with positive regulators of receptor signalling (Figure 1.5c)[161].

### 1.5.5. Kinetic-segregation model

Another theory of receptor signalling, which has not been directly explored in the context of BCR signalling, is the kinetic-segregation (KS) model. The KS model, initially devised to explain events in TCR signalling, suggests that immune cells interacting with ligand-bearing surfaces generate close-contact sites, with the distance between the cell membrane and the opposing surface dictated by receptor interactions and/or adhesion molecules[195]. The formation of zones of decreased intermembrane distance leads to the passive exclusion of proteins containing large, rigid ectodomains, which are sterically excluded from such contacts (Figure 1.6)[196].

The KS model explains productive signalling events by suggesting transient receptor phosphorylation, which occurs in the resting state, can be prolonged when receptors are present in phosphatase-depleted areas of membrane contact. In the resting state, transient phosphorylation events can be rapidly inhibited by RPTPs. However, upon close-contact formation, depletion of phosphatases by steric exclusion allows phosphorylation events to be sustained and propagated[195]. The key phosphatase CD45 contains a rigid ectodomain[135] which drives its exclusion from sites of T-cell contact with antigen-bearing membranes[134,135,197–200]. Decreasing the size of the CD45 ectodomain through the use of alternate ectodomains leads to phosphatase access in contact zones, which in turn blocks signalling[134]. Similar effects are observed at the

interface between macrophages and particles during FcγR-mediated phagocytosis[201,202], or that of mast cells and IgE-opsonised surfaces[203]. The large phosphatase CD148 is also excluded from sites of TCR engagement[134]. Receptor sensitivity to ligand affinity and density is thought to rely on the constrained diffusion of monomeric receptors generated by ligand binding, with high-affinity or multiple binding events increasing the 'dwell time' of the receptor within the contact and increasing the probability of receptor triggering[197,204].

Importantly, phosphatase exclusion has been shown to play a central role in tyrosine immunoreceptor signalling. Increasing the molecular height of ligands impairs TCR, FcγR and FcεRI signalling[200,202,203,205,206]. This is thought to occur through an increase in the size of the intermembrane gap[205,206], leading to impaired phosphatase exclusion. Similarly, truncation of the phosphatase ectodomain, or expression of chimaeric phosphatases with small ectodomains which are not excluded from contacts, impairs TCR[134,135], FcγR[202] and FcεRI[203] signalling in response to membrane antigens.

The role of phosphatase exclusion in the signalling outcomes by several other ITAM-containing immune receptors prompts the question of whether it can also influence BCR triggering. B cells often respond to antigen presented on cellular membranes *in vivo* (Section 1.2.3), and express both CD45 and CD148, as described above (Section 1.4.2). B cells express the B220 isoform of CD45[136], containing a highly glycosylated ectodomain, expected to have increased molecular height among CD45 variants[207,208]. Importantly, in B cells interacting with model lipid bilayers, CD45 exclusion from sites of antigen accumulation has already been described[139,179]. As such, the role of phosphatase exclusion in BCR signalling to membrane antigens merits further study.

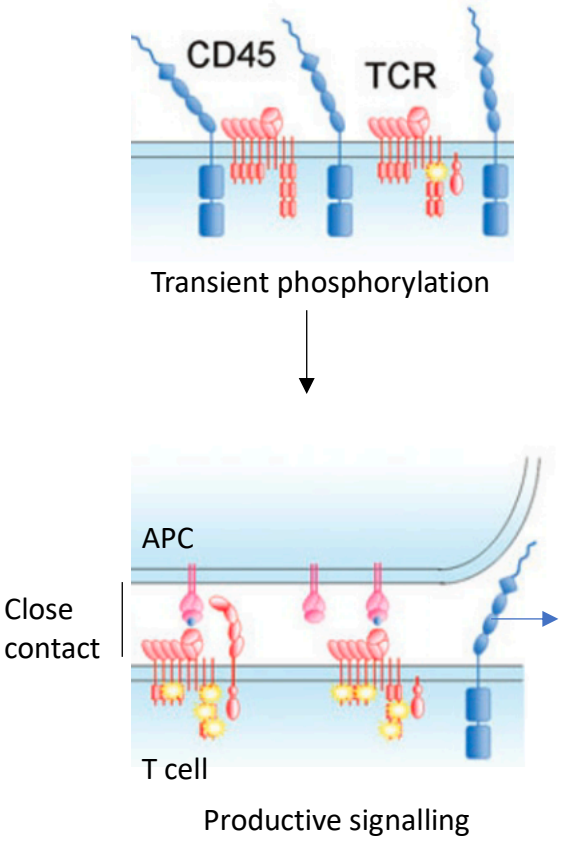



**Figure 1.6 | The kinetic-segregation (KS) model of receptor signalling.** In the resting state, ITAM-containing receptors (red) are transiently phosphorylated, but this is quickly reversed by the phosphatase CD45 (blue). Upon surface engagement, a close contact between membranes is formed which sterically excludes large phosphatases, extending phosphorylation time and permitting downstream signalling. Shown is TCR signalling as an example. Adapted from Davis and van der Merwe (ref. 195).

### 1.5.6. Organisation of the resting BCR complex

The models described above vary in their predictions of receptor behaviour prior to and following antigen binding. In particular, the cross-linking, force-induced oligomerisation and kinetic-segregation models predict receptors to exist as monomeric units in the resting state, while the dissociation-activation and collision-coupling models predict oligomeric BCR assemblies to exist in the resting state.

Extensive effort has gone into clarifying the contradictory observations that the receptor is either monomeric[102] or oligomeric[178,189] in the resting state. Studies using super-resolution microscopy have aimed to pinpoint the localisation of individual receptor molecules with sub-diffraction precision[209], mapping the distribution of the receptor on the cell membrane. These have predominantly used direct stochastic optical reconstruction microscopy (dSTORM[209]) to achieve this, and the results have generally suggested the receptors can form clusters in resting cells. Mattila and colleagues described the distribution of IgM and IgD molecules on the surface of primary murine B cells, suggesting that ~70% of IgD molecules and ~38% of IgM molecules existed in separate nanoclusters, structures ranging between 60 and 80nm in radius[192]. Maity and colleagues, however, suggest IgM and IgD BCRs form distinct 'protein islands', sensitive to actin depolymerisation[191]. IgM and IgD islands had an average radius of 151nm and 240nm, respectively, and contained 30-50 receptors per island[191]. Cao and colleagues described IgM BCR nanoclusters containing ~30 receptors within a 20nm radius[210]. Overall, these studies have suggested that the BCR is not randomly distributed in the resting state, with variations in the number and size of the clusters. Notably, the propensity for dSTORM studies to artefactually induce clustering due to overcounting molecules has recently been highlighted. Recent studies using variable-density labelling of the TCR in T cells showed that using novel methodologies to account for this can alter the predicted stoichiometry of receptors, in this case suggesting that the TCR is predominantly monomeric[211,212] rather than in the clustered state suggested by earlier studies[213,214].

Conversely, recent studies using stimulated emission depletion (STED) microscopy on the surface of primary human B cells have suggested that IgM BCRs on the cell surface

are predominantly monomeric complexes[168]. This was further validated with dSTORM imaging, which suggested IgM BCR molecules were as randomly distributed as free dye plated on a glass slide[168]. As such, the resting distribution of the receptor on the cell surface remains controversial, despite having important implications for the proposed models of BCR signalling.

## 1.6. FcεRI signalling

### 1.6.1. IgE-mediated immunity

As described above (Section 1.3.3), antibody function is partly mediated by interactions with Fc receptors on effector cells. Among these, the high affinity IgE Fc receptor, FcεRI, is a key component of IgE-mediated immune responses[215]. Although the FcεRI receptor is expressed on a variety of cell types (Section 1.6.2), particular interest has been given to the effect of IgE engagement on mast cells[216]. Mast cells are tissue-resident granulocytes which can respond to various stimuli, releasing cytotoxic, proteolytic, and pro-inflammatory mediators upon ligand engagement[18]. IgE antibodies generated in response to helminth-derived antigens[117], venoms[217] and allergens[218] have been shown to induce degranulation of mast cell vesicles. Importantly, FcεRI is thought to be another immunoreceptor for which responsiveness to antigen is predominantly initiated by receptor cross-linking (Section 1.6.4), as in the case of the BCR (Section 1.5). Moreover, understanding IgE-mediated immunity in allergy is essential, as allergen-driven FcεRI signalling has emerged as a key driver of allergic disease[218].

### 1.6.2. FcεRI structure and function

The FcεRI complex is composed of three subunits: FcεRIα, FcεRIβ and FcεRIγ. In the presence of all three chains, it assembles in an $\alpha\beta\gamma_2$ tetrameric stoichiometry, with the α and β chain noncovalently associated with a disulphide-bonded $\gamma_2$ homodimer. This form of the complex is expressed in mast cells and basophils[219]. However, some antigen-presenting cells, including DCs, can express the complex in the absence of FcεRIβ, forming a trimeric $\alpha\gamma_2$ complex[219].

In mast cells and basophils, FcεRI plays a central role in the release of effector molecules in response to allergens and helminths. The antigen specificity of the FcεRI-mediated response is determined by the specificity of the IgE antibody engaging the receptor[38]. The high affinity interaction between IgE and FcεRI ($K_D$~0.1-1nM)[220] allows long-term binding of the IgE molecule to the receptor. Due to the low half-life of free IgE *in vivo*, and the fact FcεRI-bound complexes seem to be preferentially retained on the cell surface, signalling events are thought to rely on long-lived IgE-FcεRI complexes on the surface of mast cells and basophils signalling in response to antigen[221], rather than FcεRI responsiveness to IgE-opsonised antigens. Sequestration of free soluble IgE leads to a decrease in FcεRI expression levels in mast cells, yet this decrease takes up to 70 days to occur, confirming that the retention of IgE-bound complexes on the cell surface and the long-term binding of IgE to the mast cell surface both occur[222].

Mast cells and basophils release several effector molecules within minutes of antigen engagement[221]. This is mostly due to the release of pre-synthesised effector molecules from storage vesicles (a process known as degranulation)[221]. Degranulation leads to

the release of proteases, including tryptase and chymases, as well as inflammatory agents, such as histamine and pro-inflammatory cytokines, including TNFα[215]. Moreover, IgE-mediated signalling leads to the rapid production of eicosanoids, lipid-derived molecules which promote a variety of inflammatory effects in tissues, including vasodilation and the chemoattraction of other effector cells[223]. As such, the function of these cells in response to IgE antigens plays a role in the rapid response to many antigenic determinants, typified by the immediate hypersensitivity response in allergy[218].

### 1.6.3. Events in FcεRI signalling

The initial events in FcεRI triggering are similar to those occurring in other immunoreceptors (see Section 1.4). Phosphorylation of ITAM domains in FcεRIβ and FcεRIγ plays a critical role in the initiation of FcεRI signalling. This is mediated by SFKs, which in mast cells include Lyn and Fyn[219]. As in BCR signalling, Lyn is thought to be the predominant kinase involved in ITAM phosphorylation[216]. The control of these SFKs in mast cells is similar to that described in B cells (Section 1.4.2), with CD45 playing a key role in priming Lyn kinase through removal of the autoinhibitory tyrosine[123]. This is highlighted by studies suggesting that CD45-deficient mast cells cannot degranulate in response to cross-linking of receptor-bound IgE[224]. Lyn trans-autophosphorylation allows the enzyme to become active[127], phosphorylating ITAM tyrosine residues on FcεRIβ and FcεRIγ[219]. Phosphorylated ITAM residues recruit the kinase Syk via its SH2 domains, and Lyn-dependent phosphorylation of Syk is essential for FcεRI signal initiation[225]. In addition to the key roles of Lyn and Syk in FcεRI signalling, Fyn kinase has also been implicated in ITAM phosphorylation and may initiate a distinct signalling cascade upon FcεRI phosphorylation[226].

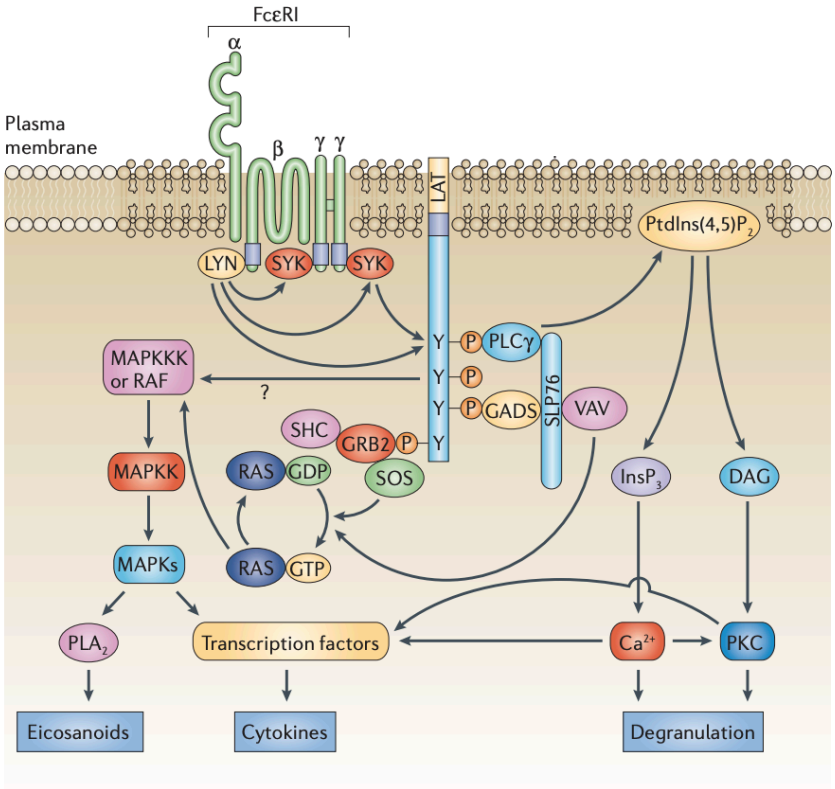



**Figure 1.7 | Events in FcεRI signalling.** FcεRI engagement leads to receptor ITAM phosphorylation by Lyn and recruitment and activation of Syk kinase. Phosphorylation of target molecules by Syk, particularly the adaptor molecule LAT, drives recruitment and phosphorylation of downstream effector molecules. In mast cells, phosphorylation events downstream of Syk lead to degranulation, eicosanoid synthesis and transcriptional changes driving cytokine production. Adapted from Gilfillan and Tkaczyk (ref. 216)

These initial events in FcεRI signalling mimic those that occur upon BCR stimulation. However, the downstream targets of Syk in mast cells are distinct from those expressed in B cells (Figure 1.7). Mast cells express different adaptor molecules, including the linker protein LAT[216], an important component in signal integration in T cells[227]. LAT phosphorylation by Syk induces the recruitment of downstream effector molecules to LAT, facilitating their activation by Syk phosphorylation[216]. Among these, the proteins Vav and Grb2, already described above (Section 1.4.3), mediate activation of MAPK signalling pathways, as well as cytoskeletal modifications[228]. MAPK signalling

also leads to the activation of phospholipase A2 ($PLA_2$), which initiates the rapid synthesis of eicosanoids from arachidonic acid[223]. Mast cells express two phospholipase Cγ enzymes, PLCγ1 and PLCγ2, which upon recruitment to LAT and subsequent phosphorylation promote the generation of the signalling molecules $IP_3$ and DAG[216]. As in BCR signalling, these molecules promote increases in intracellular calcium concentrations and protein kinase C (PKC)-dependent transcription factor activation (Section 1.4.3). Both these events promote the nuclear translocation of transcription factors[229], which together with MAPK signalling trigger the expression of cytokines. In mast cells, these signals also induce degranulation and the rapid release of effector molecules[216]. It has also been suggested that a second adaptor molecule, NTAL, might initiate a separate signalling cascade to LAT, inducing PI3K signalling in mast cells[216].

### 1.6.4. Mechanisms of FcεRI signalling

As described above, FcεRI signalling plays an important role in the antigen-specific response of mast cells and basophils. However, the mechanisms by which antigen binding leads to signalling have not been fully determined. IgE-FcεRI complexes are thought to be the minimal antigen binding unit of the receptor (Section 1.6.2).

The main mechanism proposed for FcεRI signalling has been receptor cross-linking. Early studies had concluded that receptor crosslinking by bivalent antigens or anti-IgE induced mast cell degranulation[230]. The same effect can be induced by anti-FcεRIα antibodies[231]. The multivalent nature of some allergen molecules reinforces this concept[232]. The crystal structure of dimeric β-lactoglobulin simultaneously bound by two Fab arms derived from the IgE repertoire of an allergic patient are one example of

how allergic IgE may be directed to repeated epitopes capable of inducing receptor cross-linking[233].

However, as in the case of the BCR, evidence has emerged that the receptor can signal to monomeric IgE in certain contexts. Cytokinergic antibodies are a class of IgE molecules capable of inducing FcεRI signalling in the absence of antigen, a scenario where monomeric IgE molecules are likely inducing signalling[234]. The most studied cytokinergic clone, SPE-7, can induce FcεRI triggering and downstream calcium signalling and morphological changes in the absence of antigen[235]. However, it has been suggested that the cytokinergic potential of certain IgE clones is itself dependent on induced cross-linking. SPE-7 activity is disrupted by binding to its ligand, the hapten DNP[235]. Moreover, the same inhibition of signalling is observed when cell-bound SPE-7 is blocked by addition of an SPE-7 Fab fragment[236]. This has led to the proposal of a model whereby homotypic interactions directed by the variable regions of cytokinergic antibodies drive receptor cross-linking in the absence of antigen[236,237]. As such, even monomers that induce signalling in solution may do so through receptor cross-linking. Despite this, FcεRI signalling has been shown to occur in response to monomeric antigens when coordinated on a surface. Early studies demonstrated that rat basophil cell lines could respond to monomeric haptens incorporated into lipid bilayers[238]. More recently, it has been shown that basophils respond to monomeric IgE Fc fragments diffusing on fluid lipid surfaces, a process which required CD45 exclusion[203]. In short, the mechanisms driving FcεRI signalling are still under investigation, and may involve several concomitant factors, as discussed for the BCR (Section 1.5).

## 1.7 Aims of this thesis

The work in this thesis seeks to test some of the predictions of various models of immune receptor signalling using both single-molecule methods and functional assays, with a focus on receptors traditionally thought to signal through cross-linking, i.e. the BCR and FcεRI. In Chapter 3, using a novel super-resolution imaging method, the three-dimensional distribution of the BCR on resting B cells will be explored. This will seek to elucidate the stoichiometry of the receptor, a key prediction of several proposed models of receptor signalling (Section 1.5.6). In Chapter 4, the effects of antigen molecular height on BCR signalling will be examined using an artificial membrane model, testing a key prediction of the KS model of receptor signalling (Section 1.5.5). In Chapters 5 and 6, fully assembled BCR and FcεRI receptor complexes will be purified in the presence and absence of their ligands from mammalian cells for analysis using cryo-electron microscopy (cryo-EM), with the goal of elucidating the intramolecular interactions driving receptor assembly and signalling by these important receptors.

# Chapter 2. Materials and Methods

## 2.1 Cell culture

Eukaryotic cell culture was conducted under Category 2 conditions in HEPA-filtered biological safety cabinets, using sterile medium and supplements. Cell cultures were generated by rapidly thawing cells from frozen stocks. Thawed cells were diluted in culture medium, centrifuged at 526g for 5 minutes, and placed into culture in an adequate volume and surface area. Cell density and viability were assessed through dilution in an equal volume of 0.4% trypan blue solution, using an automatic cell counter (Countess II) or a haemocytometer. When required, cells were subcultured into fresh sterile flasks. Suspension cells were subcultured by dilution into fresh medium and maintained at the recommended densities (see Table 2.1). Adherent cells were washed in sterile PBS and detached from the surface through incubation in 0.25% (w/v) porcine trypsin in PBS, unless otherwise specified. The trypsin solution was diluted in culture medium, cells were collected and centrifuged at 526g for 5mins, and resuspended in fresh culture medium. A subset of the resuspended cells was plated into a fresh tissue culture flask in an adequate final volume of culture medium based on the culture confluency. Cell lines were stored by cryo-preservation. Suspension or lifted adherent cells were pelleted at 526g for 5mins and resuspended in freezing solution (foetal calf serum (FCS) supplemented with 10% (v/v) DMSO). Cells were aliquoted into cryovials and frozen at -80°C, using a freezing chamber to produce a gradual decrease in temperature. For long-term storage, cryovials were maintained in liquid nitrogen storage.

| Culture type | Cell line | Species | Culture medium | Density range | Culture conditions |
|---|---|---|---|---|---|
| Suspension cells | A20 (ATCC TIB-208) | *Mus musculus* (BALB/c) | RPMI-1640 + 10% (v/v) FCS + 6mM L-Glutamine + 10mM HEPES + 50U/mL Pen + 50µg/ml Strep + 100µg/ml Neo + 50µM 2-mercaptoethanol | $10^5$-$10^6$ cells/mL | 37°C, 5% $CO_2$ |
| | CHO-S (ThermoFisher, Cat. No. R80007) | *Cricetulus griseus* | FreeStyle CHO Expression medium + 8mM L-Glutamine | | 37°C, 8% $CO_2$, 125rpm, 80-85% humidity |
| Adherent cells | HEK293T (ATCC CRL-3216) | *Homo sapiens* | DMEM + 10% (v/v) FCS + 4mM L-Glutamine + 1mM sodium pyruvate + 50U/mL Pen + 50µg/ml Strep + 100µg/ml Neo | 10-100% confluency | 37°C, 5% $CO_2$ |
| | CHO-K1 (ATCC CCL-61) | *Cricetulus griseus* | DMEM (Gibco, 10938-025) + 10% (v/v) FCS + 2mM L-Glutamine + 1mM sodium pyruvate + 50U/mL Pen + 50µg/ml Strep + 100µg/ml Neo | | |
| | NIH/3T3 | *Mus musculus* (NIH/Swiss) | DMEM + 10% (v/v) FCS + 2mM L-Glutamine + 50U/mL Pen + 50µg/ml Strep | | |

**Table 2.1** | Cell culture conditions for cell lines used in this work. Pen – penicillin; strep – streptomycin; neo – neomycin.

## 2.2 Molecular biology

### 2.2.1. DNA cloning

#### Vectors used in this work

Plasmids were used for protein expression in target cells. DNA constructs were introduced into these vectors through restriction cloning. These were obtained through direct amplification of sequences from templates through PCR, or by purchasing synthesised dsDNA gene fragments (gBlocks, IDT). For the expression of mammalian proteins, DNA sequences encoding the target protein were introduced into the pHR lentiviral vector, downstream of the SFFV viral promoter. The pHR plasmid contains a WPRE sequence and encodes the ampicillin resistance gene AmpR for antibiotic selection. For bacterial protein expression, constructs were cloned into the pET28a(+) vector, downstream of a T7 polymerase-dependent promoter. The pET28a(+) encodes a kanamycin resistance gene (KanR) for antibiotic selection.

#### Polymerase chain reaction

Amplification of target DNA was achieved using a Phusion polymerase enzyme. DNA oligonucleotides flanking the region for amplification (Merck) were designed using SnapGene (version 4.1.9). Polymerase chain reactions (2x 20.25µL reactions) were set up as follows:

| Reagent | Volume (µL) |
|---|---|
| MQ water | 28 |
| HF buffer (5x) | 8 |
| dNTPs (10mM) | 1 |
| Forward primer (10µM) | 1 |
| Reverse primer (10µM) | 1 |
| Template DNA (20-50ng/µL) | 1 |
| Phusion polymerase (2U/µL) | 0.5 |
| TOTAL | 40.5 |

**Table 2.2** | Reagent volumes used for PCR DNA amplification.

DNA amplification was achieved through denaturation of the template at 95°C for 3mins, followed by repeated cycles of denaturation (95°C, 10s), annealing (at 55°C, 20s) and elongation (at 72°C, for 30s per kilobase), with a final incubation at 72°C for 10mins. Restriction sites were introduced into the 5' and 3' ends of amplified DNA to allow digestion and insertion into linearised plasmid DNA. PCR products diluted 5:1 in Purple Loading Dye (NEB) were loaded on a set agarose gel containing 1% (w/v) agarose in TBE (89mM Tris, 89mM boric acid, 2mM EDTA) supplemented with 0.5µg/mL ethidium bromide (EtBr). DNA was separated by gel electrophoresis in TBE buffer at 100V for 40mins. EtBr-stained DNA was visible under UV light. DNA fragments of the correct size were sectioned from the gel under UV illumination, and isolated using a QIAquick Gel Extraction Kit (Qiagen).

**Restriction enzyme digest**

To introduce target sequences into plasmids, both the plasmid and the insert were digested using restriction enzymes (NEB). In most cases, two distinct enzymes cleaving different sequences on either terminus were used to maintain directionality. All NEB enzymes used displayed 100% efficiency in CutSmart buffer (NEB) at 37°C, so this buffer was used for all digestions. Up to 2.5µg vector DNA, or PCR products, were diluted in a final volume of 50µL 1x CutSmart buffer, supplemented with 800 units/mL of each enzyme. Plasmids were digested by incubation at 37°C for 1-3h.

For vector DNA, the digested products were separated by gel electrophoresis and gel extracted (as described above) to ensure only the fragment of interest was purified. For PCR products that had previously been gel extracted, the digested DNA was purified using a QIAquick PCR purification kit (Qiagen).

**DNA Ligation**

To ligate DNA fragments onto plasmid backbones, 100ng of digested backbone was incubated with equimolar amounts of digested insert DNA in 20µL 1x T4 DNA ligase buffer (NEB), supplemented with 20000 units/mL T4 DNA ligase (NEB). Ligations were conducted at 16°C overnight and stored at 4°C.

### 2.2.2. Plasmid preparation

**Transformation**

To reamplify plasmids, or to purify plasmids generated through restriction cloning, DNA was transformed into chemically competent TOP10 *E. coli* cells. Cells were incubated with DNA mixtures for 30mins on ice. Cells were heat-shocked for 45s at 42°C and incubated for 1 minute on ice. Cells were topped up to a final volume of 200µL in lysogeny broth (LB) and incubated at 37°C for 1h. Cells were plated into LB agar supplemented with the required antibiotics. For pHR amplification, growth medium was supplemented with 100µg/mL ampicillin. For pET28a(+) amplification, growth medium was supplemented with 50µg/mL kanamycin. Plates were incubated at 37°C for 16h and stored at 4°C for up to one week.

**Plasmid preparation**

10mL (for high copy number plasmids) or 50mL (for low copy number plasmids) cultures of LB supplemented with adequate antibiotics (as described above) were inoculated with single colonies of antibiotic-selected, transformed bacteria. Cultures were incubated at 37°C for 16h with rotation. Cells were collected by centrifugation at 3739g for 30mins. DNA was extracted from bacterial pellets using a PureLink HiPure Miniprep kit (Invitrogen) according to the manufacturer's instructions.

DNA concentration and quality was verified using a NanoDrop One spectrophotometer by assessing absorbance at 260nm and 280nm, and by agarose gel electrophoresis. DNA sequences of plasmid inserts were verified through Sanger sequencing conducted by a third-party company (Source Bioscience) and validated against the predicted sequence using the SnapGene software (version 4.1.9).

### 2.2.3. Lentiviral transduction

#### Lentivirus production

Lentiviral particles were used to stably transduce cell lines with genes of interest, through genomic integration of LTR-flanked inserts from lentiviral backbones. VSV-pseudotyped 3rd generation lentiviral particles were generated by co-transfection of lentiviral plasmids (pHR) with p8.91 and pMD2.G, which encode the HIV gag/pol, tat and rev proteins, and the VSV-G glycoprotein, respectively[239,240].

HEK293T cells were used as a packaging cell line. Cells were trypsonised, resuspended at $0.5x10^6$ cells/mL, and 6-well plates were seeded with $1x10^6$ cells per well. The following day, cells were transfected with the plasmids of interest at ~80-90% confluency. For each well, 1µg of lentiviral plasmid (pHR) was incubated with 0.5µg p8.91 and 0.25µg pMD2.G in 100µL DMEM medium without supplements. 4.5µL GeneJuice Transfection Reagent (Merck) was added to the mixture, and the sample was incubated for 30mins at room temperature. The mixture was added dropwise to the cells. Transfected HEK293T cells were incubated for 48-72h in culture. Supernatant containing lentiviral particles with the incorporated DNA of interest was collected, filtered using a 0.45µm PES membrane filter, and used immediately to transduce cell lines.

**Lentiviral transduction**

Cells were incubated directly with lentiviral supernatant in a minimal volume, and restored to normal culture volumes. Unless otherwise stated, $10^6$ cells were incubated with 2mL viral supernatant for 24h, then diluted to an adequate density in their normal culture medium.

## 2.3 Flow cytometry

### 2.3.1. Labelling cells

Surface expression of proteins of interest was verified using flow cytometry. Detection was conducted using either recombinant antibodies against target proteins (Section 2.3.2) or recombinant probes purified and labelled in-house (see Section 2.4.9). For antibody staining, $0.5x10^6$ cells were harvested by centrifugation at 395g (935g for primary cells) for 2 minutes, washed once in PBS and stained in 50µL of antibody diluted in PBS at the concentrations recommended by the manufacturer, unless otherwise specified. Where fluorescent recombinant proteins were used, cells were stained using a solution of 40µg/mL fluorescent probe in PBS, unless otherwise specified.

Cells were stained for 30mins at 4°C, washed twice in 200µL PBS, and fixed in a solution of 1% (w/v) PFA in PBS at room temperature. Fixed cells were analysed using an Attune NxT system (ThermoFisher) using appropriate excitation lasers and filters. Control staining using isotype-matched antibodies was used to assess background binding to cells.

### 2.3.2. Antibodies used

| Target molecule | Clone | Isotype | Fluorophore | Catalogue no. | Supplier |
|---|---|---|---|---|---|
| mCD79b | HM79-12 | Hamster IgG | PE | 132804 | Biolegend |
| mCD45 | 30-F11 | Rat IgG2b,κ | PE | 103102 | |
| | | | AF647 | 103124 | |
| mCD45 (B220) | RA3-6B2 | Rat IgG2a,κ | PE | 103208 | |
| hIgM | MHM-88 | Mouse IgG1,κ | PE | 314508 | |
| hIgκ | MHK-49 | Mouse IgG1,κ | PE | 316508 | |
| hCD79B | CB3-1 | Mouse IgG1,κ | PE | 341404 | |
| hFcεRIα | CRA-1 | Mouse IgG2a,κ | PE | 365303 | |

**Table 2.3** | Antibodies used for experiment in this thesis. Targets prefixed with m- are murine proteins; h- for human proteins.

## 2.4 Production of soluble proteins

### 2.4.1 Protein design and purification overview

Protein sequences were designed with reference to the published literature. Where sequences were sought for full-length mammalian proteins, the consensus sequence and domain architecture as defined in the UniProt[241] database was used. The sequences of all proteins produced in this work are described in Appendix B.

### 2.4.2 Bacterial protein production

Proteins of bacterial origin were expressed in competent *E. coli* Rosetta2 cells (Merck), derived from the BL21 strain, which express T7 polymerase under an IPTG-inducible system[242]. The coding sequence of the target protein was encoded in the pET28a(+) plasmid backbone under the T7 promoter. 100ng of pET28a(+) plasmid was transformed into Rosetta2 cells through heat-shock for 45s at 42°C, following the transformation protocol above. Transformed cells were grown in LB agar supplemented with kanamycin (50µg/mL) and chloramphenicol (34µg/mL) (hereafter, kan50/chlor34) for 16h at 37°C with rotation. Colonies were grown in LB high salt (5g/L yeast extract, 10g/L casein, 10g/L NaCl) supplemented with kan50/chlor34 for 14h at 37°C. Cultures were diluted 1:50 into 1L cultures in LB high salt kan50/chlor34 and grown for 2h at 37°C. IPTG was added at a final concentration of 1mM to induce T7 polymerase-dependent protein expression and the cells remained in culture at 37°C for 4 hours post-induction. Cells were pelleted at 3739g, washed in 0.9% (w/v) NaCl, snap-frozen in dry ice and stored at -80°C until further use. Cell pellets were thawed and resuspended in PBS supplemented with 15µg/mL DNAseI and cOmplete protease inhibitors, EDTA free (Roche). Cells were disrupted at 30Kpsi using a CF1 1.1kW cell disruptor (Constant Systems). After further centrifugation to

ensure removal of intact cells, the lysate pH was adjusted to pH8 and the lysate was 0.22μm filtered prior to affinity purification.

### 2.4.3 Mammalian protein production

Coding sequences were introduced into the pHR lentiviral backbone, and VSV-G-pseudotyped lentiviral particles were produced as described in Section 2.2.3. CHO-K1 cells were trypsonised and placed at a final density of $10^6$ cells/mL in culture medium. $10^6$ cells were transduced by incubation with 2mL lentiviral supernatant overnight. For heterodimeric proteins (e.g. Fab fragments and derivatives), cells were incubated with 2mL of lentiviral supernatant produced from plasmids encoding each chain.

Transduced cell cultures were expanded to 20x T175 flasks until 100% confluent. Culture medium was replaced with 50mL harvest medium - CHO-K1 medium supplemented with 1% (v/v) FCS rather than 10% - per flask. Supernatant was collected after 7 days, cell debris removed at 526g for 10mins, and supernatant was supplemented with 0.1% (w/v) $NaN_3$ and 0.22μm filtered. This process was repeated for a second week by replacing the cell culture supernatant if required. Supernatant was stored at 4°C.

### 2.4.4 Affinity chromatography – His purification

Recombinant proteins containing His-Tags (6 tandem histidine residues, HHHHHH) can be purified through their high affinity interaction with nickel nitrilotriacetic acid (NiNTA) groups. This interaction has a $K_D \sim 10^{-13}$ M at pH8[243]. Free imidazole can be used as a competitor for binding, disrupting nonspecific interactions at low concentrations and allowing protein elution at higher concentrations[243].

For the purification of His-tagged proteins, NiNTA agarose (Qiagen) was packaged into an Econo-column (BioRad), washed in 10 column volumes (CV) MilliQ water, and rinsed in 10CV PBS pH8 by gravity flow. For prokaryotic proteins, bacterial lysates were applied directly to the chromatography resin by gravity flow. For eukaryotic proteins, CHO-K1 supernatant was diluted 1:1 in PBS, pH8 before being applied to the resin by gravity flow. The resin was washed in 10CV PBS pH8 supplemented with NaCl to a final concentration of 0.5M, and subsequently washed in the same solution supplemented with 10mM imidazole (10CV) and 20mM imidazole (15CV) by gravity flow. His-Tagged proteins were eluted in PBS 0.5M NaCl, pH8 supplemented with 200mM imidazole (bacterial production) or 250mM imidazole (mammalian production).

NiNTA agarose resins were regenerated and used up to 10 times. Resins were washed in 10CV MilliQ water and stripped of nickel ions through ethylenediaminetetraacetic acid (EDTA) chelation using 5CV 0.1M EDTA, pH8, followed by another wash in 10CV MilliQ water. The resin was regenerated with nickel by incubation with 0.1M nickel(II) sulfate for 30mins at room temperature. The resin was washed in 10CV MilliQ water to remove excess nickel salts and stored in 20% ethanol at 4°C for further use.

### 2.4.5 Affinity chromatography – CTag purification

Recombinant proteins containing a peptide tag (EDQVDPRLIDGK) derived from the human C-Protein can be purified by their high affinity interaction with the HPC4 antibody[244]. This interaction is dependent on the presence of calcium ions[245], and tagged proteins can be eluted through the introduction of free C-Protein peptide as a competitor for resin binding.

For CTag purification, Sepharose resins with CNBr-coupled HPC4 antibody were used (previously generated by M. Vuong[240]). HPC4 resins were washed in 10CV MilliQ water and equilibrated into dilution buffer (20mM HEPES pH7.5, 150mM NaCl, 2mM $CaCl_2$, pH7.5) by gravity flow. CHO-K1 supernatant was diluted 1:1 in dilution buffer before being applied to the resin by gravity flow. The resin was subsequently washed with 20CV dilution buffer by gravity flow. Target proteins were eluted in elution buffer containing elution peptide (Generon) (20mM HEPES, 150mM NaCl, 1mM EDTA, pH7.5, supplemented with 0.2mg/mL CTag peptide).

HPC4 resins were regenerated by sequential washes in high pH regeneration buffer (0.1M Tris-HCl, pH8, 0.5M NaCl, pH8.5) and low pH regeneration buffer (0.1M sodium acetate, 0.5M NaCl, pH4.5). Resins were washed in 10CV MilliQ water, and then washed three times in 3CV high pH regeneration buffer interspersed with 3CV washes with low pH regeneration buffer. Resins were stored in HBS (10mM HEPES, 150mM NaCl, pH7.4) supplemented with 0.05% (w/v) sodium azide and used up to five times.

### 2.4.6 Affinity chromatography – Twin-StrepTag purification

Proteins containing Twin-StrepTag sequences can be purified through its interaction with StrepTactin, a modified version of streptavidin[246] with increased affinity for the StrepTagII peptide (WSHPQFEK)[247]. Elution of proteins of interest can be mediated by addition of D-desthiobiotin, a small-molecule competitor for StrepTactin binding[247]. CHO-K1 supernatant could be incubated directly with StrepTactin resins as DMEM does not contain free biotin[248], which would irreversibly block StrepTactin binding sites[247]. 1L of CHO-K1 supernatant was concentrated to 50mL volume using a Vivaflow system using a 10kDa cut-off membrane and diluted 1:1 in Buffer W (100mM Tris-HCl,

150mM NaCl, 1mM EDTA, pH8) before being applied to a StrepTactin Sepharose High Performance resin (Cytiva). The supernatant was bound to the resin for 90mins in batch with rotation at room temperature. The resin was washed in 25CV Buffer W by gravity flow and the protein of interest was eluted in Buffer W supplemented with 2.5mM D-desthiobiotin (Sigma). StrepTactin resins were regenerated by sequential washes using 3CV MilliQ water, 3CV 0.5M NaOH and 3CV MilliQ water. Resins were stored in 20% ethanol and used up to three times.

### 2.4.7 Size-exclusion chromatography (SEC)

To ensure protein purity and stoichiometry, eluted material was further purified using size-exclusion chromatography (SEC). Elutions from affinity chromatography containing the protein of interest were pooled and concentrated using 10kDa MWCO filters (Amicon). To remove insoluble material, samples were centrifuged at 17,000g for 10mins at 4°C. The supernatant was applied to a S200 size-exclusion column fitted to an AKTA Pure system (Cytiva). For soluble proteins, S200 10/300GL (Cytiva) or S200 16/600 200pg (Cytiva) columns were used for protein purification. Prokaryotic proteins were purified into PBS pH8, and mammalian proteins were purified into HBS (10mM HEPES, 150mM NaCl, pH7.4). All buffers were 0.22μm filtered prior to use.

### 2.4.8 SDS-PAGE and protein storage

Collected fractions from SEC were further assessed by sodium dodecyl sulfate-polyacrylamide gel electrophoresis (SDS-PAGE) and Coomassie staining to ensure no aggregation or degradation were present. Samples collected from SEC fractions were diluted 1:1 in 2x Laemmli buffer (BioRad), in the presence (reducing condition) or absence (non-reducing conditions) of 2.5% (v/v) 2-mercaptoethanol (Sigma-Aldrich).

Diluted samples were boiled for 10 minutes at 95°C. Samples were loaded onto NuPage 12% Bis-Tris gels or NuPage 4-12% Bis-Tris gels (ThermoFisher) and gel electrophoresis was conducted in 1x NuPage buffer (ThermoFisher) at 150V for 1 hour. Gels were stained in Coomassie Blue solution (10% (v/v) acetic acid, 40% (v/v) methanol, 1g/L Coomassie Blue) for 30mins at room temperature. Background stain was removed by overnight incubation in destain solution (10% (v/v) acetic acid, 12% (v/v) methanol). Destained gels were transferred to deionised water and gels were imaged using a GelDocXR+ imager (BioRad).

Relevant SEC fractions were pooled and placed at final concentrations between 1-2mg/mL. Proteins were aliquoted, snap-frozen in dry ice and stored at -80°C. Wherever possible, protein dye labelling (Section 2.4.9) was conducted immediately after purification to minimise freeze/thaw cycles.

### 2.4.9 Fluorescent labelling of soluble proteins

Throughout this work, recombinant proteins are used as probes for light microscopy, flow cytometry, or fluorescent SEC (FSEC). To this end, soluble proteins were labelled with fluorescent dyes. These dyes were covalently attached to proteins either non-specifically (using NHS ester labelling of amine groups[249]) or using site-specific labelling through the self-labelling enzyme HaloTag[250] in fusion proteins containing this domain. Proteins were non-specifically labelled with NHS ester dyes using Alexa Fluor 488, 555 or 647 Antibody Labelling kits (ThermoFisher) according to the manufacturer's instructions. 100µg of recombinant protein were labelled using each of the provided reactions.

HaloTag-containing proteins were labelled via direct incubation with chloroalkane linker-containing dyes[250]. These included the commercially available Alexa Fluor 488 and Janelia Fluor 549 HaloTag ligands (Promega), and an Alexa Fluor 647-derived ligand (kindly provided by Markus Koerbel, University of Cambridge). Proteins were incubated with 2x molar excess of dye for 90mins at room temperature. Excess dye was removed using a Bio-Spin P-6 Gel Column, Tris buffer (Bio-Rad).

Protein concentration and the degree of labelling were assessed through spectrophotometry using a NanoDrop One system and calculated according to manufacturer's intructions. A280 and absorbance of the conjugate dye ($A_{dye}$) at 494nm (for AF488), 555nm (AF555) and 650nm (AF647) were measured. The molar protein concentration and dye:protein ratio was calculated according to the manufacturer's instructions (Antibody Labelling Kits, ThermoFisher).

In all cases, NHS ester labelling resulted in a degree of labelling of 0.5-3 dyes/protein. In turn, HaloTag labelling was very efficient for recombinant proteins in solution, with degrees of labelling most commonly between 0.85 and 1 (the theoretical maximum), suggesting a labelling efficiency above 85% in most cases (not shown). Labelled proteins were aliquoted, snap-frozen in dry ice and stored at -80°C until further use.

## 2.5 Data processing and presentation

Data processing was conducted using a variety of different software. Specific analysis is discussed in the methods sections of individual chapters. DNA constructs were designed and *in silico* cloning validated using SnapGene (version 4.1.9). Images of polyacrylamide gels present throughout this work were collected using a GelDocXR+

system. Flow cytometry data was analysed and plotted using FlowJo (v10, BD). For most point-based data presented, data points were transferred to PRISM (v8, GraphPad). Microscopy images were processed and rendered using ImageJ (v2.1.0). Individual analyses described in Chapters 3 and 4 using custom MATLAB scripts were conducted in MATLAB (MATLAB_R2020b, MathWorks). All statistical analyses were conducted using PRISM (v8, GraphPad).

# Chapter 3. The stoichiometry of the BCR complex in resting cells

## 3.1 Introduction

Clarifying the mechanisms driving BCR triggering relies on understanding the organisation of the receptor prior to signalling. It has previously been claimed that changes to receptor stoichiometry upon antigen binding govern BCR signalling. This is a fundamental claim of the conformational change model, in which clustering mediated by the membrane-proximal Ig domains occurs upon antigen engagement[26]. Conversely, the dissociation-activation model predicts the opposite effect, with antigen binding leading to the dissociation of clusters present in the resting state[189]. Other models of receptor signalling do not require a modification to receptor organisation, such as the rigid-body interactions predicted by the kinetic-segregation model[195].

Extensive effort has been placed into understanding the distribution of B-cell receptors on the cell membrane, as described in the Introduction (Section 1.5.6). Both indirect fluorescence methods and super-resolution microscopy studies have yielded varied results. Direct stochastic optical reconstruction microscopy (dSTORM) has predominated as the method of choice, with contrasting conclusions. BCR distributions ranged from predominantly monomeric molecules with some receptors clustered[251] to largely clustered in 'protein islands' with a diameter in the hundreds of nanometres[191,192]. Isotype-specific differences have also been noted, with IgD and IgG

receptors in a more clustered state than IgM BCRs[192,251]. However, assessing stoichiometry with dSTORM data presents a problem due to overcounting, where dye blinking dynamics can give rise to multiple measurements for the same molecule, leading to artificially clustered localisations[252]. Attempts at correcting such limitations have given rise to new interpretations of receptor organisation for other antigen receptors, suggesting for example that TCRs are mostly monomeric in the resting state[211,212,253]. Recent studies using stimulated emission depletion (STED) microscopy, which does not involve *post hoc* fitting, have suggested a mixture of monomeric and dimeric IgM BCRs predominate in primary human B cells[168]. The generation of flat membrane surfaces in these studies facilitates assessment of receptor distributions, avoiding membrane curvature as a potential confounder. However, these approaches modify the structure of the cell membrane, masking the context of cellular ultrastructure. Recent studies using diffraction-limited lattice light-sheet imaging have highlighted a possible association of IgM BCRs with membrane protrusions, suggesting that up to ~20% of the receptors may be organised in clusters that occupy membrane ridges and microvilli[254].

The work in this chapter seeks to elucidate the organisation of the BCR complex in its native membrane environment. It describes the generation of a novel single-dye labelling strategy for proteins of interest on the B-cell surface. Using dSTORM, resting murine primary B cells were imaged using an imaging modality capable of resolving 3D localisations across the whole cell volume. Applying this method to the BCR as well as to the monomeric control protein, CD45, allowed for the characterisation of the 3D distribution of B-cell receptor complexes on the surface of resting, naïve B cells.

## 3.2 Methods

### 3.2.1. Isolation of primary mouse B cells

For all experiments described in this chapter, cells from the parental C57BL/6J strain or from the MD4 mouse strain[181] (Section 4.2.1) were used. Splenic B cells were isolated using a B Cell Isolation Kit, mouse (Miltenyi), according to the manufacturer's instructions.

### 3.2.2. Generation of imaging probes

The HM79b and 30F11 Fab-Halo proteins were expressed in CHO-K1 cell lines as per Section 2.4.3. HM79b Fab-Halo was purified by HPC4 purification (Section 2.4.5) and 30F11 was purified by StrepTactin purification (Section 2.4.6), with SEC, SDS-PAGE and protein labelling conducted as per Sections 2.4.7-2.4.9. Fab-Halo binding to target molecules was validated by flow cytometry as described in Section 2.3.1.

### 3.2.3. QuantiBrite quantification of receptor expression

To determine the number of molecules on the surface of cells, QuantiBRITE PE Fluorescence Quantification beads (BD Biosciences) were used. Using a saturating amount of antibody to ensure monovalent binding to target molecules, the PE fluorescence of cells is compared to a standard curve using beads with a known number of PE molecules.

$0.5 \times 10^6$ splenic B cells were washed in PBS and stained in 50µL PBS supplemented with 40µg.mL$^{-1}$ PE-labelled antibody. Cells were washed twice in PBS and fixed in 1% (w/v) paraformaldehyde. Samples were analysed by flow cytometry as per the general

Methods chapter, using an Attune NxT system, alongside Quantibrite beads. A linear regression between the geometric mean of the stain and the number of molecules was fitted using the quantification beads. The total number of molecules on the cell surface was calculated from the geometric mean of the antibody labelling in accordance with the linear relationship determined by bead fluorescence, according to the manufacturer's instructions.

### 3.2.4. Cell labelling for dSTORM

Fab-Halo molecules were labelled using Alexa Fluor 647 HaloTag ligand (synthesised by M. Koerbel, University of Cambridge) as per Section 2.4.9. Splenic B cells were labelled at 4°C with saturating concentrations of recombinant Fab-Halo proteins labelled with Alexa Fluor 647. $2x10^6$ cells were washed in 200µL PBS, and stained with 50µL 2.5µM Fab-Halo(AF647) for 45mins at 4°C. For conditions where BCR cross-linking was induced, Fab-Halo stains were supplemented with 10µg/mL polyclonal anti-mouse Igκ. Cells were washed twice in 200µL PBS at 4°C, and samples were fixed in 100µL 4% (w/v) paraformaldehyde for 30mins at 4°C. Samples were resuspended in 50µL PBS and stored for up to 2 weeks without visible degradation.

### 3.2.5. dSTORM sample preparation

For dSTORM imaging, Alexa Fluor 647-labelled cells were imaged under a commonly used chemical system to control the rate of AF647 blinking. Cells were plated onto clean glass slides coated with a layer of poly-L-lysine (PLL) prior to imaging. Glass slides were rinsed in pure isopropanol and Milli-Q water, dried under nitrogen gas, and cleaned in an argon plasma cleaner for 1h. The clean glass surface was coated in 50µL 0.01% PLL (Sigma-Aldrich) and incubated for 1h at room temperature. The

functionalised surface was washed in PBS and placed in 50µL PBS. For fiducial correction, 100nm gold nanoparticles (Sigma-Aldrich) were added to the surface for 20mins. Nanoparticles were previously washed in MQ water, sonicated using a sonicator bath and filtered through a 0.22µm PES membrane filter to remove any aggregated particles. The nanoparticle-coated surfaces were washed in PBS, and placed in dSTORM buffer (50mM Tris-HCl, 10mM NaCl, 10% (w/v) glucose, 10mM MEA, 84µg.mL$^{-1}$ bovine catalase, 0.2 mg.mL$^{-1}$ glucose oxidase, pH8). 0.1x10$^{6}$ labelled cells were washed in PBS, then dSTORM buffer, and plated onto the surface for 20mins, to allow cell attachment. Surfaces were then washed twice into freshly made dSTORM buffer prior to imaging.

### 3.2.6. TIRF/dSTORM imaging

TIRF/dSTORM was conducted using a bespoke instrument previously described by Chen and colleagues[204]. Samples were excited with a 638nm diode laser. AF647 blinking dynamics were enhanced using a 405nm laser, as excitation with ultraviolet radiation can return AF647 molecules from a 'dark state' back to an excitable state[255]. Samples were imaged using a TIRF oil immersion objective with NA 1.49.

### 3.2.7. SMLFM/dSTORM imaging

Single-molecule light field microscopy (SMLFM)[256] was conducted using a novel bespoke epifluorescence microscope setup[257] (built by S. Daly, University of Cambridge). Briefly, light field microscopy makes use of a microlens array to obtain both 2D location and angular information from incident light. The microlens array splits photons from a single source into several different 'perspective views', encoding in the process angular information and 2D positioning for a given fluorophore across

these distinct 'views'[256]. The function of the microlens array in splitting light depending on its incident angle results in a reduced effective numerical aperture (NA) for each perspective view, which in turn leads to a larger depth of field (DOF) than that expected from the NA of the objective used in conventional light microscopy[256]. In the hexagonal array used in this study (described by Daly and colleagues[257]), the DOF was calculated to be ~8μm, with the PSF area in the central view remaining unaltered across the DOF, a consequence of the reduced microlens NA. As a consequence, emitters in each perspective view can be fitted to a 2D Gaussian distribution, permitting the sub-diffraction localisation of a fluorophore within each view and the inference of its 3D localisation from the encoded angular information provided by the position of the same fluorophore in multiple perspective views[256]. Therefore, the axial and lateral resolution of 3D localisations depends on the number of perspective views for which images of an individual fluorophore can be identified. In the setup used in this study, for the minimum amount of perspective views used (four views), the lateral localisation precision was calculated to be ~40nm, and the axial precision ~47nm, with some improvements obtained when up to seven perspective views were used[257]. For experiments described in this study, samples were excited using a 640nm laser, together with excitation using a 405nm laser, as described above. Samples were imaged using a 1.27 NA water objective.

### 3.2.8. Image reconstruction

Example reconstructed images from 2D imaging shown were reconstructed using GDSC SMLM plugin using the Fiji software. In examples provided, no further correction was applied to showcase instrument drift. For 3D reconstruction, initial reconstruction of 2D localisations was conducted using the same plugin. 3D localisations were

obtained from 2D points in several perspective views using a custom-made MATLAB script, including fiducial correction using gold nanobead position, based on published code[256]. 3D localisations and nearest-neighbour analysis were plotted using ViSP[258].

### 3.2.9. Cross K-function analysis

Cross K-function analysis was conducted using a custom-made script (B. Fu, University of Cambridge). The distribution of localisations for each individual cell across all conditions was compared with that of each CD45-labelled cell (n=9). To control for density differences, each comparison was done by randomly selecting 5000 points from each pair of cells. This selection was conducted randomly 100 times to ensure the distributions were adequately sampled. The K(r) value, the ratio of neighbours within a given radius of all localisations for a test condition compared to CD45, was calculated:

$$K(r) = \frac{K_N(r)}{K_0(r)} = \frac{\sum_{i=1}^{5000} Np_i(r)}{\sum_{j=1}^{5000} Mp_i(r)}$$

where $K_N$ and $K_0$ are the sum of the number of points (N,M) within a radius r of the i-th test point ($p_i$) for each distribution, across all 5000 points chosen, for the test distribution ($K_N$) and the CD45 distribution ($K_0$). The average K(r) value for all 100 comparisons for each cell was used as a metric of receptor clustering on a per-cell basis.

## 3.3 Results

### 3.3.1. Reagents for super-resolution imaging of B-cell surface proteins

To characterise the distribution of the surface BCR, super-resolution imaging of the receptor was undertaken in unstimulated naïve B cells. Investigating the stoichiometry of the BCR complex would rely on the comparison of its distribution to that of a monomeric protein, expressed at similar densities on the target cell. The membrane phosphatase CD45 was selected as a monomeric control, in light of its relatively high abundance on the B-cell surface. Despite initial reports that CD45 may form dimers[259], later fluorescence coincidence studies have demonstrated that CD45 is predominantly monomeric on the cell surface[260]. Probes against the extracellular domains of murine BCR and CD45 were therefore designed with the goal of attaching a single dye molecule per receptor. Such an approach would avoid the common problem of overcounting molecules through the use of probes with several dye molecules[251].

Recombinant probes based on Fab fragments were designed for optimal receptor labelling. As monovalent binders, Fab fragments can be used to ensure a single probe is bound to the target molecule. Moreover, the use of Fab fragments rather than antibody labelling can prevent potential perturbations to receptor organisation. Recent studies in Ramos B cells have suggested that the use of primary bivalent antibodies as labelling reagents, but not monovalent binders, can induce BCR clustering even following fixation[261]. To ensure single-dye labelling of the probe, a HaloTag domain was added to the C-terminus of the Fab heavy chain. The HaloTag is a self-labelling enzyme, which catalyses the covalent attachment of its substrate to itself[250]. As a result, ligated HaloTag domains are site-specifically labelled and ensure 1:1 probe-to-dye stoichiometry.

For BCR imaging, the requirement for monovalent labelling favoured probes against CD79a or CD79b, as the only components of the complex for which a single chain is present. This also facilitated the labelling of the different receptors on the surface of naïve B cells - both IgM and IgD BCRs are expressed, with possible expression of either kappa or lambda light chains[52]. The use of an anti-CD79b probe ensured all BCRs on the cell surface of primary B cells were labelled indiscriminately. For BCR labelling, a Fab-Halo fragment based on the hamster anti-mouse CD79b antibody HM79-16 (hereafter, HM79b) was used[262]. The Cγ1 and Cλ constant regions of the parental hamster antibody were maintained, and the protein could be expressed and purified as a monovalent Fab-Halo heterodimer of the predicted size (~85kDa) (Fig. 3.1a-b). The HM79b Fab-Halo probe bound to BCR-expressing mouse cells but did not label cells that did not express CD79b (Fig. 3.1c-f), confirming its specificity for murine CD79b. For CD45 labelling, the variable regions of the well-characterised pan-CD45 clone 30F11 were used[263]. The resulting Fab-Halo could also be purified as a monovalent heterodimer of the same size (Fig. 3.2a-b) and bound to $CD45^+$ cells as predicted (Fig. 3.2c-d).

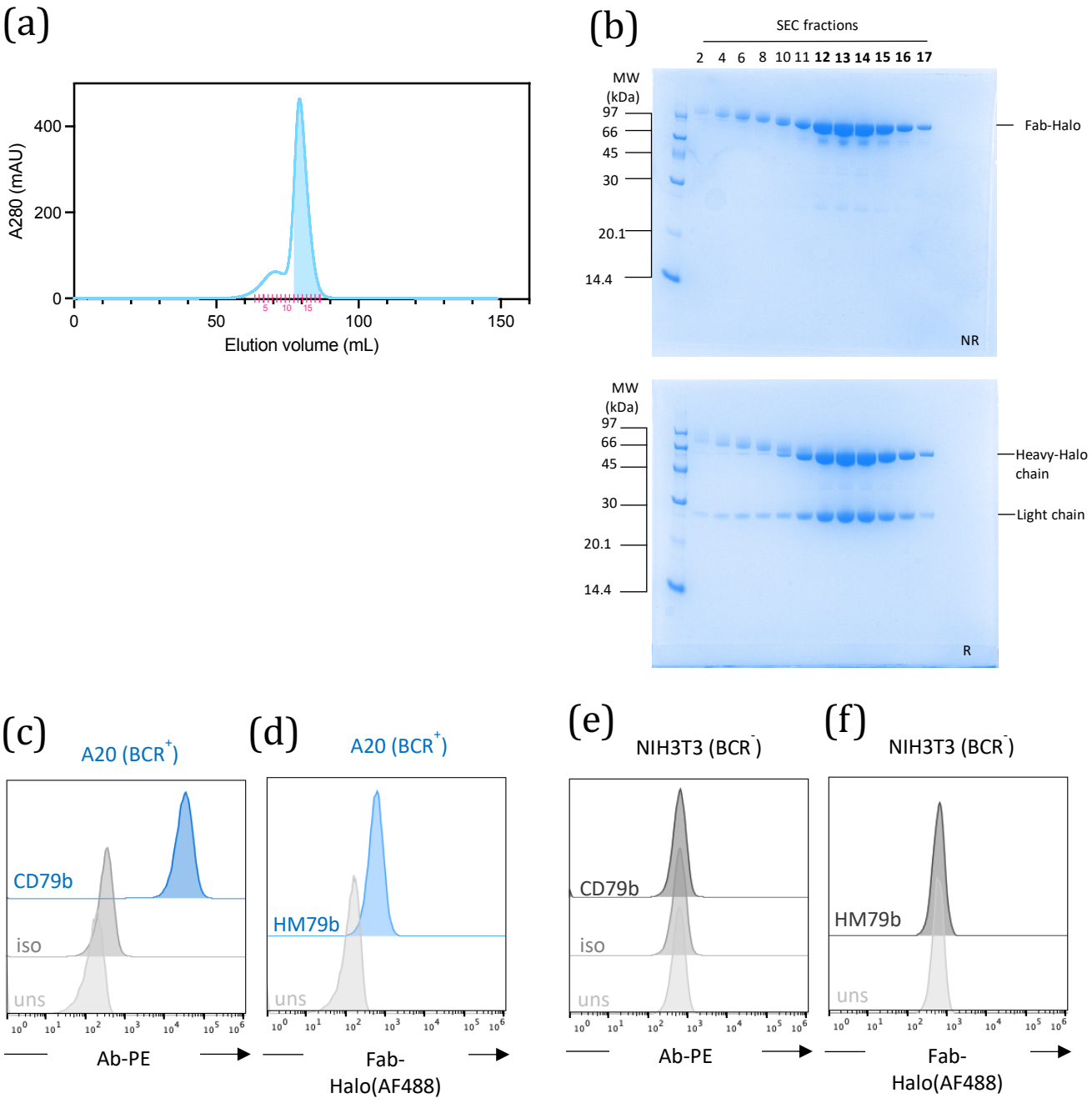



**Figure 3.1 | Purification of HM79b Fab-Halo. (a)** SEC profile of affinity-purified Fab-Halo. Area under the curve represents fractions pooled for further use. **(b)** Coomassie stain of SDS-PAGE analysis of fractions from SEC, boiled under non-reducing (NR, top) or reducing (R, bottom) conditions. Fractions kept are highlighted with bold text. **(c)** Flow cytometry staining of A20 cells ($BCR^+$) labelled with anti-CD79b antibody (dark blue), compared to unlabelled cells (light grey) or those stained with an isotype control (grey). This confirms expression of CD79b on the cell surface. **(d)** Flow cytometry staining of A20 cells with recombinant HM79b Fab-Halo labelled with Alexa Fluor 488 (dark blue), compared to unstained cells (light grey). **(e)** Flow cytometry staining of fibroblast NIH3T3 cells ($BCR^-$) with anti-CD79b antibody (dark grey), compared to unlabelled cells (light grey) or an isotype control (grey). **(f)** Flow cytometry staining of NIH3T3 cells with recombinant HM79b Fab-Halo labelled with Alexa Fluor 488 (dark grey), compared to unstained cells (light grey).

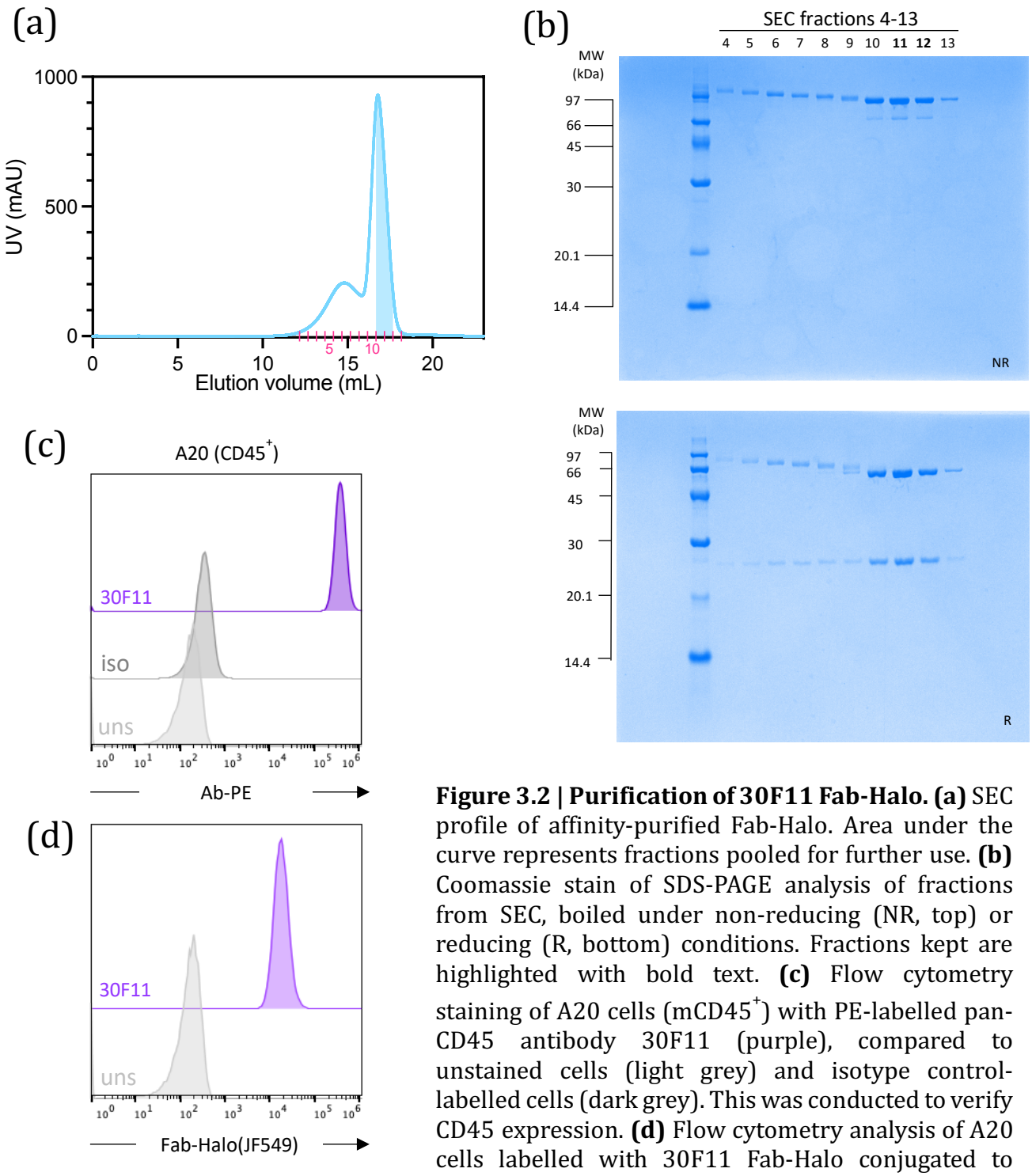



**Figure 3.2 | Purification of 30F11 Fab-Halo. (a)** SEC profile of affinity-purified Fab-Halo. Area under the curve represents fractions pooled for further use. **(b)** Coomassie stain of SDS-PAGE analysis of fractions from SEC, boiled under non-reducing (NR, top) or reducing (R, bottom) conditions. Fractions kept are highlighted with bold text. **(c)** Flow cytometry staining of A20 cells (mCD45$^+$) with PE-labelled pan-CD45 antibody 30F11 (purple), compared to unstained cells (light grey) and isotype control-labelled cells (dark grey). This was conducted to verify CD45 expression. **(d)** Flow cytometry analysis of A20 cells labelled with 30F11 Fab-Halo conjugated to Janelia Fluor 549 (purple), compared to unstained cells (light grey).

### 3.3.2. Initial 2D TIRF/dSTORM experiments

The aim of this study was to fully characterise the organisation of the BCR complex in the resting B cell. Initial experiments used primary murine B cells isolated from the MD4 mouse strain, which produces an almost clonal population of B cells through transgenic expression of the HyHEL10 BCR[181]. To ensure saturation binding, cells were labelled with increasing concentrations of HM79b and 30F11 Fab-Halo (Fig. 3.3), reaching saturation at 2μM concentration as determined by flow cytometry. Subsequently, imaged cells were labelled with 2.5μM Fab-Halo in all experiments.

The method initially used for super-resolution imaging of receptors – 2D dSTORM – relies on the stochastic activation of single emitters at low densities[209]. The commonly used approach for the excitation of dye molecules, TIRF microscopy, permits localisation of emitters within an evanescence field only (~100nm from the glass surface)[264]. The exclusion of dyes more distant from the glass surface allows for the two-dimensional fitting of the localisations on the planar surface[264].

The requirement for the generation of a cell-glass interface for TIRF microscopy poses issues for the study of receptor organisation. The majority of studies of lymphocyte receptor valency allow for living cells to interact with the glass surface, often functionalised with antibodies or adhesion molecules to facilitate membrane spreading, ensuring a sufficient contact surface area is formed[191,192,211,214,251]. However, these approaches can be highly perturbative to the diffusion and stoichiometry of membrane receptors. Nonspecific interactions between T-cell receptors and glass surfaces have been previously shown to impact receptor

diffusion[260,265]. This occurs even when the surface is functionalised with common additives such as poly-L-lysine[266].

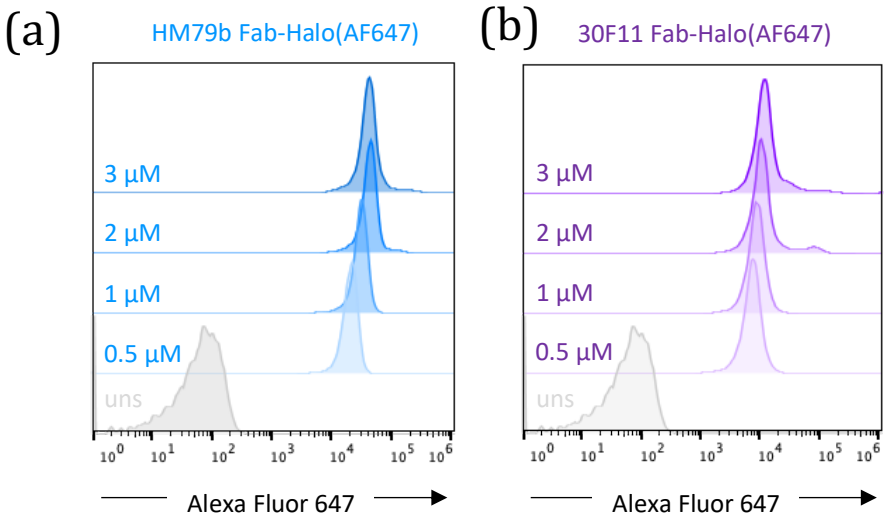



**Figure 3.3 | Saturation of receptor labelling on primary B cells.** Flow cytometry analysis of isolated primary MD4 B cells stained with Alexa Fluor 647-labelled Fab-Halo molecules. **(a)** Histograms representing AF647 intensity for cells labelled with increasing concentrations of HM79b Fab-Halo (anti-BCR, blue), compared to unstained cells (light grey) **(b)** Histograms representing AF647 intensity for cells labelled with increasing concentrations of 30F11 Fab-Halo (anti-CD45, blue), compared to unstained cells (light grey)

To avoid potential cytoskeletal rearrangements and signalling events downstream of interactions with the surface, cells were fixed in solution prior to their deposition onto coverslips. This presented an initial challenge in that fixed cells formed relatively small contacts with the surface, as exemplified in Figure 3.4. In avoiding live cell interactions with a functionalised surface, this setup failed to induce the same contact surface area as those of previous studies using mouse lymphocytes (which could create surface areas larger than 10µm$^2$)[191,192,194,210,211,214]. These initial observations also showed the importance of correcting for imaging-induced artefacts, such as instrument drift. Gold nanobeads added as fiducials markers to the glass surface displayed some motion in the absence of *post hoc* correction (Fig. 3.4.). This is a common issue with dSTORM imaging, and repeated blinking of a single dye, paired with this motion, can give rise to

artefactual clusters. This was addressed using fiducial correction in future experiments[252].

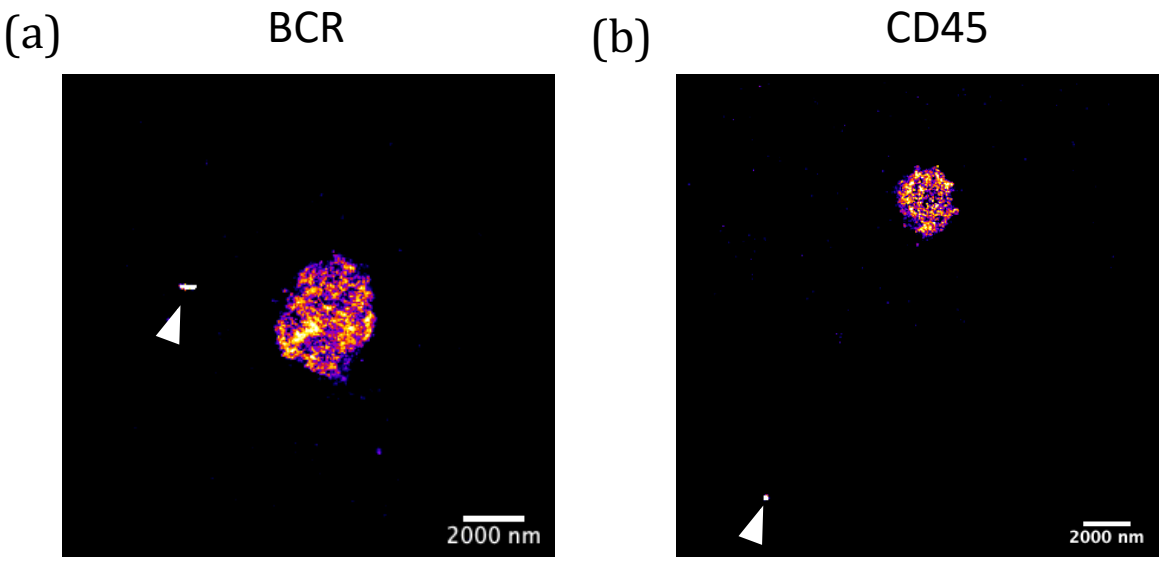



**Figure 3.4 | Reconstructed 2D TIRF/dSTORM images of primary B cells (without fiducial correction).** Example images of AF647 localisations on primary B cells imaged using TIRFM. Panel **(a)** represents localisations from an example primary MD4 B cell labelled with HM79b Fab-Halo(AF647). Panel **(b)** represents the surface localisations of a single 30F11-labelled primary B cell. Bright spots on the surface labelled with white arrows represent gold nanoparticles to be used as fiducial markers. The linear movement of the particle in **(a)** compared to the motionless particle in **(b)** showcases the error in localisations introduced by microscope drift. Scale bar = 2μm.

### 3.3.3. 3D SMLFM/dSTORM experiments

One caveat of using TIRF microscopy to determine receptor localisation is that it only samples coverslip-proximal receptors as opposed to the whole receptor population. Furthermore, it relies on generating flat surfaces and on approximating any curvature that can still be illuminated within the evanescence field to a flat surface. This omits important information regarding the effects of membrane topology on receptor organisation, as any differential variation in z-position will be superimposed on a presumed flat surface. This is important in that topology may play a role in the distribution of some TCR signalling components[267], as well as in BCR organisation[254].

To explore native receptor organisation in the context of cellular ultrastructure, a novel imaging modality was applied to the setup optimised for 2D dSTORM. Single-molecule light field microscopy (SMLFM) had previously been developed as a method capable of determining the 3D localisation of molecules. This is due to the use of a microlens array which allows the same molecule to be recorded from different angles ('perspective views'), determining the position of the molecule through the use of parallax[256]. This can be conducted at the same density of molecules to be imaged in 2D, as overlap in the central view will be overcome by the use of alternative perspective views. This property of SMLFM was expected to be ideal for imaging high-density receptors on the cell membrane. The use of a novel microscope setup which generated a depth of field of ~8μm was ideal due to the small diameter of murine lymphocytes (~7-8μm)[268]. This technique could therefore be used to image the majority of the murine B-cell membrane in a single imaging volume.

For the study of BCR organisation in three dimensions, primary B cells from wildtype C57BL/6J mice were used. This change was introduced to sample BCR distributions more accurately across multiple clonotypes, rather than focusing on a single receptor. As homotypic interactions induced through variable region binding are known to occur in some cases[168,169], the distribution of receptors cannot be assumed to be independent of specificity. C57BL/6J B cells were labelled with anti-CD45 or anti-CD79b Fab-Halo. To ensure the analysis method used was sensitive to protein clusters, a third condition was included, with BCR-labelled cells stained in the presence of a polyclonal anti-mouse Igκ antibody mixture. Such antibodies can cross-link receptors into lattices, as previously described[251]. Anti-light chain antibodies were used as they crosslink both IgM and IgD BCRs. Although not all cells express a kappa light chain, Igκ

is expressed in ~90% of murine B cells[269], and therefore most cells should exhibit cross-linking in this condition.

Application of the 2D dSTORM protocol to labelled B cells proved to work in the SMLFM setup without modifications. Excitation using a highly inclined illumination angle (HILO)[209] allowed for illumination of most of the cell simultaneously. Single molecules could be observed across several perspective views, as exemplified in Fig. 3.5. This allowed for their reconstruction in three dimensions. Importantly, cells were imaged for as long as dyes could still be excited, to ensure that the maximum number of localisations could be acquired. The use of deposited gold nanoparticles allowed for fiducial correction. Images of cells labelled under all three conditions could be reconstructed in 3D, with examples shown in Fig. 3.6.

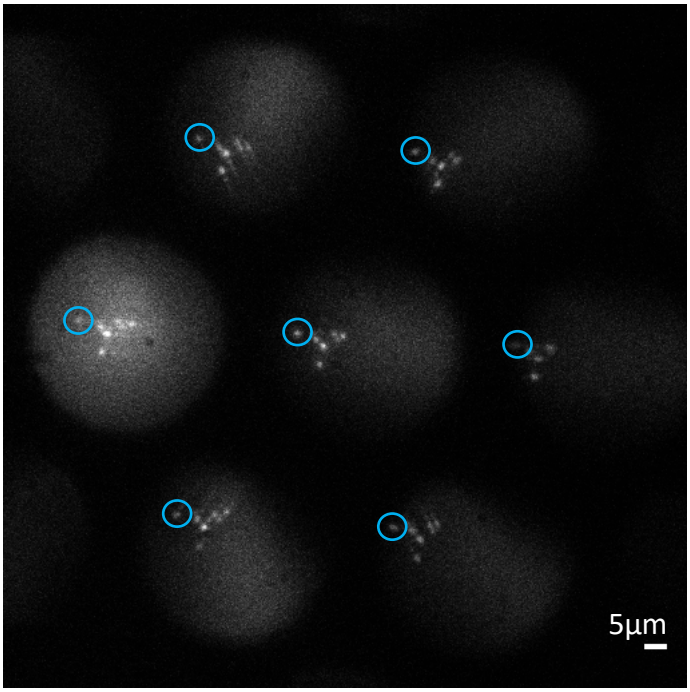



**Figure 3.5 | Example raw data from SMLFM/dSTORM.** Still example frame depicting fluorescent AF647 spots recorded using the SMLFM setup. These are recorded from a single primary C57BL/6J B cell labelled with anti-BCR Fab-Halo(AF647). Each spot is represented in the central view and all six addition views introduced by the hexagonal array. One gold nanobead settled onto the surface has been recorded next to the cell for use as a fiducial marker. The spot generated by the bead is highlighted across all seven perspective views (blue circles). Scale bar = 5µm.

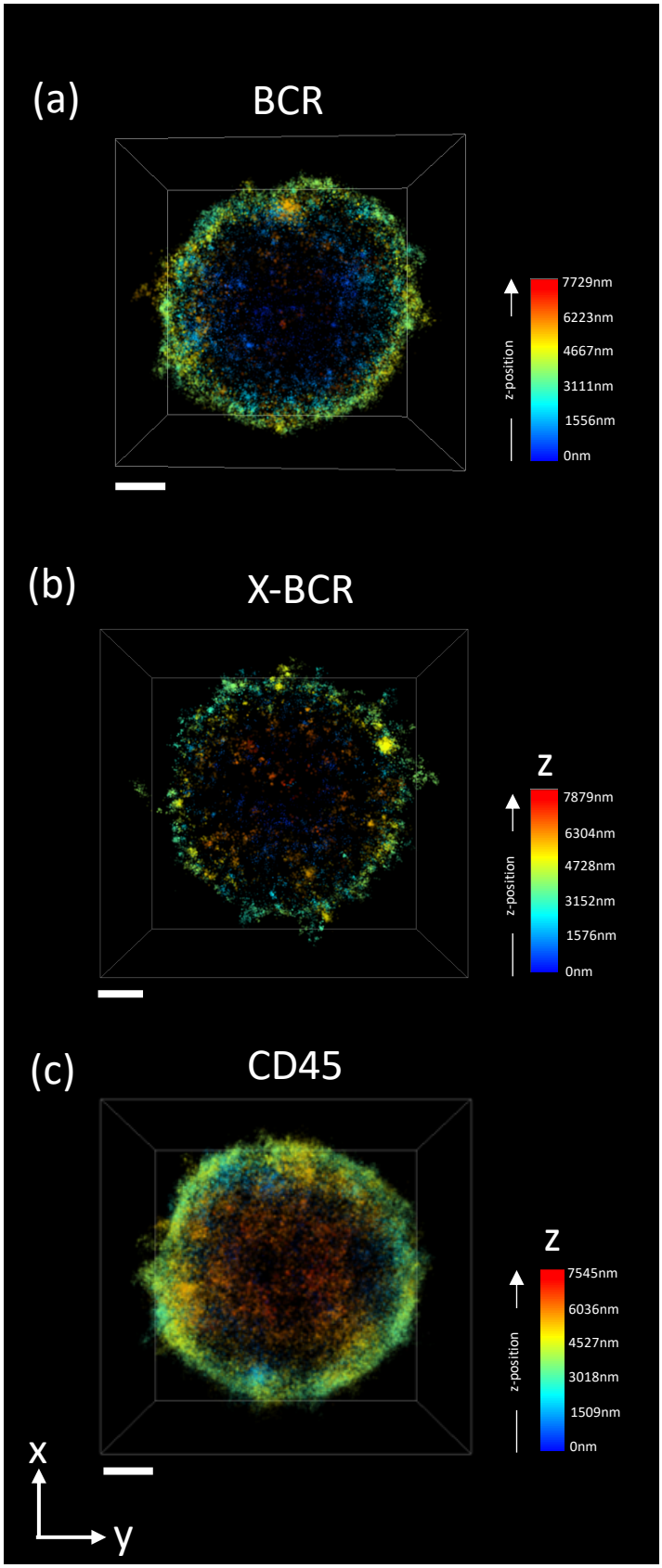



**Figure 3.6 | Primary B cells imaged in a single illumination volume using SMLFM.** 3D localisations (post-fiducial correction) plotted in three dimensions for representative cells labelled with probes against **(a)** the BCR, under resting conditions; **(b)** the BCR, in the presence of cross-linking antibodies (X-BCR); or **(c)** CD45. The z-position of each localisation is encoded in its colour; colour bar for each cell is depicted to the right. In the cases shown, the localisations recorded for each cell span 7.5-7.9μm in the axial dimension, approximately the diameter of a mouse lymphocyte. Scale bar = 1μm.

Reconstructions of localisations in BCR- and CD45-labelled cells revealed a detailed membrane structure, approximately 7-8μm in diameter, as predicted (Fig. 3.7). No internal localisations were observed, suggesting no internalised receptors were observable in this setup. Importantly, curved membrane domains could be observed, including some resembling microvillar structures (Fig. 3.7b)[270], suggesting SMLFM could be used to image receptor organisation in the context of complex membrane topology.

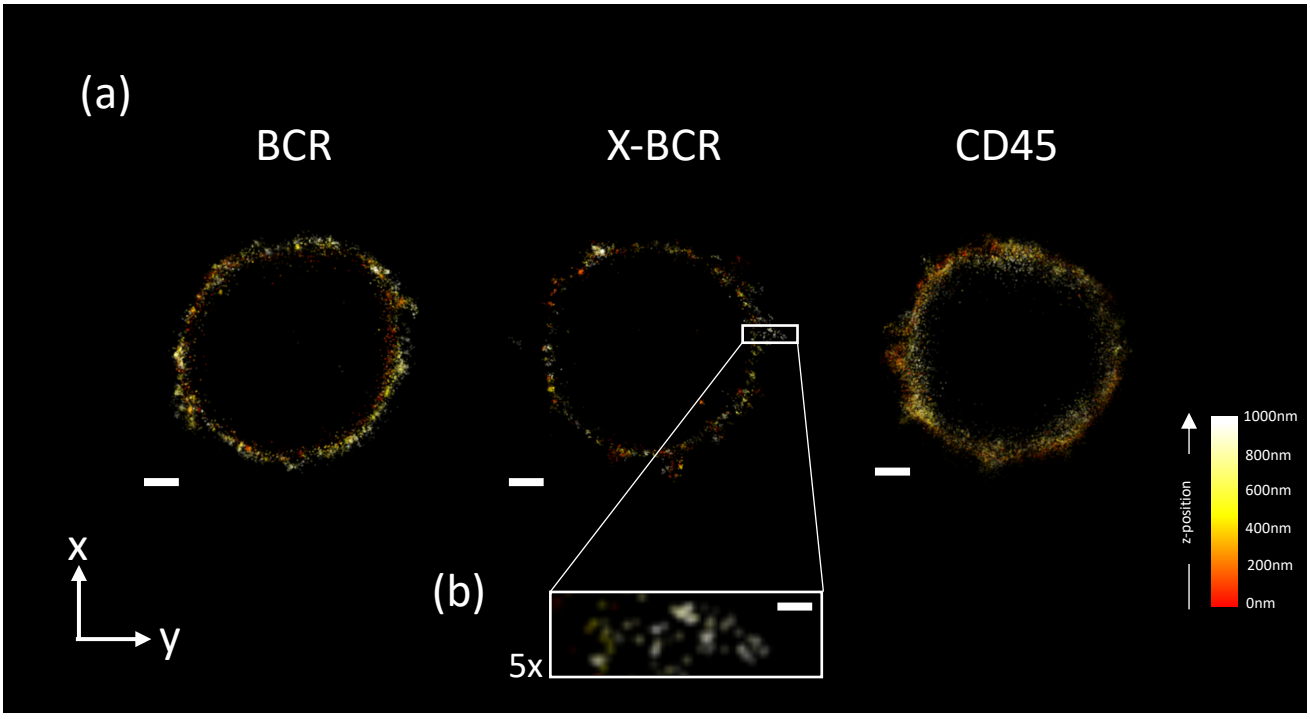



**Figure 3.7 | Membrane protrusions are preserved in fixed B cells. (a)** Z-slices from the example cells shown in Fig. 3.6, depicting a section across the cell midplane (standardised to 1μm in thickness). Colour encodes z-position, from 0–1000nm, with the colour bar depicted shared for all images. Scale bar = 1μm. **(b)** 5x magnification of a finger-like cellular protrusion. Scale bar = 200nm.

The single-dye approach undertaken for receptor labelling should yield a total number of localisations similar to the total receptor number on the cell, as virtually the entire cell volume was imaged. To verify this, the surface expression of CD79b and CD45 on primary murine B cells was quantified using a flow cytometric approach. The fluorescence intensity of antibody-labelled cells was compared to that of standardised beads containing a set number of fluorophores to infer the number of molecules on the cell surface (Fig. 3.8a,b). This approach suggested an average of ~23,200 BCR molecules was present on the B-cell surface (Fig. 3.8c). This was substantially lower than the number of receptors quantified by two previous studies[192,194] which reported a joint IgM and IgD population of ~300,000-350,000 complexes per cell. In turn, ~64,900 CD45 molecules were present when the protein was labelled specifically for the pan-CD45 30F11 epitope used (Fig. 3.8c). CD45 labelling targeting the B-cell-specific B220 CD45 isoform yielded a smaller number of molecules (~48,700 B220 molecules, Fig. 3.8c), suggesting either a disparity in antibody labelling or the expression of several CD45 isoforms on the B-cell surface. This quantification approach relies on saturating antibody labelling to achieve near-monovalent binding of antibody probes. However, due to the bivalent nature of antibody binding, and the likely selection of bivalent binders due to reduced fall-off (a consequence of their increased avidity), this staining is likely to represent a mixture of bivalently- and monovalently-bound antibodies. Therefore, this data likely represents an underestimate of the number of receptors, as some antibodies could be counted as a single molecule despite binding up to two target epitopes. Thus, this metric provides only an estimate of the total number of surface molecules.

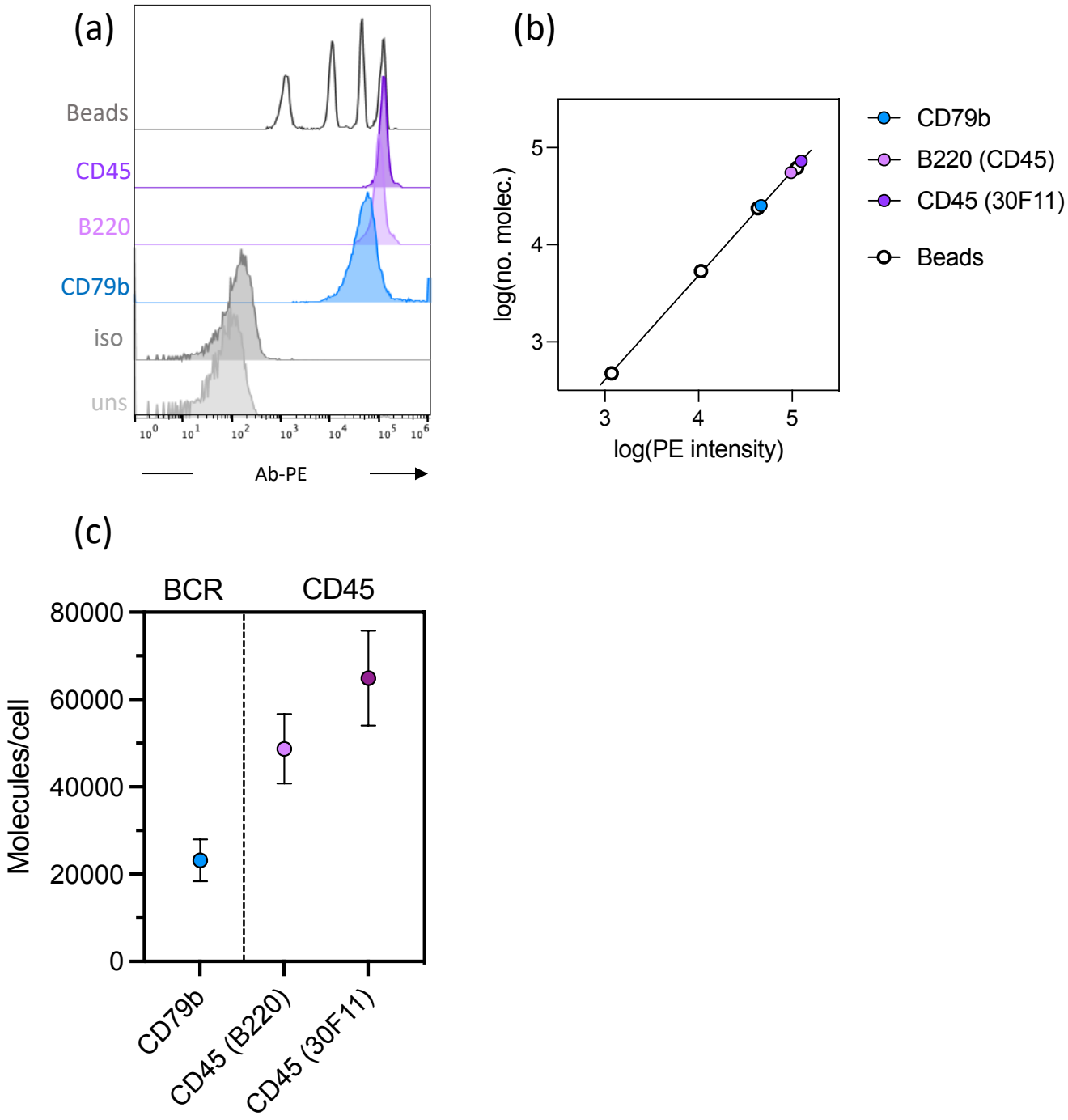



**Figure 3.8 | Quantification of receptor expression on primary C57BL/6J B cells. (a)** Representative histograms of PE antibody staining of key molecules on the B-cell surface. Histograms represent unstained cells (light grey), stained with an isotype control (dark grey) or stained for CD79b (blue), B220 (light purple), or CD45 (purple). PE fluorescence from standard QuantiBRITE beads is shown on the top row (open histograms) **(b)** Representative linear regression of the number of PE molecules and PE fluorescence using QuantiBRITE beads. The relationship inferred from bead intensities (open symbols) is compared to that of cellular staining (full symbols) to obtain the number of molecules on the cell surface. This is an example of a linear fit from a single repeat. **(c)** Number of molecules per cell determined from the linear regression for several B-cell surface proteins, from 3-4 independent experiments (n = 4 for CD79b and B220, n=3 for CD45). Symbols and error bars represent mean ± SD, respectively.

Importantly, the number of localisations obtained from SMLFM closely matched the measured number of receptors on the cell surface. On average, ~58,500 3D localisations were obtained from CD45-labelled cells (Fig. 3.9), similar to the ~64,900 molecules per cell measured by flow cytometry (Fig. 3.8c). BCR-labelled cell images displayed an average 33,570 3D localisations per cell (Fig. 3.9), with ~31,650 localisations for cells labelled under antibody cross-linking conditions (Fig. 3.9). These values were slightly increased compared to the ~23,200 CD79b molecules measured by flow cytometry (Fig. 3.8c). This increase could reflect the multiple-blinking behaviour of dye molecules. Moreover, the similar number of localisations obtained for BCR- and X-BCR-labelled cells suggests that the cross-linking antibody mix did not hinder receptor labelling and that comparisons across both conditions can be made in the absence of density-dependent artefacts.

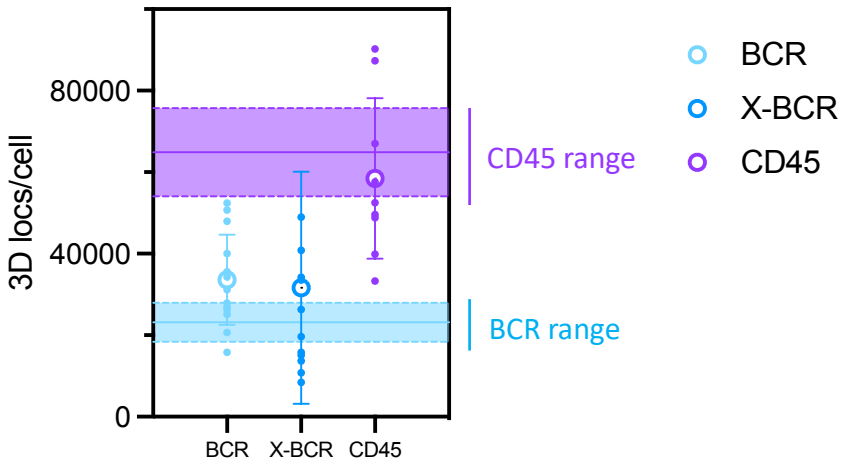



**Figure 3.9 | Quantification of 3D localisations from SMLFM/dSTORM imaging.** Number of 3D localisations obtained per cell for BCR-labelled cells in the resting condition (light blue) or under cross-linking conditions (X-BCR, dark blue), or CD45-labelled cells (purple). Empty symbols and error bars represent mean ± SD, respectively, and full symbols represent individual 3D localisation measurements per cell. (n=14 cells for BCR, n=12 cells for X-BCR, n=9 cells for CD45). The enveloped lines represent the mean and standard deviations of the number of receptors quantified for the BCR (blue) and CD45 (purple) determined in Figure 3.8(c). Line represents the mean and the envelope the standard deviation.

### 3.3.4. Cross K-function analysis of BCR organisation

To compare the surface BCR distribution under native or cross-linking conditions to that of CD45, cross K-function analysis was undertaken[271]. This method is predicated on Ripley's K-function analysis, which computes the density of neighbouring points over intervals around each point, compared to a random distribution. A sphere of increasing radius around a point encloses more molecules per unit volume near that point if it forms part of a cluster than it would for a homogenous distribution (Fig. 3.10)[272]. This method has been used to assess protein clustering from super-resolved point distributions in 2D, including in studies of antigen receptor valency[214,251]. Cross-K analysis was used to measure the localisation density around each receptor when compared to the CD45 distribution, which as a predicted monomer can be used as a representative random distribution. To avoid density-dependent effects derived from the differential expression of CD45 and the BCR, 5000 localisations were randomly selected from distributions for comparison, an iterative process repeated 100 times to ensure the distributions were fully sampled. As a technical control for variation introduced by the selection process, the CD45 distribution was compared with itself.

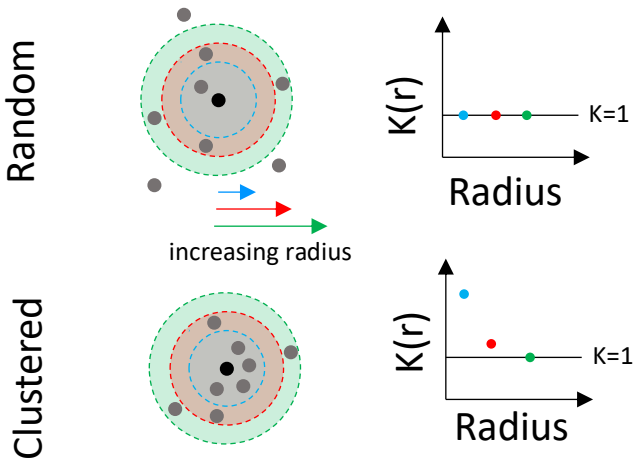



**Figure 3.10 | Principles of K-function analysis.** Schematic depicting the interpretation of the K-function. Spheres of increasing radius around each point will enclose a number of neighbouring points. For a homogenous distribution (top), the density of neighbours enclosed in each volume does not change (K=1). If the central point is part of a cluster (bottom), more points will be present in its vicinity than elsewhere, and the density will be greater nearer to that point (K>1).

The BCR distribution exhibited an increase in local density (K(r)~1.7) at 100nm radius, suggesting that the probability of encountering another BCR molecule within 100nm of a BCR localisation was 1.7x higher than in the CD45 distribution (Fig. 3.11a). This increase was not statistically significant compared to the technical variation of the CD45 distribution (Fig. 3.11c,d). Importantly, in the presence of cross-linking antibodies, the probability of finding another BCR molecule within 100nm increased to ~2.9x that of CD45 (Fig. 3.11b), with statistically significant increases compared to the resting BCR distribution (Fig. 3.11c,d). This increase suggested cross-K analysis was sensitive to the formation of clusters upon induced receptor cross-linking.

This induction of BCR clustering was also visible when plotting receptor density onto the membrane localisation distribution. As total localisation numbers in BCR-labelled cells are identical in the presence or absence of other binders, the local density of receptors can be directly compared. Figure 3.12. contains images of a representative cell depicting native BCR organisation compared to one labelled under cross-linking conditions. In the presence of cross-linking antibodies, regions containing hundreds of receptors within 100nm radius are larger and more frequent, consistent with cluster formation.

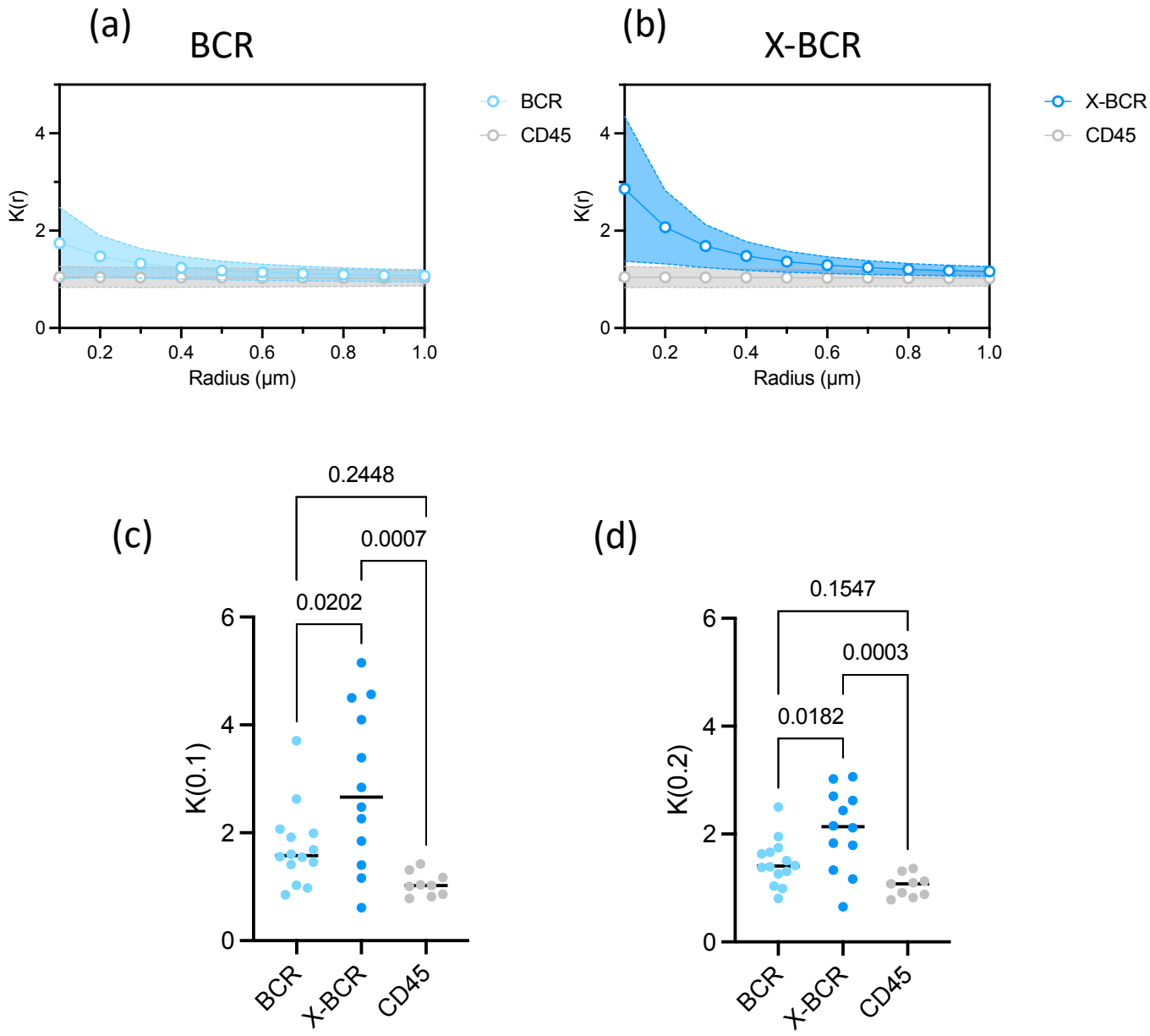



**Figure 3.11 | Cross K-function analysis of BCR distribution in the presence or absence of crosslinking. (a-b)** Average K(r) ratio for the resting BCR distribution (**a**, light blue) or cross-linked BCR (**b**, X-BCR, dark blue) when compared to the distribution of CD45 molecules. The comparison of CD45 to its own distribution is shown in grey in both graphs. Symbols represent the mean measurement of the average K(r) of each cell. The coloured envelope represents the standard deviation across average K(r). **(c-d)** Scatter plot of the values of K(r) at **(c)** 0.1µm radius and **(d)** 0.2µm radius for all conditions depicted in (a-b). Symbols represent the average K(r) for each cell after comparison with n=9 CD45 cells, bar represents mean value for each condition. Statistical significance was determined using a one-way unpaired ANOVA with Tukey's multiple comparisons test. p-values for each comparison are shown. For all plots, n=14 BCR cells, n=12 X-BCR cells, n=9 CD45 cells, from two different imaging sessions conducted with cells from n=2 mice.

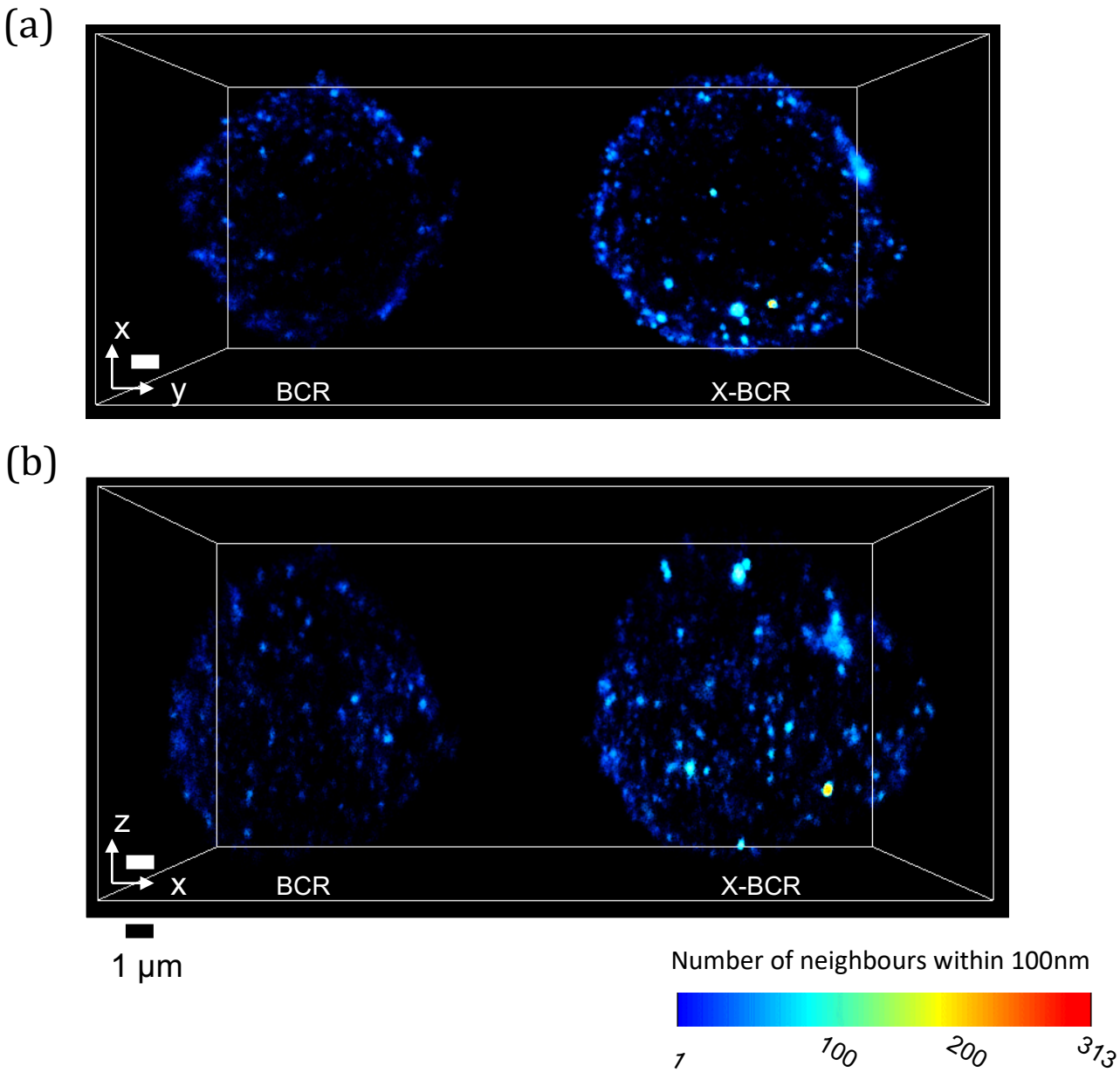



**Figure 3.12 | Nearest-neighbour representation of localisations in BCR-labelled cells.** Comparison of two representative cells labelled with anti-BCR Fab-Halo under resting conditions (left) or crosslinking conditions (right). Localisations are coloured by number of neighbours present within 100nm radius (ranging from 1 to 313 localisations, as per colour bar). **(a)** represents a view of the cells along the z-axis (xy plane), while **(b)** represents the same cells viewed from the side (xz plane). Scale bar = 1µm.

## 3.4 Discussion

The work in this chapter describes the use of a novel approach to studying receptor distribution at the cell surface. The generation of recombinant Fab-Halo probes based on publicly available antibody sequences allowed for single-dye labelling of receptors in primary naïve B cells. Most studies use probes containing several dye molecules, which can give rise to overcounting, or rely on genetic modifications to introduce fusion proteins, often in clonal B cell lines[102,189]. Moreover, in using monovalent binders, this work avoids perturbative receptor association that may be induced by bivalent probes[261]. Together, these considerations form an optimal setting to study receptor organisation, following similar improvements in recent studies[168,261].

Using a new iteration of a previously described 3D super-resolution method[256], receptors could be imaged in the context of the native cell membrane. This avoided the requirement for cell spreading onto coverslips, which can in cases lead to cell signalling and constrained receptor diffusion[260,265,266]. In preserving the cellular ultrastructure, 3D imaging also allowed for the localisation of receptors without perturbing or ignoring areas of membrane curvature, which may play an essential role in lymphocyte activation[267]. Murine B lymphocytes could be imaged due to the large depth-of-field of SMLFM, and cells of the expected diameter contained features including presumed microvillar structures, still detectable in fixed cells.

The number of super-resolved receptor localisations per cell was in accordance with the number of receptors expressed on B cells, with no evidence of poor labelling despite the disparity with the number of previously reported BCR molecules on the murine cell surface[192,194]. This was an important consideration because sub-sampling

distributions can have an impact on studies of receptor valency, as measurements of sparsely labelled molecules tend towards monomericity[212]. An explanation for the increase in the number of BCR localisations (~32,000) compared to the number of receptors determined by flow cytometry (~23,000) may be attributable to the 're-blinking' behaviour of Alexa Fluor 647 dyes[251]. This can induce clustering artefacts and may require further investigation of dye blinking dynamics. However, as all datasets were collected under equivalent imaging conditions, any such effects should not influence clustering analysis when comparing the BCR distribution to that of CD45.

Application of cross K-function analysis to the 3D distributions of the BCR revealed a difference in the local enrichment of BCR receptors around each BCR molecule, consistent with some degree of accumulation when compared to the CD45 distribution. Although this increase was not statistically significant, it suggested a 1.7-fold increase in the probability of encountering another molecule within 100nm radius of any BCR molecule. However, a significant increase in K(0.1) and K(0.2) was observed when cross-linking antibodies were introduced (Fig. 3.11c-d), suggesting this analysis method is sufficiently sensitive to detect receptor association. It is worth noting that the variance in the BCR distribution, which underlies this statistical analysis, is driven both by experimental and biological variation. In particular, biological variation in this setting can be derived from several factors, including clonal diversity across the cells imaged, and differential signalling states which occur in resting cells, such as tonic signalling (discussed in Section 7.2). In line with this, it is worth noting that, for some cells, the BCR distribution is unclustered when compared to that of CD45 (Fig. 3.11c-d). It is therefore difficult to interpret what the variation of this data without further experimental perturbations of the resting cell state, to further

clarify whether this variation across cells is driven by experimental variability or derives from possibly important biological variability (this is further discussed in the general Discussion, Section 7.2).

There are important limitations in the use of cross K-function analysis in the study of 3D receptor valency. The first is shared across most methods evaluating point distributions in super-resolution microscopy. This is the inability to distinguish between clustered molecules and a small area of increased receptor density. Metrics such as Ripley's K function cannot validate whether receptors are associated through intermolecular interactions, or whether they are still monomers constrained in areas of the membrane. Reports of the preferential localisation of the T cell receptor and its co-receptor CD4 to microvilli are examples of such inhomogeneous receptor disributions[267,273]. Enrichment at such structures cannot be readily distinguished from clusters of similar radii using these approaches. Fluorescence microscopy approaches such as resonance energy transfer, which rely on increased proximity at shorter ranges (~10nm), may be a complementary approach in clarifying such interactions[274,275].

Membrane proteins are distributed on a 2D surface, albeit one that exists in 3D space, and can contain significant deformations. As such, the radial distance between molecules, as used in this analysis, does not reflect the geodesic distance between them on the 2D membrane (the distance between molecules along the cell surface). Thus, the number of neighbours within a certain radius of a localisation can also be affected by membrane curvature. This is depicted in Figure 3.13. Membrane folding at protrusions such as microvilli brings regions of the membrane closer together. This does not alter the distance between molecules on the surface but brings them closer

together in 3D space. However, this confounding effect, which should equally affect any set of molecules on imaged cells, could in principle be controlled by comparison with the CD45 distribution.

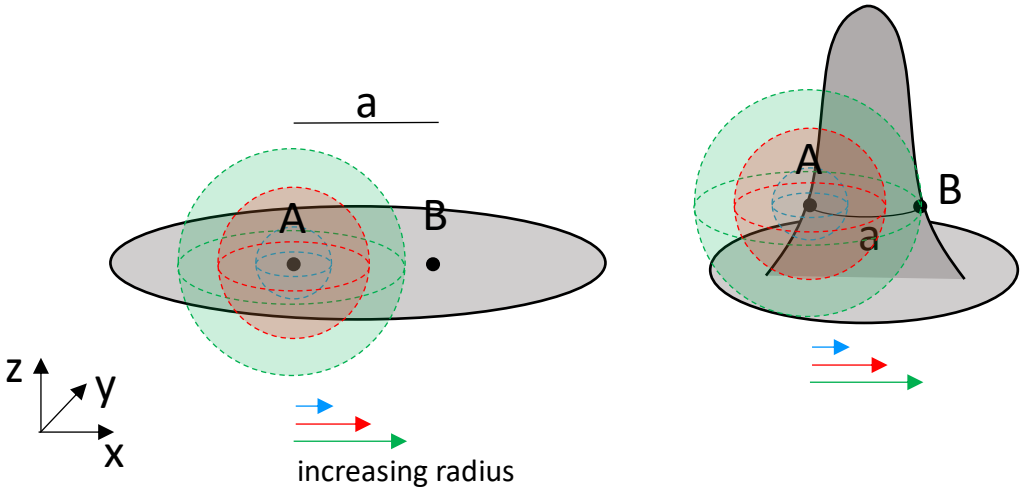



**Figure 3.13 | Impact of membrane folding on cross-K function analysis.** This diagram represents two points, A and B, that exist on a 2D surface and are spaced apart a distance, *a*. In the first case, on a flat surface (left), spheres drawn around point A with radius below *a* do not enclose point B. Upon folding of that surface (right), point B can now be enclosed within spheres of the same radius. This occurs despite the fact that the distance between the points on the surface remains the same.

Future improvements on this method could be achieved by defining the position of the cell membrane with the help of a membrane marker. Dual-colour, or sequential-labelling, imaging experiments could help define the location of the membrane as well as the receptor of interest. The parametrisation of the membrane surface and the receptor localisations enclosed within it could then be used to characterise the 2D distribution of receptors on the cell surface. Importantly, paired with well-defined metrics to characterise areas of membrane curvature (for example, the use of curvature tensors[276]), the 2D surface can be partitioned and categorised, and the density and clustering of localisations across membrane features, such as microvilli or

the cell body, can be compared. While computationally laborious, these approaches would allow for a better understanding of receptor organisation within the complex architecture of the cell membrane.

# Chapter 4. Increased antigen molecular height impairs BCR triggering

## 4.1 Introduction

BCR cross-linking has long been suggested as a mechanism of BCR triggering. With notable exceptions[175–177], the majority of studies of BCR signalling describe a receptor which relies on higher-valency antigens for signal transduction[163,165,166]. Monovalent antigens, or Fab fragments against receptors, are generally reported to not induce signalling in solution[163,165,166].

However, a growing body of evidence has shown that BCR sensitivity to monomeric antigens is dependent on its presentation. Monomeric antigens incapable of inducing signalling in solution may do so when present on surfaces[139,180,181]. Membrane-tethered antigens play a key role in B-cell activation *in vivo*. Antigen, often associated in immune complexes, can be presented on FDCs and other antigen-presenting cells through interactions with Fc receptors and complement receptors[277]. As such, while antigens can be present in solution in secondary lymphoid organs, the mechanisms driving BCR signalling to membrane-associated antigens are physiologically relevant[23].

Several mechanisms have been proposed to explain the requirement for membrane association. Surface coordination is thought to be essential for the induction of mechanical forces on the receptor (Section 1.5.2). The 'pulling' forces generated by BCR binding to tethered antigens has been suggested as a principal mechanism for the generation of receptor conformational changes needed for signalling[167,186]. Moreover, as the BCR plays a key role in antigen internalisation upon binding, pulling forces would likely be exerted on it as it extracts antigen from the apposite surface. In fact, antigen internalisation itself has been suggested to depend on forces generated by high-affinity antigen binding[184].

However, surface coordination in the absence of cross-linking is also a requirement of the kinetic-segregation model (Section 1.5.5). This model explains the differential response to soluble antigens by assigning the steric exclusion of phosphatases with large extracellular domains from sites of membrane contact as being causative of receptor signalling[195]. B cells express the largest isoform of CD45 (B220) and the likely larger phosphatase CD148[128,134], which may play a role in receptor signalling in this context. CD45 exclusion from sites of contact with apposite membranes has been previously described in B cells interacting with antigen-loaded membranes[139].

The functional role of phosphatase exclusion in BCR signalling has not been characterised. The requirement for passive phosphatase exclusion from sites of contact has been studied in other cell types through the use of two separate types of perturbations. Increasing antigen height is thought to increase the height of close contacts, impairing phosphatase exclusion and by extension receptor triggering[134,200,203,205,206]. Conversely, the role of phosphatase exclusion can be tested

by the expression of membrane phosphatases with truncated ectodomains or chimaeric ectodomains with reduced molecular height[134,203]. Such molecules can still diffuse into close contacts and would be predicted to impair signalling compared to wildtype phosphatases if phosphatase exclusion plays a role in receptor signalling.

To study these effects, a system to present surface-coordinated antigen to B cells must be generated. Many studies focusing on B-cell signalling to membrane antigen have used supported lipid bilayers (SLBs)[139,180,181] which, through incorporation of lipids containing certain moieties (e.g. biotin, nickel ions, etc), allow for the tethering of proteins in the correct orientation relative to the surface. Proteins in these fluid surface retain the mobility expected of a surface-bound ligand on an interacting cell, diffusing along the artificial membrane[278]. As a consequence, SLBs provide a model system that can be used to study cell interactions with a phospholipid surface onto which soluble, tagged proteins can be titrated on a fully characterised flat surface[278–280]. By using purified monomeric antigens, signalling events caused by higher-valency antigens can be avoided.

The work in this chapter seeks to characterise the functional role of phosphatase exclusion on BCR triggering. Fusion proteins incorporating the hen egg lysozyme (HEL) antigen were generated, spanning a range of affinities, and also varying in height. SLBs functionalised with these proteins could then be used as model membrane surfaces to study signalling events in antigen-specific primary mouse B cells.

## 4.2 Methods

### 4.2.1. Isolation of primary mouse B cells

For all experiments described in this chapter, cells from the MD4 mouse strain (C57BL/6-Tg(IghelMD4)4Ccg/J) were used[281]. Splenic B cells were isolated using a B Cell Isolation Kit, mouse (Miltenyi), according to the manufacturer's instructions.

### 4.2.2. Generation of model antigen molecules

All recombinant proteins described in this chapter were expressed in CHO-K1 cells as described in Section 2.4.3. Antigens for use on SLB surfaces were purified using the His-tag purification protocol defined in Section 2.4.4. The HH10 (HyHEL10) Fab fragment, containing a Twin-StrepTag on the C-terminus of the Fab heavy chain, was purified using the StrepTactin purification protocol described in Section 2.4.6.

### 4.2.3. Surface plasmon resonance

Surface plasmon resonance was conducted using a Biacore 8K system (Cytiva), using a Series S Sensor Chip NTA (Cytiva). All experiments were conducted at 37°C using 0.22µm-filtered HBS-P+ buffer (10mM HEPES, 150mM NaCl, 0.05% (v/v) Surfactant P20, pH7.4). To capture protein onto the chip, His-tagged protein (150nM in HBS-P+) was injected at a flow rate of 10µL/min for 60s contact time. The analyte (HH10 Fab) was then injected for 120s at a flow rate of 30µL/min. Dissociation was allowed to occur for 240s at the same flow rate. Serial dilutions of HH10 Fab were injected in a multi-cycle experiment, starting from a concentration of 10µM or 20µM and serially diluted 1:3 in HBS-P+ for a total of eight concentrations. In between runs, the chip was regenerated by dissociation of nickel ions from the chip using 350mM EDTA solution.

Reintroduction of nickel ions was conducted by incubation with 0.5mM $NiCl_2$, with subsequent recapture of His-tag proteins as described above.

Sensorgrams obtained from these runs were reference-subtracted, i.e. removing nonspecific signal obtained from runs where the same concentration of analyte is flowed over the chip without any captured protein present. Moreover, these were also blank-subtracted, i.e. removing nonspecific signal as determined by flowing only buffer over the captured protein. Subtracted sensorgrams were analysed using a 1:1 binding fit model using the Biacore Insight Evaluation software (Cytiva).

### 4.2.4. Supported lipid bilayer generation and functionalisation

Supported lipid bilayers (SLBs) were used as model surfaces as previously described[204]. Lipid mixtures containing predominantly phosphatidylcholine (POPC), one of the most common phospholipid classes on the cell membrane[282], were used. 2% of the total molar amount of lipid molecules was substituted with DGS-NTA(Ni), a nickelated lipid that could be used to tether His-tag-containing proteins to the cell surface. Stocks solutions of 25mg/mL POPC (*1-palmitoyl-2-oleoyl-sn-glycero-3-phosphocholine*, Avanti Polar Lipids) and 5mg/mL DGS-NTA(Ni) (*1,2-dioleoyl-sn-glycero-3-[(N-(5-amino-1-carboxypentyl)iminodiacetic acid)succinyl] (nickel salt),* Avanti Polar Lipids) were made by dissolving lipids in chloroform.

For SUV generation, 38.9µL POPC stock solution and 5.5µL DGS-NTA(Ni) stock solution were added to 70µL chloroform and dried under nitrogen gas. The lipid mixture was dissolved in 1mL 0.22µm-filtered PBS and incubated at 4°C for 30mins. The lipid mixture was sonicated using a tip sonicator to dissociate lipid assemblies into small unilamellar vesicles (SUVs). For surface preparation, glass slides were cleaned by immersion in a 3:1 $H_2SO_4$:$H_2O_2$ mixture (Piranha solution) overnight. After extensive washing in deionised water, slides were air-dried and cleaned under oxygen plasma for 1 minute. Clean glass slides were fitted with CultureWell wells (3µm diameter, 1µm thickness, Grace Bio-Labs). Glass slides were incubated in a humidified chamber to limit evaporation during bilayer formation.

Bilayers were generated by SUV spreading, through incubation of a 1:1 PBS-SUV solution mix (10µL/well) on clean glass for 45 minutes at room temperature. Bilayers were washed five times by replacing half of the volume in each well with fresh PBS. Bilayers were functionalised with labelled proteins. Protein stocks were thawed on ice and centrifuged at 17,000g for 10 minutes at 4°C to remove any aggregates. Concentrations were measured using a NanoDrop One system and proteins were diluted to working concentrations in filtered PBS. Washed bilayers were functionalised by replacing half of the volume in each well with 5µL protein solution and incubated for 75mins at room temperature in a humidified chamber. Bilayers were washed by replacing half the volume ten times with 5µL 0.22µm-filtered imaging solution (PBS supplemented with 0.5% (w/v) bovine serum albumin (BSA), 1mg/mL D-Glucose(+), 2mM $MgCl_2$, 0.5mM $CaCl_2$). This was a modified solution based on previously used buffers for B-cell studies on SLB surfaces[139].

### 4.2.5. Point fluorescence correlation spectroscopy

Point fluorescence correlation spectroscopy (pFCS) was used to describe the density and diffusion of fluorescent molecules on bilayer surfaces[278]. Bilayers functionalised with Alexa Fluor 647 HaloTag-labelled proteins were imaged at the axial position of maximum fluorescence intensity, at 37°C. Bilayers were illuminated using a 633nm helium-neon laser at 0.5% laser intensity with the pinhole set to 1 airy unit and imaged using a 40x water objective in an LSM780 inverted confocal microscope (Zeiss). Data was collected in quintuplicates, from 3 random spots on the bilayer surface. Data was analysed using PyCorrFit[283]. All autocorrelation curves for a single bilayer were used to generate an average autocorrelation curve, which was fit using a Levenberg-Marquardt algorithm to a pre-defined 2D confocal Gaussian diffusion model with triplet state (2D+T).

The number of particles (n) and the transit time ($\tau$) were obtained from this average curve. To calculate the protein density and diffusion, the beam waist radius of the confocal volume must be determined[284]. 100nM solution of Alexa Fluor 647 HaloTag ligand was plated onto the same CultureWell setup and dye in solution was imaged under equal imaging conditions at three different spots across the dye volume. The autocorrelation curves were averaged and fit using the Levenberg-Marquardt algorithm to a pre-defined 3D confocal Gaussian diffusion model with triplet state (3D+T) model.

The beam waist radius (ω) was calculated using the relationship[285]

$$D = \frac{\omega^2}{4 * \tau}$$

where D is the diffusion coefficient of the dye molecule in solution, τ is the transit time of the dye in solution and ω is calculated from the two other parameters.

The diffusion coefficient of Alexa Fluor 647 at 37°C was calculated from the published diffusion coefficient[285] of 370μm$^2$/s measured at 40°C using the relationship[284]

$$D_{37\circ C} = D_{40\circ C} * \frac{(37 + 273.15) * \eta_{40\circ C}}{(40 + 273.15) * \eta_{37\circ C}} = 345.99\mu m^2/s$$

where $D_T$ is the diffusion coefficient at temperature T (in μm$^2$/s) and $\eta_T$ is the viscosity of water at temperature T (in mPa*s).

The protein density was calculated by normalising the number of particles by the observation area (the circular cross-section of the confocal volume on the planar bilayer):

$$\rho = \frac{n}{A} = \frac{n}{\pi\omega^2}$$

where ρ is the protein density on the bilayer, n is the measured number of particles and ω is the beam waist radius.

### 4.2.6. Calcium signalling experiments

Primary mouse B cells were labelled with the calcium-sensitive dye Fluo4-AM (ThermoFisher), which displays increased fluorescence intensity upon binding to calcium ions[266]. Cells were maintained at $10^7$/mL for all labelling steps. Cells were washed in filtered PBS, and labelled in a 1:1 mixture of PBS:RPMI-1640 supplemented with 25μg/mL Fluo4-AM for 45mins at 37°C, 5% $CO_2$. Labelled cells were washed in filtered imaging buffer (PBS, 0.5% (w/v) BSA, 1g/L D-Glucose(+), 2mM $MgCl_2$, 0.5mM $CaCl_2$), and resuspended at a final density of $4x10^7$/mL in imaging buffer.

Labelled cells and bilayer surfaces were equilibrated to 37°C prior to confocal imaging using an LSM780 inverted scanning confocal microscope (Zeiss) fitted with a temperature-controlled chamber. Cells were introduced onto the surface and imaged at 1 frame/second for 600 seconds using a 25x air objective and illuminated using a 488nm argon laser. Cellular calcium responses were determined by the presence of fluxes of increased Fluo4-AM intensity upon interaction with the surface. To calculate the fraction of cells undergoing a calcium response, videos were analysed using a previously described custom MATLAB code[266]. Briefly, cells were segmented and tracked across all frames. Cells that could be tracked for at least 240 frames (240s) were maintained for analysis. Baseline fluorescence intensity for each cell was defined as the value below which 25% of recorded fluorescence was observed. Cells displaying fluorescence increases above 1.75 times the baseline were considered to undergo a calcium flux (i.e. 'triggered'). Data was plotted and analysed using PRISM (GraphPad, version 9) and fit for each protein tested using a nonlinear regression model.

## 4.3 Results

### 4.3.1. Soluble proteins for the study of antigen height

To study BCR signalling to membrane antigens, an experimental system based on the HEL antigen was generated. HEL is among the most common antigens used in B cell signalling studies, in large part due to the existence of several well-established mouse models that encode anti-HEL receptors[96,281]. The MD4 mouse strain is a commonly used transgenic mouse line in which ~95% of B cells express an anti-HEL BCR[286]. The transgene allows expression of IgM and IgD BCRs containing the variable regions of the HyHEL10 antibody, a high-affinity antibody which binds to HEL with a dissociation constant ($K_D$)~20-50pM[180,281]. Thus, naïve B cells extracted from the MD4 mouse strain provide a well-characterised system to study antigen-specific BCR responses. The use of HEL in previous studies has identified lower-affinity variants of the antigen, spanning a range of affinities similar to those of unmatured BCRs in naïve B cells[180,181,287,288].

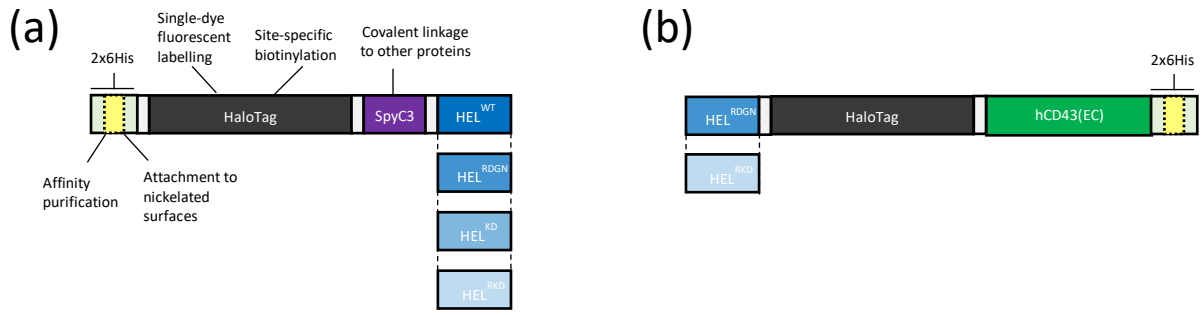



**Figure 4.1 | Design of HEL fusion proteins.** Schematic representation of **(a)** HSpyC-HEL proteins and **(b)** HEL-Halo-CD43 proteins. SpyC3 is short for SpyCatcher003 (see Chapters 5 and 6); EC is short for extracellular domain.

Supported lipid bilayers have previously been used to study BCR signalling in response to membrane-tethered antigens. Such model surfaces can be functionalised with proteins of interest and retain the fluidity of the plasma membrane, allowing for protein diffusion[278]. Bilayers functionalised with HEL have previously been used to study B-cell behaviour on activating surfaces[139,180,181].

To generate antigens that could be used to study B-cell responses to membrane antigens, histidine-tagged HEL fusion proteins were designed and purified (Fig. 4.1a). These proteins (hereafter, HSpyC-HEL) contained additional N-terminal domains which were introduced to the HEL protein to ensure it could be site-specifically modified if required. A HaloTag domain was introduced, permitting site-specific covalent labelling with dye or biotin ligands[250]. Moreover, a SpyCatcher domain was also added to the protein, to allow for covalent attachment of the HEL proteins to other proteins[289]. Most importantly, two histidine tags were introduced to the N-terminus of the HEL fusion proteins, to allow tethering of the protein to nickel-coordinating lipids incorporated onto a lipid bilayer[278–280]. Based on previously characterised mutational data[180], wildtype HEL and three mutants with decreasing affinity for HyHEL10 were produced: HSpyC-HEL$^{WT}$, -HEL$^{RDGN}$, -HEL$^{KD}$ and -HEL$^{RKD}$. All purified HSpyC-HEL proteins looked identical by size-exclusion chromatography and could be readily purified as clean monomers of the predicted size (~65kDa, Fig. 4.2).

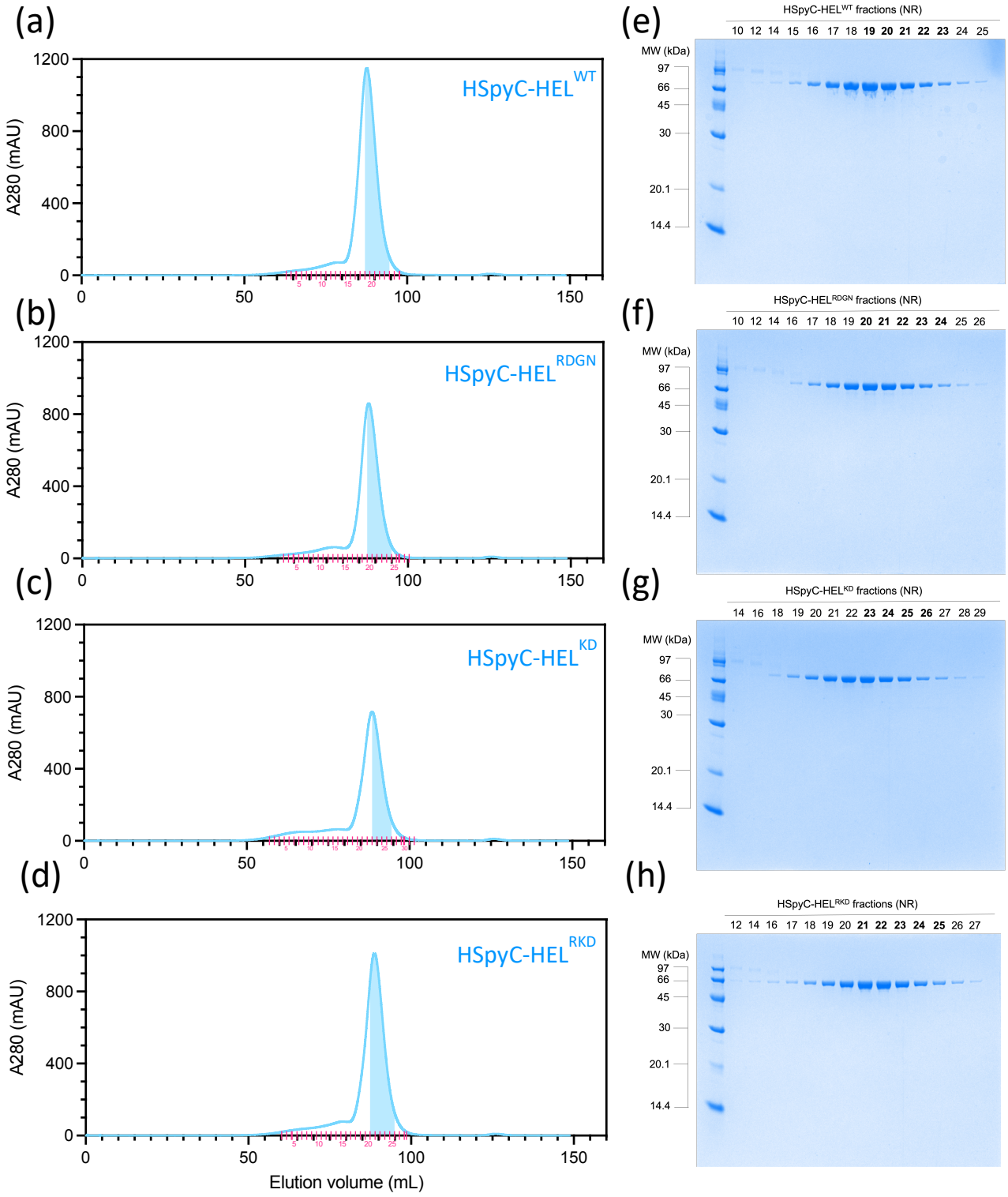



**Figure 4.2 | Purification of HSpyC-HEL proteins. (a-d)** SEC profiles of affinity-purified HEL fusion proteins. Protein fractions are labelled in pink. The shaded area under the curve represents fractions pooled for future use. Profiles are shown for **(a)** HEL$^{WT}$, **(b)** HEL$^{RDGN}$, **(c)** HEL$^{KD}$ and **(d)** HEL$^{RKD}$. **(e-h)** SDS-PAGE analysis of protein fractions boiled under nonreducing conditions. Fractions kept are highlighted with bold text for purified **(e)** HEL$^{WT}$, **(f)** HEL$^{RDGN}$, **(g)** HEL$^{KD}$ and **(h)** HEL$^{RKD}$ proteins. In all cases, 12% polyacrylamide gels were stained with Coomassie Blue for protein detection.

The effect of ligand size has been an important perturbation used to examine the effect of phosphatase exclusion from close contacts on receptor signalling[200,202,203,205,206]. Fusion proteins presenting ligands on the membrane-distal terminus of large protein ectodomains are a commonly used method to increase antigen height[200,202,203,205,206]. In particular, the ectodomain of human CD43 has been previously used as an ectodomain of choice[200,203,206]. CD43 is a highly glycosylated protein and a key component of the glycocalyx of some leukocytes[290]. The CD43 ectodomain is predicted to be rigid, as rod-like, extended structures were observed for soluble ectodomains using electron microscopy[291]. Antigens positioned on the membrane-distal terminus of the human CD43 ectodomain have been shown to impair TCR[200,206] and FcεRI[203] signalling. The use of CD43-fused antigens lead to increased inter-cell contact distance for T cells interacting with antigen-presenting cells[206]. T cells interacting with CD43-OKT3 ligands displayed impaired CD45 exclusion in contacts generated with lipid bilayers[200], and the same effect has been observed for basophils interacting with bilayer-bound CD43-Fcε[203]. Prompted by these results, CD43-HEL fusion proteins were produced (Fig. 4.1b). HEL proteins containing a C-terminal HaloTag and hCD43 ectodomain were designed, with a double-histidine tag introduced to anchor the hCD43 'stalk' to the bilayer in the correct orientation. Two variants of the HEL-CD43 proteins were generated, based on one high-affinity ($HEL^{RDGN}$) and one low-affinity ($HEL^{RKD}$) variant of the antigen. Both HEL-CD43 proteins could be purified as monomers (Fig. 4.3), displaying a broad distribution by SEC attributable to the variable glycosylation of the CD43 ectodomain.

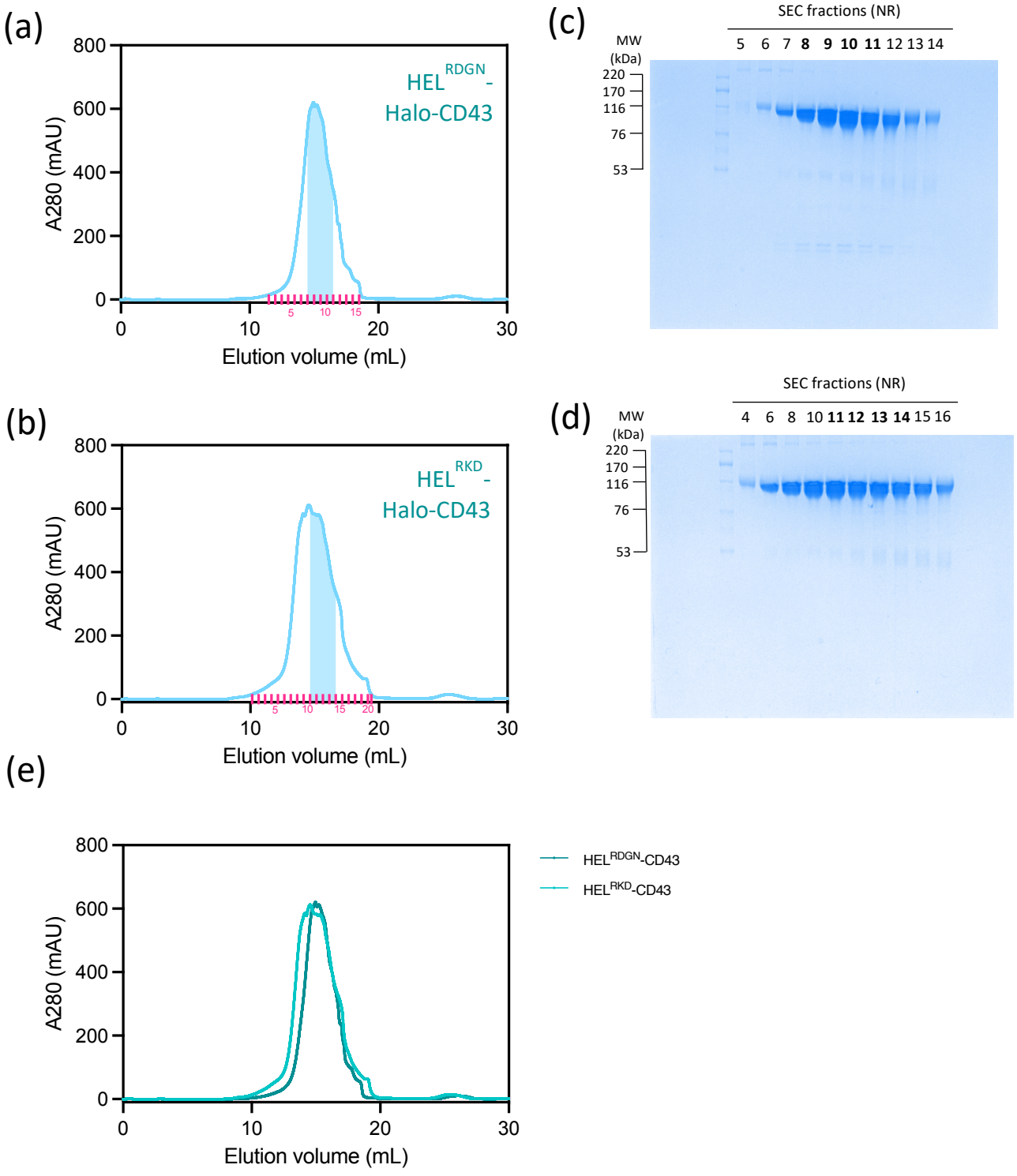



**Figure 4.3 | Purification of HEL-Halo-CD43 proteins. (a-b)** SEC profiles of affinity-purified HEL-CD43 fusion proteins. Protein fractions are labelled in pink. The shaded area under the curve represents fractions pooled for future use. Profiles are shown for **(a)** HEL$^{RDGN}$-Halo-CD43 and **(b)** HEL$^{RKD}$-Halo-CD43. **(c-d)** SDS-PAGE analysis of protein fractions boiled under nonreducing conditions. Fractions kept are highlighted with bold text. Coomassie Blue-stained 4-12% polyacrylamide gels are shown for purified **(a)** HEL$^{RDGN}$-Halo-CD43 and **(b)** HEL$^{RKD}$-Halo-CD43. **(e)** Overlay of the SEC profiles for HEL$^{RDGN}$-Halo-CD43 (dark green) and HEL$^{RKD}$-Halo-CD43 (light green) displayed in (a,b).

Surface plasmon resonance (SPR) was used to verify the affinities of HEL proteins compared to those reported in the literature[180]. These measurements were also used to ensure HyHEL10 binding to HEL variants of varying heights was not impacted by the fusion to different protein domains. To measure the monovalent affinity of HyHEL10 for the HEL proteins of interest, a Fab fragment based on the original murine IgG1,κ HyHEL10 antibody[292] was produced. The Fab fragment could be readily purified as a monovalent heterodimer of the predicted size (Fig. 4.4).

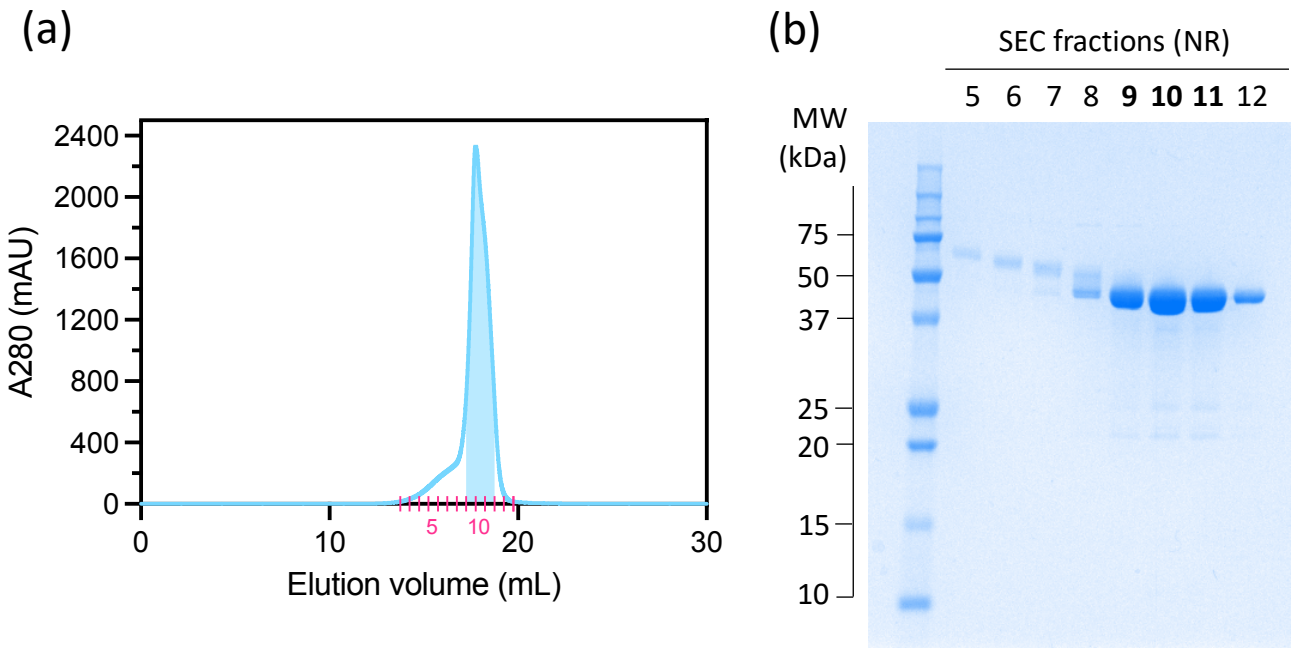



**Figure 4.4 | Purification of HyHEL10 Fab. (a)** SEC profile of affinity purified HyHEL10 Fab fragment. Protein fractions collected are labelled in pink. The area under the curve represents fractions kept for further use. **(b)** SDS-PAGE analysis of fractions collected in (a), boiled under nonreducing conditions. Proteins run on 12% polyacrylamide were stained using Coomassie Blue. Fractions kept are highlighted in bold text.

SPR experiments were conducted by tethering His-tag proteins to a nickelated surface, mimicking the orientation that the proteins adopt on the bilayer systems to be used (Section 4.2.3). Increasing concentrations of HyHEL10 Fab were used as the analyte. All HEL fusion proteins were bound by the Fab fragment in solution, as depicted in the sensorgrams in Figure 4.5. The $K_D$ was calculated from the sensorgrams obtained (Fig. 4.6a). The $K_D$ values obtained by SPR did not match those previously reported in the literature, corresponding to 15- to 50-fold decreases in affinity (Fig. 4.6b). However, these occurred for all antigens irrespective of what domains HEL had been fused to, suggesting this is unlikely to represent a decrease generated by fusion protein design. Moreover, the fold change in affinity between the wildtype HEL protein and HEL mutants remained similar to that previously reported (Fig. 4.6b).

Importantly, the $K_D$ values for HyHEL10 Fab binding to HSpyC-HEL proteins and their HEL-CD43 counterparts were consistent (Fig. 4.6a,b), confirming that the relevant HyHEL10 epitope remains equally accessible. The difficulty in obtaining a sufficient response for the lowest affinity antigens (Fig. 4.5e-f) introduced substantial variation in the $k_{on}$ and $k_{off}$ values obtained from the fit. As HEL-CD43 proteins were harder to immobilise on the chip (Appendix A, Fig. S1), the response obtained for $HEL^{RKD}$-CD43 was even lower than that observed for $HEL^{RKD}$. The fits for the $HEL^{RKD}$-CD43 antigen yielded concomitant increases in $k_{on}$ and $k_{off}$ compared to the HSpyC-$HEL^{RKD}$ protein (Fig. 4.6b), resulting in the $K_D$ value remaining consistent across $HEL^{RKD}$ proteins, and this effect was not observed for the higher affinity $HEL^{RDGN}$ protein pair (Fig. 4.6b). This does not suggest a true impairment in HEL accessibility to HyHEL10 when fused to CD43, but rather it is likely to be a by-product of the low binding response observed at low affinities.

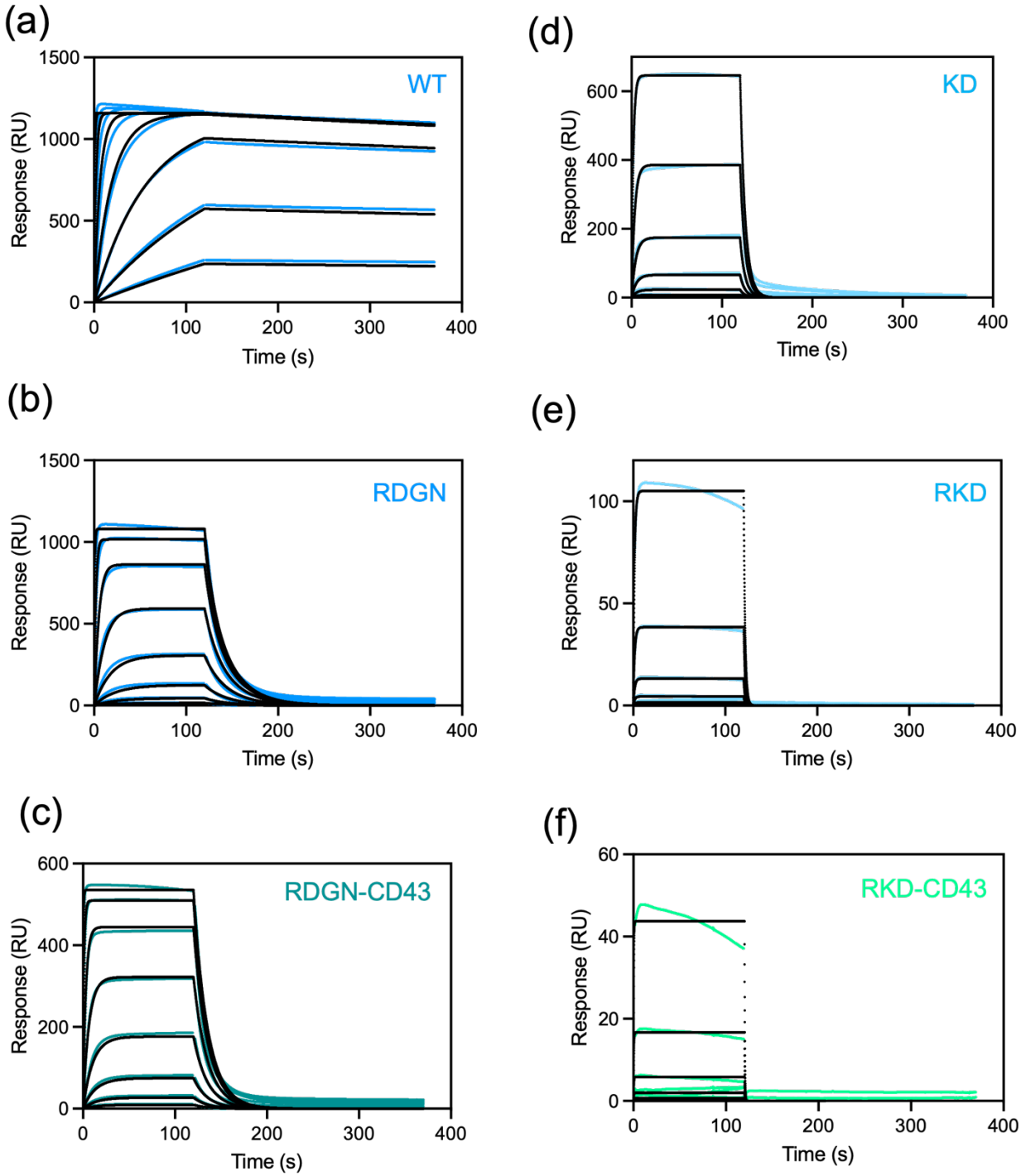
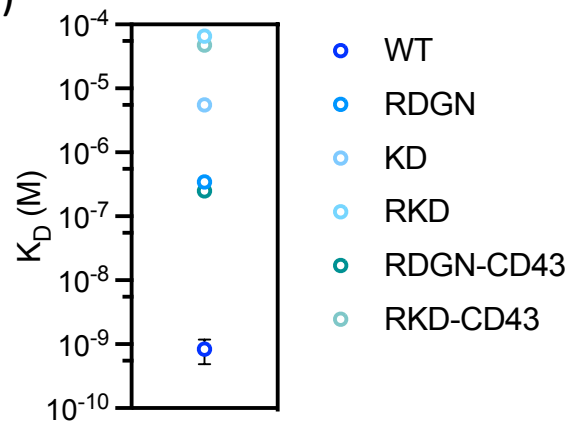



**Figure 4.5 | Representative sensorgrams for HyHEL10 Fab binding to immobilised HEL proteins.** SPR sensorgrams generated through flow of equal dilutions of HyHEL10 Fab over equal densities of NTA(Ni)-immobilised **(a)** HSpyC-HEL$^{WT}$, **(b)** HSpyC-HEL$^{RDGN}$, **(c)** HEL$^{RDGN}$-Halo-CD43, **(d)** HSpyC-HEL$^{KD}$, **(e)** HSpyC-HEL$^{RKD}$, **(f)** HEL$^{RKD}$-Halo-CD43.

(a)




(b)

| Protein | $k_{on}$ ($M^{-1}s^{-1}$) | $k_{off}$ ($s^{-1}$) | $K_D$ (M) | Published $K_D$ (Fleire et al., 2006) |
|---|---|---|---|---|
| $HEL^{WT}$ | $3.76x10^5$ | $3.01x10^{-4}$ | $8.3x10^{-10}$ | $4.8x10^{-11}$ |
| $HEL^{RDGN}$ | $1.88x10^5$ | $6.45x10^{-2}$ | $3.44x10^{-7}$ | $1.92x10^{-8}$ |
| $HEL^{RDGN}$-CD43 | $2.59x10^5$ | $6.47x10^{-2}$ | $2.51x10^{-7}$ | |
| $HEL^{KD}$ | $3.26x10^4$ | $1.79x10^{-1}$ | $5.52x10^{-6}$ | $2.5x10^{-7}$ |
| $HEL^{RKD}$ | $9.88x10^3$ | $6.51x10^{-1}$ | $6.59x10^{-5}$ | $1.25x10^{-6}$ |
| $HEL^{RKD}$-CD43 | $3.32x10^5$ | $1.69x10^1$ | $4.74x10^{-5}$ | |

**Figure 4.6 | SPR-determined affinities of HEL fusion proteins. (a)** $K_D$ values for HyHEL10 binding to HSpyC-HEL proteins (blue) or HEL-CD43 proteins (green). Symbols and error bars represent mean ± standard deviation. Data shown for two independent experiments, conducted at 37°C with two different batches of captured protein and analyte. **(b)** Table depicting the average $k_{on}$, $k_{off}$ and $K_D$ parameters obtained from the two independent SPR experiments depicted in (a). For comparison, the $K_D$ values determined for HyHEL10 binding to HEL mutants by Fleire and colleagues (ref. 180) is shown.

### 4.3.2. Generating HEL-bearing supported lipid bilayers

To test B-cell responses to membrane antigens, functionalised SLBs were generated on glass surfaces. Phosphatidylcholine bilayers containing DGS-NTA lipids coordinating nickel ions were used to tether His-tag-containing proteins to the surface, as previously described[204]. Bilayers functionalised with HEL proteins were assessed by point fluorescence correlation spectroscopy (pFCS) to determine the density and confirm free diffusion of molecules bound to the fluid surface[278].

In pFCS, variations in fluorophore intensity are measured as particles diffuse across a small volume, in this case illuminated using a confocal microscope. These variations can then be used to generate autocorrelation functions ($G(\tau)$). The fluctuations in photon counts are dependent on how rapidly molecules enter and diffuse out of the confocal volume, and how many particles are present in the confocal volume on average. Both these parameters are encoded in the resulting $G(\tau)$ functions. The amplitude of the $G(\tau)$ function is correlated with the number of particles in the confocal volume. In turn, the transit time ($\tau_D$) is the average time for a particle to cross the volume[284].

Figure 4.7. depicts an example of average autocorrelation curves generated through illumination of bilayers incubated with varying concentrations of $HEL^{RDGN}$-CD43. Molecules diffusing on a lipid bilayer are only imaged in the area consisting of the 2D intersection of the bilayer and the confocal volume. Calculating the surface area of this intersection allows for the normalisation of the number of particles per unit area, yielding the density of molecules on the surface (Section 4.2.5). Similar normalisations

allow for the calculation of the average diffusion coefficient from the average transit time of a particle crossing the cross-section area (Section 4.2.5)[293].

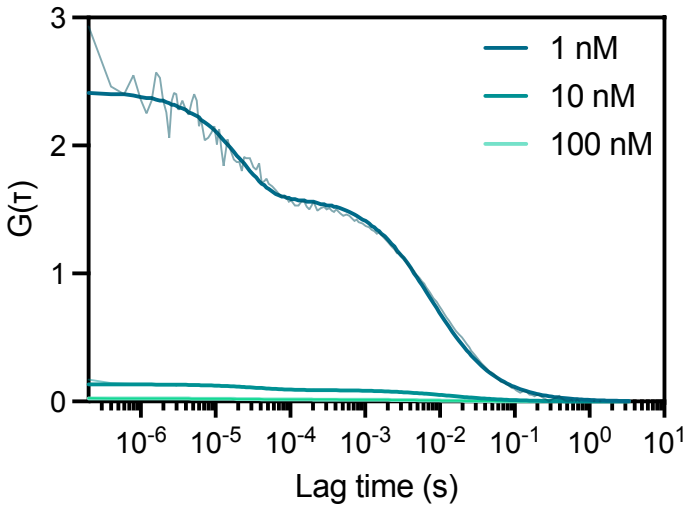



**Figure 4.7 | Example autocorrelation curves from confocal imaging of functionalised HEL bilayers.** Average autocorrelation (G(τ)) curves from pFCS measurements of bilayers incubated with 1nM (dark green), 10nM (green) and 100nM (light green) concentrations of $HEL^{RDGN}$-CD43 labelled with Alexa Fluor 647. The fit (thick line) and the experimental data (thin line) are shown. Each curve represents the average measurement for a single bilayer per condition. The amplitude of the curves, and by extension the y-intercept, decrease as the number of particle increases.

pFCS conducted on lipid bilayer surfaces was used to verify that bilayers incubated with equimolar concentrations of different antigens yielded surfaces with similar properties. SLBs incubated with increasing concentrations of HEL antigens site-specifically labelled with Alexa Fluor 647 were measured using pFCS. Increasing the concentration of His-tag proteins lead to a linear increase in protein densities (Fig. 4.8a), as expected. Importantly, the densities for bilayers generated using four HEL-derived proteins were identical, irrespective of protein size or affinity (Fig. 4.8a).

The average diffusion coefficient for molecules diffusing on bilayer surfaces ranged between 1-3$\mu m^2/s$ (Fig. 4.8b), comparable to the diffusion coefficients previously reported for His-tagged proteins diffusing on similar bilayers[278]. Slower diffusion was observed at higher densities, likely due to molecular crowding on the lipid surface, as is known to occur in three dimensions[294]. However, for all proteins tested, diffusion was identical across all bilayers for a given density (Fig. 4.8b). This suggests that despite the addition of the large ectodomain of hCD43, HEL-CD43 proteins (~100-115 kDa) show similar diffusion dynamics to HSpyC-HEL proteins. The addition of other domains to HEL in HSpyC-HEL proteins has increased their molecular weight (~65 kDa) to one closer to that of the larger antigen, likely mitigating for the effects of molecular weight on diffusion that have been previously reported[295].

In short, SLBs incubated with equimolar concentrations of HEL molecules generated lipid surfaces functionalised with equivalent densities of protein diffusing at equal rates, regardless of antigen affinity or height. This system could thus be used for direct and systematic comparisons of the effects of antigen height and affinity on BCR signalling.

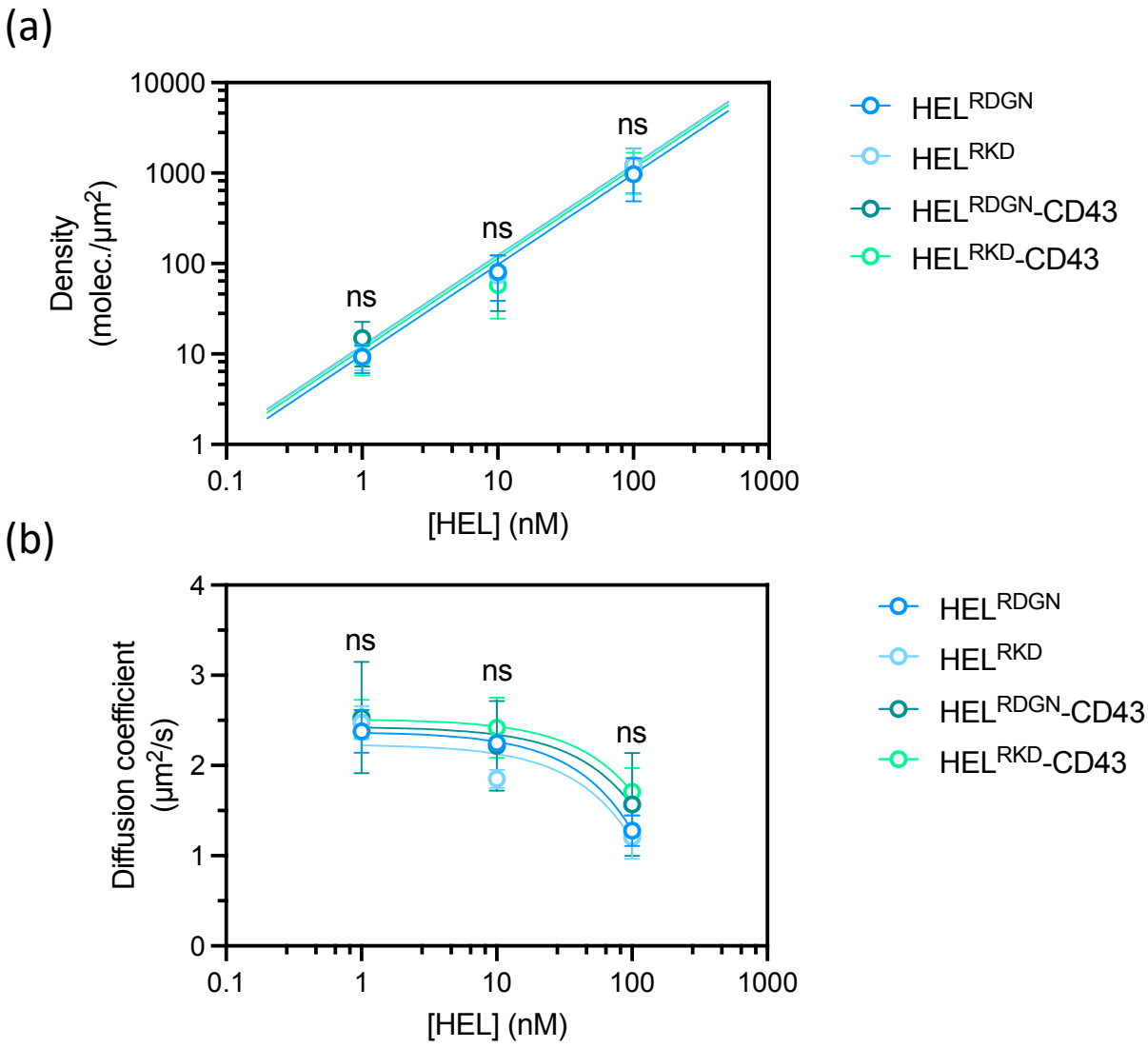



**Figure 4.8 | Characterising protein density and diffusion on HEL bilayers. (a)** Protein density (in molecules per µm$^2$ unit area) for bilayers generated through incubation with increasing concentrations of HEL$^{RDGN}$ (dark blue), HEL$^{RKD}$ (light blue), HEL$^{RDGN}$-CD43 (dark green) or HEL$^{RKD}$-CD43 (light green). Symbols and error bars represent mean ± standard deviation, respectively. Lines represent a linear regression for each condition. **(b)** Average diffusion coefficient for molecules diffusing on the same bilayers depicted in (a), generated through incubation with increasing concentrations of HEL$^{RDGN}$ (dark blue), HEL$^{RKD}$ (light blue), HEL$^{RDGN}$-CD43 (dark green) or HEL$^{RKD}$-CD43 (light green). Symbols and error bars represent mean ± standard deviation, respectively. Lines represent a linear regression in all cases. n=3 bilayers for all measurements. Statistical significance was determined using an unpaired one-way ANOVA for each concentration with Tukey's test for multiple comparisons. ns = not significant.

### 4.3.3. BCR triggering in response to HEL proteins of varying molecular height

One commonly used method to study antigen receptor signalling, which has been broadly applied to BCR triggering, is the detection of calcium influxes into the cytoplasm upon receptor stimulation. BCR triggering initiates a signalling cascade which results in both the release of intracellular calcium stores from the ER and the influx of extracellular calcium ions[149]. The resulting increase in cytoplasmic calcium concentration can be measured in real-time with the use of calcium-sensitive fluorescent probes, displaying fluorescence intensity increases (or emission spectra changes) upon calcium binding. Calcium ion influx into the cytoplasm, often measured using flow cytometry, is widely used as a proxy for BCR triggering[139,165–167,175–177,189,192].

The use of such calcium probes adapted to the study of BCR signalling to membrane molecules has been reported[139]. Cells loaded with calcium-sensitive dyes can be imaged upon interaction with functionalised surfaces using fluorescence microscopes, providing information about the dynamics of receptor triggering at a single-cell level. Live-cell confocal microscopy of dye-loaded cells interacting with bilayers has been used as a metric of receptor signalling for lymphocytes and other cell types[139,197,203,266]. To study BCR signalling in response to membrane antigens, HEL-specific primary MD4 B cells were isolated and labelled with the calcium-sensitive dye Fluo4-AM. These cells have been previously used to study BCR triggering to HEL of varying affinities attached to bilayer surfaces[139,180,181]. MD4 B cells could be readily labelled and displayed calcium fluxes upon interaction with lipid bilayers coordinating HEL molecules, but not on bilayers that were not functionalised with proteins, as exemplified in Figure 4.9.

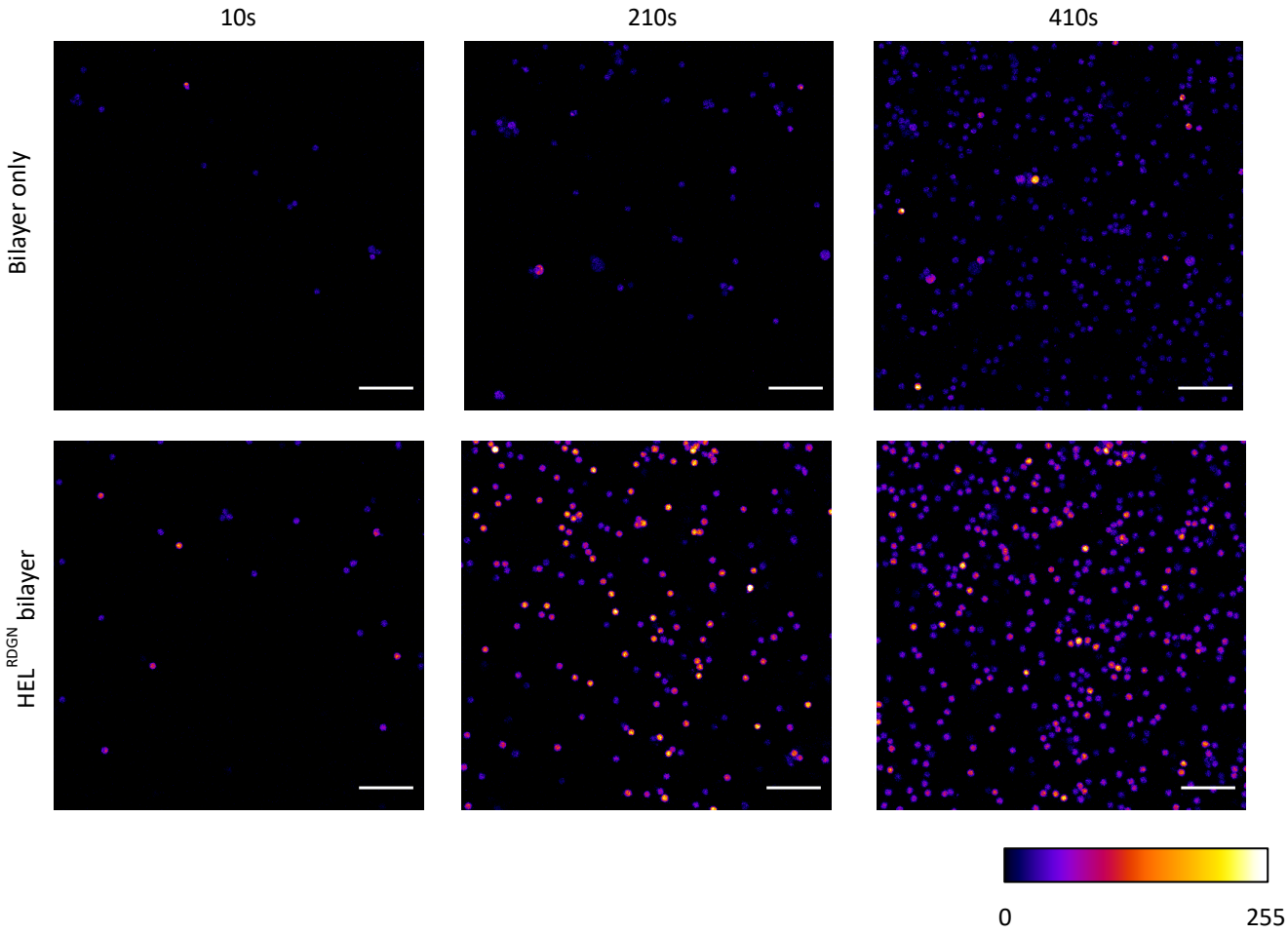



**Figure 4.9 | Example stills from confocal microscopy videos of MD4 B cells interacting with bilayer surfaces.** Stills from videos of Fluo4-loaded MD4 B cells interacting with bilayers not incubated with antigen (top) or one incubated with 100nM $HEL^{RDGN}$ (bottom). Stills from 600s videos taken at 10s (left), 210s (centre) and 410s (right) post-incubation of cells with the surface are shown. Colour encodes Fluo4-AM intensity (colour bar, bottom). Scale bar = 50μm.

Fluo4-labelled MD4 B cells were settled on bilayer surfaces incubated with increasing antigen concentrations of $HEL^{RDGN}$ (high-affinity) and $HEL^{RKD}$ (low-affinity) fusion proteins. The fraction of cells exhibiting calcium fluxes was calculated using a published bespoke analysis code[266], as defined by the parameters described in Section 4.2.6. MD4 B cells exhibited a density-dependent response to antigen, up to a saturating point at which a maximum response of ~80% of cells triggering was observed (Fig. 4.10). Minimal responses (~9% of cells triggered) were observed in the absence of HEL antigens (Fig. 4.10, left panel). The HSpyC-$HEL^{RDGN}$ antigen could induce signalling responses at lower concentrations than HSpyC-$HEL^{RKD}$, consistent with its higher affinity for HyHEL10 (Fig. 4.10).

Significantly, the percentage of cells responding to $HEL^{RKD}$-CD43 was smaller than that of cells responding to HSpyC-$HEL^{RKD}$ at certain densities (Fig. 4.10). Cells interacting with bilayers incubated with 10nM $HEL^{RKD}$ exhibited a significant difference in the fraction of cells responding: 40% of cells responding in the presence of the short form of the antigen and ~14% in the presence of the CD43 fusion protein. The lower response was comparable to the background response observed on bilayers without antigens. Therefore, $HEL^{RKD}$-CD43 fails to induce a significant response at some densities for which responses are observed for equal densities of 'short' antigens of the same affinity. The fraction of cells responding to $HEL^{RDGN}$-CD43 was not significantly different from that of cells responding to HSpyC-$HEL^{RDGN}$ at any density (Fig. 4.10). However, a trend towards a decrease in the fraction of cells triggered on bilayers incubated with 1nM $HEL^{RDGN}$-CD43 (~62%) was observed compared to the fraction of cells signalling on bilayers with an equal density of $HEL^{RDGN}$ (~79%).

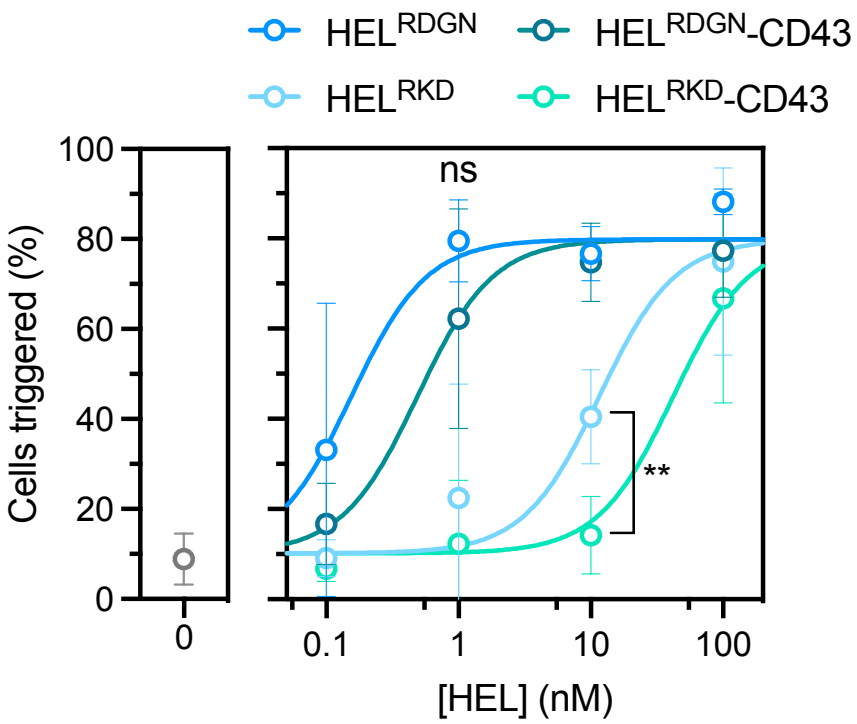



**Figure 4.10 | Primary MD4 B-cell triggering in response to HEL bilayers.** Percentage of cells experiencing calcium fluxes ('triggered') upon interactions with bilayers incubated with varying concentrations of HEL antigens. Percentage of cells triggered in response to bilayers not incubated with antigen are shown on the lefthand panel (grey). Symbols and error bars represent mean ± standard deviation, respectively. n=4 independent repeats per condition, utilising sets of B cells isolated from different animals imaged on different days. Statistical significance was determined using an unpaired one-way ANOVA with Tukey's test for multiple comparisons, conducted for each concentration individually. ** - $p<0.005$.

Notably, any effects induced by varying affinity and molecular height were not apparent at high densities of antigen (Fig. 4.10). Together, these results suggest that increased molecular height impairs BCR signalling to low-affinity antigens. These effects were observed only at density ranges where B cells can discriminate different antigen densities, i.e., these effects are not detected at saturating densities of antigen. This implies that molecular height impairs BCR sensitivity to antigen but does not limit B-cell responses when antigen is sufficiently abundant.

## 4.4 Discussion

The work described in this chapter seeks to assess the role of antigen molecular height in BCR triggering. Antigens based on hen egg lysozyme were generated (Fig. 4.1-3), spanning an affinity range similar to that experienced by unmutated, naïve B cells[296]. HEL antigens tethered to surfaces using the hCD43 ectodomain were produced to ensure these molecules were presented on a rigid domain (Fig. 4.3), increasing molecular height. All antigens could be produced as monomeric proteins, an important factor in avoiding cross-linking-induced signalling. SPR verification of binding affinities to the HyHEL10 paratope confirmed all paired antigen molecules retained comparable affinities irrespective of their molecular height (Fig. 4.6).

The variation in signalling responses upon stimulation with membrane-bound monomers or those in solution has been well-characterised. To explore the role of molecular height in receptor signalling, model membrane surfaces were functionalised with these antigens. Supported lipid bilayers could be generated and HEL proteins bound to these surfaces via His-tag interactions with nickelated lipids (Fig. 4.8). pFCS confirmed that antigens could be titrated onto the surface in a linear manner. The density of molecules tethered to the surface was dependent on the concentration of antigen incubated with the bilayer. Importantly, incubation with equimolar amounts of any given antigen yielded equal densities of antigens on the bilayer surface. Moreover, the average diffusion coefficient of the particles was shown to be constant for a given density, irrespective of which antigen molecules were titrated onto the bilayer. As such, bilayers functionalised with the various HEL proteins produced yielded bilayers with similar densities of equally diffusing molecules, allowing for a direct comparison of the effect of molecular height on BCR signalling (Fig. 4.8).

Naïve primary MD4 B cells expressing HyHEL10 BCRs could be tested upon interaction with bilayer surfaces bearing HEL antigens (Fig. 4.10). Importantly, these surfaces differed from previously used systems in that they lacked accessory molecules often included on bilayers for lymphocyte signalling studies. The adhesion molecules ICAM-1 and VCAM-1, which are expressed by FDCs and other antigen-presenting cells, have previously been included in HEL bilayers used for B-cell activation studies, and modulate BCR sensitivity in such systems[181]. Adhesion molecules are thought to stabilise contact sites between lymphocytes and APCs, dictating the molecular distance between the apposing surfaces[197]. Bilayers bearing ICAM-1 or other adhesion molecules as well as antigen could generate contacts wherein the B-cell surface is closer to the bilayer than the height of the HEL-CD43 molecules, possibly leading to their steric exclusion from the contact. The goal of this comparison has been to measure the extent to which molecular height affects BCR sensitivity to membrane antigens, by allowing 'taller' antigens to create contacts with larger inter-membrane distances[205,206]. The use of adhesion molecules would have confounded the effects of molecular height by allowing a second mechanism, antigen exclusion from contacts, to potentially impair BCR signalling. This work has therefore focused on bilayers containing HEL molecules only.

MD4 B cells responded to HEL antigens of differing affinities at identical density ranges as those previously reported (Fig. 4.10). Events associated with productive signalling, such as contact formation with the surface upon antigen engagement, and antigen accumulation, had been previously reported by Carrasco and colleagues[181]. Responses to $HEL^{RDGN}$ appeared to occur at densities <10 molec./$\mu m^2$ in their study, with higher concentrations yielding a saturated response. This is identical to the range at which

signalling responses have been identified in the present study (Fig. 4.10; this is equivalent to bilayers incubated with concentrations lower than ~1nM, as shown in Fig. 4.8a). Conversely, MD4 B cells responded to $HEL^{RKD}$ antigens on bilayers incubated with HEL at concentrations above 1nM (Figure 4.10; equivalent to ~10 molecules/$\mu m^2$, Fig. 4.8a). Carrasco and colleagues also observed responses only at densities above 12 molecules/$\mu m^2$. This work therefore recapitulates previous observations about primary B cell responses to membrane antigens. The functional response has not changed despite the differences in antigen affinity measured in this study by SPR from those in the published literature (Fig. 4.6b), suggesting these disparities in $K_D$ values are more likely due to differences in methodology rather than *bona fide* modifications in binding affinity induced by protein design. Indeed, previous studies using SPR measurements[292] had already suggested that the affinity of the HEL-HyHEL10 interaction could be ~10-fold lower than that reported in the functional studies which used the mutants employed in this work[180,181].

The present work reveals a significant difference in the response to membrane antigens of increased molecular height, particularly to low-affinity antigens (Fig. 4.10). No statistically significant difference was observed for antigens with higher affinities. However, triggering of primary B cells interacting with antigens of higher affinity at sub-saturating levels proved to be more variable than those responding to lower-affinity antigens. Small variations in concentration would more largely impact densities at lower concentrations, and this would therefore be more likely to impact signalling to high affinity antigens, where effects are observed in bilayers incubated with lower concentrations of antigen. As such, the small shift observed in the response at higher affinities may be of importance. However, the observation that the effect of

molecular height is attenuated for high-affinity ligands has been reported previously[200,206]. Furthermore, the observation that high-affinity HEL antigens induce similar levels of B-cell signalling in bilayer systems is consistent with previous work generated in the Davis group (thesis of Martin Wilcock[297]), in which HyHEL10-expressing A20 cell lines interacting with similar long and short $HEL^{WT}$ fusion proteins on SLBs showed no statistically different percentage of triggering cells at the single density studied, similar to the data observed in $HEL^{RDGN}$ bilayers in this study.

A limitation of this study is the lack of confirmation on the increased molecular height introduced by the ectodomain of hCD43. The contour length of the molecule has been calculated to be ~45nm[291,298], but its conformation on the cell surface has not been fully defined. Recent studies have highlighted that the average molecular height of membrane proteins is often shorter than the extended length of the ectodomain, with rigid proteins often capable of adopting a variety of conformations on the cell surface[208]. Methods such as cell surface optical profilometry[208] and hydrodynamic trapping[298] have recently been used to measure the average molecular height of proteins on SLBs. As such, future measurements of the average molecular height of CD43-fused antigens may be possible. Another important consideration from these studies is that molecular height can be partly affected by density. Rigid molecules with large ectodomains experience some increases in molecular height at higher densities[208]. This is purported to occur as a result of molecular crowding, which sterically blocks proteins from adopting less upright conformations due to packing at higher densities[208]. As such, the reported impact of affinity on the effect of molecular antigen height in this study may in fact be a by-product of the range of densities at which signalling is observed. As responses to lower-affinity antigens occur only at

higher densities, it is possible that the effects of molecular crowding at these densities force molecules to adopt a taller, more rigid conformation than those at lower densities used to test responses for higher-affinity antigens.

In conclusion, the work in this chapter has sought to define the role of molecular antigen height in BCR signalling. In line with previous observations[200,206], this work has demonstrated that increasing the molecular height of low-affinity antigens impairs BCR signalling to these molecules. This has implications for the models of receptor signalling proposed to explain BCR signalling to membrane antigens and will be further explored in the context of the literature in the General Discussion (Section 7.3).

# Chapter 5. Purification of a complete human BCR complex for structural studies

## 5.1 Introduction

B-cell receptor expression plays an essential role in B-cell activation, through antigen binding and subsequent signal transduction[161]. Despite this conserved receptor function, BCR complexes on the B-cell surface are highly diverse. The human B-cell population spans a wealth of possible BCR clonotypes, generated through various diversification mechanisms[299] (Section 1.1.3). Class-switch recombination further increases possible receptor permutations and structural variability through isotype switching[92].

As described in the Introduction, membrane immunoglobulins, composed of a dimer of heavy-light chain pairs, are noncovalently associated with a heterodimeric complex, composed of disulphide-bonded CD79A and CD79B[103,300], ITAM-containing proteins responsible for kinase recruitment and downstream signalling. The association of these two disulphide-bonded dimers occurs in a 1:1 stoichiometry[36]. For most - if not all - isotypes, signal transduction is not directed by the membrane-bound immunoglobulin, which does not contain intrinsic kinase activity or intracellular domain sequences capable of recruiting such effectors[161] (Section 1.3.2). Expression of all four chains of the receptor is therefore essential for surface expression of most

receptor isotypes, including IgM[103]. A possible exception is the IgG BCR, which can be expressed in the absence of CD79A-B[103,110].

Despite its importance, the assembly of the BCR complex had not yet been fully characterised at the start of this project. In the absence of purified fully assembled complexes, the expression of mutagenized components in living cells was used to determine residues involved in transmembrane domain interactions[301,302]. The study of the association of isolated peptides corresponding to the transmembrane domains[303,304] and the use of molecular simulations[304,305] have also been used as indirect methods to understand transmembrane domain interactions in receptor assembly.

In particular, past structural studies have focused on the structure determination of soluble extracellular domains of BCR components. The structure of the CD79A-CD79B heterodimer had not been determined, but information had been inferred from the crystal structure of a CD79B homodimer[100], as well as mutational data for soluble ectodomains defining the cysteine residues involved in the covalent association of the heterodimer[306]. This complex displayed measurable binding to the Fc fragment of IgM, even in the absence of the transmembrane domains[100], suggesting extracellular domain interactions help stabilised the noncovalent interaction of mIg and the signalling chains. In turn, the cryo-EM structures of the IgM Fc (Cμ4-Cμ3) domain were initially solved in the context of secretory pentameric IgM[307,308], with further structures of the pentameric and monomeric soluble IgM Fc recently determined[309]. The expected symmetry of the Cμ4-Cμ3 homodimer, confirmed by these structures, had long been difficult to reconcile with the biochemical data suggesting the

association with a single CD79 heterodimer, as binding interfaces would be repeated on both heavy chains.

Recently, advances in the use of stabilising detergent molecules permitting membrane protein purification under mild conditions have facilitated protein structure determination[310]. Coupled with evolving electron microscope technologies, particularly direct electron detectors, the rate of determination of membrane protein structures using cryo-EM has increased in recent years[311]. Such methods have been applied to the determination of the structure of immune receptor complexes, including the αβ TCR complex in its unligated[27,312] and pMHC-bound[240] state, confirming that no allosteric conformational changes occur upon ligand binding in solution[240]. This chapter focuses on the purification of intact IgM BCR complexes from mammalian cells, in the presence and absence of antigen, for use in cryo-EM studies. The comparison of the structures of both states of the receptor could elucidate whether allosteric modifications in complex conformation occur upon antigen binding.

Following the conclusion of the body of work described in this chapter, two cryo-EM studies determined the structure of human IgM[97,98] and IgG BCRs[98], with a third study similarly predicting the structure of a murine IgM BCR from a truncated receptor[99]. As these did not inform the work undertaken here, they will not be directly contrasted with the results as they are provided. Comparison of the properties of the complexes purified in the human BCR studies[97,98] and the results obtained in this chapter will be drawn in the discussion section at the end of the chapter.

## 5.2 Methods

### 5.2.1 Transduction of CHO-S cell lines

The Chinese hamster ovary cell line CHO-S was used for mammalian complex expression. Lentiviral particles containing a single sequence encoding the $VRC01_{GL}$ IgM BCR chains as a polycistronic construct were generated as described in Section 2.2.3. Transductions were conducted at 37°C, 5% $CO_2$. $10^6$ cells were transduced by incubation with 4mL lentiviral supernatant in a T25 flask and allowed to adhere to the surface. Culture volume was restored to 10mL with CHO-S medium after 24h and the cells were incubated in the viral supernatant for a further 72h. Cells were lifted using PBS supplemented with 5mM EDTA and placed into suspension culture under normal CHO-S growing conditions (Section 2.1). After 72h in culture, $10^6$ cells were again transduced with 4mL lentiviral supernatant, and the process was repeated. Cells were then placed into normal CHO-S culture conditions (Section 2.1). Expression of surface complex expression was validated by flow cytometry (see Section 2.3). Transduced cells were labelled with saturating concentrations of anti-IgM-PE antibody (clone MHM-88, Section 2.3.2), and the 10% highest expressing cells were cell sorted using a BD FACSAria Fusion sorter (with thanks to the WIMM Flow Cytometry facility).

### 5.2.2 Saturation test for BCR binders

To mimic the labelling process used for purification, CHO-S cells were stained with varying concentrations of AF647-labelled SpyCatcher3 or eOD-GT8 at equivalent densities to those used for the purification of the BCR complex. Cells were washed in ice cold PBS and $3x10^6$ cells/well were plated in 96-well plates. Cells were stained in triplicates for 45 mins at 4°C with varying concentrations of soluble protein in a 50µL

volume ($6x10^7$ cells/mL). Where counterstains were used, cells were washed in cold PBS and stained with 20μg/mL labelled HPC4 antibody or fluorescent streptavidin for 30mins at 4°C. Cells were washed twice in PBS, fixed in 1% (w/v) PFA in PBS and acquired using an Attune NxT (ThermoFisher) system.

### 5.2.3 Surface complex labelling

Prior to complex purification, SpyTag-containing $VRC01_{GL}$ IgM receptors were labelled using either soluble SpyCatcher3 or eOD-GT8 proteins containing affinity tags, mimicking the approach used by Sušac, Vuong and colleagues[240]. An initial labelling step using AF647-labelled protein (2.5% of final protein concentration) was conducted to ensure preferential binding of labelled soluble proteins. CHO-S cells were cultured to a final density of 3-$4x10^6$ cells/mL in 1L cultures. Cells were counted and $3x10^9$ cells per culture were harvested by centrifugation at 560g, 15mins at 4°C. Cells were washed once in cold PBS and resuspended in PBS to a final volume of 48mL. 50μg SpyC3-AF647 or 37.5μg eOD-GT8-AF647 were added, and the cells were incubated for 10mins at 4°C. Subsequently, 2mg unlabelled SpyC3 (final concentration $40\mu g.mL^{-1}$) or 1.5mg unlabelled eOD-GT8 (final concentration $30\mu g.mL^{-1}$) was added to the cells, bringing the final volume to 50mL. Cells were thus at a density of $6x10^7$ cells/mL, matching the conditions under which saturation was determined (see Section 5.2.2). Cells were incubated for 45mins at 4°C, washed twice with 40mL ice cold PBS, and pelleted at 526g, 10mins. Supernatant was discarded and cell pellets were snap frozen in dry ice. Pellets were stored at -80°C for under 2 weeks prior to purification.

### 5.2.4 Membrane complex purification

Surface complexes were purified through isolation of CHO-S plasma membranes and membrane solubilisation[240] (Part 1), followed by affinity purification using HPC4[244] (Part 2.1) or StrepTactin[247] (Part 2.2) resins. As described in Section 5.2.3, cells were labelled in $3x10^9$ batches. Small-scale experiments, used to optimise protocols, involved purification from 2 pooled batches of cells (2L). Large-scale experiments conducted to produce enough material for cryo-EM pooled 10 batches of cells (10L). Each batch contained $3x10^9$ cells processed as per Section 5.2.3. The protocols below describe purification on a 'per batch' basis and are readily applicable to both small- and large-scale experiments.

**Part 1. Solubilisation of CHO-S plasma membranes**

Cell pellets prepared according to Section 5.2.3 were thawed at room temperature. All subsequent purification steps were conducted at 4°C. This section follows directly from the work described by Sušac, Vuong and colleagues[240]. Cells were pooled and resuspended in 120mL/batch in ice cold resuspension buffer (30mM Tris-HCl, pH8, 750mM NaCl, supplemented with 10µg/mL DNAseI, ≥2.5U/mL benzonase, and cOmplete protease inhibitor cocktail, EDTA-free (Roche)). Cells were dounce homogenised three times in a glass homogeniser and mixed using a magnetic stirrer for 45mins at 4°C. Homogenised cells were further disrupted at 5Kpsi using a CF1 1.1kW cell disruptor (Constant Systems). Cells were sequentially centrifuged at 600g for 10mins and 15,000g for 5mins. The remaining cell membranes were ultracentrifuged for 1h at 100,000g. Protein complexes were solubilised from CHO-S membranes using the synthetic digitonin analogue glyco-diosgenin (GDN-101, hereafter GDN) or lauryl maltose neopentyl glycol (LMNG). Pelleted membranes were

resuspended in 0.22µm-filtered solubilisation buffer (10mL/batch). This buffer was composed of 20mM HEPES, pH7.5, 500mM NaCl, 15% (v/v) glycerol, supplemented with 1% (w/v) GDN or 1% (w/v) LMNG (Anatrace), ≥2.5U/mL benzonase, and cOmplete protease inhibitor cocktail, EDTA-free (Roche). For HPC4 purification (see Part 2.1), this buffer was further supplemented with 1mM $CaCl_2$. Membranes were dounce homogenised 5x in a glass homogeniser, and solubilised with rotation overnight at 4°C. The following morning, solubilised membranes were ultracentrifuged at 142,000g for 4h to remove the insoluble fraction. Solubilised proteins were filtered using 5µm and 0.45µm PES filters to remove insoluble material.

**Part 2.1. HPC4 (GDN) purification**

For complexes labelled with proteins containing the C-protein-derived CTag, purification was conducted using custom-made CNBr-coupled HPC4 antibody Sepharose resins[240]. Elution was achieved by competition for HPC4 binding via incubation with CTag peptide[240] (custom made, Generon). All buffers were 0.22µm filtered prior to use. 1mL (small-scale) or 5mL (large-scale) resin beds were placed in a glass Econo-column (Bio-Rad), and all wash and elution steps were conducted by gravity flow. The HPC4 resin was washed in 3CV 20mM HEPES pH7.5, 500mM NaCl, 15% (v/v) glycerol, 1mM $CaCl_2$ prior to protein binding. The solubilised protein was bound to the resin by gravity flow. The resin was washed in 2CV wash buffer (20mM HEPES, pH7.5, 500mM NaCl, 1mM $CaCl_2$, 2mM ATP, supplemented with 0.15% (w/v) GDN), then in 23CV of buffer supplemented with 0.05% (w/v) GDN. Protein was eluted in elution buffer (20mM HEPES, pH7.5, 500mM NaCl, 1mM EDTA, 0.05% (w/v) GDN, 0.2mg/mL CTag peptide). 12x0.2mL elutions (small-scale) or 12x1mL elutions (large-scale) were collected by gravity flow. The column was regenerated as in Section 2.4.6.

**Part 2.2. StrepTactin (GDN or LMNG) purification**

For complexes labelled with proteins containing a Twin-StrepTag, purification was achieved using StrepTactin Sepharose High Performance resins (Cytiva). Elution was conducted via incubation with the reversible StrepTactin binder, D-desthiobiotin[247]. All buffers were 0.22µm filtered. Resins were packed in Econo-columns and washed in 5CV MilliQ water and equilibrated by passing 5CV equilibration buffer (20mM HEPES, pH7.5, 500mM NaCl, 15% (v/v) glycerol) through gravity flow. Clarified lysates were applied to the resin and bound in batch with rotation at 4°C for 90mins. Flow-through was removed by gravity flow and the resin was washed with 30CV wash buffer (20mM HEPES, 500mM NaCl, 0.05% (w/v) GDN or LMNG, 1mM EDTA, pH 7.5) by gravity flow. The complex was eluted in wash buffer supplemented with 4mM d-Desthiobiotin (Sigma). The StrepTactin resin was regenerated as in Section 2.4.7.

### 5.2.5 Optimisation of solubilisation conditions

To compare the effects of detergents and salt concentrations on complex solubilisation, an indirect measurement of solubilisation was used. 2 batches of $3x10^9$ cells were labelled with SpyCatcher3 and their membranes extracted following the protocols described in Sections 5.2.3 and 5.2.4. Prior to membrane ultracentrifugation, the lysed cells were divided into 4 equal volumes and ultracentrifuged at 100,000g for 1h at 4°C. Each membrane pellet was solubilised overnight in 5mL solubilisation buffer as in Section 5.2.4, with variations in salt concentration and detergent used. The solubilised membranes were topped up to a final volume of 20mL (1:4 dilution) and the lysate was clarified by ultracentrifuged at 142,000g for 4h at 4°C. The supernatant was then 0.5µm and 0.45µm filtered as in Section 5.2.4. Aliquots removed before or after lysate clarification and filtration were further diluted in solubilisation buffer. AF647 intensity

was measured using a Clariostar system. The retention of AF647 in the soluble fraction post-clarification was used as a proxy for complex solubilisation.

### 5.2.6 FSEC and SDS-PAGE

Complex purity was assessed using fluorescent size-exclusion chromatography (FSEC). For small-scale purifications, all elutions were pooled and concentrated using a 100kDa MCWO filter (Amicon) to 250µL. 100µL of complex was centrifuged at 17,000g for 10mins at 4°C and injected into an AktaPure system, coupled to a Shimadzu system. SEC was conducted using a Superose 6 10/300 GL column (Cytiva), and AF647 intensity was measured using the Shimadzu system. In large-scale purifications, to preserve material for cryo-EM, 1% of the volume of each elution was pooled, centrifuged, and assessed using FSEC as above. Material from FSEC fractions was diluted in 2x Laemmeli buffer supplemented with 5% (v/v) 2-mercaptoethanol and boiled at 95°C for 10mins. Protein was loaded into 4-12% polyacrylamide gradient NuPage gels (ThermoFisher) and run at 150V for 1h. Gels were stained for protein detection using the Pierce Silver Stain kit (ThermoFisher) according to the manufacturer's instructions and imaged using a GelDocXR system.

### 5.2.7. Cryo-EM data collection and processing

All cryo-EM data shown was collected and analysed by Lukas Sušac, Goethe University Frankfurt. Size-excluded and non-size-excluded complexes were vitrified and data was collected using a Glacios cryo-TEM microscope (ThermoFisher) at 200kV acceleration voltage using a Falcon III direct electron-counting detector. Motion correction, CTF estimation, particle selection and reference-free 2D classification were undertaken using cryoSPARC and cryoSPARC Live.

## 5.3 Results

### 5.3.1 Generating a system for BCR complex expression

For the purification of a complete BCR complex, an IgM,κ BCR containing the variable regions of the germline precursor of VRC01 ($VRC01_{GL}$)[165] was expressed in a mammalian cell line. IgM was selected as the isotype of interest due to its importance in the initiation of the humoral immune response, as one of two isotypes expressed by naïve B cells[92]. Moreover, as one of two isotypes without a hinge region, IgM is more likely to adopt a more restricted set of conformations than those isotypes containing highly flexible hinges[309], possibly facilitating the conformational uniformity required for structure determination using cryo-EM.

The variable regions of the $VRC01_{GL}$ clone were used. $VRC01_{GL}$ is the inferred germline precursor of the therapeutic VRC01 antibody[313], a broadly neutralising antibody which binds to the CD4-binding site (CD4bs) of the HIV-1 gp120 glycoprotein[314]. This cross-reactivity is shared across several antibodies derived from the same IGHV1-2*02 gene segment, termed VRC01-class bnAbs[165,313]. Therapeutic interest in producing VRC01-class bnAbs in HIV-naïve individuals through vaccination has led to the development of the eOD-GT8 immunogen, derived from the outer domain of gp120, which binds with picomolar affinity to conserved features of IGHV1-2*02-derived, germline VH domains[313]. The $VRC01_{GL}$ IgM BCR therefore represents a putative germline receptor which would have been expressed on the surface of a naïve B cell yet binds with high affinity to therapeutically relevant ligands.

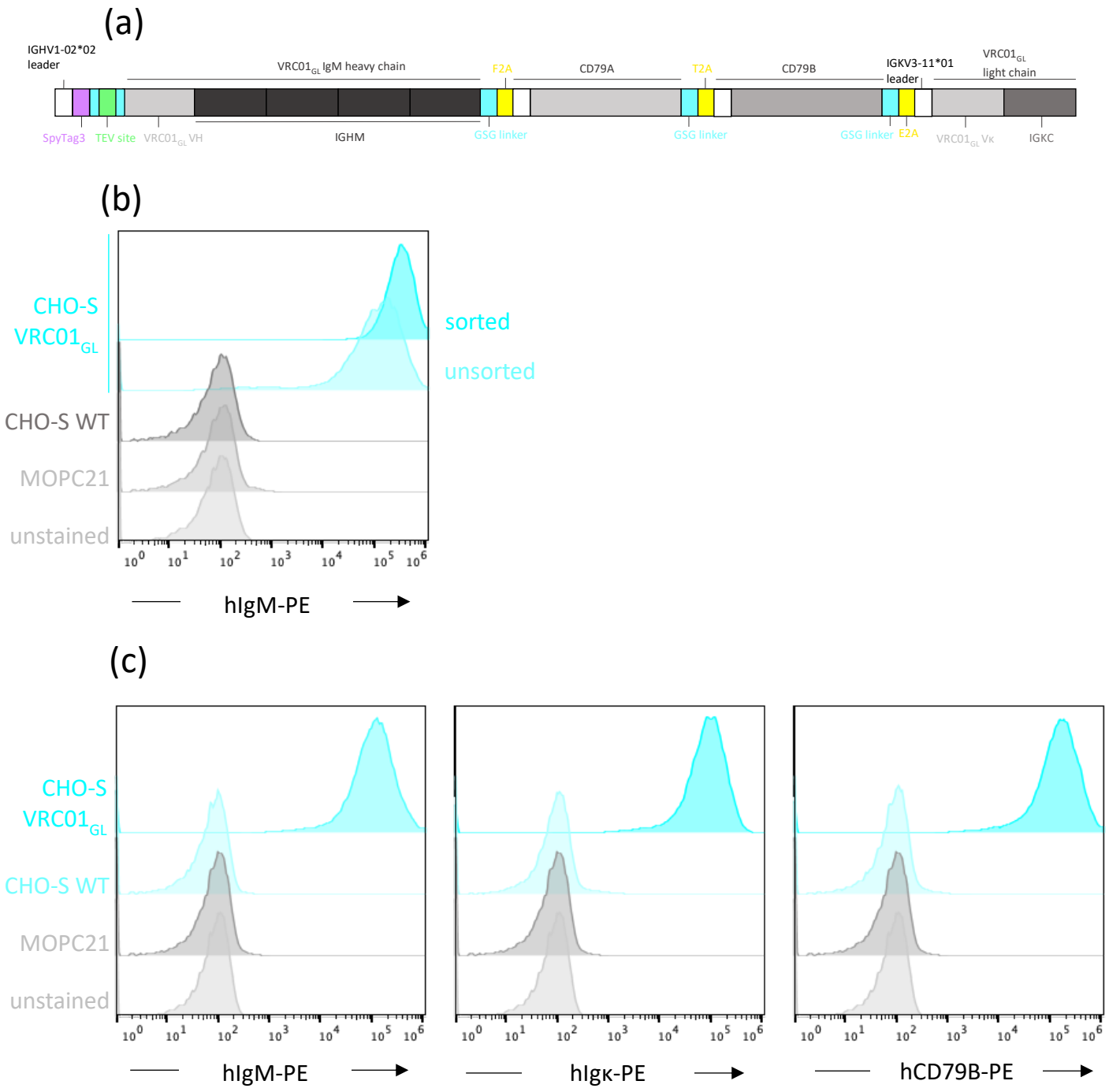



**Figure 5.1 | Generation of a mammalian system for VRC01$_{GL}$ IgM BCR expression. (a)** Schematic depicting chain arrangement on the VRC01$_{GL}$ IgM BCR construct. White boxes represent endogenous signal peptides for each protein chain, which will not form part of the membrane complex. *IGHM* encodes the IgM constant region and *IGKC* encodes the Igκ constant region. **(b)** Flow cytometric analysis of IgM heavy chain expression on transduced cells before (light blue) or after (darker blue) cell sorting. Wildtype CHO-S cells stained with an isotype control (MOPC21, grey) or with anti-IgM (dark grey) were used as controls, along with unstained wildtype cells (light grey). **(c)** Flow cytometry analysis of surface receptor expression in CHO-S VRC01$_{GL}$ cells (dark blue) compared to the parental CHO-S cell line (light blue). Cells stained with antibodies against human IgM (left), human Igκ (middle) and human CD79B (right) are shown. Unstained cells (light grey) and cells stained with an isotype control (MOPC21, dark grey) are shown as controls in all panels.

The four chains of the IgM BCR complex were expressed as a polycistronic construct, as depicted in Fig. 5.1a. To this end, viral 2A self-cleaving peptides[315] were introduced after the C-terminus of the membrane-spanning chains, allowing co-translational expression of BCR subunits from a single transcript. This design was used to ensure the extra residues introduced by the 2A peptides were at the end of the cytoplasmic tails, and therefore did not affect the extracellular organisation of the chains. For purification in the absence of functional ligands, a SpyTag003 sequence was introduced at the N-terminus of the VH domain. The Chinese hamster ovary suspension cell line, CHO-S, was used for protein expression[240]. CHO-S cells were stably transduced with lentiviral particles containing the $VRC01_{GL}$ IgM sequence, and the 10% highest expressors were FACS sorted to create a uniform population of IgM-expressing cells with high levels of expression (Fig. 5.1b). Surface expression of the IgM heavy chain, Igκ light chain and CD79B was readily detected in the CHO-S $VRC01_{GL}$ cell line, but not in the parental cell line (Fig. 5.1c).

To isolate the complex in both its antigen-bound and -unbound states, no affinity-purification tags were added to the sequence of the BCR chains. Instead, tagged soluble proteins capable of binding the surface receptor were bound to the complex, allowing purification of the receptor[240] (Fig. 5.2). This ensures that the same receptor could be extracted in different states but also allowed the extracted receptors to be restricted to fully assembled complexes on the cell membrane. For purification of the complex in the absence of its ligand, the complex was extracted using the SpyTag system. This system is based on the attachment of a SpyCatcher domain to the SpyTag peptide tag through the formation of a covalent bond[316]. SpyCatcher003 (hereafter, SpyCatcher or SpyC3) was evolved as an improved variant of the original SpyTag system, with

improved kinetics for complex formation with its partner, SpyTag003 (hereafter, SpyTag)[289]. The purification of the ligated complex was achieved using eOD-GT8, taking advantage of the high affinity interaction ($K_D$<1.6x10$^{-11}$ M)[313] between the antigen and VRC01$_{GL}$. This latter approach to receptor purification had been previously used for the isolation of an αβTCR complex[240] through its ligand, an HLA-A2-peptide complex that bound to this receptor with similar affinity ($K_D$=1.5x10$^{-11}$ M)[317]. The dissociation rate of the eOD-GT8 immunogen for VRC01$_{GL}$ ($k_{off}$<5x10$^{-5}$ s$^{-1}$)[313] is within the same order of magnitude as that of the previously used TCR-pMHC interaction ($k_{off}$=6.7x10$^{-6}$ s$^{-1}$)[318]. This suggested that eOD-GT8 could also be a promising ligand for receptor purification, which requires molecules to remain bound to receptors for several days throughout the purification protocol.

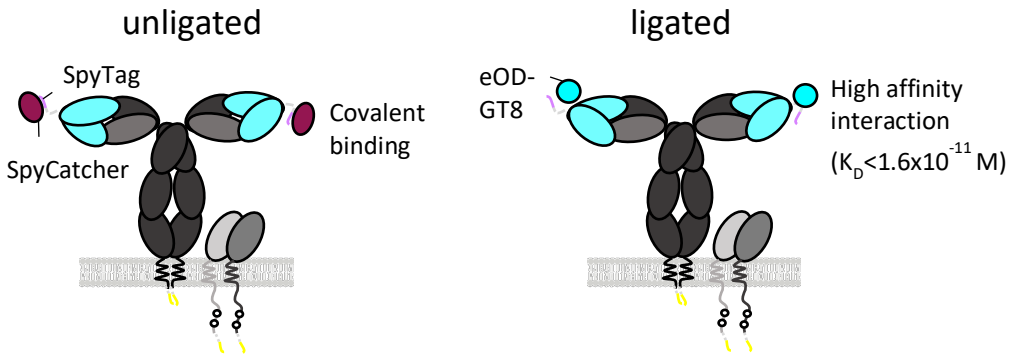



**Figure 5.2 | Schematic representing two approaches for BCR purification.** Extraction of the complex in its native (left) and ligand-bound (right) states.

### 5.3.2 Purification of soluble proteins for receptor extraction

The initial purification procedure was designed to follow a previously optimised protocol used to purify a complete, pMHC-ligated TCR complex from CHO-S cells[240]. As such, to trial unligated receptor purification, a SpyCatcher molecule containing a CTag sequence was produced, allowing purification using the anti-CTag HPC4 antibody as in the work by Sušac, Vuong and colleagues[240].

For SpyC3 purification, an N-terminal 6His-tag was added for affinity purification, while a C-terminal CTag sequence was introduced to allow purification of the complex through HPC4. The SpyCatcher protein could be purified in large quantities as a monomer of the predicted size (Fig. 5.3a,b). AF647-labelled SpyC3 protein bound to CHO-S VRC01$_{GL}$ cells, but only minimally to the wild-type CHO-S cell line, suggesting that this recombinant protein specifically bound to the IgM complex on the surface of the cells (Fig. 5.4a). The labelled cells could also be counterstained with the anti-CTag HPC4 antibody[244], suggesting that the CTag sequence remained accessible in solution following complex binding (Fig. 5.4b). To maximise SpyTag occupancy, CHO-S VRC01$_{GL}$ cells were labelled with increasing SpyC3 concentrations to determine the saturating concentration to be used for complex purification (Fig. 5.4c,d).

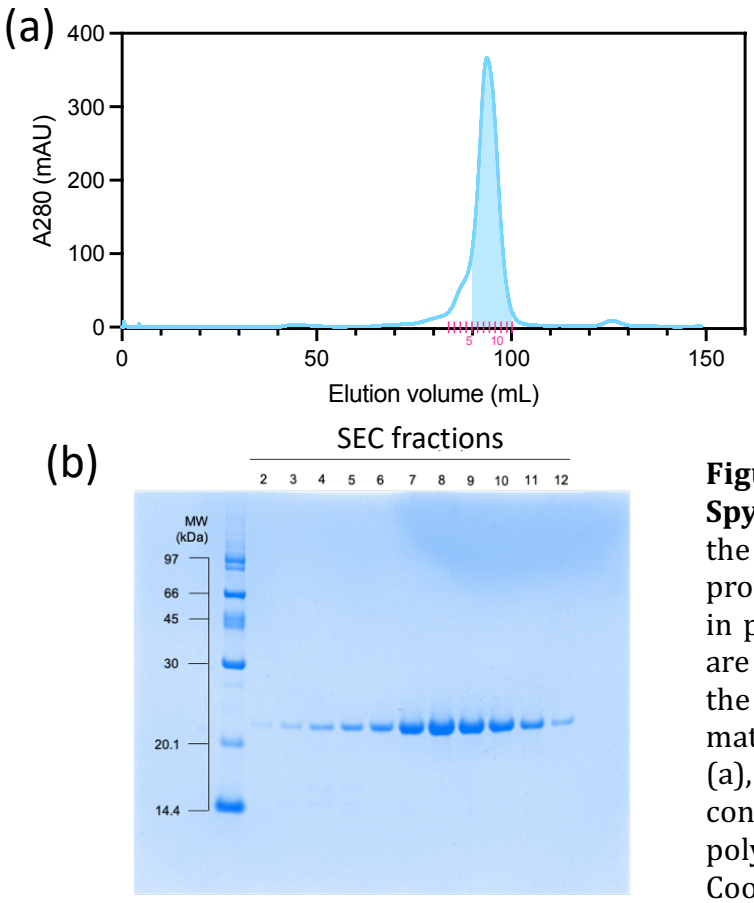



**Figure 5.3 | Purification of the 6His-SpyC3-CTag protein. (a)** SEC profile of the affinity-purified SpyCatcher protein. Fractions collected are labelled in pink, and those pooled for later use are represented by the filled area under the curve. **(b)** SDS-PAGE analysis of material from the fractions collected in (a), boiled under non-reducing conditions. Image shows a 12% polyacrylamide gel stained with Coomassie Blue.

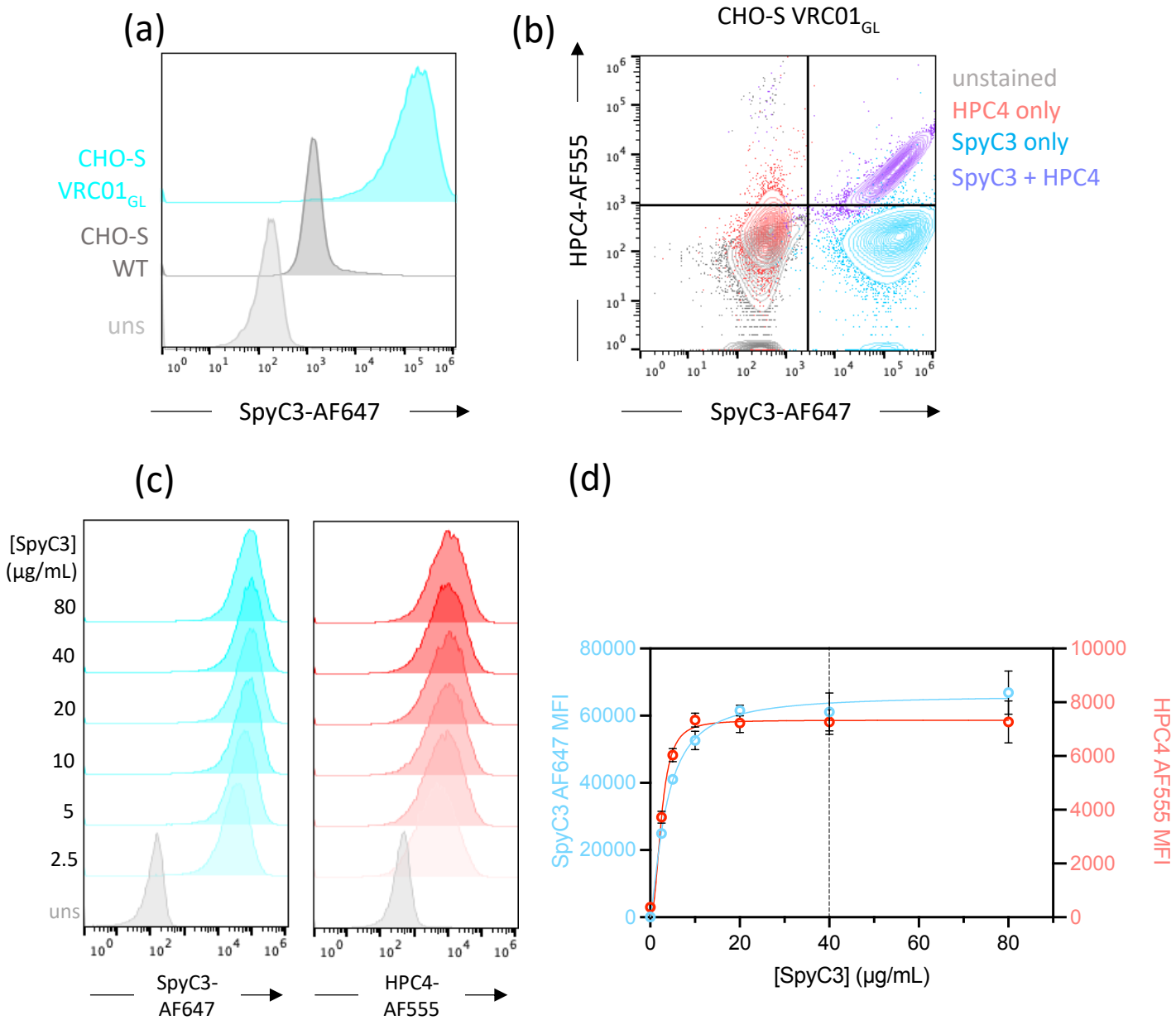



**Figure 5.4 | Characterising SpyCatcher labelling of CHO-S VRC01$_{GL}$ cells. (a)** Flow cytometry analysis of CHO-S VRC01$_{GL}$ cells (blue) or wildtype CHO-S cells (dark grey) labelled with fluorescent SpyCatcher. Unstained cells are used as a control (light grey, 'uns'). **(b)** Flow cytometry analysis of HPC4 binding to CHO-S VRC01$_{GL}$ cells in the presence (purple) or absence (red) of SpyCatcher binding. As a control, CHO-S VRC01$_{GL}$ cells labelled with SpyCatcher only (blue) or left unstained (grey) were also evaluated. **(c)** Flow cytometry analysis of SpyC3 labelling (blue) and HPC4 counterstain (red) of CHO-S VRC01$_{GL}$ cells labelled with increasing concentrations of SpyCatcher. In both cases, unlabelled cells are shown in grey. This represents one example stain, with histograms for stain and counterstained matched from a single labelled set of cells, from the data shown in (d). Inset values represent the concentration of SpyCatcher3 used for labelling. **(d)** Quantification of the mean fluorescence intensity (MFI) of SpyCatcher-AF647 staining (blue) and HPC4-AF555 staining (red) for CHO-S VRC01$_{GL}$ cells labelled with increasing concentrations of SpyCatcher. Symbols and error bars represent mean ± standard deviation of three replicates from a single independent experiment. The dashed line represents the concentration used in further experiments.

Structure determination of purified proteins by cryo-EM often requires ligation of further soluble binders to the target protein[319]. Most commonly, the addition of Fab fragments specific for membrane complexes is used to increase complex size and facilitate particle detection for smaller complexes[319]. However, Fab fragments can also prove advantageous for the structure determination of larger complexes. In particular, for TCR complexes, Fab fragments were used to stabilise complexes during vitrification[240].

To this end, a Fab fragment against the BCR complex was designed in advance of complex purification. The Fab fragment was based on the high affinity anti-CD79B antibody polatuzumab[320], which in a drug-conjugated form, polatuzumab vedotin, is used as a therapeutic agent in B-cell neoplasms[321]. The humanised variable regions of polatuzumab[322] were introduced into a murine Fab fragment, containing a C-terminal CTag on the heavy chain. The Fab fragment was purified as a monovalent heterodimer of the predicted size (Fig. 5.5a,b). Fluorescently labelled polatuzumab Fab fragment readily labelled CHO-S VRC01$_{GL}$ cells, but not wildtype CHO-S cells, confirming that the Fab fragment binds specifically to the human BCR complex (Fig. 5.5c).

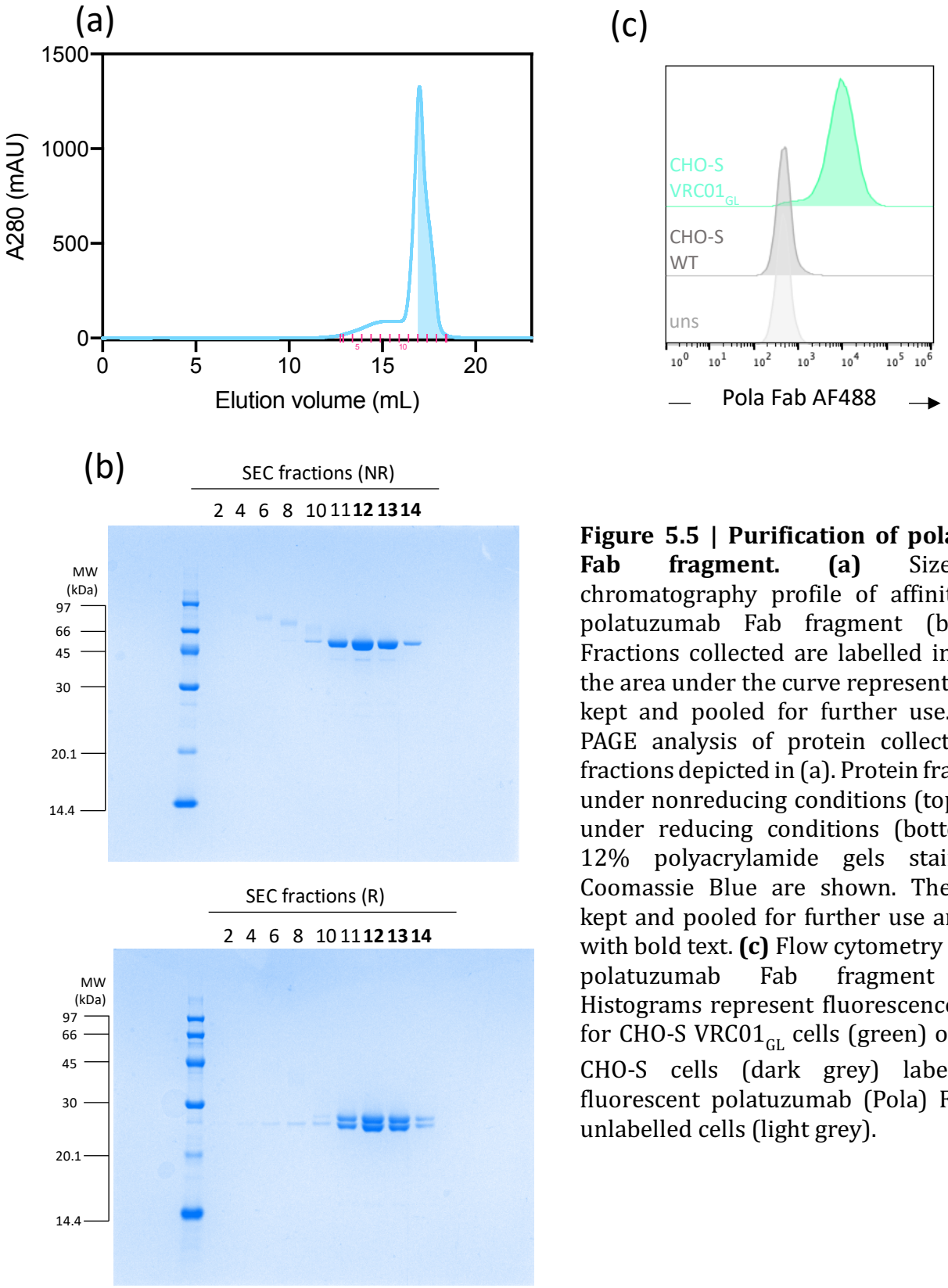



**Figure 5.5 | Purification of polatuzumab Fab fragment. (a)** Size-exclusion chromatography profile of affinity-purified polatuzumab Fab fragment (blue line). Fractions collected are labelled in pink and the area under the curve represents fractions kept and pooled for further use. **(b)** SDS-PAGE analysis of protein collected in the fractions depicted in (a). Protein fractions run under nonreducing conditions (top, NR) and under reducing conditions (bottom, R) in 12% polyacrylamide gels stained with Coomassie Blue are shown. The fractions kept and pooled for further use are labelled with bold text. **(c)** Flow cytometry analysis of polatuzumab Fab fragment binding. Histograms represent fluorescence intensity for CHO-S $VRC01_{GL}$ cells (green) or wildtype CHO-S cells (dark grey) labelled with fluorescent polatuzumab (Pola) Fab, or for unlabelled cells (light grey).

### 5.3.3 Initial BCR complex purification

The extraction of membrane proteins from the cell surface can be achieved with the use of detergents[323]. Commonly used detergents such as n-dodecyl-β-D-maltopyranoside (DDM), glyco-diosgenin (GDN) and lauryl maltose neopentyl glycol (LMNG) form micellar structures at concentrations above the critical micelle concentration (c.m.c). These structures can accommodate the hydrophobic transmembrane domains of membrane complexes within their hydrophobic core[310], shielding these from the aqueous buffers used to preserve native domain confirmations.

To trial purification of the unligated BCR, a previously established protocol[240] was used for complex isolation from SpyC3(CTag)-labelled CHO-S VRC01$_{GL}$ cells (Sections 5.2.3-5.2.4). A small percentage of SpyC3 protein was fluorescently labelled with AF647, to allow for fluorescence intensity to be tracked throughout purification as an indirect measurement of complex concentration. Labelled cells were lysed, and plasma membranes were isolated by ultracentrifugation, solubilised in buffers containing GDN[240,310], and purified using an affinity resin with coupled anti-CTag HPC4 antibody (Fig. 5.6a). Purified material was assessed using FSEC and contained species of varying molecular weight (Fig. 5.6b). All SEC peaks contained AF647-labelled material, suggesting differential states of the BCR complex rather than the presence of other protein impurities (Fig. 5.6b). In addition to a small amount of insoluble, aggregated material in the void volume, and a small amount of degradation, most of the purified protein was present as a single, mostly monodispersed peak (Fig. 5.6b).

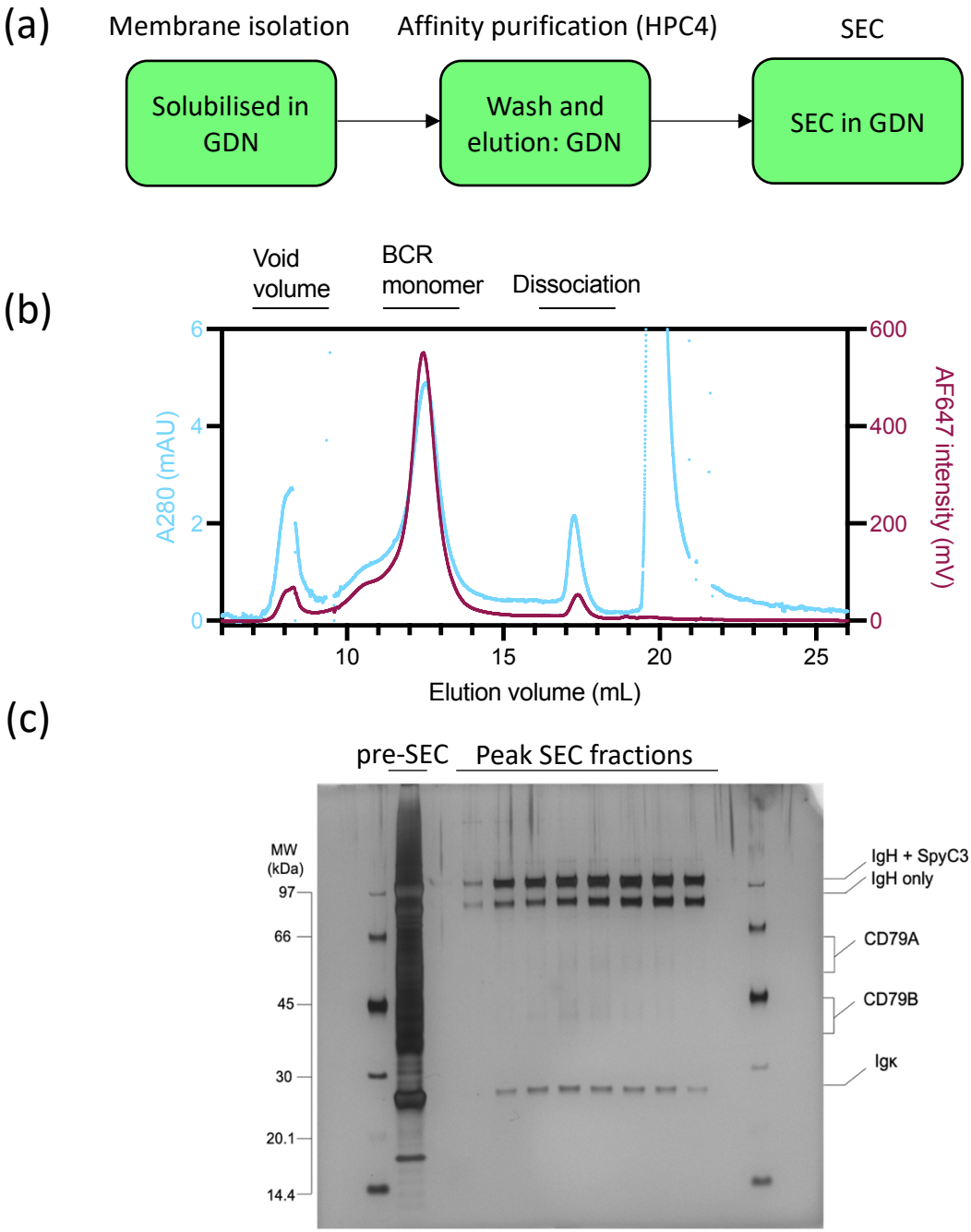



**Figure 5.6 | Initial SpyCatcher extraction of BCR complexes via GDN/HPC4 purification. (a)** Schematic representation of the workflow for this experiment. **(b)** FSEC profile for HPC4 affinity-purified BCR material. Total protein is depicted in light blue (A280, left axis) and fluorescence intensity derived from the presence of fluorescent SpyCatcher3 in purple (AF647 intensity, right axis). **(c)** SDS-PAGE analysis of material collected from the main peak obtained by FSEC (peak SEC fractions) depicted in (b). Initial lane contains affinity purified protein prior to SEC (pre-SEC). 4-12% polyacrylamide gradient gels were loaded with samples boiled under reducing conditions and stained with silver ions using a Silver Stain kit (see section 5.2).

Protein fractions from this peak were assessed by SDS-PAGE under reducing conditions, dissociating disulphide bonds, and separating all the subunits of the complex into individual units (Fig. 5.6c). All subunits of the $VRC01_{GL}$ IgM complex were present in these fractions, and co-eluted together. IgM heavy chain subunits with bound or unbound SpyCatcher were detectable at the predicted molecular weight[97,98,324], as determined by the presence of two bands with a difference in size of approximately 20 kDa (the molecular weight of SpyCatcher, Fig. 5.3b). As all BCR complexes purified must contain at least one SpyCatcher molecule for affinity purification, the presence of IgM heavy chains without SpyCatcher suggests some BCR complexes were only monovalently bound despite the use of a saturating concentration of SpyCatcher protein. The light chain was detected at the expected molecular weight (~25kDa)[97,103]. CD79A and CD79B were detected as faint smears of the predicted molecular weight[97,98], likely due to differential glycosylation[301].

### 5.3.4 Optimisation of receptor purification

This initial result suggested that the BCR could be purified as an intact complex, providing scope for the optimisation of the protocol to ensure that adequate yields were obtained from preparations. To this end, both the detergents used for complex solubilisation and the affinity tags used for purification were tested and modified to improve protein yield. Previous purifications of the human TCR complex had been achieved using DDM[27] and GDN[240] solubilisation, yielding similar structures with little variation in transmembrane domain organisation within the micelle[240]. To optimise the conditions for BCR solubilisation, two different detergents, GDN and LMNG, were trialled[310]. Furthermore, physiological (150mM) or high (500mM) NaCl concentrations were compared, as this factor can affect protein solubility[323].

To assess the impact of detergents and salt concentrations on BCR solubilisation, CHO-S VRC01$_{GL}$ cells were labelled with SpyC3(CTag) protein, including a small fraction of AF647-labelled protein. Fluorescence intensity was monitored before and after the removal of insoluble material, as an indirect measurement of how much labelled SpyCatcher, and by extension bound complex, remained in solution under different solubilisation conditions. This approach showed that varying salt concentrations had a minimal effect on the retention of the complex in the soluble fraction (Fig. 5.7). However, more AF647-labelled material remained in solution after LMNG solubilisation than GDN solubilisation. This suggested that LMNG solubilisation was likely to be more efficient than GDN solubilisation, and thus LMNG-based buffers were used for receptor solubilisation in further purifications (Fig. 5.7).

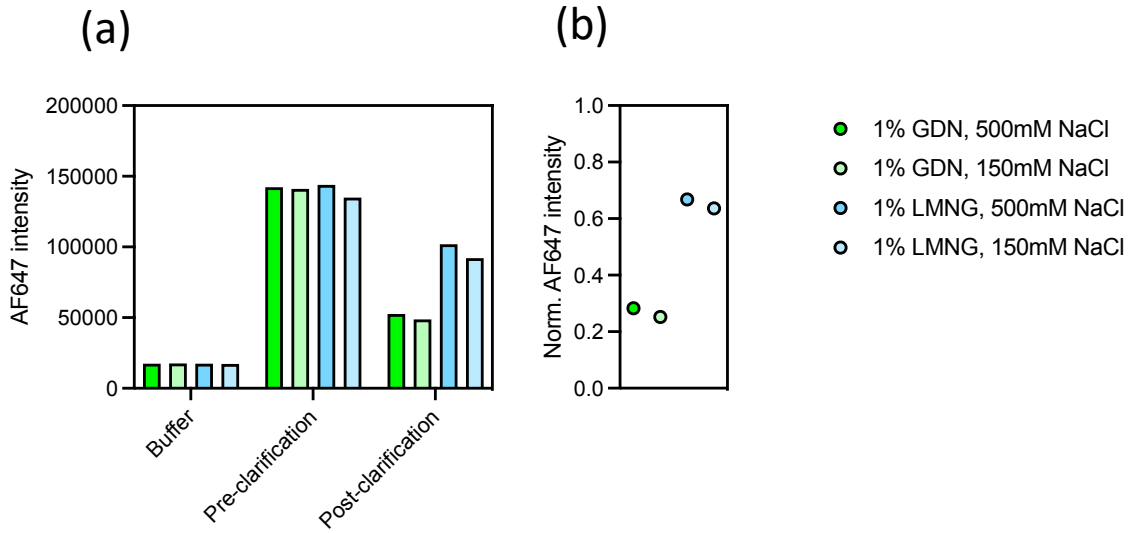



**Figure 5.7 | Optimisation of BCR solubilisation. (a)** Fluorescence AF647 intensity (from bound SpyCatcher protein) in buffers containing solubilised membranes prior to (pre-clarification) or following (post-clarification) removal of insoluble material by ultracentrifugation. Fluorescence for base buffers is also shown as a baseline. **(b)** Normalised AF647 intensity for clarified samples as the fraction of retained fluorescence from the pre-clarified sample. Symbols represent fluorescence samples solubilised in 1% (w/v) LMNG (blue) and 1% (w/v) GDN (green), in buffers containing 500mM NaCl (darker shading) or 150mM NaCl (lighter shading). Data from a single experiment is shown.

To further improve complex capture to affinity resins, soluble proteins containing an alternative purification tag were produced. Modifications to the purification method were motivated by observations that a large fraction of the labelled complex did not bind the HPC4 resin (not shown). In a second iteration of the SpyCatcher003 protein, the CTag epitope was exchanged for Twin-StrepTag[246,247]. The new tag binds with nanomolar affinity[246] to the modified streptavidin tetramer StrepTactin, allowing purification of tagged proteins by affinity chromatography[247]. Production in *E. coli* yielded monomers similar to the previous iteration of the protein (Fig. 5.8a,b; compared to Fig. 5.3a,b). CHO-S VRC01$_{GL}$ cells reached labelling saturation at equivalent concentrations of SpyCatcher to those of the previous iteration (Fig. 5.8c).

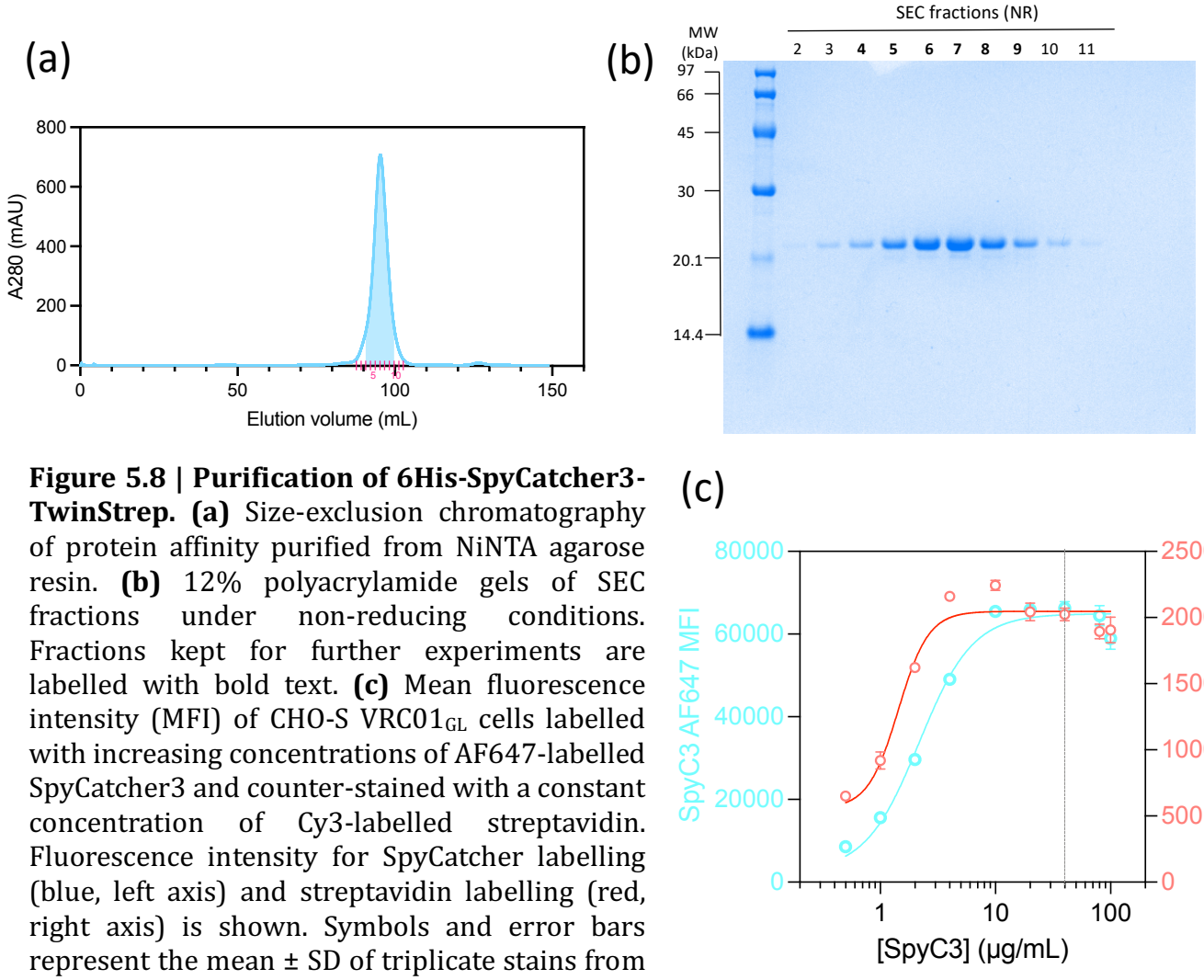



**Figure 5.8 | Purification of 6His-SpyCatcher3-TwinStrep. (a)** Size-exclusion chromatography of protein affinity purified from NiNTA agarose resin. **(b)** 12% polyacrylamide gels of SEC fractions under non-reducing conditions. Fractions kept for further experiments are labelled with bold text. **(c)** Mean fluorescence intensity (MFI) of CHO-S VRC01$_{GL}$ cells labelled with increasing concentrations of AF647-labelled SpyCatcher3 and counter-stained with a constant concentration of Cy3-labelled streptavidin. Fluorescence intensity for SpyCatcher labelling (blue, left axis) and streptavidin labelling (red, right axis) is shown. Symbols and error bars represent the mean ± SD of triplicate stains from a single experiment. The dotted line represents the concentration used for receptor purification, matching that determined in Fig. 5.4d.

This modified version of SpyCatcher was used in a small-scale purification to determine whether the complex could be purified through a separate purification protocol based on commercial and published protocols[27,240]. The LMNG-solubilised, SpyC3(Twin-StrepTag)-bound $VRC01_{GL}$ complex could be readily purified using a StrepTactin affinity resin, and the SEC profile was similar to that of GDN-solubilised, HPC4-purified complex (Fig. 5.9). However, the yield was significantly increased for the StrepTactin protocol, despite the use of fivefold fewer cells as starting material. Given the improvements in yield obtained by these modifications, further purifications of the complex were undertaken using LMNG solubilisation and StrepTactin purification.

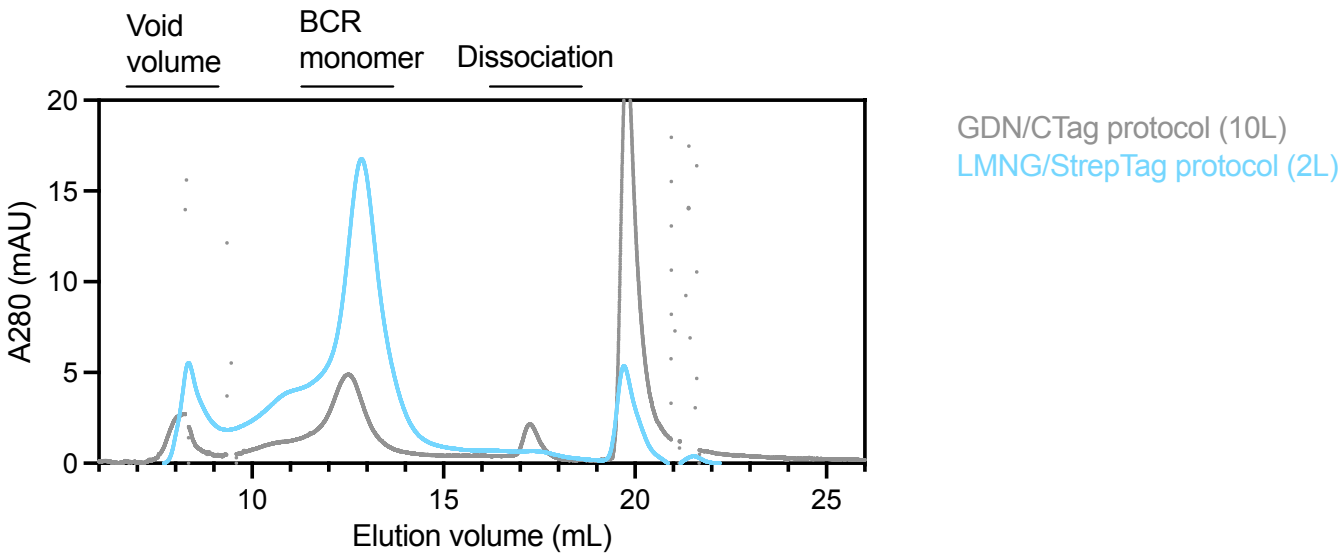



**Figure 5.9 | Comparison of BCR purification protocols by SEC.** Comparison of affinity-purified material from the initial purification described in Fig. 5.6b (GDN/HPC4, grey) and affinity-purified material following solubilisation with 1% (w/v) LMNG and StrepTactin purification (blue). In both cases, 40% of total purified material is injected for SEC. Even though the second purification has used only 20% of the number of cells used in the initial purification (grey), more material is obtained using the modified protocol, as evident from the increase in A280 measurements.

The LMNG/StrepTactin protocol was then used to conduct large-scale purifications of the complex (Fig. 5.10a). The protocol was readily scalable, and material purified in this large-scale protocol was apparently identical (Fig. 5.10b) to that purified in the small-scale purification (Fig. 5.9). SDS-PAGE was used to verify that all chains remained present in the fractions collected and all expected chains co-eluted together (Fig. 5.10c). Material purified under this protocol resembled that from the initial purification with GDN/HPC4 (Fig. 5.6c). This improved protocol for solubilisation using LMNG-containing buffers and the modification of the resin used were kept for all further purifications. Following the successful purification of complete SpyCatcher-bound (unligated) receptors, work was undertaken to purify the same receptor from the CHO-S VRC01$_{GL}$ cell line using the eOD-GT8 antigen.

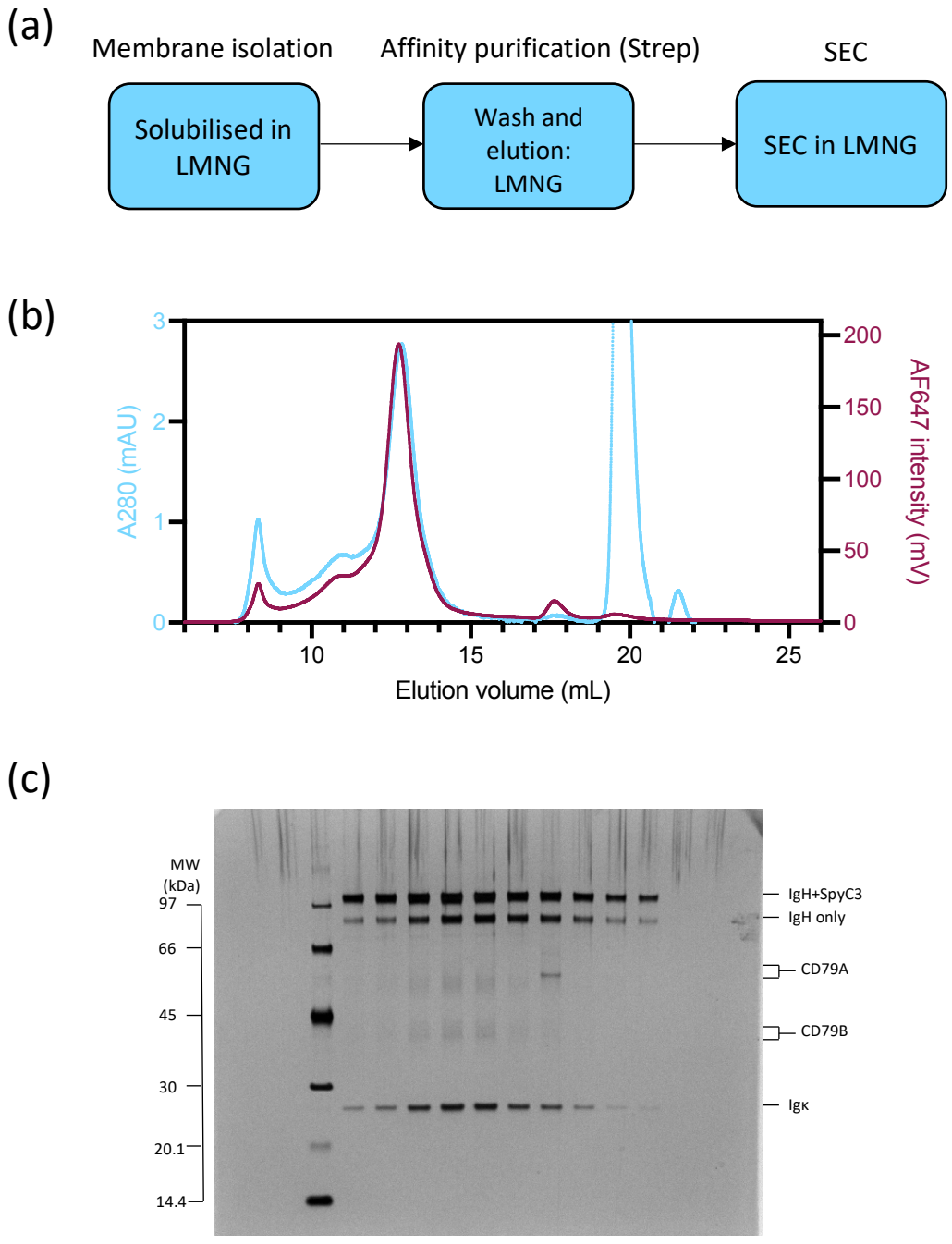



**Figure 5.10 | SpyCatcher extraction of BCR complexes using LMNG/StrepTag purification. (a)** Schematic representation of workflow for this experiment. **(b)** FSEC profile for StrepTactin affinity-purified BCR material. Total protein is depicted in light blue (A280, left axis) and fluorescence intensity of material containing fluorescent SpyCatcher3 in purple (AF647 intensity, right axis). **(c)** SDS-PAGE analysis of material collected from the main peak obtained by FSEC (each lane represents material from consecutive fractions collected from SEC) depicted in (b). 4-12% polyacrylamide gradient gels were loaded with samples boiled under reducing conditions and stained with silver ions using a Silver Stain kit (see section 5.2).

### 5.3.5 Purification of a BCR-antigen complex

Following the optimisation of complex purification using SpyCatcher3, the purification of the ligand-bound form of the receptor was also undertaken. To this end, soluble eOD-GT8 antigen was purified, containing a C-terminal Twin-StrepTag to allow purification using StrepTactin affinity resins as before. eOD-GT8 could be purified as a monodispersed monomer (Fig. 5.11a). This was verified by SDS-PAGE, with the highly glycosylated antigen running at the predicted size, as previously described[325] (Fig. 5.11b). As before, flow cytometry was used to confirm that the antigen could bind to the $VRC01_{GL}$ IgM BCR. CHO-S $VRC01_{GL}$ cells could be readily stained with fluorescent eOD-GT8, with minimal binding obtained for wildtype CHO-S cells compared to unstained cells, suggesting that eOD-GT8 binding is largely specific for the IgM BCR (Fig. 5.11c). Maximum binding of the soluble protein to the receptor was desirable to both extract as much material as possible but also to ensure maximum occupancy of the Fab arms, in order to reduce potential variability across particles. To ensure optimal binding, CHO-S $VRC01_{GL}$ cells were labelled with varying concentrations of fluorescent eOD-GT8, at equal densities to those used for receptor purification (Fig. 5.11d-e). Further experiments were conducted using saturating concentrations as determined by this method.

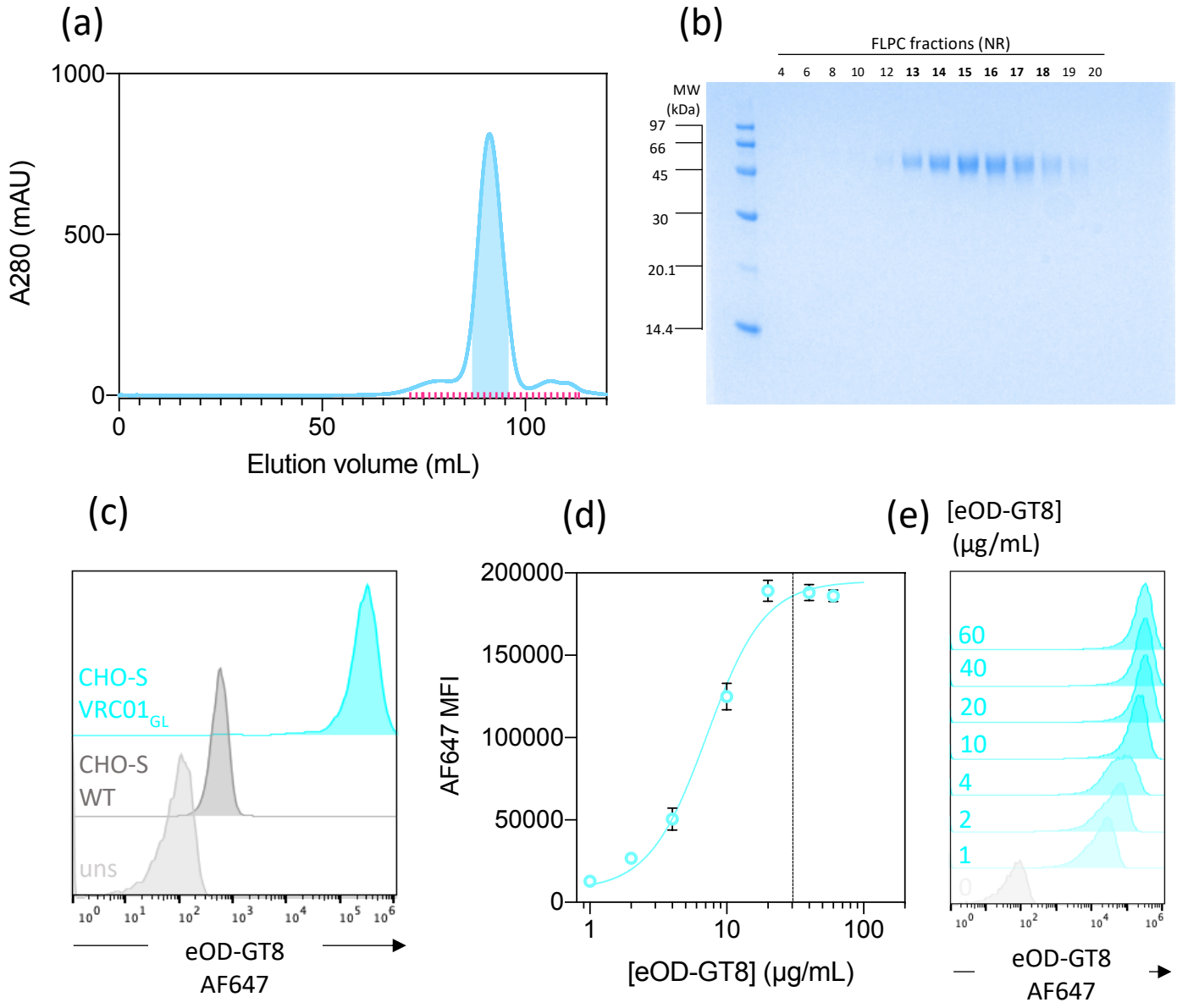



**Figure 5.11 | Purification of monomeric eOD-GT8. (a)** Size-exclusion chromatography profile of His-purified eOD-GT8. Fractions are labelled in pink, and the area corresponding to the fractions kept is shaded in blue. **(b)** Coomassie-stained SDS-PAGE of select fractions from SEC. Fractions kept for further use are labelled with bold text. **(c)** Flow cytometry analysis of fluorescence intensity of cells labelled with fluorescent eOD-GT8. Histograms are shown for labelled CHO-S VRC01$_{GL}$ (blue) or wildtype CHO-S (dark grey) cells, with unstained cells (light grey) as a control. **(d-e)** Saturation test of CHO-S VRC01$_{GL}$ staining with AF647-labelled eOD-GT8. **(d)** represents AF647 mean fluorescence intensity (MFI) plotted against eOD-GT8 concentration, with the concentration used for purification experiments depicted by the dashed line. Values represent measurements from a single experiment conducted in triplicates, symbol and error bar represent mean ± SD. **(e)** is an example repeat of this staining, with histograms depicting AF647 fluorescence intensity of cells labelled with increasing concentration of eOD-GT8 (blue) or unstained cells (grey). Inset numbers represent eOD-GT8 concentration used (in µg/mL).

Prior to purification, modifications to the improved protocol (Fig. 5.10) were introduced to prevent downstream issues in grid preparation: (1) the large size of LMNG micelles can complicate removal of free detergent micelles by size-exclusion chromatography[310,326]; (2) protein-free micelles can complicate the detection of protein-containing particles[326]; and (3) LMNG can also form linear artefacts at high concentrations[323].To transfer the receptor to a different detergent, the resin-bound complex was washed and eluted in buffers containing GDN, allowing the high solubilisation obtained with LMNG in earlier steps to be exploited, while transferring the complex to a detergent better suited for downstream applications[327]. GDN was chosen as initial purifications had already demonstrated the complex was stable in this detergent (Fig. 5.6) and it had been successfully used in grid preparations for previous projects[240].

This modification did not disrupt BCR purification, and antigen-bound complex could be isolated using this protocol (Fig. 5.12a). The purified complex contained similar material to the unligated complex as determined by SEC (Fig. 5.12b), and SDS-PAGE confirmed the presence of heavy and light chains (Fig. 5.12c). In the absence of SpyCatcher binding, a single band was identified for the heavy chain (~80 kDa), as expected[324]. This further confirmed that the two bands observed for the heavy chain in previous SDS-PAGE analyses were derived from the bound and unbound states of the SpyTag-containing chain to SpyCatcher. A third band of material approximately 50kDa in mass was identifiable, which was attributed to the antigen, eOD-GT8. However, due to the similar molecular weight of eOD-GT8 and CD79A or CD79B, and the highly glycosylated nature of all three components, the two signalling chains could not be identified as they are likely to co-migrate with eOD-GT8 at similar sizes.

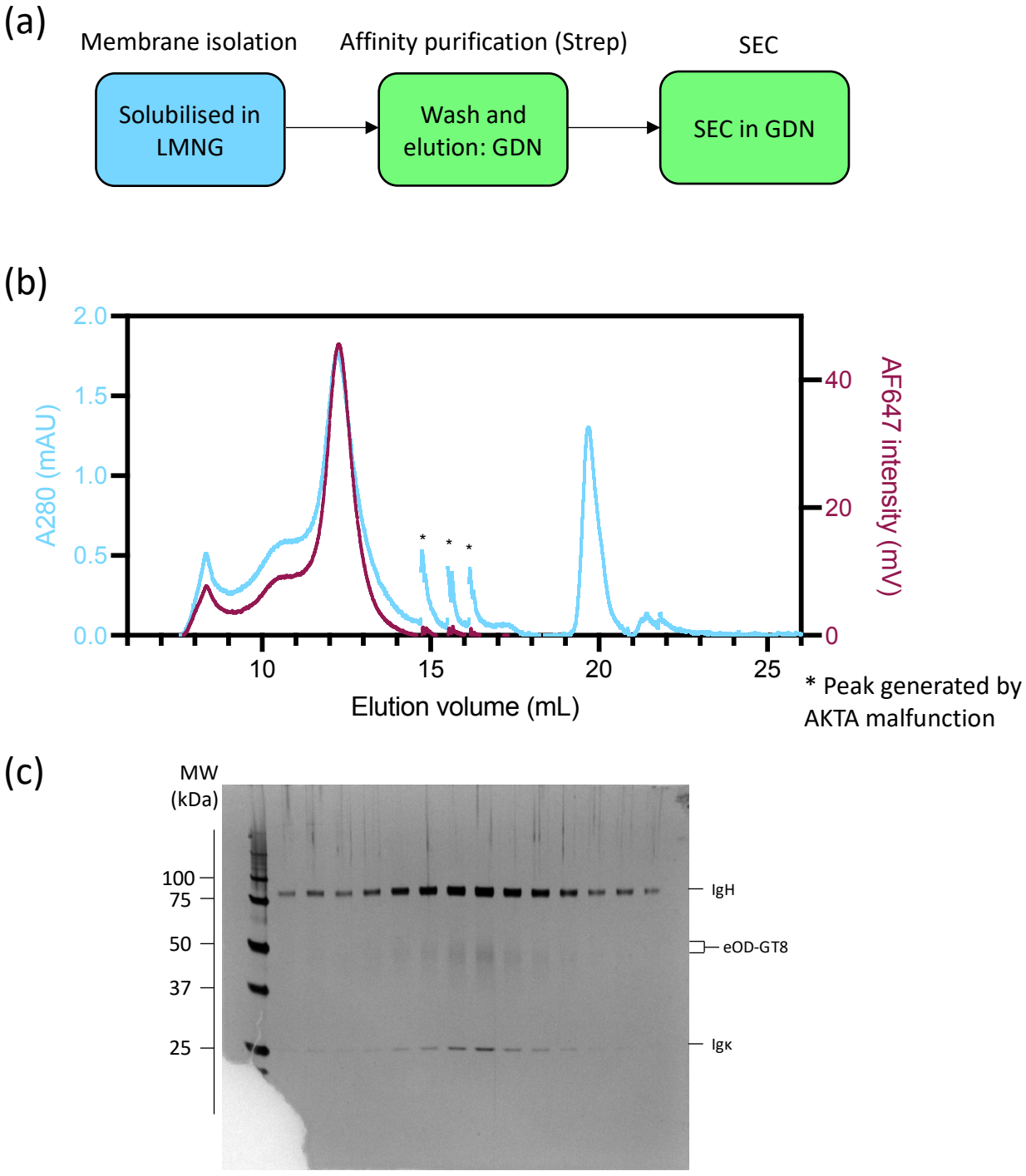



**Figure 5.12 | eOD-GT8 extraction of BCR complexes using LMNG/StrepTag purification with detergent exchange. (a)** Schematic representation of workflow for this experiment. **(b)** FSEC profile for StrepTactin affinity-purified BCR material. Total protein is depicted in light blue (A280, left axis) and fluorescence intensity of material containing fluorescent eOD-GT8 in purple (AF647 intensity). **(c)** SDS-PAGE analysis of material from consecutive fractions collected from the main peak obtained by FSEC (peak SEC fractions) depicted in (b). 4-12% polyacrylamide gradient gels were loaded with samples boiled under reducing conditions and stained with silver ions using a Silver Stain kit (see section 5.2).

The molecular weight of eOD-GT8 (~50 kDa, Fig. 5.11b) is larger than that of SpyCatcher003 (~20 kDa, Fig. 5.8b). The bivalent nature of soluble protein binding in this setting further increases the difference in molecular weight between the unligated and ligated complexes. In line with this, a shift in the migration of the complex by SEC was observed for eOD-GT8-bound complex compared to SpyCatcher3-bound complex (Fig. 5.13). This is congruent with an increase in the size of the complex, as expected. The complexes incorporated into GDN micelles appeared to elute earlier in the column to those present in LMNG, irrespective of complex size (Fig. 5.13). It is expected that proteins may migrate differently by SEC in different detergent buffers[328], and so these shifts likely do not represent an actual difference in complex size. Any differences in size due to the presence of the two different micelles is hard to assess from the literature, as LMNG micelles vary in size depending on detergent concentration and GDN micelle size is undetermined[310].

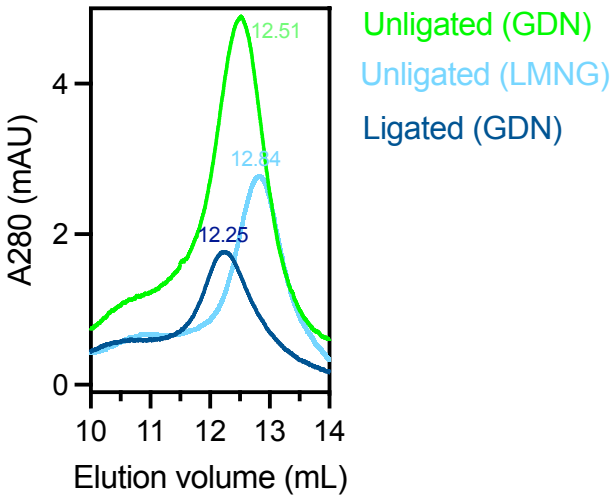



**Figure 5.13 | Comparison of SEC profiles for complexes isolated using different soluble proteins and eluted in different detergents.** Comparison of purified material from unligated complexes in GDN (green, Fig. 5.6) and in LMNG (light blue, 5.10) with ligated complexes in GDN (dark blue, Fig. 5.12). Inset numbers represent the volume at which maximum A280 was observed.

### 5.3.6 Cryo-EM imaging of the ligated BCR complex

The successful purification of the eOD-GT8-bound complex was followed by preliminary experiments using cryo-electron microscopy, conducted by Lukas Sušac, from Goethe University Frankfurt. Purified complexes were vitrified and imaged using a Glacios cryo-TEM microscope (see Section 5.2.7). Particles selected from collected micrographs were subjected to reference-free 2D classification (Section 5.2.7)[329], yielding 2D classes for detected protein-detergent complexes (Fig. 5.14).

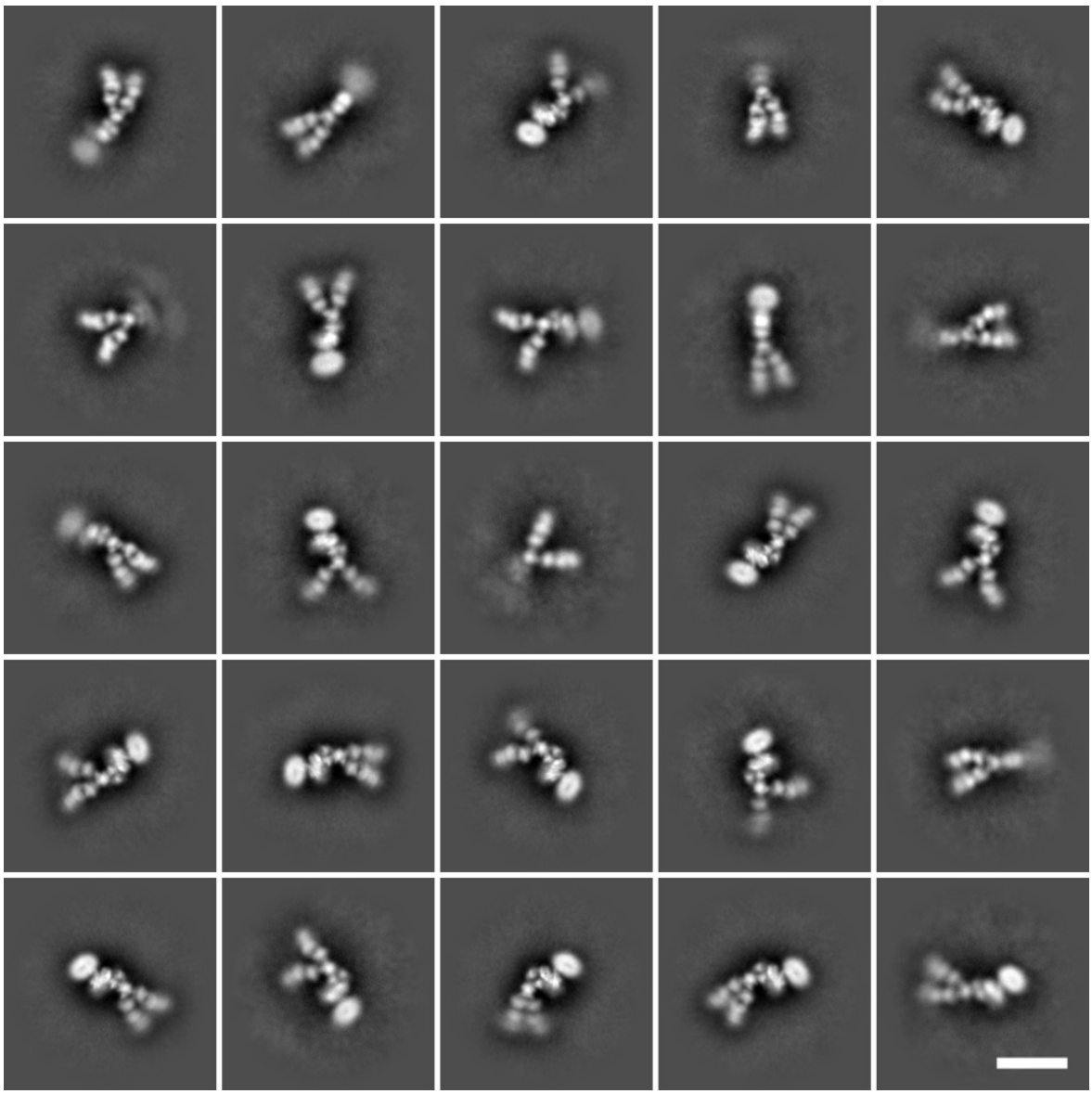


**Figure 5.14 | Reference-free 2D classification of eOD-GT8-bound IgM BCR complexes.** Images depicting class averages for particles selected from micrographs of vitrified eOD-GT8-bound BCR complex. Scale bar = 20nm. Data collected and processed by Dr. Lukas Sušac, Tampé group, Goethe University Frankfurt.

Micellar structures were readily identifiable, containing membrane complexes sharing several key features similar to those predicted for the IgM BCR complex (Fig. 5.14). In line with the preliminary nature of the data collected, and in the absence of a 3D density or structural model, inferences about the nature of the features observed should be treated with caution. With this caveat, it is notable that several features which could be ascribed to individual Ig domains were visible in the images (Figure 5.15). The micelle-proximal features contained (1) an asymmetrically positioned ring-like structure, similar to the predicted 'horseshoe' conformation of the Cμ4-Cμ3 domains[307], interacting with (2) another region of density, which could represent the CD79 heterodimer, as predicted. Above such features a junctional point (3), which could correspond to Cμ2[112], is readily visible. The micelle-distal features detectable in the class averages showed two identical O-shaped structures (4), which are very similar to those observed for complex-bound Fab fragments and can be ascribed to the receptor Fab arms[319]. These features are differentially oriented across class averages with respect to the membrane-proximal domains, as would be expected from the constrained flexibility of the IgM Fab arms. This represents a source of conformational variability that is to be expected in immunoglobulin molecules[112], which will likely increase the difficulty in generating 3D density maps corresponding to these features.

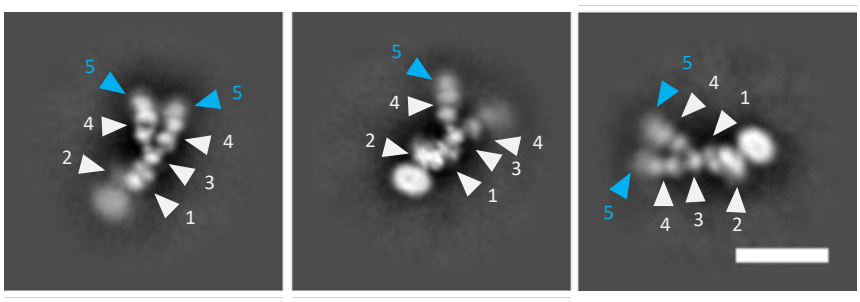



**Figure 5.15 | Selected 2D class averages from Fig. 5.14.** Annotated example class averages from the data presented in Figure 5.14, depicting numbered features potentially associated with components of the BCR complex described in the text. Scale bar = 20nm. Data collected and processed by Dr. Lukas Sušac, Tampé group, Goethe University Frankfurt.

Importantly, extra features (5) were observed beyond these predicted features of the IgM BCR molecule. For most, if not all, class averages, an extra feature was detected bound to the membrane-distal portion of these ring-like structures, which should correspond to the variable regions. This is likely to represent the high affinity eOD-GT8 antigen used to extract the receptor. As receptor purification must be achieved through the Twin-StrepTag added to the antigen, each complex must contain at least one eOD-GT8 molecule at the time of affinity purification. By virtue of the high affinity of the antigen-receptor interaction, and the use of a saturating concentration of antigen to label CHO-S VRC01$_{GL}$ cells prior to purification (Fig. 5.11d), it would be expected that most receptor Fab arms would be bound by the antigen if no significant dissociation has occurred. In line with this, this ring-bound feature was detected in most, if not all, potential Fab arms for all class averages, suggesting receptor occupancy is likely to be highly efficient. This is of particular importance in ensuring that, even if the Fab arms cannot be resolved by virtue of their flexibility, any structural data obtained of the rigid Fc portion of the receptor would be derived from mostly homogeneous antigen-bound receptors only.

These preliminary results suggest that the purified antigen-bound IgM BCR complex likely represents an intact receptor, and that the eOD-GT8 antigen remains bound throughout purification and vitrification. The collection of this data provides a promising first step in the determination of the structure of an intact BCR complex bound to a cognate antigen.

## 5.4 Discussion

The work described in this chapter aimed to purify complete IgM BCR complexes from the surface of mammalian cells, building on the work on the TCR complex by Sušac, Vuong and colleagues[240]. In avoiding the presence of affinity tags on the complex itself, purification of the receptor from the same cell line was possible using different soluble binders. This in turn would allow a comparison to be drawn between complexes extracted using an artificial covalent binder (SpyCatcher3) or a functional antigen (eOD-GT8).

The complex could be expressed on CHO-S cells and extracted using previously established protocols[240], yielding predominantly monodispersed complexes as observed by SEC (Fig. 5.6b). However, relatively poor protein yield prompted an attempt to optimise receptor extraction and purification. Trialling different detergents for receptor extraction provided a means to increase solubilisation efficiency through the use of LMNG (Fig. 5.7). The use of a different affinity tag, the Twin-StrepTag, also improved the extracted protein yield by improving affinity resin capture of the complex. These modifications did not alter the protein behaviour and migration by SEC, allowing purification of complete IgM BCR molecules isolated via SpyCatcher3.

Following the success in purifying SpyCatcher-bound IgM BCR complexes, the same protocol was to be applied to the purification of eOD-GT8-bound complexes. Exchange of the final detergent was introduced to facilitate grid preparation post-SEC. The transfer detergent chosen was GDN, as the complex was known to be stable in this detergent from its use in the initial trial purification (Fig. 5.6), and had been favourably used for grid preparations for the TCR complex[240].

eOD-GT8-purified complexes could be extracted using this modified protocol. The similarity in size between the eOD-GT8 antigen and the CD79A and CD79B chains made it difficult to identify the CD79 subunits by SDS-PAGE (Fig. 5.12c). The shift in SEC observed for this complex when compared to unligated BCR complexes (Fig. 5.13) suggests these complexes have increased molecular weight. This effect, likely due to the increased in size of the bound soluble protein, would not likely be observed if the CD79 chains had dissociated from the complex.

The purified material produced in this chapter can be directly compared with that used by Su and colleagues[97] and Ma and colleagues[98] in their recent structural characterisation of IgM BCR assembly in unligated complexes. The IgM BCR purified by both groups, which contained the variable regions of VRC01, coincidentally closely resembles the complex purified in the present study. The behaviour of the complexes purified here closely resembles that of the complex purified by Su and colleagues, which has coincidentally been size-excluded in the same buffer and column as that used in this work[97]. In the case of the published work, the BCR complex is also present as a predominantly monodispersed peak with a 'shoulder' of larger material. Moreover, the analysis of the material purified by SDS-PAGE by Su and colleagues[97], as well as in that published by Ma and colleagues[98], shows fainter bands for CD79A and CD79B chains compared to those of those observed for the immunoglobulin heavy and light chains in both cases, as is in part predictable from their stoichiometry[97,98]. These examples further clarify the behaviour of the proteins purified in the present study and suggest that these too represent fully assembled BCR complexes suitable for further studies of the ligated receptor using cryo-EM.

Preliminary single-particle cryo-EM imaging of vitrified, eOD-GT8-bound IgM receptors revealed that the complex likely represents an intact IgM BCR (Fig. 5.14). The class averages obtained by reference-free 2D classification are similar to those obtained from the micrographs that gave rise to the structures published by Su and colleagues[97] and Ma and colleagues[98]. Importantly, a key difference between these complexes is the existence of a Fab-bound feature, predicted to represent the eOD-GT8 antigen, as expected. This preliminary work is to be continued by Lukas Sušac and the Tampé group in Goethe University Frankfurt and will hopefully give rise to a structural model of an antigen-bound IgM BCR complex, which can then be compared to the published structures of human IgM BCR complexes without ligands (this will be elaborated in the Discussion chapter).

In conclusion, this work has demonstrated that the isolation of membrane complexes from CHO-S cells via tethered soluble proteins is a promising avenue for membrane protein purification as initially demonstrated by Sušac, Vuong and colleagues[240]. The work conducted in this chapter was to directly inform the project described in Chapter 6, where these methods were applied to the isolation of a different immune receptor complex.

# Chapter 6. Purification of a complete human FcεRI complex for structural studies

## 6.1 Introduction

IgE antibodies play an essential role in the induction of allergic responses, as well as immunity against helminths[330]. Their effector functions are mediated predominantly through the engagement of two receptors through the Fc region: the high affinity receptor, FcεRI, and the low affinity receptor CD23[218].

The FcεRI receptor, expressed on mast cells and basophils (among other cell types), has a key role in inducing degranulation by these cells in response to allergens, an important driving mechanism in allergy[331]. On mast cells and basophils, the receptor is composed of three subunits, in an $\alpha\beta\gamma_2$ stoichiometry. The β chain is not expressed in all FcεRI-expressing cells, with dendritic cells and other cell types expressing an $\alpha\gamma_2$ form of the receptor in humans, suggesting the β chain may not be essential for receptor assembly[116,219]. The α subunit, which contains an extracellular domain composed of two Ig-like domains, mediates binding to IgE independently of the other chains[332]. The β chain, and the disulphide-bonded homodimer $\gamma_2$, are ITAM-containing subunits, which can be phosphorylated by Src-family kinases, including Lyn, and initiate downstream signalling upon antigen binding[219].

Structural studies have focused on the conformational variability of IgE in solution and in its receptor-bound state. The crystal structure of the minimal Fcε fragment, Cε3-Cε4, was determined in the presence[333] and absence[334] of the ectodomain of FcεRIα. These studies characterised the asymmetric binding of the symmetric Fc region to two distinct sites on the α chain ectodomain. This asymmetry ensures the 1:1 binding stoichiometry observed for symmetric, homodimeric IgE binding to FcεRIα[333]. The flexibility between the Cε3 and Cε4 domains allows this two-step binding process to both sites and accounts for the very low dissociation rate which underpins FcεRI function[219,333]. However, studies suggesting that further engagement of the receptor occurred through Cε2 domain binding provided evidence that this was an incomplete characterisation[335]. Fcε fragments containing the Cε2-Cε4 domains of IgE were initially crystallised in the absence of FcεRI[336]. Crystal structures suggested that residues within the Cε2 domain of the Fc fragment interacted with Cε3-Cε4, causing the fragment to adopt a highly 'bent' conformation which would not be compatible with the binding model initially proposed for Cε3-Cε4 without some modification[336]. Importantly, the transient nature of the interaction between Cε2 and Cε3-4 ($K_D \sim 4.5x10^{-6}$ M)[335] suggests that Cε2 rearrangement upon receptor engagement does not necessarily represent a conformational change between two distinct states, but rather a transient, preferred conformation among many that may exist when Cε2 is not bound to other Cε domains[337]. In the case of the structurally related isotype IgM, a similar restricted set of conformations adopted between the Cμ2 and Cμ3-4 domains has been described in the soluble pentamer, with the site of Fc flexibility positioned between Cμ3 and Cμ2[309]. Similarly to the Cε2 and Cε3-4 interaction described above, contacts between Cμ2 and Cμ3-4 lead to the transient capture the IgM BCR in a 'bent' conformation[97]. The crystal structure of the Cε2-Cε4 fragment bound to the soluble

ectodomain of FcεRIα was determined by Holdom and colleagues[220]. The interaction between ligand and receptor was found to be predominated by hydrophobic interactions at both sites. This study confirmed that, despite no contacts being present between Cε2 and FcεRIα, the presence of this domain stabilises the interaction between the Cε3 and the FcεRIα ectodomain. This was in line with the observation that the high-affinity interaction between the receptor and the Fcε fragment relies on the presence of Cε2[220,335].

Together, these studies have described the binding of the FcεRIα ectodomain and IgE in great detail. However, the interactions mediating the assembly of the FcεRI complex have not been characterised. The association of the transmembrane domain of the α chain with those of the $\gamma_2$ homodimer have been studied using mutagenesis and molecular simulations, drawing a comparison between the residues involved and those present on other Fc receptors that associate with the $\gamma_2$ homodimer, such as the Fcγ receptors CD16 and CD64[338]. As such, determining the structure of the fully assembled FcεRI complex may not only help inform the design of therapeutic targets and validate previous structural studies, but also provide insight into the assembly of other Fc receptors.

This chapter describes work undertaken to purify fully assembled complexes following a similar protocol to that described in Chapter 5 for BCR purification. As in the case of the BCR complex, an approach was used to allow purification of the receptor in its unligated and Fcε-bound state, as structure determination for both states of the complex could help determine whether any conformational rearrangements occur, which could inform the causes of kinase recruitment and receptor signalling.

## 6.2 Methods

The methods used in this chapter follow directly from those described in Section 5.2. Modifications will be described below.

### 6.2.1. CHO-S cell line and soluble protein generation

The generation of CHO-S cell lines expressing the complex was conducted as described in Section 5.2. The validation of expression by flow cytometry followed the protocol described in Section 2.3. The expression and His-tag purification of soluble proteins was conducted using the protocols of Sections 2.4.3-2.4.4.

### 6.2.2. Optimisation of receptor solubilisation

Optimisation of FcεRI solubilisation followed the protocol described in Section 5.2.5.

### 6.2.3. Membrane complex purification

The SpyCatcher-bound and Fcε-bound complexes were isolated using a StrepTactin purification protocol as described in section 5.2.3-4. $3x10^9$ cells/batch were labelled in 50mL PBS supplemented with 40μg/mL SpyCatcher3(Twin-StrepTag) or Fcε(C225A) protein for 45mins at 4°C and labelled cells were washed and frozen as in Section 5.2.3. Complex purification was conducted as in Section 5.2.4.

The protocol was modified for the purification of a third complex, 22E7-bound FcεRI. This was due to lack of availability of the previously used affinity resin. To this end, a StrepTactin-XT resin was used, containing a modified StrepTactin variant with improved (picomolar) affinity for Twin-StrepTag[246]. Cells were labelled as above with

40µg/mL 22E7 Fab-Halo as per the protocol in Section 5.3.2, and membranes were isolated, solubilised, and clarified as in Part 1 of Section 5.3.4.

5mL StrepTactin-XT resin (Cytiva) was packed in an Econo-column (Bio-Rad). The resin was washed in 5CV MilliQ water and equilibrated using 5CV equilibration buffer (20mM HEPES, pH7.5, 500mM NaCl, 15% (v/v) glycerol) through gravity flow. Clarified lysates were applied to the resin and bound in batch with rotation at 4°C for 90mins. Flow-through was removed and the resin was washed with 30CV wash buffer (20mM HEPES, 500mM NaCl, 0.05% (w/v) GDN, 1mM EDTA, pH 7.5) by gravity flow. The complex was eluted in wash buffer supplemented with 50mM biotin (Sigma). Regeneration was conducted by washing the resin in 3CV MilliQ water, 3CV 0.05M NaOH, and 3CV MilliQ water. Resins were stored in 20% ethanol.

### 6.2.4. SDS-PAGE and FSEC

Characterisation of purified material by SEC and SDS-PAGE was conducted as described in Section 5.2.6.

### 6.2.5. Cryo-EM data collection and processing

Cryo-EM data was collected and analysed by Lukas Sušac, Goethe University Frankfurt, as described in Section 5.2.7.

### 6.2.6. Rendering representations of previous crystal structures

The ribbon representation of the model of the crystal structure from Holdom and colleagues[220] (PDB 2Y7Q) was constructed and coloured using the online tools of the Protein Data Bank[339] (PDB).

## 6.3 Results

### 6.3.1 Generating a system for FcεRI purification

In line with the approach taken in Chapter 5, a single cell line expressing human FcεRI was generated for the purification of two states of the complex. The complex was expressed without an intrinsic affinity tag, with purification achieved through ligation of a Twin-StrepTag-containing soluble protein (Fig. 6.1). For the unligated complex, cells were labelled with SpyCatcher003[289], as purified and characterised in Fig 5.8. For the ligated complex, the Fc fragment of IgE (Fcε) was used for cell labelling. Fcε-mediated purification was feasible due to the high-affinity interaction between IgE and FcεRI ($K_D$~0.1-1x$10^{-9}$ M)[220,340].




**Figure 6.1 | Diagram depicting purification strategies for FcεRI extraction.** Diagrams depicting fully assembled FcεRI ($\alpha\beta\gamma_2$ stoichiometry). The two tandem circles represent a single ITAM domain. An N-terminal SpyTag has been added to the α chain of the complex, and a modified version of EGFP has been added to the C-terminus of the γ chain. Purification of the complex is to be achieved using affinity tags present on either covalently-bound SpyCatcher molecules (left panel) or on the bound ligand, the IgE Fc fragment (Fcε, right panel) by virtue of its high affinity interaction with FcεRI.

As in the previous chapter, the components of the FcεRI complex were expressed in CHO-S cells. The three chains of the complex were expressed as a polycistronic construct with the use of 2A self-cleaving peptides (Fig. 6.2a)[240]. The SpyTag003 peptide sequence was introduced at the N-terminus of the FcεRIα chain for purification of the unligated complex with SpyCatcher. The green fluorescent protein EGFP(T65S) (also known as GFP2[240]), was introduced to the C-terminal sequence of the FcεRIγ chain, to increase complex size and to allow tracking of complex concentration indirectly using fluorescence intensity.

CHO-S cells were transduced with lentiviral particles containing the construct. Following two rounds of transduction, a uniform population of cells with high levels of receptor expression was present without cell sorting or selection (Fig. 6.2b). The expression of surface FcεRIα, and its binding to SpyCatcher, were readily detectable in the resulting cell line, CHO-S FcεRI (Fig. 6.2b-c), as was the expression of EGFP(T65S) (Fig. 6.2d).

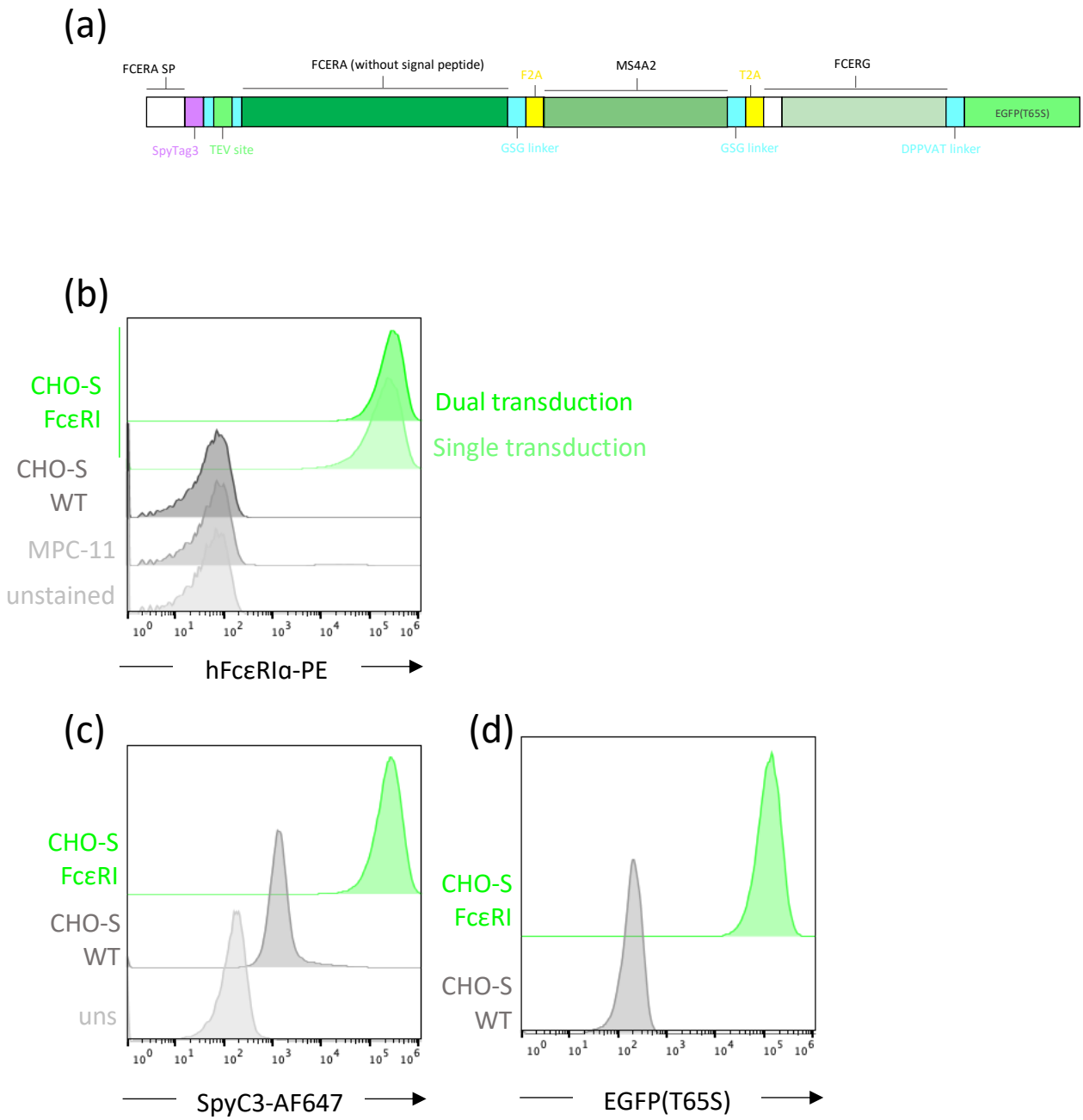



**Figure 6.2 | Generation of CHO-S FcεRI cells. (a)** Schematic of the polycistronic construct for hFcεRI expression. *FCERA* encodes FcεRIα, *MS4A2* encodes FcεRIβ, and *FCERG* encodes FcεRIγ. White boxes represent endogenous signal peptide sequences, which do not form part of the final complex. **(b)** Flow cytometry analysis of surface FcεRIα expression in wildtype CHO-S cells (dark grey) and CHO-S cells after a single round of lentiviral transduction (light green) or following re-transduction (dark green). Cells stained with an isotype control (MPC-11, grey), and unstained cells (light grey) are also shown as a control. **(c)** Flow cytometry analysis of surface receptor expression in CHO-S FcεRI (green) compared to wildtype CHO-S cells (dark grey), as measured by fluorescent SpyCatcher3 staining, with unstained cells shown as a control (light grey). **(d)** Flow cytometry analysis of EGFP(T65S) expression in CHO-S FcεRI cells (green) compared to wildtype CHO-S cells (grey).

For the purification of the ligated complex, a Twin-StrepTag-containing soluble IgE Fc fragment was purified. The Fcε fragment, containing the Cε2-Cε4 domains of human IgE, was mutated from the consensus sequence to remove a free cysteine (C225A) in Cε2 which in the complete IgE molecule forms a disulphide bond with Cε1, in line with previous studies[220,336]. It differed from the Fc fragment in the crystal structure of the bound FcεRIα ectodomain only in that residues mutated to remove glycosylation in the previous structural study were not altered in the ligand produced in this work[220]. The tagged Fcε fragment was purified as a homodimer of the predicted size (Fig. 6.3a-b). Under reducing conditions, the individual monomer chains could be observed (Fig. 6.3b). The presence of two distinct bands when a single chain is present (Fig. 6.3b) was surprising, but has been previously described in the reduction of Fcε fragments[341]. Fluorescently labelled Fcε fragment bound to CHO-S FcεRI cells, with minimal binding detected in the parental cell line (Fig. 6.3c). Receptor-bound protein could be counterstained with streptavidin, suggesting the Twin-StrepTag present in the ligand is still available in solution upon receptor binding (Fig. 6.3d). Together, the CHO-S FcεRI cell line and the two soluble ligands produced formed the basis for purifications using the protocols derived from BCR complex purifications (see Chapter 5).

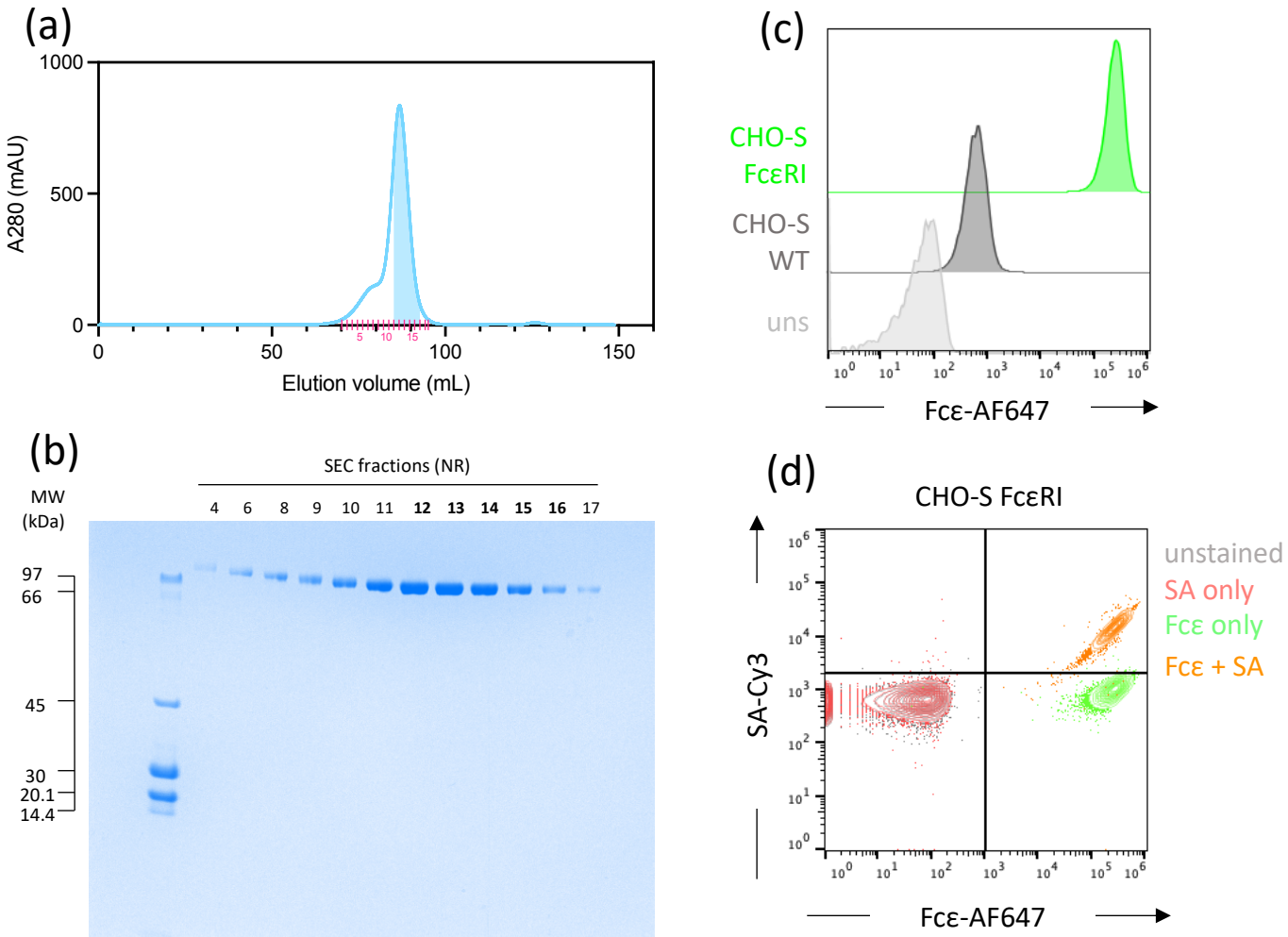



**Figure 6.3 | Purification of the Fcε(C225A) fragment. (a)** SEC profile of His-purified Fcε homodimer. Fractions are labelled in pink and the shaded area represents fractions pooled for further experiments. **(b)** SDS-PAGE analysis of selected SEC fractions, run in 12% polyacrylamide gels under nonreducing (NR, top) or reducing (R, bottom) conditions. Fractions in bold text represent fractions kept for further experiments. Samples are paired across both gels. **(c)** Flow cytometry analysis of CHO-S WT (dark grey) and CHO-S FcεRI cells (green) stained with fluorescently labelled Fcε. Unstained cells are shown as a control (light grey). **(d)** Flow cytometry analysis of CHO-S FcεRI cells labelled with Fcε fragment counterstained with StrepTag-binding streptavidin (orange), compared to cells stained with Fcε only (green), streptavidin only ('SA only', red) or unstained cells ('uns', grey).

### 6.3.2 Purification of the SpyCatcher-bound FcεRI complex

Initial experiments focused on the purification of the SpyCatcher-bound complex. To facilitate receptor solubilisation, the solubilisation test trialled in Fig. 5.7 was applied to the CHO-S FcεRI cell line. The complex, as measured by bound SpyCatcher fluorescence intensity, was more readily solubilised in LMNG-containing buffers than in those containing GDN (Fig. 6.4), as had been the case for the BCR complex (Fig. 5.7).

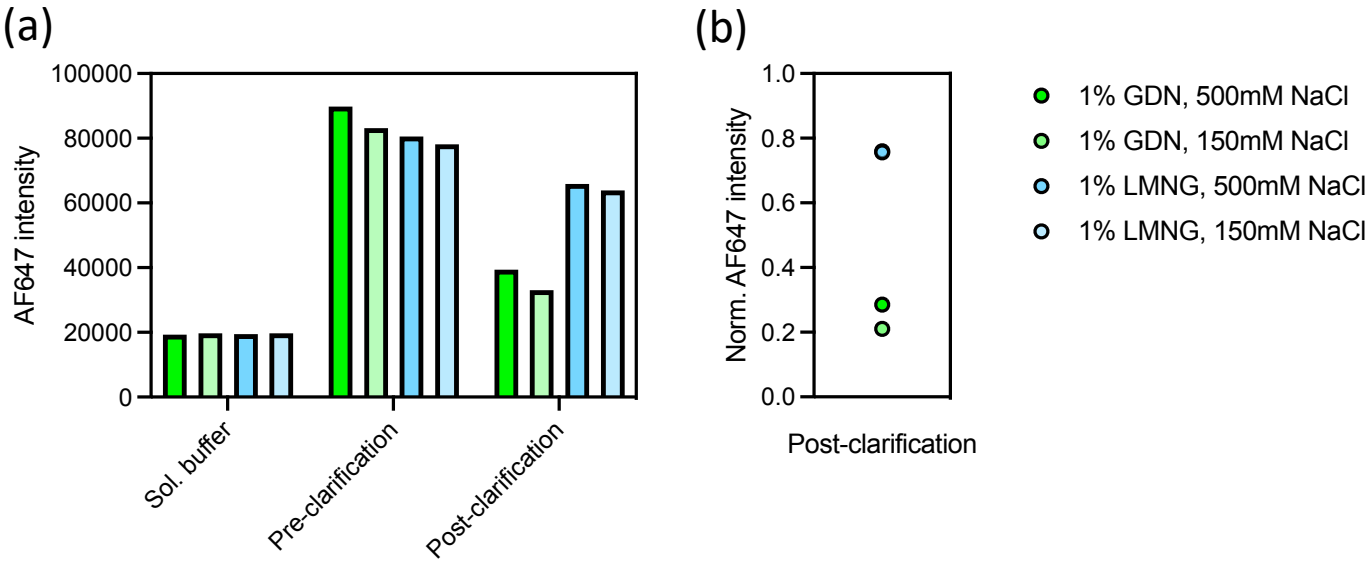



**Figure 6.4 | Solubilisation of the FcεRI complex under different conditions. (a)** Measurements of Alexa Fluor 647 intensity in buffers containing solubilised CHO-S FcεRI cell membranes before or after lysate clarification using a Clariostar plate reader. Solubilisation buffers were also measured as the baseline for intensity normalisation. **(b)** Normalised AF647 intensity for clarified lysates solubilised under different conditions from the data in (a). The measurements were normalised with the pre-clarified samples as the maximum intensity and the solubilisation buffer as the minimum possible intensity. For both panels, blue and green symbols or bars represent intensities collected for samples solubilised with 1% (w/v) LMNG or 1% (w/v) GDN, respectively. Data from a single independent experiment is shown in all cases.

Accordingly, the complex was solubilised with LMNG and purified using a StrepTactin resin as before. The complex was initially maintained in LMNG throughout all purification steps (Fig. 6.5a). Size-exclusion chromatography revealed that the complex was not present as a single species, as a large fraction of the purified material was eluted at earlier volumes than expected, although a peak likely to represent the monomeric complex was also detectable (Fig. 6.5b). As AF647 fluorescence was also detectable at these earlier elution volumes, this was taken to represent possible higher molecular weight forms of the receptor. SDS-PAGE analysis of the eluted complex showed that, across all species detected by SEC, the three chains of the complex were detected, and present at a similar ratio irrespective of the elution volume (Fig. 6.5c), confirming that all peaks represented the same complex without significant contaminants.

Importantly, the γ-EGFP(T65S) band (predicted size ~35-40kDa, accounting for GFP insertion[342–344]) was stained more intensely than that of the β chain (predicted size, ~25kDa[344,345]), as predicted from their 2:1 stoichiometry in the complex[219]. The SpyCatcher-FcεRIα chain was detected at the predicted size[346] (with the expected 20kDa increase in size due to the bound SpyCatcher molecule bringing the size of the chain to approximately 70kDa). However, an upper band was detected between the 66-97kDa markers. This behaviour of the α chain by SDS-PAGE had been previously described for the truncated ectodomain of FcεRIα, with both bands present upon immunoprecipitation with IgE or the monoclonal antibody 15-1, suggesting that in both cases these bands represent correctly folded protein[347].

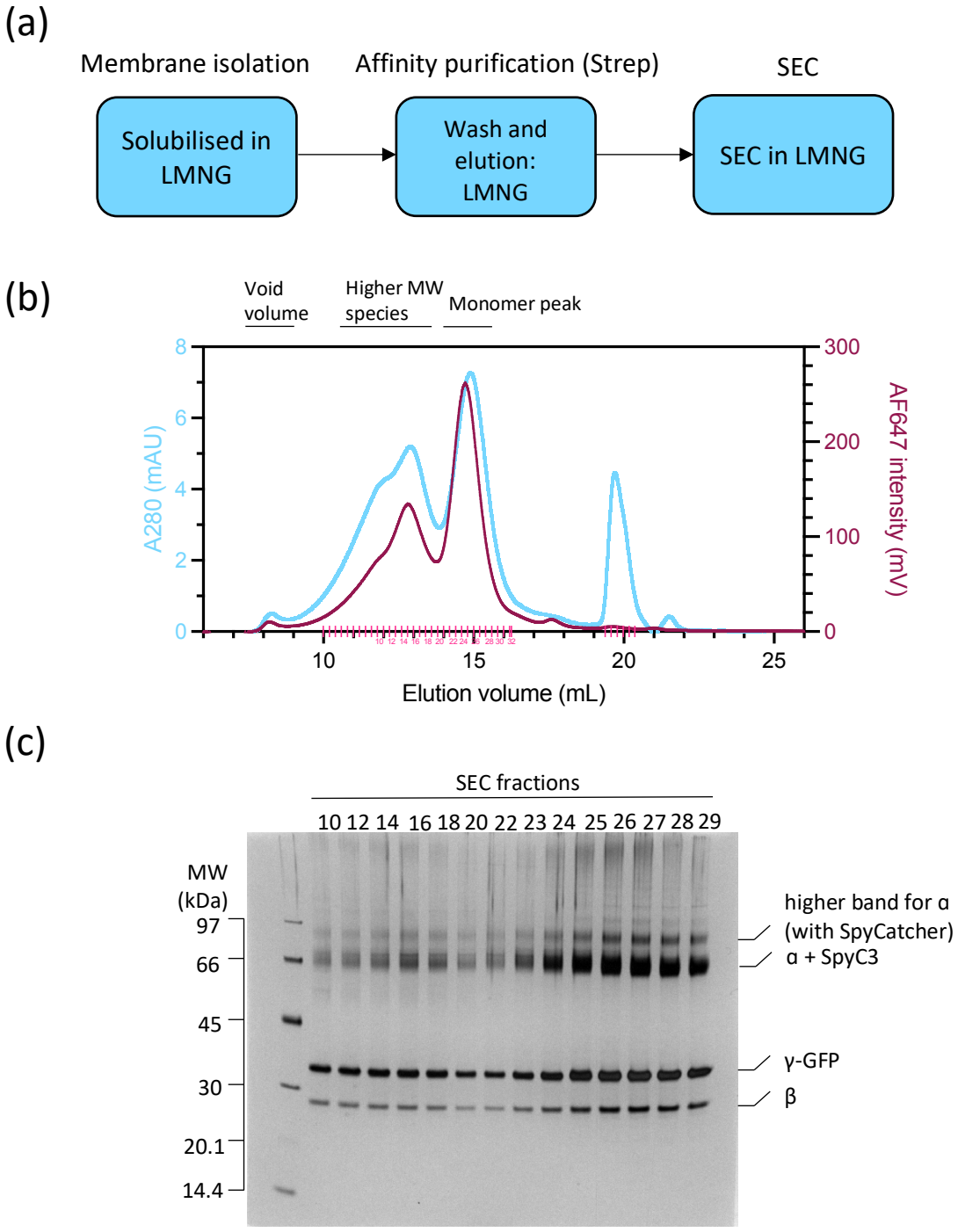



**Figure 6.5 | Purification of SpyCatcher-bound FcεRI (without detergent exchange). (a)** Diagram of purification workflow. **(b)** FSEC profile of affinity-purified SpyCatcher-bound FcεRI. The blue line represents A280 intensity (a measurement of total protein) and the purple line represents the AF647 intensity of eluting material (derived from fluorescent SpyCatcher). Fractions are labelled in pink. **(c)** SDS-PAGE analysis of material obtained from the SEC fractions depicted in (b). Samples boiled under reducing condition were run in 4-12% polyacrylamide gradient gels and detected using silver staining.

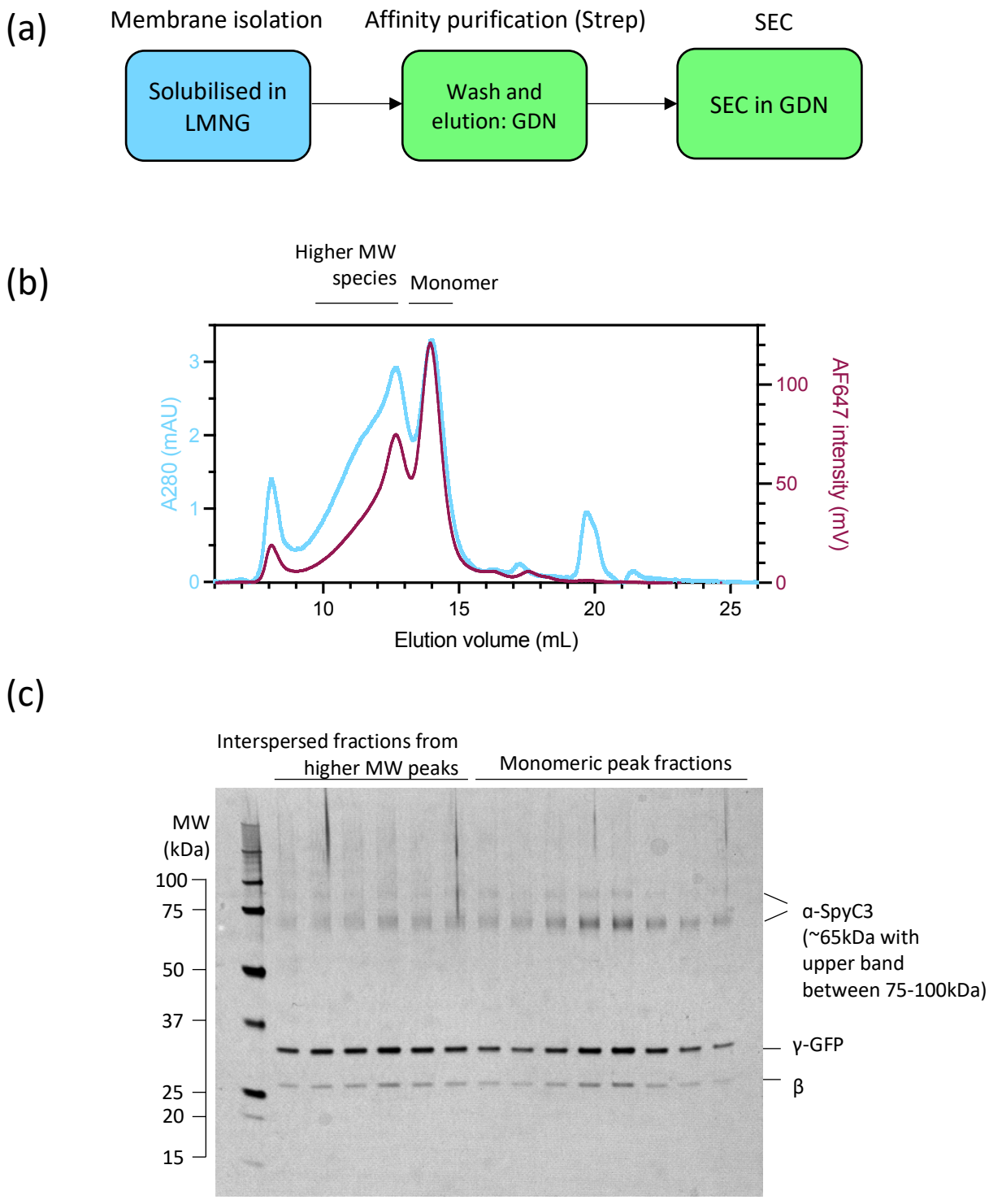



**Figure 6.6 | Purification of SpyCatcher-bound FcεRI (with detergent exchange). (a)** Diagram of purification workflow. **(b)** FSEC profile of affinity-purified SpyCatcher-bound FcεRI. The blue line represents A280 intensity (a measurement of total protein) and the purple line represents the AF647 intensity of eluting material (derived from fluorescent SpyCatcher). **(c)** SDS-PAGE analysis of material obtained from SEC depicted in (b). Samples boiled under reducing condition were run in 4-12% polyacrylamide gradient gels and detected through silver staining.

Following difficulties with BCR complex grid optimisation, this initial purification was followed by a modified protocol that exchanges the complex from LMNG into GDN micelles, as previously discussed in relation to Fig. 5.12. The protocol was modified to allow for resin-bound, LMNG-solubilised complex to be washed, eluted and size-excluded into GDN-containing buffers as before (Fig. 6.6a). The exchange of detergent did not modify the overall SEC profile of the complex, and higher molecular weight species of FcεRI were still observed (Fig. 6.6b). SDS-PAGE of the SEC fractions demonstrated all three chains of the complex were still present (Fig. 6.6c), which together with the similar SEC profile confirmed the complex could be safely exchanged into GDN micelles. Even so, size-exclusion chromatography of the complex in GDN-containing buffers caused a shift in the elution of the complex compared to that eluted in LMNG (Fig. 6.7). This was expected, as the same effect had been noted for the BCR complex (Fig. 5.13, discussed in Section 5.3.5). In light of this, the same protocol was then applied to the purification of the Fcε-bound complex.

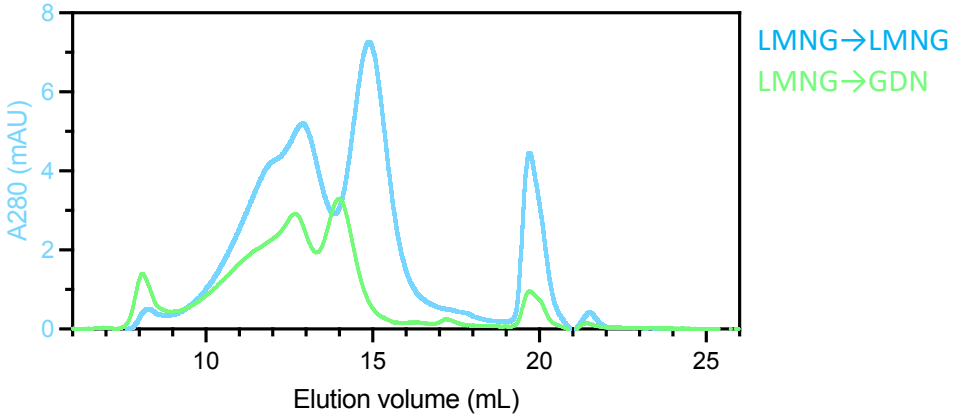



**Figure 6.7 | Comparison of SEC profiles for differently purified FcεRI complexes.** SEC profiles for LMNG-solubilised FcεRI complexes maintained in LMNG micelles (blue, from Figure 6.5b) or exchanged into GDN-containing buffers (green, from Figure 6.6b).

### 6.3.3 Purification of the ligated FcεRI complex

For the purification of the ligated complex, the receptor was bound *in situ*, by labelling intact CHO-S cells with the Fcε fragment in solution. The affinity of the FcεRI-Fcε interaction[220,340] is lower than those previously used - the eOD-GT8-VRC01$_{GL}$ interaction described in Chapter 5[313] and the high-affinity pMHC-TCR interaction used by Sušac, Vuong and colleagues[240]. Both these previously used antigens had monovalent interactions with dissociation rates ($k_{off}$) below $5x10^{-5}$ $s^{-1}$ (refs[313,318]). Conversely, the dissociation rate of IgE from FcεRI has been characterised to vary between 1.07-12.4x$10^{-5}$ $s^{-1}$ for different clones[340], with a dissociation rate of ~15x$10^{-5}$ $s^{-1}$ characterised for the near-identical Cε2-Cε4 construct used by Holdom and colleagues[220].

Despite this reduction in affinity, the receptor could be extracted from CHO-S FcεRI cells and purified using the same protocol used for the SpyCatcher-bound complex (Fig. 6.8a). Size-exclusion chromatography of the purified complex demonstrated that, unlike the SpyCatcher-bound form of the complex, the receptor eluted as a mostly monodispersed species (Fig. 6.8b). This distinction in the purified product was surprising in that the receptor had been purified from the same cell line, with the differential labelling of the receptor the only difference between protocols. SDS-PAGE confirmed the presence of the three subunits of the receptor, with the two bands representing the reduced Fcε fragment (matching those in Fig. 6.3b) co-migrating with the complex chains (Fig. 6.8c).

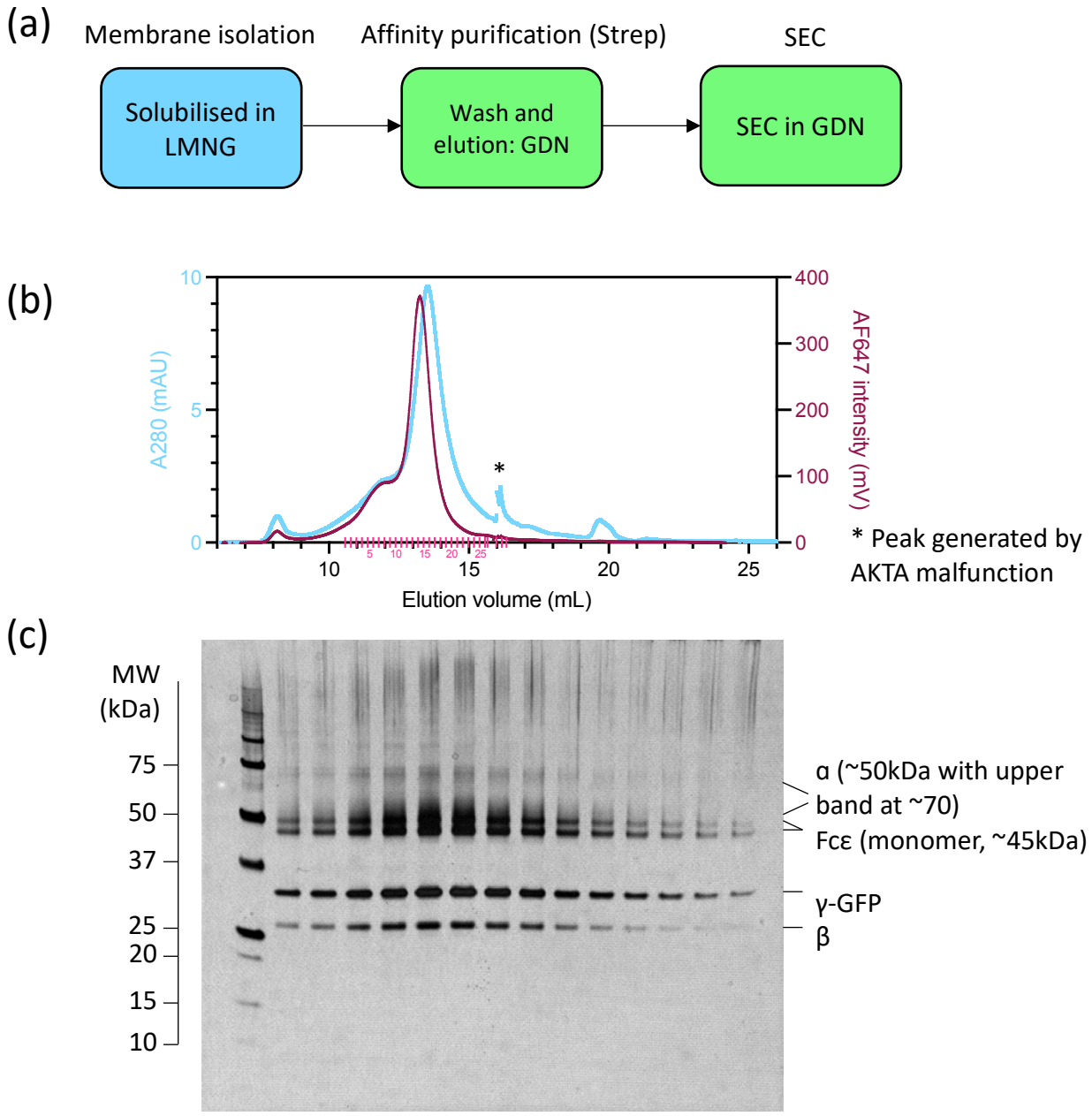



**Figure 6.8 | Purification of Fcε-bound FcεRI (with detergent exchange). (a)** Diagram of purification workflow. **(b)** FSEC profile of affinity-purified Fcε-bound FcεRI. The blue line represents A280 intensity (a measurement of total protein) and the purple line represents the AF647 intensity of eluting material (derived from fluorescent Fcε fragment). Fractions are labelled in pink. **(c)** SDS-PAGE analysis of material from consecutive fractions obtained from SEC. Samples boiled under reducing condition were run in 4-12% polyacrylamide gradient gels and protein detected using silver staining.

Importantly, in the absence of SpyCatcher, both bands corresponding to the FcεRIα chain displayed a ~20kDa reduction in size (compared to the data in Fig. 6.6c), further validating that both are likely to represent the SpyTag-FcεRIα chain. A comparison of the SEC profiles of both unligated and ligated complexes (Fig. 6.9) further revealed that the ligated complex was slightly larger than the monomeric peak of the unligated complex, likely due to the difference in size between the Fcε fragment (~80kDa, Fig. 6.3b) and SpyCatcher (~20kDa, Fig. 5.8b).

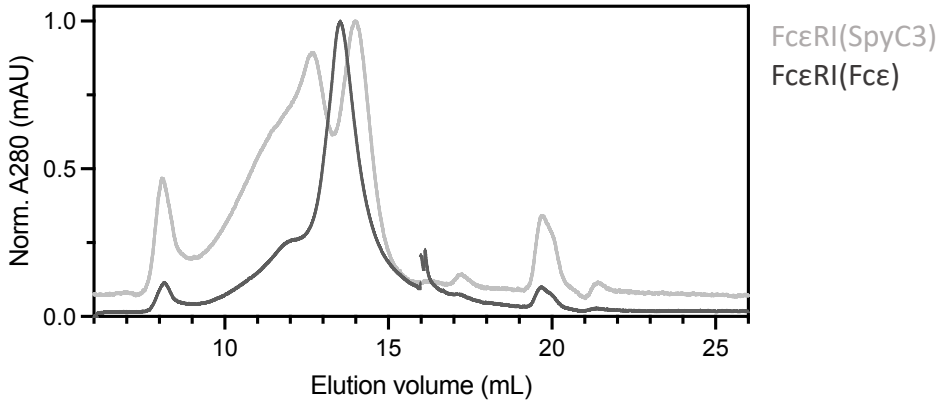



**Figure 6.9 | Comparison of SEC profiles for unligated and ligated FcεRI complexes.** Comparison of SEC profiles for complexes purified under equal purification protocols and size-excluded in the same GDN-containing buffer. SpyCatcher-bound complex (from Fig. 6.6b, grey) appears to contain other predominant peaks, compared to the mostly monodispersed peak observed for Fcε-bound complex (from Fig. 6.8b, black). A280 readings have been normalised (with maximum and minimum absorbances for each run set to 1 and 0, respectively) to facilitate comparisons between the positions of the peaks.

### 6.3.4. Preliminary cryo-EM imaging of the ligated FcεRI complex

In light of the homogeneity of the ligated complex by SEC, compared to the possible mixture of species seen previously (Fig. 6.9), this assembly was prioritised for further investigation using cryo-EM. The putative rigidity of the FcεRIα-Fc fragment association, as previously characterised by X-ray crystallography[220], and the increased complex size, were also considerations in prioritising this assembly. Preliminary cryo-EM data collection on grids containing vitrified Fcε-bound receptor was conducted by Lukas Sušac, Goethe University Frankfurt. Reference-free 2D classification of particles[329] selected from micrographs yielded 2D class averages containing similar features to those that could be expected from the crystal structure of Fcε-bound FcεRIα[220].

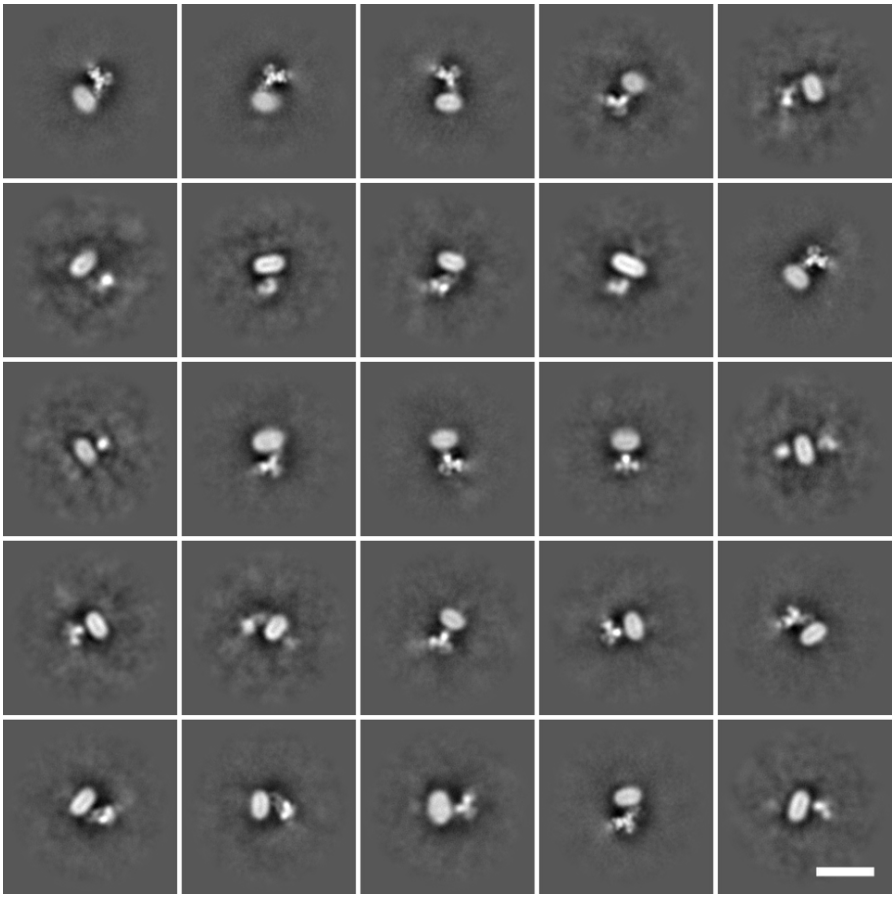


**Figure 6.10 | Class averages of particles selected from micrographs of grids containing vitrified Fcε-bound FcεRI.** Class averages from reference-free 2D classification of ligated FcεRI particles. The micellar structure is observable as an oval feature. Scale bar = 20nm. Data from Dr. Lukas Sušac, Tampé group, Goethe University Frankfurt.

Several features could be detected in these class averages (Fig. 6.11). A micelle-proximal feature (1), likely to represent the FcεRIα ectodomain, was present. Attached to this feature was a U-shaped feature (2) likely to represent the Fcε fragment, in line with the previously published structures of both receptor-bound and free Fcε[220,336]. No features associated with the FcεRIβ and FcεRIγ chains were detectable, which was to be expected as no intramicellar features were detectable and these subunits to do not contain significant regions that extend into the extracellular space[219]. However, in some 2D class averages, a feature (3) is observable on the opposite side of the micelle (Fig. 6.11), which are likely to represent the EGFP(T65S) protein present at the C-terminus of the FcεRIγ chain. Similar fluorescent proteins introduced to the truncated cytoplasmic tails of immune receptors have sometimes still been observed in 2D classifications[99,240]. These are not always visible in all class averages and they often do not form part of the final three-dimensional density due to the conformational flexibility of the cytosolic residues preceding them[240]. However, this further confirms that the FcεRIγ forms part of the vitrified complex. In conclusion, this initial dataset has provided preliminary data suggesting that Fcε-bound FcεRI complexes can be successfully vitrified and that structural information from particles likely to represent individual complexes, of sufficient size for particle detection, can be extracted from micrographs.

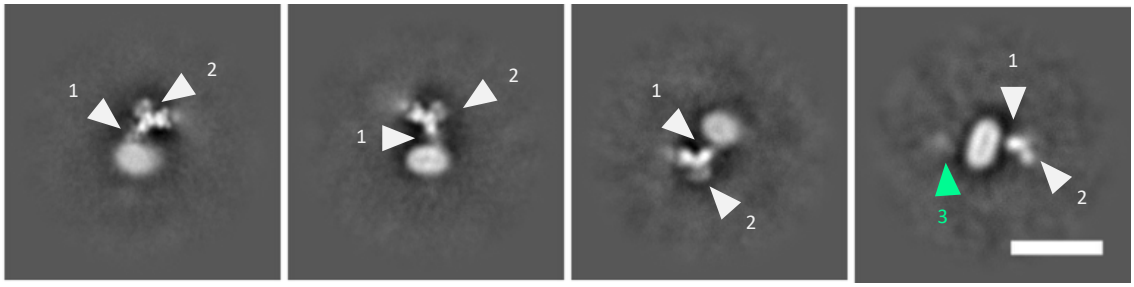



**Figure 6.11 | Selected 2D class averages.** Annotated example class averages from the data presented in Figure 6.10, depicting numbered features potentially associated with components of the FcεRI complex described in the text. Scale bar = 20nm. Data collected and processed by Dr. Lukas Sušac, Tampé group, Goethe University Frankfurt.

### 6.3.5 Purification of a Fab-bound FcεRI complex

In the absence of its ligand, micelles containing the FcεRI complex could potentially be difficult to differentiate from free micelles in electron micrographs. This is in part because the cytosolic domains of the complex may be unstructured and not resolvable, as was the case for the human TCR[27,240] and BCR[97,98] complexes, in which case the GFP density is also not likely to contribute to particle alignment[240]. Only the small ectodomain of FcεRIα (composed of two Ig-like domains) is likely to contribute a significant density, as the other two chains do not have extracellular domains[219]. In line with the approaches taken for previous membrane complex purifications, complex formation with a Fab fragment was ideal to increase receptor size[319]. The initial results obtained from previous purifications placed constrains on the choice of Fab fragment used. The potential alteration of receptor behaviour by SEC upon ligand binding precluded the use of antibodies against epitopes near the ligand-binding site, to retain potentially relevant protein heterogeneity which could be driven by these sites.

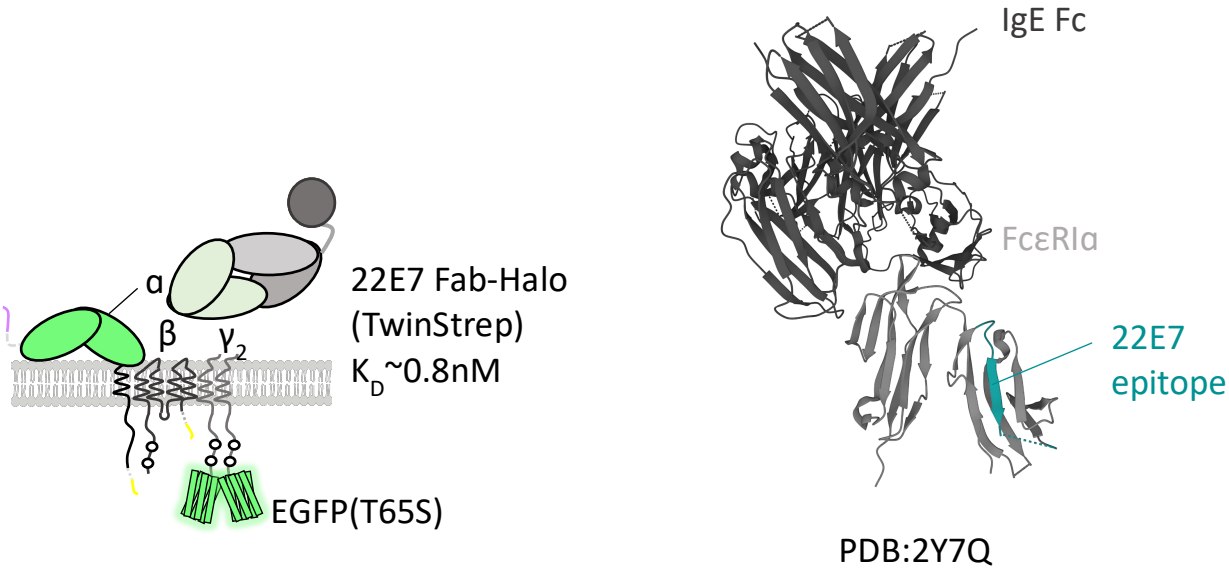



**Figure 6.12 | Diagrammatic depiction of 22E7-based purification of the FcεRI complex. (a)** Schematic of purification strategy using the high affinity anti-FcεRIα 22E7 Fab-Halo. **(b)** Ribbon representation of the crystal structure of the Fcε-bound FcεRIα ectodomain from Holdom and colleagues (ref. 220). The Fcε fragment is labelled in black and the FcεRIα soluble ectodomain in grey, with the 22E7 epitope labelled in green. This shows that the epitope of the 22E7 antibody does not overlap with the IgE binding site.

A Fab fragment was designed that comprised the variable regions of the anti-FcεRIα 22E7 clone[231,348] (Fig. 6.12). This antibody binds to a characterised epitope on domain 1, away from the ligand-binding site present on domain 2 and the interdomain region[349] (Fig. 6.12). Its binding affinity had previously been characterised[349] ($K_D$~0.8x$10^{-9}$ M), placing this antibody in the same range of affinities as IgE[340]. The Fab fragment was designed as a Fab-Halo protein (these have been previously described in Chapter 3), containing a self-labelling HaloTag enzyme which further increased its size. The 22E7 Fab-Halo could be purified as a heterodimeric protein of the predicted size (Fig. 6.13a,b). Fluorescently labelled 22E7 Fab-Halo could readily bind the CHO-S FcεRI cell line but not wildtype CHO-S cells, confirming its specificity for the complex (Fig. 6.13c). Importantly, pre-labelling the cells with Fcε fragment only minimally impacted 22E7 binding (Fig. 6.13d), as predicted from its epitope and previous studies on non-blocking FcεRIα antibodies[231].

The 22E7-bound complex was purified under similar conditions to those used for the other two forms of the complex (Fig. 6.14a). Minor changes were introduced to allow for the use of an improved affinity resin (StrepTactin-XT[246]). The purified material could not be fully resolved by SEC, displaying a broad peak of purified complex (Fig. 6.14b). The complex had not fully aggregated (minimal material was detected in the void volume) but was also not present as a single peak, as had been the case for the ligated complex. However, fractions collected from this broad, poorly resolved distribution did contain the three chains present in the other complex as detected by SDS-PAGE (Fig. 6.14c). The Fab-Halo heavy and light chains were also identifiable and co-eluted with the remaining complex chains (Fig. 6.14c), suggesting that the complex remained intact.

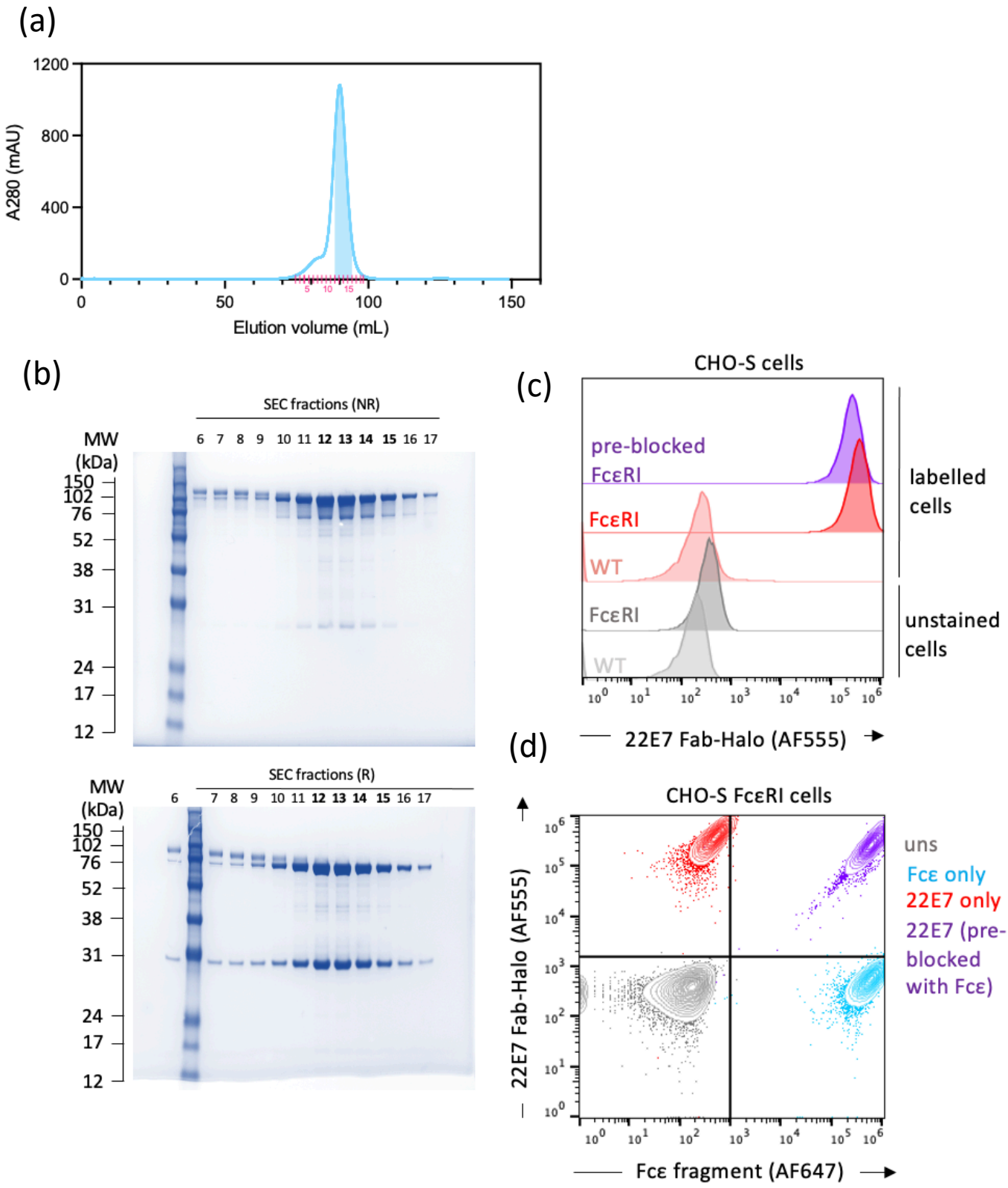



**Figure 6.13 | Purification of the 22E7 Fab-Halo fragment. (a)** SEC profile of His-purified 22E7 Fab-HaloTag. Fractions are labelled in pink and the shaded area represents fractions pooled for further experiments. **(b)** SDS-PAGE analysis of selected SEC fractions, run in 12% polyacrylamide gels under nonreducing (NR, top) or reducing (R, bottom) conditions. Fractions in bold text represent fractions kept for further experiments. **(c)** Flow cytometry analysis of 22E7 labelling of wildtype CHO-S cells (light red), CHO-S FcεRI cells (red) or CHO-S FcεRI cells pre-stained with Fcε (purple). Unstained wildtype CHO-S cells (light grey) and unstained CHO-S FcεRI cells (dark grey) shown as controls. **(d)** Flow cytometry analysis of CHO-S FcεRI cells stained with AF555-labelled 22E7 Fab-Halo in the presence (purple) or absence (red) of receptor blocking with AF647-labelled Fcε. Cells labelled with Fcε only (blue) or unstained CHO-S FcεRI cells (grey) are shown as controls.

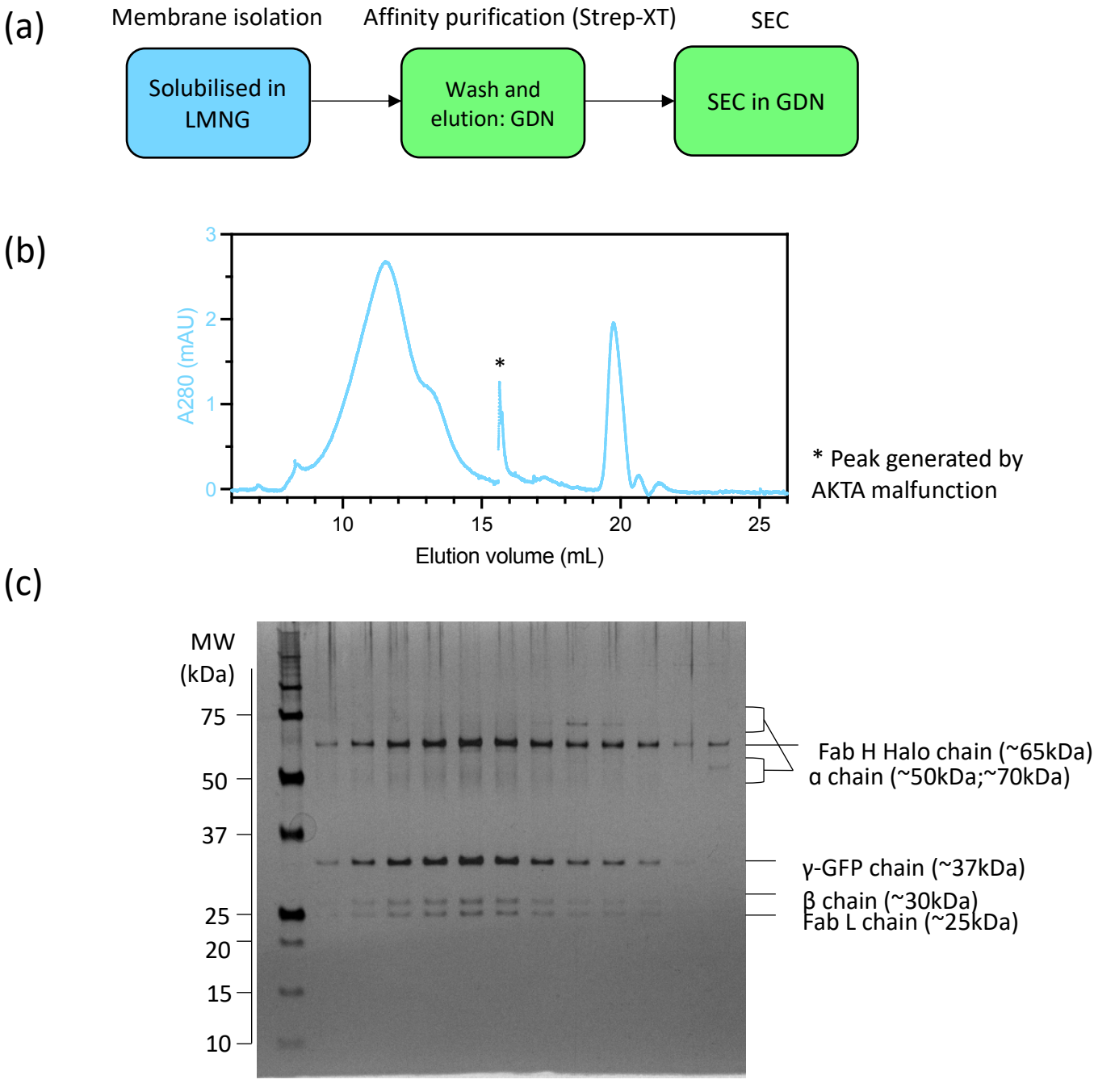



**Figure 6.14 | Purification of 22E7-bound FcεRI (with detergent exchange). (a)** Diagram of purification workflow. **(b)** FSEC profile of affinity-purified 22E7 Fab-Halo-bound FcεRI. The blue line represents A280 intensity (measuring total protein). **(c)** SDS-PAGE analysis of material obtained from SEC depicted in (b). Samples boiled under reducing condition were run in 4-12% polyacrylamide gradient gels and detected using silver staining.

The increased size of the complex as determined by SEC (Fig. 6.15) was likely due to the bound Fab-Halo molecule (molecular weight ~85kDa, Fig. 6.13b). This increase is exacerbated by the possible presence of higher-valency species, which would be capable of binding more than one Fab-Halo fragment, increasing the molecular weight of some complexes to beyond the resolution of the SEC column used for other purifications. Despite this limitation, the complex was maintained for future structural evaluation using cryo-EM.

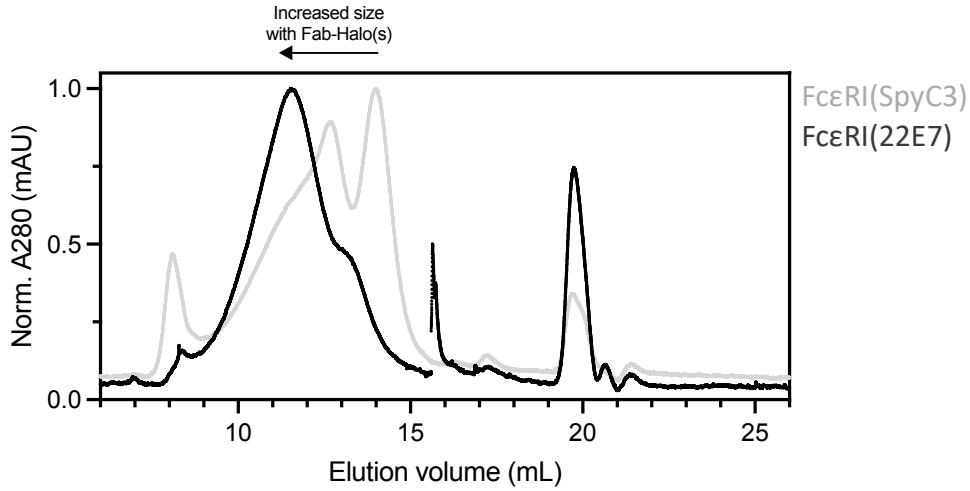



**Figure 6.15 | Comparison of SEC profiles for unligated FcεRI complexes.** Comparison of SEC profiles for complexes size-excluded in the same GDN-containing buffer. A notable shift is seen between SpyCatcher-bound complex (from Fig. 6.6b, grey) and 22E7-bound complex (from Fig. 6.14b, black), corresponding to increasing molecular weight.

## 6.4 Discussion

This chapter describes attempts to purify the human FcεRI complex for use in structural studies. To this end, stable expression of the receptor in CHO-S cells was used as initially described by Sušac, Vuong and colleagues[240]. Purification of the receptor was achieved by applying the protocols described in Chapter 5, previously used for BCR purification. Following the rationale described in Chapter 5, unligated receptor purification was achieved using SpyCatcher binding, with purification of the ligand-receptor pair undertaken through ligation of the receptor with its high-affinity ligand, the Fc fragment of IgE (Fcε). The Fcε fragment was designed to match that used in the previously determined crystal structure of the FcεRIα ectodomain complexed to its ligand[220], facilitating future comparisons between the published crystal structure and an eventual cryo-EM-determined structure of the complete complex bound to Fcε.

As in the case of BCR solubilisation, extraction of the complex into the soluble fraction was most efficient when LMNG-containing buffers were used (Fig. 6.4). SpyCatcher-bound receptors could be purified through the use of the Twin-StrepTag present in the attached SpyCatcher3 molecule, as previously demonstrated for the BCR complex (see Chapter 5). Importantly, the SEC profile of SpyCatcher-bound FcεRI was identical whether complexes were maintained in LMNG throughout the purification process or exchanged into the mild detergent GDN. All three chains of the complex could be identified in purified material and co-eluted as determined by SDS-PAGE (Fig. 6.5b, Fig. 6.6b), confirming that the complex was likely to be fully assembled. In both cases, independently of the detergent used, the complex did not appear to exist as a single monodispersed species but contained a significant portion of soluble material that eluted earlier from the size-exclusion column, revealing the presence of material of

increased molecular weight (Fig. 6.5b, Fig. 6.6b). The chains of the complex were identifiable in similar ratios and without impurities in material from these peaks, suggesting that these may represent higher-order assemblies of the complex (Fig. 6.5c, Fig. 6.6c).

The complex was also purified using bound Fcε fragments containing the same affinity tag. The ligated complex was purified under the same conditions to those used for the purification of the unligated complex. Despite the lower affinity of Fcε for the receptor when compared to the antigen used for the purifications in Chapter 5, the receptor could still be purified. Interestingly, the material purified by size-exclusion chromatography no longer contained evidence of larger receptor assemblies, producing a predominantly monodispersed peak (Fig. 6.8b). All chains of the receptor and the Fcε fragment were readily identifiable by SDS-PAGE and co-eluted together (Fig. 6.8c).

Preliminary data collected using cryo-EM imaging of vitrified, Fcε-bound complex revealed micelle-protein assemblies likely to represent individual ligated FcεRI complexes (Fig. 6.10). The existence of a micelle-proximal density bound to a domain adopting a U-shaped conformation strongly resembles the mode of binding of the 'bent' Fc fragment to FcεRIα[220], supporting that the same monovalent ligand binding is present here. This work will be continued by Lukas Sušac and the Tampé group in Goethe University Frankfurt, and will hopefully give rise to a structural model which will define the interactions involved in FcεRI assembly and validate the interactions mediating binding between IgE and FcεRI in the context of the fully assembled receptor complex.

The small size of the FcεRI complex in the absence of the IgE Fc fragment could prove to be a difficulty in particle selection and structure determination, as is the case for many small complexes imaged under cryo-EM[319]. To produce receptors with an additional bound molecule to increase complex size, a Fab-Halo molecule based on the high affinity, nonblocking 22E7 antibody was selected[231]. The fact that ligand binding disrupted these larger species could be suggestive of a role for the ligand-binding site in their formation, so mitigating engagement via the ligand-binding site was important to avoid the possible perturbation of the differences observed in the behaviour of SpyCatcher3-bound and Fcε-bound complexes. 22E7-bound FcεRI could be readily purified, although this generated a large, poorly resolved distribution of the complexes by SEC (Fig. 6.14b). SDS-PAGE analysis of protein purified from this distribution confirmed that all chains of the complex and of the bound Fab-Halo molecule co-eluted together, suggesting complete assemblies (Fig. 6.14c). Despite the similarity in size between the Fab-Halo molecule and the Fcε fragment, 22E7 Fab-Halo binding did not produce a single monodispersed peak as observed in complexes bound to Fcε (Fig. 6.15). In fact, the broad peak of material is consistent with a shift from the distribution observed for the SpyCatcher-bound complex, allowing for the increase in size added by the 22E7 Fab-Halo molecule (Fig. 6.15). Peaks potentially containing larger assemblies of the complex would in turn undergo an increase in size concomitant with the increased Fab-Halo binding stoichiometry, creating complexes of molecular weight too large to resolve with the size-exclusion chromatography column used. As the material did not elute in the void volume, nor did it show a monodispersed peak of the predicted size, 22E7-purified FcεRI is likely to contain the same varied distribution of complexes of varying molecular size observed in other unligated complex purifications and could prove an interesting target for structure determination. Direct comparisons

between such a structure and that of Fcε-bound complex could be facilitated by the addition of the 22E7 Fab-Halo to Fcε-bound complexes, which may also facilitate particle size and detection.

In conclusion, this work has produced several different complexes of the fully assembled FcεRI. This will provide purified material for the determination of the structure of the assembled complex in several functionally relevant assemblies using cryo-electron microscopy.

# Chapter 7. General Discussion

## 7.1 Overview of the results

The work described in this thesis sought to generate reagents and experimental systems to understand the molecular mechanisms driving immune receptor assembly and signalling. This work has predominantly focused on the BCR, with the goal of understanding the organisation and structure of the receptor at the single-molecule level. Despite the extensive characterisation of the signalling events that follow BCR triggering (Section 1.4.3), several aspects of receptor behaviour before and after antigen exposure remain points of contention (Section 1.5)[161].

Different models of receptor signalling, as discussed in the Introduction (Section 1.5), have different predictions regarding both receptor valency and its responsiveness to antigens under different experimental settings[161]. The results in this thesis have aimed to test some of the predictions of these models, in particular:

- In Chapter 3, a new super-resolution imaging method was used to determine the 3D localisation of individual BCR molecules on primary naïve B cells. Spatial clustering analysis of the data revealed that B cells were more likely to have areas of increased BCR density compared to the randomly distributed CD45 molecule on the B-cell surface. However, this was not a statistically significant effect.

- In Chapter 4, signalling by antigen-specific mouse B cells was assayed in the context of supported lipid bilayers (SLBs) presenting variants of cognate antigen. Signalling in response to low-affinity antigens was significantly reduced when antigen was presented on a rigid stalk, increasing its molecular height. This effect was not statistically significant for higher-affinity antigens.

- In Chapter 5, complete human IgM BCR complexes were isolated from mammalian cells for structure determination. The receptor could be isolated as a predominantly monodispersed species, and its behaviour in solution, as assessed by SEC, was not impacted by antigen binding *in situ*. In the case of antigen-bound complexes, this corresponded predominantly to monomeric, antigen-bound BCR particles as visualised in cryo-EM experiments.

- In Chapter 6, the high affinity IgE receptor, FcεRI, was also purified using a mammalian cell expression system. Solubilised complexes contained several species of varying molecular weight in the absence of ligand. In contrast to the BCR complex, the behaviour of the purified FcεRI complex was modified by ligand binding in SEC analysis, as Fcε-extracted complexes were mostly homogeneous and did not contain higher molecular weight species. In the latter case, single-particle cryo-EM validated that the more homogenous Fcε-bound receptor comprised individual ligand-bound receptors.

## 7.2 The stoichiometry of the resting BCR

Chapter 3 describes the use of a novel approach to labelling and imaging individual murine BCR complexes. Monovalent binding probes, containing a single fluorescent dye per probe, were designed, and saturation labelling using probes with high fluorophore labelling efficiency (see Section 2.4.9) was essential to counter possible undercounting of molecules. This design was therefore used to minimise artefactual overcounting of receptor molecules[252]

These molecules were used to label (IgM and IgD) BCR complexes on primary naïve B cells, as well as the monomer control protein[260], CD45. Stochastic activation of these fluorescent probes using a novel microscope setup (a new iteration of single-molecule light-field microscopy, SMLFM[256]) allowed detection and reconstruction of individual protein localisations in three dimensions using dSTORM. This allowed the characterisation of the distribution of the BCR and CD45 in the context of the complex membrane architecture of the B-cell surface. Using spatial clustering analysis methods, the distribution of BCR molecules was compared to that of CD45 on the cell surface. In doing so, the complexities inherent in comparing the distribution of membrane-constrained molecules to random 3D distributions were partially controlled. Cross K-function analysis[271] revealed that there was no significant difference in the distributions of BCR and CD45 at shorter radii (100-200nm), i.e. the distance wherein *bona fide* clusters driven by intermolecular interactions have been reported to occur (Section 1.5.6)[191,192,210]. However, a non-statistically significant increase in the number of neighbours around each BCR molecule was observed at these scales, suggesting clustering may occur in some cases. Such differences could become statistically significant at larger sample sizes. As such, the data presented does not exclude the

existence of some clusters, nor does it reject a potentially random BCR distribution on the cell surface.

The valency of the BCR in the resting state remains a matter of active debate, in terms of the global distribution of the receptor over the cell membrane, and the underlying mechanisms that could drive its self-association at the molecular level have been extensively studied. The stoichiometry of the receptor, explored by both indirect biochemical[36,302] and fluorescence microscopy studies[102,189,190], had yielded contrasting results, as described in the Introduction (Section 1.5). The use of super-resolution microscopy for the detection of individual receptors on the cell surface has also failed to resolve this discrepancy. Overwhelmingly, previous studies using super-resolution microscopy have characterised the BCR distribution on the cell surface as containing some clustered molecules, with clusters varying in size and number of receptors (Section 1.5.6)[191,192,210,251]. Several studies have conducted dSTORM imaging of the BCR using stochastically labelled probes with several dyes per molecule, which could potentially introduce artefactual clustering, although some have controlled for such effects and still observed clustering of IgM and IgD BCRs on the surface of primary naïve B cells[192]. Therefore, issues pertaining to overcounting[252] do not fully explain these results for all studies and may reflect the presence of real clusters. In contrast, methods that do not require localisation reconstruction, such as STED microscopy, have suggested that BCR molecules on the cell surface are predominantly organised as monomers, with some dimeric assemblies and small oligomers[168]. As such, the results in this thesis provide a further contribution to the assessment of receptor valency, this time in the context of membrane ultrastructure.

It is important, however, to consider the possible interpretations of these results. There is a distinction between *clusters*, driven by direct receptor-receptor interactions, and *regions of increased receptor density* on the cell surface. The existence of clusters forms part of some theories of BCR signalling (Section 1.5). They are expected to exist in the resting state by the dissociation-activation model, or to form upon antigen binding in models of force-induced conformational change[186,350]. However, regions of receptor enrichment can exist in the presence or absence of direct BCR-BCR interactions and can occur as a result of constrained diffusion in certain areas of the membrane. This has previously been suggested to occur due to enrichment linked to local lipid membrane compositions[351,352], or constrained receptor diffusion in areas of actin polymerisation (as predicted by the collision-coupling model)[192,193]. As actin-rich structures are essential in the formation of lymphocyte membrane protrusions[270,273], it would be an interesting application of the current experimental setting to investigate if these past observations are consistent with preferential enrichment of the receptor at microvillar tips. Freeman and colleagues have noted that LPS stimulation of B cells, which leads to the loss of small microvilli-like protrusions seen in the resting state in favour of large membrane ruffles, also releases BCR molecules which display constrained diffusion in the resting state, suggesting molecules may be transiently constrained specifically in microvilli[353]. Notably, STED-based studies suggesting that the BCR is mostly unclustered were conducted on membrane sheets extracted from cells, in the absence of the cytoskeleton, and special care was taken to ensure only localisations in flat membrane areas were analysed, avoiding regions of membrane curvature[168]. Potential enrichment of the BCR complex at microvilli has been recently observed in B cells[254], while TCR enrichment at equivalent sites on the T-cell surface has also been reported[267,270,273]. As CD45 has been shown to be randomly distributed

on the cell surface of T cells[273], such enrichment could help explain the distinction between the BCR and CD45 distributions in the data presented in Chapter 3. This behaviour at microvillar structures, the sites of lymphocyte surface scanning[197,354], could potentiate antigen sensitivity by both increasing receptor density and constraining receptor diffusion, facilitating antigen binding events during surface scanning[197]. The experimental setting used in Chapter 3 is well suited to exploring such questions, and further investigations of receptor distribution, coupled with an orthogonal membrane labelling strategy, would help elucidate whether such preferred localisation occurs at sites of membrane curvature.

The study of BCR distribution in three-dimensions has yielded results consistent with the observation that some degree of clustering may occur in the resting state, as predicted by dissociation-based models of receptor signalling. However, this was not observed in all cells imaged, suggesting it may not be an obligatory state in resting cells. Whether this observation can be ascribed to experimental variation, or represents biological variation derived from different signalling states across cells, remains to be clarified (Section 3.4).

The presence of possible clusters at the B-cell surface in the absence of antigenic stimuli is not intrinsically incompatible with theories of signalling that rely on receptor clustering. Mature, naïve B cell require continuous basal levels of signalling (tonic signalling) to survive *in vivo*[355]. Resting B cells, therefore, are not expected to contain only non-signalling receptors. In theories of signalling involving induced clustering, such tonic signalling events may be driven by transient clustering. This has been proposed in the context of the conformation-dependant oligomerisation model, where

the observation that up to 20% of receptors in the resting state display constrained diffusion is consistent with transient microcluster formation in resting cells[350]. Conversely, even in the absence of receptor-receptor interactions, receptors undergoing signalling events may be brought together by other mechanisms. Models involving monomeric receptors (including the kinetic-segregation model) may suggest that some degree of local accumulation is expected to occur upon receptor triggering, allowing receptor-bound kinases to trans-phosphorylate other receptors[122], transiently slowing molecular diffusion in regions of signal amplification. To fully understand the potential differences between the valency of signalling and inactive receptors, further studies must be conducted to understand in what contexts this possible clustering occurs. SMLFM imaging of cells treated with SFK inhibitors (e.g. the small molecule PP2[190]) may help explore whether such clusters are a consequence of signalling events. Similarly, disrupting the actin cytoskeleton using actin polymerisation inhibitors, such as latrunculin A[193], may further clarify if a non-random distribution relies on direct interactions with actin or on the presence of membrane structures generated by actin polymerisation, as predicted by the dissociation-activation and collision-coupling models[161].

## 7.3 Increased molecular height impairs BCR sensitivity to low-affinity antigens

In Chapter 4, several antigen variants were prepared for studying the effects of molecular height on BCR sensitivity to membrane antigens. The impairment of immune receptor signalling in response to increased ligand molecular height had previously been reported in TCR signalling[200,205,206], FcεRI signalling[203] and FcγR

signalling[202]. Mutants of the model antigen HEL were produced with different affinities for the HyHEL10 immunoglobulin, with some variants presenting the antigen on the surface-distal terminus of the rigid stalk of the CD43 ectodomain to increase antigen height. The response of HyHEL10-expressing primary murine B cells to antigen diffusing freely on artificial membrane systems (SLBs) was assayed. Cells responding to similar densities of low-affinity antigens with increased molecular height on SLBs displayed reduced calcium signalling compared to cells responding to equivalent HEL mutants expressed without the CD43 stalk. A significant effect was not observed in response to equivalent antigens derived from a high-affinity variant of the HEL antigen ($HEL^{RDGN}$). This effect had been previously reported for TCR responsiveness to antigens of varying affinity[200,206]. In these studies, increased molecular height only affected signalling in response to antigens with low affinity for the receptor[200,206].

In previous studies, this effect has been related to the increase in the contact size formed between cells and the apposing surface[205,206], which in turn leads to impaired steric exclusion of phosphatases with large ectodomains from these areas of contact[200,202,203,205,206]. B cells express the large phosphatases CD45[136] and CD148[128]. Expression of both molecules is not required for productive BCR signalling in response to soluble cross-linkers, with one of the phosphatase being sufficient to maintain wildtype levels of signalling in solution[128]. For B cells interacting with antigen-bearing surfaces, CD45 exclusion has been shown to occur at sites of antigen accumulation[139,179], although no functional significance has been ascribed to this observation. The results observed are therefore congruent with the kinetic-segregation model of receptor signalling, where exclusion of phosphatases permits the initiation and propagation of tyrosine phosphorylation events at sites of contact

between apposing surfaces[195]. Increased molecular height has been consistently reported to affect phosphatase exclusion[200,202,203,205,206] but, as has been previously suggested, the effects of antigen height on molecular force are not fully understood, and this cannot be discounted as a confounding factor[356]. Another potential mechanism confounding this observation is impaired binding due to a decrease in 2D affinity, as previously suggested for the binding of adhesion molecules by Milstein and colleagues[357]. The effect of phosphatase exclusion on receptor signalling is often validated using experiments in which phosphatases that have truncated ectodomains[134,202] or small ectodomains from other proteins[134,203] are expressed, and their inhibition of receptor signalling compared to that of the wildtype protein overexpressed to the same levels. Similar experiments could be conducted on transduced primary mouse B cells, but substantial attempts to transduce primary B cells with retroviral constructs in this study were unsuccessful (not shown).

Molecular height and phosphatase exclusion are important considerations in B-cell activation which have been mostly overlooked. Membrane antigens are presented to B cells in association with several types of receptors in various cell types. Complement- and antibody-bound antigens, often present in high-avidity immune complexes, can be presented to B cells via FcγRIIb and the CR3 receptors in dendritic cells or via FcγRIIb and CR1/CR2 in FDCs[23], with the latter playing a key role in B-cell activation. Antigen presented on the CR1 and CR2 complement receptors on FDCs can be retained on the surface of these cells for extended periods of time after antigen exposure, supporting B-cell activation and germinal centre retention[277]. Both these molecules are very lengthy polypeptides with large contour lengths, but it is not evident whether these form rigid ectodomains, with solution data suggesting such molecules contain

substantial interdomain flexibility and may be able to adopt more compact conformations[358,359]. As such, it is not clear whether such complexes could enter B cell-FDC contacts, predicted to be stabilised by integrin interactions[181,360], although it has been suggested that folded CR1 may be required in contact sites for some of its functions in myeloid cells[361]. It is also unclear what effect presentation of antigen on such molecules could have on phosphatase exclusion, and whether the role of antigen avidity in the context of immune complexes may permit for signalling to occur in that case. Future work could focus on whether phosphatase exclusion occurs in more physiological models of antigen presentation as previously suggested (thesis of Martin Wilcock[297]), and whether this increases the affinity threshold for B-cell activation in response to cognate antigen.

The early observation that cross-linking antibodies in solution can induce signalling in B cells[163] has been re-confirmed by many studies that suggest a role for antigen valency *in vitro* and *in vivo* (Section 1.5.1). It is therefore feasible that phosphatase exclusion is not strictly required for signalling to occur in response to multimeric antigens, or that it does not perturb responsiveness for antigens at higher affinities, as observed in Chapter 4. However, phosphatase exclusion and its effect in controlling the sensitivity to antigens at lower affinity ranges may be an important contributor to B-cell activation. In this context, phosphatase exclusion may be a requirement for signalling in B cells with unmutated receptors, and the differential expression of phosphatases across B-cell subsets may have a role in their varied functions. In particularly, B1 B cells express high levels of the larger[134] CD148 phosphatase[133], which would be more readily excluded from close contacts, and could therefore enhance responsiveness to low-affinity antigens. Although an important role for CD148 has already been reported

for B1 B cell responsiveness in T-cell-independent activation[130], its role in B1 B cell responses to membrane antigens has not been characterised. This could be an important factor in their function, as B1 B cells are responsible for the production of largely unmutated (and likely to be low-affinity[362]) natural antibodies against autologous membrane antigens, including phospholipids, which play a role in the clearance of apoptotic vesicles[363]. Conversely, if mechanisms of antigen presentation, particularly presentation by complement receptors, de-sensitise cell signalling in response to lower affinity antigens in secondary/tertiary lymphoid organs, this may be an important factor in increasing the affinity threshold for B-cell responsiveness, ensuring the recruitment of higher-affinity B cell clones into the immune response[79]. As such, investigating the role of phosphatase function across B-cell subsets and in the context of various modes of antigen presentation may provide important insight into the mechanisms fine-tuning affinity selection.

## 7.4 Purified BCR complexes for cryo-EM structure determination

The results presented in Chapter 5 describe the purification of intact IgM BCR complexes from mammalian cell membranes. The successful isolation of complexes extracted using soluble binders yielded two complexes that can be used for structure determination. Purification using receptor-bound SpyCatcher molecules or through a high-affinity antigen bound to the complex was undertaken. This project initially sought to determine two distinct cryo-EM structures from these two complexes to investigate whether conformational changes occur to the IgM BCR complex upon ligand binding.

However, since the conclusion of the work described in Chapter 5, three structures have been determined for murine and human IgM BCRs[97–99], along with the structure of a human IgG BCR[98]. All BCR complexes used in these studies were purified in the absence of cognate antigen and represent the unligated state of the complex. These structures have extensively characterised the interactions in the transmembrane and extracellular regions of the IgM heavy chain and the CD79 chains of the complex, defining the basis of receptor assembly. They have thus confirmed that the IgM and IgG BCR complexes are stable as monomers[97–99].

The purification, in experiments described in Section 5.3.5, of an assembled human IgM BCR receptor ligated *in situ* to a cognate antigen was followed by the collection of promising preliminary cryo-EM data (conducted by Lukas Sušac, Goethe University Frankfurt). This line of inquiry could lead to the determination of the structure of an antigen-bound BCR complex, for comparison with the structures of the published human IgM BCR complexes[97,98]. This is facilitated by several factors arising from coincidental similarities in the experimental design. Both studies used receptors incorporating the variable regions of the mature VRC01 antibody[97,98], derived from the clone used in this study. VRC01 and its germline precursor $VRC01_{GL}$ have similar structures, including in the antigen-contacting loops[165]. Both structures were determined for complexes incorporated into GDN micelles[97,98], as is the case for the eOD-GT8-bound $VRC01_{GL}$ IgM complex used in this work. As such, the comparison of the ligated BCR complex presented in this work and the published structures could provide information about allosteric modifications to the receptor upon ligand binding.

Several theories of BCR signalling presuppose that antigen binding events extracellularly are translated to the intracellular milieu via conformational rearrangements in the BCR molecule. For example, this is predicted by the dissociation-activation model, with suggestions that monovalent antigen in solution can open auto-inhibited BCR clusters, even in solution[178]. The mechanism by which conformational changes would occur in response to soluble antigens is difficult to conceive. As has been previously argued by Liu and colleagues[26], crystal structures of Fab molecules in the presence and absence of antigen in solution do not seem to show conformational rearrangements beyond the variable regions[364], which would preclude conformational changes being translated to the membrane-proximal domains. This information has already been explored for the system used in this study. Comparisons of the crystal structure of unbound $VRC01_{GL}$ Fab with that of the Fab bound to an earlier iteration of the eOD immunogen (eOD-GT6, which has eleven mutations compared to eOD-GT8[313]) have been conducted by Jardine and colleagues[165]. This revealed that no conformational rearrangements occur in the heavy chain, and only minor conformational adaptations occur in the Fab Vκ domain upon eOD-GT6 binding[165]. It has also been shown that B cells transgenically expressing $VRC01_{GL}$ IgM BCR chains cannot respond to eOD-GT6 in solution, but display calcium responses to soluble trimeric and 60-meric eOD-GT6[165]. Together with other studies suggesting that monomeric antigen is expected to be non-activatory in solution[163,166], this poses a key limitation on the comparison of an eventual eOD-GT8-bound receptor structure to those already published, as it does not exclude the possibility that conformational changes may occur under activating conditions. Nevertheless, such a comparison could rule out the existence of allosteric modifications of receptor structure upon ligand

binding and impose structural constraints on signalling in response to monomeric soluble antigen.

The differential response to monomeric antigen when in solution or when coordinated on a surface has led to suggestions that this is explained by the presence of forces acting on the receptor in the latter setting[26,167,186,187,350]. Proposed models suggest intermolecular clustering occurs upon binding to surface-immobilised antigens, via the exposure of previously occluded epitopes in the Cμ4 domain, or the membrane-proximal Cγ3 in IgG[26,350]. The prediction that homotypic interactions occur between receptors in certain conditions, as predicted by the conformation-induced oligomerisation and the dissociation-activation models, can be recontextualised with the publication of the human IgM BCR structures[97,98]. It has been suggested by Tolar and Pierce[365] that the interaction displayed between Cμ2 and Cμ3-Cμ4 in the resting IgM BCR links Fab arm motion and the conformation of the membrane-proximal domains, so that Fc domain rearrangements can occur when Fab arms bind antigen, as recently suggested by FRET-based studies[187]. The limitations to receptor-receptor binding in the resting state (as predicted by the dissociation-activation model) are implicit in the comparison drawn by Ma and colleagues[98] between the IgM Fc region in the IgM BCR and pentameric soluble IgM. In pentameric IgM, interacting Fc regions associate via disulphide bonds formed between Cμ3 domains (largely incompatible with subsequent dissociation) or via the FG loops present in the Cμ4 domain[366]. Ma and colleagues have suggested that, in their structure, the Cμ4 FG loop, involved in these homotypic interactions in the soluble pentamer[307], interacts with the FG loop of the CD79A ectodomain in a similar manner. As this possible dimerising interface is occupied in their unstimulated receptor structure, it further complicates the formation

of large receptor assemblies in the resting state. As such, extensive homotypic interactions via the Fc domain in IgM BCRs are very unlikely in the resting state, posing a constraint on the self-assembly of the receptor as discussed in Section 7.2. It remains possible that, in some contexts (including in the presence of force), rearrangement of the CD79A-CD79B ectodomains with respect to the Fc region allows for this interaction to occur. Observations that truncated receptors containing Cμ4 domains only can still spontaneously cluster when assembled with CD79A[167] suggest that this clustering effect could occur in fully assembled BCR molecules interacting with surface antigens.

The continuous exertion of force on individual receptors in solution prior to vitrification is not yet technological feasible. However, advances in the determination of the structures of individual molecules on membrane surfaces using cryo-electron tomography[367] (cryo-ET) may one day allow *in situ* structure determination of BCR complexes on B cells interacting with surfaces of interest.

## 7.5 Purified FcεRI complexes for cryo-EM structure determination

Following the protocols established for BCR purification, the work in Chapter 6 described the purification of fully assembled FcεRI complexes from mammalian cells. These complexes were extracted using several different soluble proteins, allowing FcεRI isolation in several states. These included two complexes purified in the absence of the receptor ligand, the IgE Fc domain, and one complex extracted using this ligand.

### 7.5.1 Extraction of ligated FcεRI complexes and preliminary cryo-EM analysis

Taking advantage of the high-affinity interaction between Fcε and its receptor ($K_D$~0.1-1nM[220]), intact ligated complexes labelled at the cell surface could be purified from mammalian cells. Purified complexes, predominantly monodispersed, could be imaged under cryogenic conditions using electron microscopy (conducted by Lukas Sušac, Goethe University Frankfurt). Class averages from 2D classification of particles selected from micrographs revealed that these likely represent monomeric units of the ligand-receptor complex, recapitulating the 1:1 binding stoichiometry previously defined for this assembly[220,368]. This promising work by collaborators in the Tampé group will be continued, and will hopefully be used to generate a structural model of the assembly of the tetrameric $\alpha\beta\gamma_2$ complex[116]. This would not only characterise for the first time interchain interactions, previously predicted by indirect methods[338], but would help validate the interactions between the FcεRIα ectodomain and IgE in the context of the assembled complex. Moreover, as mentioned in Chapter 6, this may also provide some insights into the assembly of other Fc receptors containing the $\gamma_2$ signalling homodimer, which may share conserved transmembrane interactions with FcεRI[338].

### 7.5.2 Differential states of unbound and bound FcεRI

An unexpected observation arising from the purification of these complexes was that they appeared to behave differently in SEC experiments. In the case of SpyCatcher-bound complexes, different species of varying molecular weight were observed by SEC, in marked contrast with the Fcε-bound complex, which predominantly eluted as a single species. Receptors extracted using a Fab-Halo fragment that bound to an epitope on FcεRIα distinct from the ligand-binding site were similarly found to contain a broad

distribution of various molecular weight species, albeit unresolvable by SEC. This difference between receptor behaviour in the presence or absence of ligand had not been observed for BCR purifications. The protocols used to extract both forms of the complex were identical, and the complexes were extracted from cells derived from the same cell culture, which would preclude any variation due to experimental perturbations.

Two possible explanations for this effect can be suggested. Both involve the presence of higher-order assemblies of the complex in the resting state. In scenario (1), the receptor exists in several states, but only its monomeric state can bind the Fcε fragment. In such a scenario, soluble molecules that do not bind the ligand-binding site can bind to multiple forms of the receptor, while Fcε labelling is limited to the monomeric form of the receptor. Scenario (2) is one in which the ligand-binding site allows for transient homotypic interactions, which are mutually exclusive from receptor binding. In this case, the receptor would exist in an equilibrium of monomers and higher-valency species, but upon ligand binding the receptor would exist as a monomer. Both these scenarios rely on a shared interface for homodimerization and ligand binding, or on an allosteric mechanism.

Early studies had suggested that the FcεRI receptor may exist in an equilibrium of monomers and other assemblies of the complex[238,369]. This was partly fuelled by the observation that some anti-FcεRIα antibodies can cause extensive receptor aggregation[369], which should not be possible for bivalent binders ligating individual receptors. Investigations into the stoichiometry of the receptor on the cell surface has since been undertaken for the FcεRI complex using fluorescence microscopy.

Invariably[252,370–373], these studies have focused on imaging and quantifying the stoichiometry and diffusion of receptors bound to IgE, with super-resolution studies overwhelmingly reporting a randomly distributed FcεRI-Fcε assembly[252,370]. This is in accordance with the biochemical and cryo-EM data presented in Chapter 6. These studies may have perturbed any self-assembly present in the absence of IgE through their choice of ligand. Nevertheless, their characterisation of the stoichiometry of the IgE-bound receptor, as the minimal antigen-responding unit of the receptor (Section 1.6.4), is essential for our understanding of receptor signalling.

The existence of potential equilibria of different receptor states has been reported for other immune receptors. The transmembrane co-stimulatory molecule CD80 has been shown to form dimers, with structures determined by X-ray crystallography predicting this to be mediated via hydrophobic interactions[374]. Resonance energy transfer studies have been used to validate this, with BRET studies suggesting that CD80 likely exists as a mixture of monomers and higher-order species[375] and FRET assays confirming homotypic receptor interactions[376,377]. In the case of Fc receptors, most ectodomain structures have been determined, and largely comprise similar structures that crystalise as monomers[378]. This is also the case for the reported crystal structure of the FcεRIα ectodomain, which is monomeric even in the absence of Fcε binding[368]. One notable exception is the ectodomain of the low-affinity IgG receptor, FcγRIIa. Although the receptor ectodomain can be crystallised as a monomer[378,379], crystal structures of homodimers have been characterised[380], which can be disrupted upon IgG binding[379], in a similar manner to scenario (2) described above. However, other studies have suggested this is an artefact of molecular packing within crystals, and so the stoichiometry of the receptor is unclear[378].

The nature of the IgE-FcεRIα interaction may help elucidate the structural principles by which such an interaction could occur. The ligand binding surface of FcεRIα is highly hydrophobic, and by shielding this interface self-association could be an energetically favourable reaction in a similar way to ligand binding[220]. Importantly, such interactions may occur in solution even if they do not occur on the cell surface, with potential interactions between molecules occurring in orientations which would not be permissible on the cell surface, or comprising *trans* interactions between molecules in different micelles, driven by hydrophobicity, with no physiological relevance. As such, cryo-EM analysis of SpyCatcher-bound or 22E7-bound forms of the complex could help elucidate whether such higher forms of the complex exist in cells and what their architecture suggests about the formation of this assembly.

The existence of such higher-order forms of the complex in solubilised complexes, if confirmed, must be validated by measurements on receptors at the cell surface. Several microscopy techniques can be used to determine the extent of protein-protein interactions at the cell surface. Methods such as single-molecule two-colour coincidence tracking can be used to determine homodimer formation[381,382], and similar labelling approaches could be used to characterise higher-order forms of the receptor using fluorescence cross-correlation spectroscopy (FCCS), as recently described[383]. Conversely, the use of energy resonance transfer experiments in cell lines expressing differently tagged forms of the complex could also help elucidate the stoichiometry of the receptor in resting state, as described above for CD80 homodimerisation verification in living cells[375,376]. Conducting such experiments in the presence and absence of IgE would help elucidate whether scenario (2) applies in

living cells. Imaging experiment using either IgE or non-ligand blocking proteins (SpyCatcher or the 22E7 Fab-Halo) as imaging probes may reveal whether such assemblies exist but cannot be bound by IgE, as in scenario (1).

As described above, the possibility that the higher molecular weight species represent *bona fide* receptor assemblies requires further confirmation. However, it is important to consider whether such an effect would have important implications for FcεRI signalling. The possible dissociation of FcεRI molecules upon ligand binding is not dissimilar to that predicted for dissociation-based models of BCR signalling (Section 1.5). However, as explained in the Introduction, receptor signalling in response to antigen *in vivo* is driven by the long-lived FcεRI-IgE assembly maintained on the cell surface. Except in the case of cytokinergic antibodies, monomeric IgE cannot induce signalling in solution[203,370,384] (Section 1.6.4), and as such any dissociation event cannot be expected to cause signalling, but merely to create the receptor-immunoglobulin signalling unit that drives antigen recognition. The observation that FcεRI-IgE assemblies are largely individual units according to SEC and cryo-EM analysis is consistent with reports from super-resolution microscopy-based studies, and wholly congruent with models which predict monomeric receptors to drive FcεRI signalling. These include the cross-linking model and the kinetic-segregation model, both of which have been shown to play a role in FcεRI signalling to multivalent antigen in solution[203,370,384] and monovalent membrane antigens[203], respectively (Section 1.6.4). Investigating the potential role of possible self-assembly of unbound receptors in cell function will have to await both verification of this effect and the characterisation of the molecular interactions driving it. Such assemblies can then be perturbed by mutagenesis to investigate what effects these may have on events that

are affected by IgE binding in the resting state, including receptor internalisation and recycling[222].

Together, understanding both the structure of fully assembled FcεRI complexes and their dynamics before or after IgE binding may help inform the design of blocking therapeutics that do not permit IgE binding to effector cells in allergic disease, without risking adverse effects driven by receptor ligation.

## 7.6 Summary of observations and their implications for signalling

The results discussed in this chapter have important implications for models of receptor signalling.

For BCR signalling, the presence of some regions of increased BCR density in primary resting B cells observed in Chapter 3 poses some constraints on models of BCR signalling (section 7.2). Further experiments where tonic signalling is inhibited are required to assess whether the non-random distribution observed in some cases may reflect a snapshot of receptor accumulation caused by transient signalling events in the resting B cells (section 7.2). The observation that molecular height disrupts BCR sensitivity to low-affinity antigens is consistent with a role for large phosphatase exclusion in signalling to membrane antigens. As discussed in section 7.3, this result was not observed at higher antigen affinities, and as such phosphatase segregation may help govern the range of affinities B cells can respond to. This observation also suggests investigating BCR signalling in physiological settings of antigen presentation to B cells, which can depend on several different receptors of varied length, may provide further information on whether these regulate B-cell sensitivity to antigen

(section 7.3). The ongoing structural work described in section 7.4 is being undertaken to determine the structure of an antigen-bound human IgM BCR complex. This structure could be directly compared to published structures of the IgM BCR. This comparison may help clarify whether any allosteric modifications occur upon antigen binding, and whether such structural rearrangements occur upon binding to soluble monomeric antigen binding, as implicitly predicted by the dissociation-activation model (section 1.5.3). Any potential modifications to the Fc region interactions with the CD79 heterodimer may also help predict how such modifications may occur in conformational-change based models of BCR signalling.

The work discussed in section 7.6 seeks to determine the mechanism of assembly of the FcεRI complex and has provided initial solution information pertaining to the valency of the receptor in the presence or absence of antigen. Solution data has suggested that the antigen-responsive FcεRI-IgE assembly contains a single receptor-ligand pair, consistent with previous observation and with the models of receptor signalling previously proposed. Initial observations of higher molecular weight forms of the receptor in the absence of IgE have suggested that different stoichiometries may exist, but the function of these IgE-free receptors is likely limited to homeostatic processes. As such, the existence of these states, if confirmed, is not directly relevant to antigen-driven events.

## 7.7 Concluding remarks

The work described in this thesis sought to characterise the organisation and function of two ITAM-containing receptors, in particular the B-cell receptor (BCR). The use of membrane protein purification methods for cryo-EM sample preparation established

a platform for the isolation of other immune receptors. This has allowed preliminary observations of the features of individual receptor molecules and will hopefully allow a fuller characterisation of these molecules close to the atomic level. As cryo-EM will be used to study the architecture of these receptors in solution (Chapters 5 and 6), three-dimensional super-resolution microscopy methods such as those implemented in Chapter 3 were used to contextualise the BCR molecule in its native distribution at the cell membrane of naïve B cells. The mechanisms by which these receptors respond to monomeric ligands were elucidated with the use of functional assays in which the biophysical properties of antigens could be manipulated (Chapter 4). As such, this work has focused on the molecular determinants of BCR complex signalling, by exploring the intramolecular and intermolecular properties of the receptor in the resting state and following antigen exposure.

# Appendices

## Appendix A. Supplementary Figures

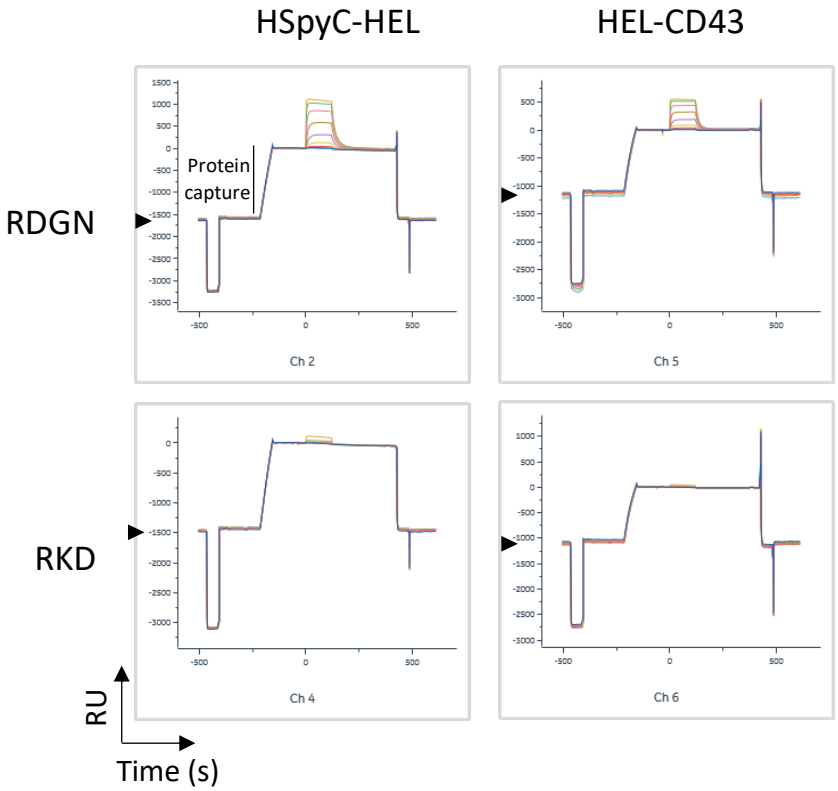



**Figure S1 | HEL capture on nickelated SPR chips.** Loading of HEL proteins onto NTA nickel chips for SPR. The total amount of protein bound to the chip (y-axis, RU) is represented by the difference in RU between the baseline (black arrow) and the surface prior to analyte injection (which has been normalised to zero). HEL capture is notably lower for HEL-CD43 proteins (black arrows, right panels) compared to HSpyC-HEL proteins (black arrows, left panels). Example data from an individual SPR run.

| | Human | | | | | Mouse | | | |
|---|---|---|---|---|---|---|---|---|---|
| | FcγRI | FcγRIIa | FcγRIIb | FcγRIIIa | FcγRIIIb | FcγRI | FcγRIIb | FcγRIII | FcγRIV |
| IgG1 | | | | | | | | | |
| IgG2 | | | | | | | | | |
| IgG3 | | | | | | | | | |
| IgG4 | | | | | | | | | |

**Supplementary Table 1 | Binding of Fc receptors to IgG antibody isotypes in mouse and human.** Immunoglobulin:FcR interactions with detectable binding are shaded green. There is no murine IgG4 isotype. Table adapted from Castro-Dopico and Clatworthy, 2019[385].

## Appendix B. Sequences of proteins used in this work

Protein sequences of proteins expressed and purified throughout this Thesis. For heterodimeric proteins, both chain sequences are listed. All signal peptide sequences are italicised and underlined and are not included in the final protein. All sequences are finished with (*) to denote where a stop codon was introduced.

### CHAPTER 3

**B1. HM79b Fab-Halo** (anti-mouse CD79b$^{262}$)

Heavy chain

*Modified cPTPRσSP*-HM79b VH-hamster Cγ1-GSGSG linker-HaloTag-GSGSG linker-HPC4 CTag

*MGILPSPGMPALLSLVSLLSVLLMGCVAGT*EVRLLESGGGLVKPEGSLKLSCVASGFTFSDYFM
SWVRQAPGKGLEWVAHIYTKSYNYATYYSGSVKGRFTISRDDSRRMLYLQMSNLRTEDTA
TYYCMDGSYGYWGQGTMVTVSSATTTAPSVYPLAPACDSTTSTTDTVTLGCLVKGYFPEPV
TVSWNSGALTSGVHTFPSVLHSGLYSLSSSVTVPSSTWPKQPITCNVAHPASSTKVDKKIEP
RTDTDTGSGSGEIGTGFPFDPHYVEVLGERMHYVDVGPRDGTPVLFLHGNPTSSYVWRNII
PHVAPTHRCIAPDLIGMGKSDKPDLGYFFDDHVRFMDAFIEALGLEEVVLVIHDWGSALGF
HWAKRNPERVKGIAFMEFIRPIPTWDEWPEFARETFQAFRTTDVGRKLIIDQNVFIEGTLP
MGVVRPLTEVEMDHYREPFLNPVDREPLWRFPNELPIAGEPANIVALVEEYMDWLHQSPV
PKLLFWGTPGVLIPPAEAARLAKSLPNCKAVDIGPGLNLLQEDNPDLIGSEIARWLSTLEISG
GSGSGEDQVDPRLIDGK*

Light chain

*Modified cPTPRσSP*-HM79b Vλ-hamster Cλ

*MGILPSPGMPALLSLVSLLSVLLMGCVAGT*QSILTQPPSISESLGSTARLTCTLRSGISVGNKNI
YWYQQMAGSAPRLFLYFFSNSDKELGPGVPNRVSGSKDTSKNAANLQISDLQVEDEAVYYC
SIYESNAYVFGSGTQLTVLGGPKSSPKVTVFPPSPEELRTNKATLVCLVNDFYPGSATVTWK
ANGATINDGVKTTKPSKQGQNYMTSSYLSLTADQWKSHNRVSCQVTHEGETVEKSLSPAE
CL*

**B2. 30F11 Fab-Halo** (anti-mouse CD45$^{263}$)

Heavy chain

*Modified cPTPRσSP*-30F11 VH-mouse Cγ1-GSGSG linker-HaloTag-GSGSA linker-TwinStrep

*MGILPSPGMPALLSLVSLLSVLLMGCVAGT*QVQLLQSGGGLVQPGRSLKLSCLASGFIFSNYGM
NWIRQAPGKGLEWVASISSTSSYIQYADTVKGRFTISRENAKNTLYLQMTSLISEDTALYYC
ARHGGYGYKGIWFAYWGQGTLVTVSSAKTTPPSVYPLAPGSAAQTNSMVTLGCLVKGYFP
EPVTVTWNSGSLSSGVHTFPAVLQSDLYTLSSSVTVPSSTWPSETVTCNVAHPASSTKVDK
KIVPRDCGKGSGSGEIGTGFPFDPHYVEVLGERMHYVDVGPRDGTPVLFLHGNPTSSYVWR
NIIPHVAPTHRCIAPDLIGMGKSDKPDLGYFFDDHVRFMDAFIEALGLEEVVLVIHDWGSAL
GFHWAKRNPERVKGIAFMEFIRPIPTWDEWPEFARETFQAFRTTDVGRKLIIDQNVFIEGT
LPMGVVRPLTEVEMDHYREPFLNPVDREPLWRFPNELPIAGEPANIVALVEEYMDWLHQS
PVPKLLFWGTPGVLIPPAEAARLAKSLPNCKAVDIGPGLNLLQEDNPDLIGSEIARWLSTLEI
SGGSGSAWSHPQFEKGGGSGGGSGGSAWSHPQFEK*

Light chain

*Modified cPTPRσSP*-30F11 Vκ-mouse Cκ

*MGILPSPGMPALLSLVSLLSVLLMGCVAGT*DIQLTQSPKSMSMSVGERVTLTCKASENVVTYV
SWYQQKPEQSPKLLIYGASNRYTGVPDRFTGSGSATDFTLTISSVQAEDLADYHCGQGYSYP
YTFGGGTKLEIKRADAAPTVSIFPPSSEQLTSGGASVVCFLNNFYPKDINVKWKIDGSERQN
GVLNSWTDQDSKDSTYSMSSTLTLTKDEYERHNSYTCEATHKTSTSPIVKSFNRNEC*

**CHAPTER 4**

**B3. HSpyC-HEL$^{WT}$** (based on HEL variants from Fleire and colleagues$^{180}$)

*cPTPRσSP*-2x6His-GSGSG linker-HaloTag-GSGSG linker-SpyCatcher3-GSSGS linker-HEL$^{WT}$

*MGILPSPGMPALLSLVSLLSVLLMGCVAE*HHHHHHSRAWRHPQFGGHHHHHHGSGSGEIGT
GFPFDPHYVEVLGERMHYVDVGPRDGTPVLFLHGNPTSSYVWRNIIPHVAPTHRCIAPDLI
GMGKSDKPDLGYFFDDHVRFMDAFIEALGLEEVVLVIHDWGSALGFHWAKRNPERVKGIA
FMEFIRPIPTWDEWPEFARETFQAFRTTDVGRKLIIDQNVFIEGTLPMGVVRPLTEVEMDH
YREPFLNPVDREPLWRFPNELPIAGEPANIVALVEEYMDWLHQSPVPKLLFWGTPGVLIPP
AEAARLAKSLPNCKAVDIGPGLNLLQEDNPDLIGSEIARWLSTLEISGGSGSGGAMVTTLSGL
SGEQGPSGDMTTEEDSATHIKFSKRDEDGRELAGATMELRDSSGKTISTWISDGHVKDFYL
YPGKYTFVETAAPDGYEVATPIEFTVNEDGQVTVDGEATEGDAHTGSSGSKVFGRCELAAA
MKRHGLDNYRGYSLGNWVCVAKFESNFNTQATNRNTDGSTDYGILQINSRWWCNDGRTP
GSRNLCNIPCSALLSSDITASVNCAKKIVSDGNGMSAWVAWRNRCKGTDVQAWIRGCRL*

**B4. HSpyC-HEL$^{RDGN}$** (based on HEL variants from Fleire and colleagues[180])

*cPTPRσSP*-2x6His-GSGSG linker-HaloTag-GSGSG linker-SpyCatcher3-GSSGS linker-HEL$^{RDGN}$ (mutant residues in red)

*MGILPSPGMPALLSLVSLLSVLLMGCVAE*HHHHHHSRAWRHPQFGGHHHHHHGSGSGEIGT
GFPFDPHYVEVLGERMHYVDVGPRDGTPVLFLHGNPTSSYVWRNIIPHVAPTHRCIAPDLI
GMGKSDKPDLGYFFDDHVRFMDAFIEALGLEEVVLVIHDWGSALGFHWAKRNPERVKGIA
FMEFIRPIPTWDEWPEFARETFQAFRTTDVGRKLIIDQNVFIEGTLPMGVVRPLTEVEMDH
YREPFLNPVDREPLWRFPNELPIAGEPANIVALVEEYMDWLHQSPVPKLLFWGTPGVLIPP
AEAARLAKSLPNCKAVDIGPGLNLLQEDNPDLIGSEIARWLSTLEISGGSGSGGAMVTTLSGL
SGEQGPSGDMTTEEDSATHIKFSKRDEDGRELAGATMELRDSSGKTISTWISDGHVKDFYL
YPGKYTFVETAAPDGYEVATPIEFTVNEDGQVTVDGEATEGDAHTGSSGSKVFGRCELAAA
MKRHGLDNYAGYSLGNWVCVAKFESNFNTQATNRNTDGSTDYGILQINSRWWCNDGRTP
GSRNLCNIPCSALLSSDITASVNCAKKIVSAAAGMSAWVAWRNRCKGTDVQAWIRGCRL*

**B5. HSpyC-HEL$^{KD}$** (based on HEL variants from Fleire and colleagues[180])

*cPTPRσSP*-2x6His-GSGSG linker-HaloTag-GSGSG linker-SpyCatcher3-GSSGS linker-HEL$^{KD}$ (mutant residues in red)

*MGILPSPGMPALLSLVSLLSVLLMGCVAE*HHHHHHSRAWRHPQFGGHHHHHHGSGSGEIGT
GFPFDPHYVEVLGERMHYVDVGPRDGTPVLFLHGNPTSSYVWRNIIPHVAPTHRCIAPDLI
GMGKSDKPDLGYFFDDHVRFMDAFIEALGLEEVVLVIHDWGSALGFHWAKRNPERVKGIA
FMEFIRPIPTWDEWPEFARETFQAFRTTDVGRKLIIDQNVFIEGTLPMGVVRPLTEVEMDH
YREPFLNPVDREPLWRFPNELPIAGEPANIVALVEEYMDWLHQSPVPKLLFWGTPGVLIPP
AEAARLAKSLPNCKAVDIGPGLNLLQEDNPDLIGSEIARWLSTLEISGGSGSGGAMVTTLSGL
SGEQGPSGDMTTEEDSATHIKFSKRDEDGRELAGATMELRDSSGKTISTWISDGHVKDFYL
YPGKYTFVETAAPDGYEVATPIEFTVNEDGQVTVDGEATEGDAHTGSSGSKVFGRCELAAA
MKRHGLDNYRGYSLGNWVCVAKFESNFNTQATNRNTDGSTDYGILQINSRWWCNDGRTP
GSRNLCNIPCSALLSSDITASVNCAKAIVSAGNGMSAWVAWRNRCKGTDVQAWIRGCRL*

**B6. HSpyC-HEL$^{RKD}$** (based on HEL variants from Fleire and colleagues[180])

*cPTPRσSP*-2x6His-GSGSG linker-HaloTag-GSGSG linker-SpyCatcher3-GSSGS linker-HEL$^{RKD}$ (mutant residues in red)

*MGILPSPGMPALLSLVSLLSVLLMGCVAE*HHHHHHSRAWRHPQFGGHHHHHHGSGSGEIGT
GFPFDPHYVEVLGERMHYVDVGPRDGTPVLFLHGNPTSSYVWRNIIPHVAPTHRCIAPDLI
GMGKSDKPDLGYFFDDHVRFMDAFIEALGLEEVVLVIHDWGSALGFHWAKRNPERVKGIA
FMEFIRPIPTWDEWPEFARETFQAFRTTDVGRKLIIDQNVFIEGTLPMGVVRPLTEVEMDH
YREPFLNPVDREPLWRFPNELPIAGEPANIVALVEEYMDWLHQSPVPKLLFWGTPGVLIPP
AEAARLAKSLPNCKAVDIGPGLNLLQEDNPDLIGSEIARWLSTLEISGGSGSGGAMVTTLSGL
SGEQGPSGDMTTEEDSATHIKFSKRDEDGRELAGATMELRDSSGKTISTWISDGHVKDFYL
YPGKYTFVETAAPDGYEVATPIEFTVNEDGQVTVDGEATEGDAHTGSSGSKVFGRCELAAA
MKRHGLDNYAGYSLGNWVCVAKFESNFNTQATNRNTDGSTDYGILQINSRWWCNDGRTP
GSRNLCNIPCSALLSSDITASVNCAKAIVSAGNGMSAWVAWRNRCKGTDVQAWIRGCRL*

**B7. HEL$^{RDGN}$-hCD43** (based on HEL variants from Fleire and colleagues[180])

*cPTPRσSP*- HEL$^{RDGN}$ (mutant residues in red)-GSGSG linker-HaloTag-GSGSG linker-hCD43(EC)-2x6His

*MGILPSPGMPALLSLVSLLSVLLMGCVAE*KVFGRCELAAAMKRHGLDNYAGYSLGNWVCVA
KFESNFNTQATNRNTDGSTDYGILQINSRWWCNDGRTPGSRNLCNIPCSALLSSDITASVN
CAKKIVSAAAGMSAWVAWRNRCKGTDVQAWIRGCRLGSGSGEIGTGFPFDPHYVEVLGER
MHYVDVGPRDGTPVLFLHGNPTSSYVWRNIIPHVAPTHRCIAPDLIGMGKSDKPDLGYFFD
DHVRFMDAFIEALGLEEVVLVIHDWGSALGFHWAKRNPERVKGIAFMEFIRPIPTWDEWP
EFARETFQAFRTTDVGRKLIIDQNVFIEGTLPMGVVRPLTEVEMDHYREPFLNPVDREPLW
RFPNELPIAGEPANIVALVEEYMDWLHQSPVPKLLFWGTPGVLIPPAEAARLAKSLPNCKA
VDIGPGLNLLQEDNPDLIGSEIARWLSTLEISGGSGSGTSTTAVQTPTSGEPLVSTSEPLSSKM
YTTSITSDPKADSTGDQTSALPPSTSINEGSPLWTSIGASTGSPLPEPTTYQEVSIKMSSVPQE
TPHATSHPAVPITANSLGSHTVTGGTITTNSPETSSRTSGAPVTTAASSLETSRGTSGPPLTM
ATVSLETSKGTSGPPVTMATDSLETSTGTTGPPVTMTTGSLEPSSGASGPQVSSVKLSTMMS
PTTSTNASTVPFRNPDENSRHHHHHHSRAWRHPQFGGHHHHHH*

**B8. HEL$^{RKD}$-hCD43** (based on HEL variants from Fleire and colleagues[180])

*cPTPRσSP*- HEL$^{RKD}$ (mutant residues in red)-GSGSG linker-HaloTag-GSGSG linker-hCD43(EC)-2x6His

*MGILPSPGMPALLSLVSLLSVLLMGCVAE*KVFGRCELAAAMKRHGLDNYAGYSLGNWVCVA
KFESNFNTQATNRNTDGSTDYGILQINSRWWCNDGRTPGSRNLCNIPCSALLSSDITASVN
CAKAIVSAGNGMSAWVAWRNRCKGTDVQAWIRGCRLGSGSGEIGTGFPFDPHYVEVLGER
MHYVDVGPRDGTPVLFLHGNPTSSYVWRNIIPHVAPTHRCIAPDLIGMGKSDKPDLGYFFD
DHVRFMDAFIEALGLEEVVLVIHDWGSALGFHWAKRNPERVKGIAFMEFIRPIPTWDEWP
EFARETFQAFRTTDVGRKLIIDQNVFIEGTLPMGVVRPLTEVEMDHYREPFLNPVDREPLW
RFPNELPIAGEPANIVALVEEYMDWLHQSPVPKLLFWGTPGVLIPPAEAARLAKSLPNCKA
VDIGPGLNLLQEDNPDLIGSEIARWLSTLEISGGSGSGTSTTAVQTPTSGEPLVSTSEPLSSKM
YTTSITSDPKADSTGDQTSALPPSTSINEGSPLWTSIGASTGSPLPEPTTYQEVSIKMSSVPQE
TPHATSHPAVPITANSLGSHTVTGGTITTNSPETSSRTSGAPVTTAASSLETSRGTSGPPLTM
ATVSLETSKGTSGPPVTMATDSLETSTGTTGPPVTMTTGSLEPSSGASGPQVSSVKLSTMMS
PTTSTNASTVPFRNPDENSRHHHHHHSRAWRHPQFGGHHHHHH*

**B9. HH10 Fab** (anti-HEL[386])

Heavy chain

*Mouse IGHV3-08*01 leader*-HH10 VH-mouse Cγ1-GSGSA linker-TwinStrep

*MMVLSLLYLLTALPGILS*DVQLQESGPSLVKPSQTLSLTCSVTGDSITSDYWSWIRKFPGNRL
EYMGYVSYSGSTYYNPSLKSRISITRDTSKNQYYLDLNSVTTEDTATYYCANWDGDYWGQG
TLVTVSAAKTTPPSVYPLAPGSAAQTNSMVTLGCLVKGYFPEPVTVTWNSGSLSSGVHTFP
AVLQSDLYTLSSSVTVPSSTWPSETVTCNVAHPASSTKVDKKIVPRDCGKGSGSAWSHPQF
EKGGGSGGGSGGSAWSHPQFEK*

Light chain

*Mouse IGKV5-43*01 leader*-HH10 Vκ-mouse Cκ

*MVFTPQILGLMLFWISASRG*DIVLTQSPATLSVTPGNSVSLSCRASQSIGNNLHWYQQKSHES
PRLLIKYASQSISGIPSRFSGSGSGTDFTLSINSVETEDFGMYFCQQSNSWPYTFGGGTKLEIK
RADAAPTVSIFPPSSEQLTSGGASVVCFLNNFYPKDINVKWKIDGSERQNGVLNSWTDQDS
KDSTYSMSSTLTLTKDEYERHNSYTCEATHKTSTSPIVKSFNRNEC*

**CHAPTER 5**

**B10. VRC01$_{GL}$ hIgM polyprotein** (anti-HIV gp120$^{165}$)

*Human IGHV1-2*02 leader*-SpyTag3-SGGGSG linker-TEV protease site-GGSGESGSG linker-VRC01$_{GL}$ VH-membrane hIgM heavy chain (IGHM)-GSG linker-F2A-*hCD79aSP*-hCD79a-GSG linker-T2A-*hCD79bSP*-hCD79b-GSG linker-E2A-*human IGKV3-11*01 leader*-VRC01$_{GL}$ Vκ-hIgκ constant domain

*MDWTWRILFLVAAATGAHS*MGRGVPHIVMVDAYKRYKSGGGSGENLYFQGGSGESGSGQV
QLVQSGAEVKKPGASVKVSCKASGYTFTGYYMHWVRQAPGQGLEWMGWINPNSGGTNYA
QKFQGRVTMTRDTSISTAYMELSRLRSDDTAVYYCARGKNSDYNWDFQHWGQGTLVTVS
SGSASAPTLFPLVSCENSPSDTSSVAVGCLAQDFLPDSITFSWKYKNNSDISSTRGFPSVLRG
GKYAATSQVLLPSKDVMQGTDEHVVCKVQHPNGNKEKNVPLPVIAELPPKVSVFVPPRDG
FFGNPRKSKLICQATGFSPRQIQVSWLREGKQVGSGVTTDQVQAEAKESGPTTYKVTSTLTI
KESDWLGQSMFTCRVDHRGLTFQQNASSMCVPDQDTAIRVFAIPPSFASIFLTKSTKLTCLV
TDLTTYDSVTISWTRQNGEAVKTHTNISESHPNATFSAVGEASICEDDWNSGERFTCTVTH
TDLPSPLKQTISRPKGVALHRPDVYLLPPAREQLNLRESATITCLVTGFSPADVFVQWMQR
GQPLSPEKYVTSAPMPEPQAPGRYFAHSILTVSEEEWNTGETYTCVVAHEALPNRVTERTV
DKSTEGEVSADEEGFENLWATASTFIVLFLLSLFYSTTVTLFKVKGSGVKQTLNFDLLKLAG
DVESNPGP*MPGGPGVLQALPATIFLLFLLSAVYLGPGCQA*LWMHKVPASLMVSLGEDAHFQC
PHNSSNNANVTWWRVLHGNYTWPPEFLGPGEDPNGTLIIQNVNKSHGGIYVCRVQEGNES
YQQSCGTYLRVRQPPPRPFLDMGEGTKNRIITAEGIILLFCAVVPGTLLLFRKRWQNEKLGL
DAGDEYEDENLYEGLNLDDCSMYEDISRGLQGTYQDVGSLNIGDVQLEKPGSGEGRGSLLT
CGDVEENPGP*MARLALSPVPSHWMVALLLLLSAEPVPA*ARSEDRYRNPKGSACSRIWQSPR
FIARKRGFTVKMHCYMNSASGNVSWLWKQEMDENPQQLKLEKGRMEESQNESLATLTIQ
GIRFEDNGIYFCQQKCNNTSEVYQGCGTELRVMGFSTLAQLKQRNTLKDGIIMIQTLLIILFII
VPIFLLLDKDDSKAGMEEDHTYEGLDIDQTATYEDIVTLRTGEVKWSVGEHPGQEGSGQCT
NYALLKLAGDVESNPGP*MEAPAQLLFLLLLWLPDTTG*EIVLTQSPATLSLSPGERATLSCRAS
QSVSSYLAWYQQKPGQAPRLLIYDASNRATGIPARFSGSGSGTDFTLTISSLEPEDFAVYYCQ
QYEFFGQGTKLEIKRTVAAPSVFIFPPSDEQLKSGTASVVCLLNNFYPREAKVQWKVDNAL
QSGNSQESVTEQDSKDSTYSLSSTLTLSKADYEKHKVYACEVTHQGLSSPVTKSFNRGEC*

**B11. 6His-SpyC3-CTag** (SpyTag binding protein$^{289}$)

MGSS linker-6His-GSSGS linker-SpyCatcher3-GSSGS linker-HPC4 CTag

MGSSHHHHHHGSSGSGAMVTTLSGLSGEQGPSGDMTTEEDSATHIKFSKRDEDGRELAGA
TMELRDSSGKTISTWISDGHVKDFYLYPGKYTFVETAAPDGYEVATPIEFTVNEDGQVTVD
GEATEGDAHTGSSGSEDQVDPRLIDGK*

**B12. Polatuzumab Fab** (anti-hCD79b[322])

Heavy chain

*Modified cPTPRσSP*-Pola VH-mouse Cγ1-GGSGSG linker-HPC4 CTag

*MGILPSPGMPALLSLVSLLSVLLMGCVAGT*EVQLVESGGGLVQPGGSLRLSCAASGYTFSSYWI
EWVRQAPGKGLEWIGEILPGGGDTNYNEIFKGRATFSADTSKNTAYLQMNSLRAEDTAVY
YCTRRVPIRLDYWGQGTLVTVSSAKTTPPSVYPLAPGSAAQTNSMVTLGCLVKGYFPEPVT
VTWNSGSLSSGVHTFPAVLQSDLYTLSSSVTVPSSTWPSETVTCNVAHPASSTKVDKKIVPR
DCGKGGSGSGEDQVDPRLIDGK*

Light chain

*Modified cPTPRσSP*-Pola Vκ-mouse Cκ

*MGILPSPGMPALLSLVSLLSVLLMGCVAGT*DIQLTQSPSSLSASVGDRVTITCKASQSVDYEGD
SFLNWYQQKPGKAPKLLIYAASNLESGVPSRFSGSGSGTDFTLTISSLQPEDFATYYCQQSNE
DPLTFGQGTKVEIKRADAAPTVSIFPPSSEQLTSGGASVVCFLNNFYPKDINVKWKIDGSER
QNGVLNSWTDQDSKDSTYSMSSTLTLTKDEYERHNSYTCEATHKTSTSPIVKSFNRNEC*

**B13. 6His-SpyC3-TwinStrep** (SpyTag binding protein[289])

MGSS linker-6His-GSSGS linker-SpyCatcher3-GSSGSA linker-TwinStrep

MGSSHHHHHHGSSGSGAMVTTLSGLSGEQGPSGDMTTEEDSATHIKFSKRDEDGRELAGA
TMELRDSSGKTISTWISDGHVKDFYLYPGKYTFVETAAPDGYEVATPIEFTVNEDGQVTVD
GEATEGDAHTGSSGSAWSHPQFEKGGGSGGGSGGSAWSHPQFEK*

**B14. eOD-GT8 2x6His-TwinStrep** (VRC01c antibody-binding immunogen[313])

*Modified hCD5SP*-eOD-GT8-GSG linker-2x6His-GSGSA linker-TwinStrep

*MPMGSLQPLATLYLLGMLVASVLA*DTITLPCRPAPPPHCSSNITGLILTRQGGYSNDNTVIFR
PSGGDWRDIARCQIAGTVVSTQLFLNGSLAEEEVVIRSEDWRDNAKSICVQLNTSVEINCTG
AGHCNISRAKWNNTLKQIASKLREQYGNKTIIFKPSSGGDPEFVNHSFNCGGEFFYCDSTQL
FNSTWFNSTGSGHHHHHHSRARRHPQFGGHHHHHHGSGSAWSHPQFEKGGGSGGGSGGS
AWSHPQFEK*

## CHAPTER 6

**B15. hFcεRI EGFP(T65S) polyprotein** (EGFP(T65S) by Sušac, Vuong and colleagues[240])

*hFcεRIαSP*-SpyTag3-SGGGSG linker-TEV protease site-GGSGESGSG linker-hFcεRIα-GSG linker-F2A-hFcεRIβ- GSG linker-T2A- *hFcεRIγSP*-hFcεRIγ-DPPVAT linker-EGFP(T65S)

*MAPAMESPTLLCVALLFFAPDGVLA*MGRGVPHIVMVDAYKRYKSGGGSGENLYFQGGSGES
GSGVPQKPKVSLNPPWNRIFKGENVTLTCNGNNFFEVSSTKWFHNGSLSEETNSSLNIVNA
KFEDSGEYKCQHQQVNESEPVYLEVFSDWLLLQASAEVVMEGQPLFLRCHGWRNWDVYK
VIYYKDGEALKYWYENHNISITNATVEDSGTYYCTGKVWQLDYESEPLNITVIKAPREKYW
LQFFIPLLVVILFAVDTGLFISTQQQVTFLLKIKRTRKGFRLLNPHPKPNPKNNGSGVKQTLN
FDLLKLAGDVESNPGPMDTESNRRANLALPQEPSSVPAFEVLEISPQEVSSGRLLKSASSPPL
HTWLTVLKKEQEFLGVTQILTAMICLCFGTVVCSVLDISHIEGDIFSSFKAGYPFWGAIFFSIS
GMLSIISERRNATYLVRGSLGANTASSIAGGTGITILIINLKKSLAYIHIHSCQKFFETKCFMAS
FSTEIVVMMLFLTILGLGSAVSLTICGAGEELKGNKVPEDRVYEELNIYSATYSELEDPGEMS
PPIDLGSGEGRGSLLTCGDVEENPGP*MIPAVVLLLLLLVEQAAA*LGEPQLCYILDAILFLYGIVL
TLLYCRLKIQVRKAAITSYEKSDGVYTGLSTRNQETYETLKHEKPPQDPPVATMVSKGEELF
TGVVPILVELDGDVNGHKFSVSGEGEGDATYGKLTLKFICTTGKLPVPWPTLVTTLSYGVQC
FSRYPDHMKQHDFFKSAMPEGYVQERTIFFKDDGNYKTRAEVKFEGDTLVNRIELKGIDFK
EDGNILGHKLEYNYNSHNVYIMADKQKNGIKVNFKIRHNIEDGSVQLADHYQQNTPIGDGP
VLLPDNHYLSTQSALSKDPNEKRDHMVLLEFVTAAGITLGMDELYK*

**B16. Fcε(C225A)-6His-TwinStrep** (based on design by Wan and collagues[336])

*Human IGHV1-2*02 leader*-hIgE Fc (C225A mutation)-6His-GSGSA linker-TwinStrep

*MDWTWRILFLVAAATGAHS*VASRDFTPPTVKILQSSCDGGGHFPPTIQLLCLVSGYTPGTINI
TWLEDGQVMDVDLSTASTTQEGELASTQSELTLSQKHWLSDRTYTCQVTYQGHTFEDSTK
KCADSNPRGVSAYLSRPSPFDLFIRKSPTITCLVVDLAPSKGTVNLTWSRASGKPVNHSTRK
EEKQRNGTLTVTSTLPVGTRDWIEGETYQCRVTHPHLPRALMRSTTKTSGPRAAPEVYAF
ATPEWPGSRDKRTLACLIQNFMPEDISVQWLHNEVQLPDARHSTTQPRKTKGSGFFVFSR
LEVTRAEWEQKDEFICRAVHEAASPSQTVQRAVSVNPGKHHHHHHGSGSAWSHPQFEKG
GGSGGGSGGSAWSHPQFEK*

**B17. 22E7 Fab-Halo** (anti-hFcεRIα[348,349])

Heavy chain

*Modified cPTPRσSP*-22E7 VH-mouse Cγ1-GSGSG linker-HaloTag-GSGSG linker-12His-GSGSA linker-TwinStrep

*MGILPSPGMPALLSLVSLLSVLLMGCVAGT*EVKLVESGGGLVKPGGSLKLSCAASGFTFSSYG
MSWVRQTPEKRLEWVATISGGNNYTFYPDNLKGRFTISRDNAKNILYLQISSLRSVDTALY
YCASLWYRASFAYWGQGTLVTVSSAKTTPPSVYPLAPGSAAQTNSMVTLGCLVKGYFPEPV
TVTWNSGSLSSGVHTFPAVLQSDLYTLSSSVTVPSSTWPSETVTCNVAHPASSTKVDKKIVP
RDCGKGSGSGEIGTGFPFDPHYVEVLGERMHYVDVGPRDGTPVLFLHGNPTSSYVWRNIIP
HVAPTHRCIAPDLIGMGKSDKPDLGYFFDDHVRFMDAFIEALGLEEVVLVIHDWGSALGFH
WAKRNPERVKGIAFMEFIRPIPTWDEWPEFARETFQAFRTTDVGRKLIIDQNVFIEGTLPM
GVVRPLTEVEMDHYREPFLNPVDREPLWRFPNELPIAGEPANIVALVEEYMDWLHQSPVP
KLLFWGTPGVLIPPAEAARLAKSLPNCKAVDIGPGLNLLQEDNPDLIGSEIARWLSTLEISGG
SGSGHHHHHHHHHHHHGSGSAWSHPQFEKGGGSGGGSGGSAWSHPQFEK*

Light chain

*Modified cPTPRσSP*-22E7 Vκ-mouse Cκ

*MGILPSPGMPALLSLVSLLSVLLMGCVAGT*DIMMTQSPSSMYASLGERVTITCKASQDINSYLS
WFQQKPGKSPKTLISRANRLVDGVPSRFSGSGSGQDYSLTISSLEYEDMGIYYCLQYDDFPFT
FGGGTKLEIKRADAAPTVSIFPPSSEQLTSGGASVVCFLNNFYPKDINVKWKIDGSERQNGV
LNSWTDQDSKDSTYSMSSTLTLTKDEYERHNSYTCEATHKTSTSPIVKSFNRNEC*

# References


1. Valentine, J. W., Collins, A. G. & Meyer, C. P. Morphological complexity increase in metazoans. *Paleobiology* **20**, 131–142 (1994).
2. Caballero-Flores, G., Pickard, J. M. & Núñez, G. Microbiota-mediated colonization resistance: mechanisms and regulation. *Nat. Rev. Microbiol.* (2022) doi:10.1038/s41579-022-00833-7.
3. Byrd, A. L., Belkaid, Y. & Segre, J. A. The human skin microbiome. *Nat. Rev. Microbiol.* **16**, 143–155 (2018).
4. Mandujano-Tinoco, E. A., Sultan, E., Ottolenghi, A., Gershoni-Yahalom, O. & Rosental, B. Evolution of Cellular Immunity Effector Cells; Perspective on Cytotoxic and Phagocytic Cellular Lineages. *Cells* **10**, 1853 (2021).
5. Flajnik, M. F. & Kasahara, M. Origin and evolution of the adaptive immune system: genetic events and selective pressures. *Nat. Rev. Genet.* **11**, 47–59 (2010).
6. Paul, W. E. Bridging Innate and Adaptive Immunity. *Cell* **147**, 1212–1215 (2011).
7. Hoffmann, J. & Akira, S. Innate immunity. *Curr. Opin. Immunol.* **25**, 1–3 (2013).
8. Medzhitov, R. Toll-like receptors and innate immunity. *Nat. Rev. Immunol.* **1**, 135–145 (2001).
9. Geijtenbeek, T. B. H. & Gringhuis, S. I. Signalling through C-type lectin receptors: shaping immune responses. *Nat. Rev. Immunol.* **9**, 465–479 (2009).
10. Chan, Y. K. & Gack, M. U. Viral evasion of intracellular DNA and RNA sensing. *Nat. Rev. Microbiol.* **14**, 360–373 (2016).

11. Akira, S., Uematsu, S. & Takeuchi, O. Pathogen Recognition and Innate Immunity. *Cell* **124**, 783–801 (2006).
12. McNab, F., Mayer-Barber, K., Sher, A., Wack, A. & O'Garra, A. Type I interferons in infectious disease. *Nat. Rev. Immunol.* **15**, 87–103 (2015).
13. Westman, J., Grinstein, S. & Marques, P. E. Phagocytosis of Necrotic Debris at Sites of Injury and Inflammation. *Front. Immunol.* **10**, 3030 (2020).
14. Shishido, S. N., Varahan, S., Yuan, K., Li, X. & Fleming, S. D. Humoral innate immune response and disease. *Clin. Immunol.* **144**, 142–158 (2012).
15. Trouw, L. A., Pickering, M. C. & Blom, A. M. The complement system as a potential therapeutic target in rheumatic disease. *Nat. Rev. Rheumatol.* **13**, 538–547 (2017).
16. Underhill, D. M. & Goodridge, H. S. Information processing during phagocytosis. *Nat. Rev. Immunol.* **12**, 492–502 (2012).
17. Nathan, C. Neutrophils and immunity: challenges and opportunities. *Nat. Rev. Immunol.* **6**, 173–182 (2006).
18. Voehringer, D. Protective and pathological roles of mast cells and basophils. *Nat. Rev. Immunol.* **13**, 362–375 (2013).
19. Guilliams, M. *et al.* Dendritic cells, monocytes and macrophages: a unified nomenclature based on ontogeny. *Nat. Rev. Immunol.* **14**, 571–578 (2014).
20. Davies, L. C., Jenkins, S. J., Allen, J. E. & Taylor, P. R. Tissue-resident macrophages. *Nat. Immunol.* **14**, 986–995 (2013).
21. Kapsenberg, M. L. Dendritic-cell control of pathogen-driven T-cell polarization. *Nat. Rev. Immunol.* **3**, 984–993 (2003).
22. Ginhoux, F. & Jung, S. Monocytes and macrophages: developmental pathways and tissue homeostasis. *Nat. Rev. Immunol.* **14**, 392–404 (2014).

23. Batista, F. D. & Harwood, N. E. The who, how and where of antigen presentation to B cells. *Nat. Rev. Immunol.* **9**, 15–27 (2009).

24. Nemazee, D. Receptor editing in lymphocyte development and central tolerance. *Nat. Rev. Immunol.* **6**, 728–740 (2006).

25. Joglekar, A. V. & Li, G. T cell antigen discovery. *Nat. Methods* **18**, 873–880 (2021).

26. Liu, W., Sohn, H. W., Tolar, P. & Pierce, S. K. It's All About Change: The Antigen-driven Initiation of B-Cell Receptor Signaling. *Cold Spring Harb. Perspect. Biol.* **2**, a002295–a002295 (2010).

27. Dong, D. *et al.* Structural basis of assembly of the human T cell receptor–CD3 complex. *Nature* **573**, 546–552 (2019).

28. Morath, A. & Schamel, W. W. αβ and γδ T cell receptors: Similar but different. *J. Leukoc. Biol.* **107**, 1045–1055 (2020).

29. Shah, K., Al-Haidari, A., Sun, J. & Kazi, J. U. T cell receptor (TCR) signaling in health and disease. *Signal Transduct. Target. Ther.* **6**, 412 (2021).

30. De Libero, G. & Mori, L. Recognition of lipid antigens by T cells. *Nat. Rev. Immunol.* **5**, 485–496 (2005).

31. Joffre, O. P., Segura, E., Savina, A. & Amigorena, S. Cross-presentation by dendritic cells. *Nat. Rev. Immunol.* **12**, 557–569 (2012).

32. Golstein, P. & Griffiths, G. M. An early history of T cell-mediated cytotoxicity. *Nat. Rev. Immunol.* **18**, 527–535 (2018).

33. Swain, S. L., McKinstry, K. K. & Strutt, T. M. Expanding roles for CD4+ T cells in immunity to viruses. *Nat. Rev. Immunol.* **12**, 136–148 (2012).

34. Rothenberg, E. V., Moore, J. E. & Yui, M. A. Launching the T-cell-lineage developmental programme. *Nat. Rev. Immunol.* **8**, 9–21 (2008).

35. Meffre, E., Casellas, R. & Nussenzweig, M. C. Antibody regulation of B cell development. *Nat. Immunol.* **1**, 379–385 (2000).

36. Schamel, W. W. A. & Reth, M. Monomeric and Oligomeric Complexes of the B Cell Antigen Receptor. *Immunity* **13**, 5–14 (2000).

37. Yancopoulos, G. D. & Alt, F. W. Regulation of the Assembly and Expression of Variable-Region Genes. *Annu. Rev. Immunol.* **4**, 339–368 (1986).

38. Lu, L. L., Suscovich, T. J., Fortune, S. M. & Alter, G. Beyond binding: antibody effector functions in infectious diseases. *Nat. Rev. Immunol.* **18**, 46–61 (2018).

39. Cyster, J. G. & Allen, C. D. C. B Cell Responses: Cell Interaction Dynamics and Decisions. *Cell* **177**, 524–540 (2019).

40. Schroeder, H. W. & Cavacini, L. Structure and function of immunoglobulins. *J. Allergy Clin. Immunol.* **125**, S41–S52 (2010).

41. Bosselut, R. T cell antigen recognition: Evolution-driven affinities. *Proc. Natl. Acad. Sci.* **116**, 21969–21971 (2019).

42. Schatz, D. G. & Ji, Y. Recombination centres and the orchestration of V(D)J recombination. *Nat. Rev. Immunol.* **11**, 251–263 (2011).

43. Bétermier, M., Bertrand, P. & Lopez, B. S. Is Non-Homologous End-Joining Really an Inherently Error-Prone Process? *PLoS Genet.* **10**, e1004086 (2014).

44. Jackson, K. J., Gaeta, B., Sewell, W. & Collins, A. M. Exonuclease activity and P nucleotide addition in the generation of the expressed immunoglobulin repertoire. *BMC Immunol.* **5**, 19 (2004).

45. Glanville, J. *et al.* Precise determination of the diversity of a combinatorial antibody library gives insight into the human immunoglobulin repertoire. *Proc. Natl. Acad. Sci.* **106**, 20216–20221 (2009).

46. Rudikoff, S., Pawlita, M., Pumphrey, J. & Heller, M. Somatic diversification of immunoglobulins. *Proc. Natl. Acad. Sci.* **81**, 2162–2166 (1984).

47. Dalod, M., Chelbi, R., Malissen, B. & Lawrence, T. Dendritic cell maturation: functional specialization through signaling specificity and transcriptional programming. *EMBO J.* **33**, 1104–1116 (2014).

48. Reis, E. S., Mastellos, D. C., Hajishengallis, G. & Lambris, J. D. New insights into the immune functions of complement. *Nat. Rev. Immunol.* **19**, 503–516 (2019).

49. Worbs, T., Hammerschmidt, S. I. & Förster, R. Dendritic cell migration in health and disease. *Nat. Rev. Immunol.* **17**, 30–48 (2017).

50. Krummel, M. F., Bartumeus, F. & Gérard, A. T cell migration, search strategies and mechanisms. *Nat. Rev. Immunol.* **16**, 193–201 (2016).

51. Carsetti, R. The Development of B Cells in the Bone Marrow Is Controlled by the Balance between Cell-Autonomous Mechanisms and Signals from the Microenvironment. *J. Exp. Med.* **191**, 5–8 (2000).

52. Cambier, J. C., Gauld, S. B., Merrell, K. T. & Vilen, B. J. B-cell anergy: from transgenic models to naturally occurring anergic B cells? *Nat. Rev. Immunol.* **7**, 633–643 (2007).

53. Engel, I. & Murre, C. The function of E- and id proteins in lymphocyte development. *Nat. Rev. Immunol.* **1**, 193–199 (2001).

54. Patton, D. T., Plumb, A. W. & Abraham, N. The Survival and Differentiation of Pro-B and Pre-B Cells in the Bone Marrow Is Dependent on IL-7Rα Tyr449. *J. Immunol.* **193**, 3446–3455 (2014).

55. Nagata, K. *et al.* The Igα/Igβ Heterodimer on μ-Negative ProB Cells Is Competent for Transducing Signals to Induce Early B Cell Differentiation. *Immunity* **7**, 559–570 (1997).

56. Gong, S. & Nussenzweig, M. C. Regulation of an Early Developmental Checkpoint in the B Cell Pathway by Igβ. *Science* **272**, 411–414 (1996).

57. Bosticardo, M., Pala, F. & Notarangelo, L. D. RAG deficiencies: Recent advances in disease pathogenesis and novel therapeutic approaches. *Eur. J. Immunol.* **51**, 1028–1038 (2021).

58. Rickert, R. C. New insights into pre-BCR and BCR signalling with relevance to B cell malignancies. *Nat. Rev. Immunol.* **13**, 578–591 (2013).

59. Nemazee, D. Mechanisms of central tolerance for B cells. *Nat. Rev. Immunol.* **17**, 281–294 (2017).

60. Rowland, S. L., Leahy, K. F., Halverson, R., Torres, R. M. & Pelanda, R. BAFF Receptor Signaling Aids the Differentiation of Immature B Cells into Transitional B Cells following Tonic BCR Signaling. *J. Immunol.* **185**, 4570–4581 (2010).

61. Mackay, F. & Browning, J. L. BAFF: A fundamental survival factor for B cells. *Nat. Rev. Immunol.* **2**, 465–475 (2002).

62. Baumgarth, N. The double life of a B-1 cell: self-reactivity selects for protective effector functions. *Nat. Rev. Immunol.* **11**, 34–46 (2011).

63. Cerutti, A., Cols, M. & Puga, I. Marginal zone B cells: virtues of innate-like antibody-producing lymphocytes. *Nat. Rev. Immunol.* **13**, 118–132 (2013).

64. Zhang, Z. *et al.* Notch-RBP-J-Independent Marginal Zone B Cell Development in IgH Transgenic Mice with VH Derived from a Natural Polyreactive Antibody. *PLoS ONE* **7**, e38894 (2012).

65. Racine, R. & Winslow, G. M. IgM in microbial infections: Taken for granted? *Immunol. Lett.* **125**, 79–85 (2009).

66. Heesters, B. A., van der Poel, C. E., Das, A. & Carroll, M. C. Antigen Presentation to B Cells. *Trends Immunol.* **37**, 844–854 (2016).

67. Pape, K. A., Catron, D. M., Itano, A. A. & Jenkins, M. K. The Humoral Immune Response Is Initiated in Lymph Nodes by B Cells that Acquire Soluble Antigen Directly in the Follicles. *Immunity* **26**, 491–502 (2007).

68. Bournazos, S., Wang, T. T., Dahan, R., Maamary, J. & Ravetch, J. V. Signaling by Antibodies: Recent Progress. *Annu. Rev. Immunol.* **35**, 285–311 (2017).

69. Phan, T. G., Grigorova, I., Okada, T. & Cyster, J. G. Subcapsular encounter and complement-dependent transport of immune complexes by lymph node B cells. *Nat. Immunol.* **8**, 992–1000 (2007).

70. Heesters, B. A. *et al.* Endocytosis and Recycling of Immune Complexes by Follicular Dendritic Cells Enhances B Cell Antigen Binding and Activation. *Immunity* **38**, 1164–1175 (2013).

71. Aung, A. *et al.* Low protease activity in B cell follicles promotes retention of intact antigens after immunization. *Science* **379**, eabn8934 (2023).

72. Qi, H., Egen, J. G., Huang, A. Y. C. & Germain, R. N. Extrafollicular Activation of Lymph Node B Cells by Antigen-Bearing Dendritic Cells. *Science* **312**, 1672–1676 (2006).

73. Vos, Q., Lees, A., Zheng-Qi, W., Snapper, C. M. & Mond, J. J. B-cell activation by T-cell-independent type 2 antigens as an integral part of the humoral immune response to pathogenic microorganisms. *Immunol. Rev.* **176**, 154–170 (2000).

74. Young, R. M. & Staudt, L. M. Targeting pathological B cell receptor signalling in lymphoid malignancies. *Nat. Rev. Drug Discov.* **12**, 229–243 (2013).

75. Yuseff, M.-I., Pierobon, P., Reversat, A. & Lennon-Duménil, A.-M. How B cells capture, process and present antigens: a crucial role for cell polarity. *Nat. Rev. Immunol.* **13**, 475–486 (2013).

76. Schwickert, T. A. *et al.* A dynamic T cell–limited checkpoint regulates affinity-dependent B cell entry into the germinal center. *J. Exp. Med.* **208**, 1243–1252 (2011).

77. Luo, W., Weisel, F. & Shlomchik, M. J. B Cell Receptor and CD40 Signaling Are Rewired for Synergistic Induction of the c-Myc Transcription Factor in Germinal Center B Cells. *Immunity* **48**, 313-326.e5 (2018).

78. Olatunde, A. C., Hale, J. S. & Lamb, T. J. Cytokine-skewed Tfh cells: functional consequences for B cell help. *Trends Immunol.* **42**, 536–550 (2021).

79. De Silva, N. S. & Klein, U. Dynamics of B cells in germinal centres. *Nat. Rev. Immunol.* **15**, 137–148 (2015).

80. Nutt, S. L., Hodgkin, P. D., Tarlinton, D. M. & Corcoran, L. M. The generation of antibody-secreting plasma cells. *Nat. Rev. Immunol.* **15**, 160–171 (2015).

81. Tanaka, A., Shen, H. M., Ratnam, S., Kodgire, P. & Storb, U. Attracting AID to targets of somatic hypermutation. *J. Exp. Med.* **207**, 405–415 (2010).

82. Peperzak, V., Vikstrom, I. B. & Tarlinton, D. M. Through a glass less darkly: apoptosis and the germinal center response to antigen: Apoptosis and the GC response to antigen. *Immunol. Rev.* **247**, 93–106 (2012).

83. Slamanig, S. A. & Nolte, M. A. The Bone Marrow as Sanctuary for Plasma Cells and Memory T-Cells: Implications for Adaptive Immunity and Vaccinology. *Cells* **10**, 1508 (2021).

84. Radbruch, A. *et al.* Competence and competition: the challenge of becoming a long-lived plasma cell. *Nat. Rev. Immunol.* **6**, 741–750 (2006).

85. Akkaya, M., Kwak, K. & Pierce, S. K. B cell memory: building two walls of protection against pathogens. *Nat. Rev. Immunol.* **20**, 229–238 (2020).

86. Kurosaki, T., Kometani, K. & Ise, W. Memory B cells. *Nat. Rev. Immunol.* **15**, 149–159 (2015).

87. Lee, C. M. & Oh, J. E. Resident Memory B Cells in Barrier Tissues. *Front. Immunol.* **13**, 953088 (2022).

88. Tarlinton, D. & Good-Jacobson, K. Diversity Among Memory B Cells: Origin, Consequences, and Utility. *Science* **341**, 1205–1211 (2013).

89. Fusil, F. *et al.* A Lentiviral Vector Allowing Physiologically Regulated Membrane-anchored and Secreted Antibody Expression Depending on B-cell Maturation Status. *Mol. Ther.* **23**, 1734–1747 (2015).

90. James, L. K. B cells defined by immunoglobulin isotypes. *Clin. Exp. Immunol.* uxac091 (2022) doi:10.1093/cei/uxac091.

91. Duarte, J. H. Functional switching. *Nat. Immunol.* **17**, S12–S12 (2016).

92. Hobeika, E., Maity, P. C. & Jumaa, H. Control of B Cell Responsiveness by Isotype and Structural Elements of the Antigen Receptor. *Trends Immunol.* **37**, 310–320 (2016).

93. Xu, Z., Zan, H., Pone, E. J., Mai, T. & Casali, P. Immunoglobulin class-switch DNA recombination: induction, targeting and beyond. *Nat. Rev. Immunol.* **12**, 517–531 (2012).

94. Stavnezer, J., Guikema, J. E. J. & Schrader, C. E. Mechanism and Regulation of Class Switch Recombination. *Annu. Rev. Immunol.* **26**, 261–292 (2008).

95. Park, S.-R. *et al.* HoxC4 binds to the promoter of the cytidine deaminase AID gene to induce AID expression, class-switch DNA recombination and somatic hypermutation. *Nat. Immunol.* **10**, 540–550 (2009).

96. Phan, T. G. *et al.* B Cell Receptor–independent Stimuli Trigger Immunoglobulin (Ig) Class Switch Recombination and Production of IgG Autoantibodies by Anergic Self-Reactive B Cells. *J. Exp. Med.* **197**, 845–860 (2003).

97. Su, Q. *et al.* Cryo-EM structure of the human IgM B cell receptor. *Science* **377**, 875–880 (2022).

98. Ma, X. *et al.* Cryo-EM structures of two human B cell receptor isotypes. *Science* **377**, 880–885 (2022).

99. Dong, Y. *et al.* Structural principles of B cell antigen receptor assembly. *Nature* **612**, 156–161 (2022).

100. Radaev, S. *et al.* Structural and Functional Studies of Igαβ and Its Assembly with the B Cell Antigen Receptor. *Structure* **18**, 934–943 (2010).

101. Reth, M. Antigen receptor tail clue. *Nature* **338**, 383–384 (1989).

102. Tolar, P., Sohn, H. W. & Pierce, S. K. The initiation of antigen-induced B cell antigen receptor signaling viewed in living cells by fluorescence resonance energy transfer. *Nat. Immunol.* **6**, 1168–1176 (2005).

103. Venkitaraman, A. R., Williams, G. T., Dariavach, P. & Neuberger, M. S. The B-cell antigen receptor of the five immunoglobulin classes. *Nature* **352**, 777–781 (1991).

104. Huse, K. *et al.* Mechanism of CD79A and CD79B Support for IgM+ B Cell Fitness through B Cell Receptor Surface Expression. *J. Immunol.* **209**, 2042–2053 (2022).

105. Brouns, G. S., de Vries, E. & Borst, J. Assembly and intracellular transport of the human B cell antigen receptor complex. *Int. Immunol.* **7**, 359–368 (1995).

106. Grupp, S. A., Mitchell, R. N., Schreiber, K. L., McKean, D. J. & Abbas, A. K. Molecular mechanisms that control expression of the B lymphocyte antigen receptor complex. *J. Exp. Med.* **181**, 161–168 (1995).

107. Cambier, J. C., Pleiman, C. M. & Clark, M. R. Signal Transduction by the B Cell Antigen Receptor and its Coreceptors. *Annu. Rev. Immunol.* **12**, 457–486 (1994).

108. Geisberger, R., Crameri, R. & Achatz, G. Models of signal transduction through the B-cell antigen receptor. *Immunology* **110**, 401–410 (2003).

109. Xu, Y. *et al.* No receptor stands alone: IgG B-cell receptor intrinsic and extrinsic mechanisms contribute to antibody memory. *Cell Res.* **24**, 651–664 (2014).

110. Waisman, A. *et al.* IgG1 B cell receptor signaling is inhibited by CD22 and promotes the development of B cells whose survival is less dependent on Igα/β. *J. Exp. Med.* **204**, 747–758 (2007).

111. Martin, S. W. & Goodnow, C. C. Burst-enhancing role of the IgG membrane tail as a molecular determinant of memory. *Nat. Immunol.* **3**, 182–188 (2002).

112. Hiramoto, E. *et al.* The IgM pentamer is an asymmetric pentagon with an open groove that binds the AIM protein. *Sci. Adv.* **4**, eaau1199 (2018).

113. Kumar Bharathkar, S. *et al.* The structures of secretory and dimeric immunoglobulin A. *eLife* **9**, e56098 (2020).

114. Dunkelberger, J. R. & Song, W.-C. Complement and its role in innate and adaptive immune responses. *Cell Res.* **20**, 34–50 (2010).

115. Nimmerjahn, F. & Ravetch, J. V. Fcγ receptors as regulators of immune responses. *Nat. Rev. Immunol.* **8**, 34–47 (2008).

116. Kinet, J.-P. The high affinity IgE receptor (FcεRI): from physiology to pathology. *Annu. Rev. Immunol.* **17**, 931–972 (1999).

117. Sereda, M. J., Hartmann, S. & Lucius, R. Helminths and allergy: the example of tropomyosin. *Trends Parasitol.* **24**, 272–278 (2008).

118. Gauld, S. B. & Cambier, J. C. Src-family kinases in B-cell development and signaling. *Oncogene* **23**, 8001–8006 (2004).

119. Sato, I. *et al.* Differential trafficking of Src, Lyn, Yes and Fyn is specified by the state of palmitoylation in the SH4 domain. *J. Cell Sci.* **122**, 965–975 (2009).

120. Geahlen, R. L. Syk and pTyr'd: Signaling through the B cell antigen receptor. *Biochim. Biophys. Acta BBA - Mol. Cell Res.* **1793**, 1115–1127 (2009).

121. Aksentijevich, I. The sickening consequences of too much SYK signaling. *Nat. Genet.* **53**, 432–434 (2021).

122. Kulathu, Y., Zuern, C., Yang, J. & Reth, M. Synthetic biology of B cell activation: understanding signal amplification at the B cell antigen receptor using a rebuilding approach. *Biol. Chem.* **400**, 555–563 (2019).

123. Hermiston, M. L., Zikherman, J. & Zhu, J. W. CD45, CD148, and Lyp/Pep: critical phosphatases regulating Src family kinase signaling networks in immune cells. *Immunol. Rev.* **228**, 288–311 (2009).

124. Saijo, K. *et al.* Essential role of Src-family protein tyrosine kinases in NF-κB activation during B cell development. *Nat. Immunol.* **4**, 274–279 (2003).

125. Hibbs, M. L. *et al.* Multiple defects in the immune system of Lyn-deficient mice, culminating in autoimmune disease. *Cell* **83**, 301–311 (1995).

126. Takata, M. *et al.* Tyrosine kinases Lyn and Syk regulate B cell receptor-coupled Ca2+ mobilization through distinct pathways. *EMBO J.* **13**, 1341–1349 (1994).

127. Ingley, E. Functions of the Lyn tyrosine kinase in health and disease. *Cell Commun. Signal.* **10**, 21 (2012).

128. Zhu, J. W., Brdicka, T., Katsumoto, T. R., Lin, J. & Weiss, A. Structurally Distinct Phosphatases CD45 and CD148 Both Regulate B Cell and Macrophage Immunoreceptor Signaling. *Immunity* **28**, 183–196 (2008).

129. Horikawa, K. *et al.* Distinctive roles of Fyn and Lyn in IgD- and IgM-mediated signaling. *Int. Immunol.* **11**, 1441–1449 (1999).

130. Skrzypczynska, K. M., Zhu, J. W. & Weiss, A. Positive Regulation of Lyn Kinase by CD148 Is Required for B Cell Receptor Signaling in B1 but Not B2 B Cells. *Immunity* **45**, 1232–1244 (2016).

131. Justement, L. B., Campbell, K. S., Chien, N. C. & Cambier, J. C. Regulation of B Cell Antigen Receptor Signal Transduction and Phosphorylation by CD45. *Science* **252**, 1839–1842 (1991).

132. Hobeika, E., Nielsen, P. J. & Medgyesi, D. Signaling mechanisms regulating B-lymphocyte activation and tolerance. *J. Mol. Med.* **93**, 143–158 (2015).

133. Lin, J., Zhu, J. W., Baker, J. E. & Weiss, A. Regulated Expression of the Receptor-Like Tyrosine Phosphatase CD148 on Hemopoietic Cells. *J. Immunol.* **173**, 2324–2330 (2004).

134. Cordoba, S.-P. *et al.* The large ectodomains of CD45 and CD148 regulate their segregation from and inhibition of ligated T-cell receptor. *Blood* **121**, 4295–4302 (2013).

135. Chang, V. T. *et al.* Initiation of T cell signaling by CD45 segregation at 'close contacts'. *Nat. Immunol.* **17**, 574–582 (2016).

136. Coffman, R. L. & Weissman, I. L. B220: a B cell-specific member of the T200 glycoprotein family. *Nature* **289**, 681–683 (1981).

137. Yanagi, S. *et al.* CD45 Modulates Phosphorylation of Both Autophosphorylation and Negative Regulatory Tyrosines of Lyn in B Cells. *J. Biol. Chem.* **271**, 30487–30492 (1996).

138. Zikherman, J., Doan, K., Parameswaran, R., Raschke, W. & Weiss, A. Quantitative differences in CD45 expression unmask functions for CD45 in B-cell development, tolerance, and survival. *Proc. Natl. Acad. Sci.* **109**, (2012).

139. Depoil, D. *et al.* CD19 is essential for B cell activation by promoting B cell receptor–antigen microcluster formation in response to membrane-bound ligand. *Nat. Immunol.* **9**, 63–72 (2008).

140. Senis, Y. A., Mazharian, A. & Mori, J. Src family kinases: at the forefront of platelet activation. *Blood* **124**, 2013–2024 (2014).

141. Wen, Y. *et al.* The regulators of BCR signaling during B cell activation. *Blood Sci.* **1**, 119–129 (2019).

142. Pao, L. I. *et al.* B Cell-Specific Deletion of Protein-Tyrosine Phosphatase Shp1 Promotes B-1a Cell Development and Causes Systemic Autoimmunity. *Immunity* **27**, 35–48 (2007).

143. Fu, C., Turck, C. W., Kurosaki, T. & Chan, A. C. BLNK: a Central Linker Protein in B Cell Activation. *Immunity* **9**, 93–103 (1998).

144. Hendriks, R. W., Yuvaraj, S. & Kil, L. P. Targeting Bruton's tyrosine kinase in B cell malignancies. *Nat. Rev. Cancer* **14**, 219–232 (2014).

145. Jackson, J. T., Mulazzani, E., Nutt, S. L. & Masters, S. L. The role of PLCγ2 in immunological disorders, cancer, and neurodegeneration. *J. Biol. Chem.* **297**, 100905 (2021).

146. Lu, L. Mobilizing ER IP3 receptors as a mechanism to enhance calcium signaling. *Cell. Mol. Immunol.* **18**, 2284–2285 (2021).

147. de Gorter, D. J. J., Vos, J. C. M., Pals, S. T. & Spaargaren, M. The B Cell Antigen Receptor Controls AP-1 and NFAT Activity through Ras-Mediated Activation of Ral. *J. Immunol.* **178**, 1405–1414 (2007).

148. Schulze-Luehrmann, J. & Ghosh, S. Antigen-Receptor Signaling to Nuclear Factor κB. *Immunity* **25**, 701–715 (2006).

149. Scharenberg, A. M., Humphries, L. A. & Rawlings, D. J. Calcium signalling and cell-fate choice in B cells. *Nat. Rev. Immunol.* **7**, 778–789 (2007).

150. Fischer, K.-D., Tedford, K. & Penninger, J. M. Vav links antigen-receptor signaling to the actin cytoskeleton. *Semin. Immunol.* **10**, 317–327 (1998).

151. Weber, M. *et al.* Phospholipase C-γ2 and Vav cooperate within signaling microclusters to propagate B cell spreading in response to membrane-bound antigen. *J. Exp. Med.* **205**, 853–868 (2008).

152. Malhotra, S., Kovats, S., Zhang, W. & Coggeshall, K. M. Vav and Rac Activation in B Cell Antigen Receptor Endocytosis Involves Vav Recruitment to the Adapter Protein LAB. *J. Biol. Chem.* **284**, 36202–36212 (2009).

153. Vendramini, E. *et al.* KRAS and RAS-MAPK Pathway Deregulation in Mature B Cell Lymphoproliferative Disorders. *Cancers* **14**, 666 (2022).

154. Abdelrasoul, H., Werner, M., Setz, C. S., Okkenhaug, K. & Jumaa, H. PI3K induces B-cell development and regulates B cell identity. *Sci. Rep.* **8**, 1327 (2018).

155. Okada, T., Maeda, A., Iwamatsu, A., Gotoh, K. & Kurosaki, T. BCAP: The tyrosine kinase substrate that connects B cell receptor to Phosphoinositide 3-kinase. *Immunity* **13**, 817–827 (2000).

156. Fearon, D. T., Carroll, M. C. & Carroll, M. C. Regulation of B Lymphocyte Responses to Foreign and Self-Antigens by the CD19/CD21 Complex. *Annu. Rev. Immunol.* **18**, 393–422 (2000).

157. Dempsey, P. W., Allison, M. E. D., Akkaraju, S., Goodnow, C. C. & Fearon, D. T. C3d of Complement as a Molecular Adjuvant: Bridging Innate and Acquired Immunity. *Science* **271**, 348–350 (1996).

158. Doody, G. M. *et al.* A Role in B Cell Activation for CD22 and the Protein Tyrosine Phosphatase SHP. *Science* **269**, 242–244 (1995).

159. D'Ambrosio, D. *et al.* Recruitment and Activation of PTP1C in Negative Regulation of Antigen Receptor Signaling by FcγRIIB1. *Science* **268**, 293–297 (1995).

160. Müller, J. & Nitschke, L. The role of CD22 and Siglec-G in B-cell tolerance and autoimmune disease. *Nat. Rev. Rheumatol.* **10**, 422–428 (2014).

161. Treanor, B. B-cell receptor: from resting state to activate: Structure and dynamics of the BCR. *Immunology* **136**, 21–27 (2012).

162. Metzger, H. Transmembrane signaling: the joy of aggregation. *J. Immunol.* **149**, 1477–1487 (1992).

163. Woodruff, M. F. A., Reid, B. & James, K. Effect of Antilymphocytic Antibody and Antibody Fragments on Human Lymphocytes in vitro. *Nature* **215**, 591–594 (1967).

164. Fanger, M. W., Hart, D. A., Wells, J. V. & Nisonoff, A. Requirement for Cross-Linkage in the Stimulation of Transformation of Rabbit Peripheral Lymphocytes by Antiglobulin Reagents. *J. Immunol.* **105**, 1484–1492 (1970).

165. Jardine, J. *et al.* Rational HIV Immunogen Design to Target Specific Germline B Cell Receptors. *Science* **340**, 711–716 (2013).

166. Minguet, S., Dopfer, E.-P. & Schamel, W. W. A. Low-valency, but not monovalent, antigens trigger the B-cell antigen receptor (BCR). *Int. Immunol.* **22**, 205–212 (2010).

167. Tolar, P., Hanna, J., Krueger, P. D. & Pierce, S. K. The Constant Region of the Membrane Immunoglobulin Mediates B Cell-Receptor Clustering and Signaling in Response to Membrane Antigens. *Immunity* **30**, 44–55 (2009).

168. Gomes de Castro, M. A. *et al.* Differential organization of tonic and chronic B cell antigen receptors in the plasma membrane. *Nat. Commun.* **10**, 820 (2019).

169. Minici, C. *et al.* Distinct homotypic B-cell receptor interactions shape the outcome of chronic lymphocytic leukaemia. *Nat. Commun.* **8**, 15746 (2017).

170. Ziegler, C. G. K. *et al.* Constitutive Activation of the B Cell Receptor Underlies Dysfunctional Signaling in Chronic Lymphocytic Leukemia. *Cell Rep.* **28**, 923-937.e3 (2019).

171. Davis, R. E. *et al.* Chronic active B-cell-receptor signalling in diffuse large B-cell lymphoma. *Nature* **463**, 88–92 (2010).

172. Bachmann, M. F. & Zinkernagel, R. M. The influence of virus structure on antibody responses and virus serotype formation. *Immunol. Today* **17**, 553–558 (1996).

173. Silverman, G. J. & Goodyear, C. S. Confounding B-cell defences: lessons from a staphylococcal superantigen. *Nat. Rev. Immunol.* **6**, 465–475 (2006).

174. Kato, Y. *et al.* Multifaceted Effects of Antigen Valency on B Cell Response Composition and Differentiation In Vivo. *Immunity* **53**, 548-563.e8 (2020).

175. Avalos, A. M. *et al.* Monovalent engagement of the BCR activates ovalbumin-specific transnuclear B cells. *J. Exp. Med.* **211**, 365–379 (2014).

176. Kim, Y.-M. *et al.* Monovalent ligation of the B cell receptor induces receptor activation but fails to promote antigen presentation. *Proc. Natl. Acad. Sci.* **103**, 3327–3332 (2006).

177. Mukherjee, S. *et al.* Monovalent and Multivalent Ligation of the B Cell Receptor Exhibit Differential Dependence upon Syk and Src Family Kinases. *Sci. Signal.* **6**, ra1–ra1 (2013).

178. Volkmann, C. *et al.* Molecular requirements of the B-cell antigen receptor for sensing monovalent antigens. *EMBO J.* **35**, 2371–2381 (2016).

179. Batista, F. D., Iber, D. & Neuberger, M. S. B cells acquire antigen from target cells after synapse formation. *Nature* **411**, 489–494 (2001).

180. Fleire, S. J. *et al.* B Cell Ligand Discrimination Through a Spreading and Contraction Response. *Science* **312**, 738–741 (2006).

181. Carrasco, Y. R., Fleire, S. J., Cameron, T., Dustin, M. L. & Batista, F. D. LFA-1/ICAM-1 Interaction Lowers the Threshold of B Cell Activation by Facilitating B Cell Adhesion and Synapse Formation. *Immunity* **20**, 589–599 (2004).

182. Dustin, M. L. The Immunological Synapse. *Cancer Immunol. Res.* **2**, 1023–1033 (2014).

183. Tolar, P., Sohn, H. W., Liu, W. & Pierce, S. K. The molecular assembly and organization of signaling active B-cell receptor oligomers. *Immunol. Rev.* **232**, 34–41 (2009).

184. Natkanski, E. *et al.* B Cells Use Mechanical Energy to Discriminate Antigen Affinities. *Science* **340**, 1587–1590 (2013).

185. Kwak, K. *et al.* Intrinsic properties of human germinal center B cells set antigen affinity thresholds. *Sci. Immunol.* **3**, eaau6598 (2018).

186. Wan, Z. *et al.* The activation of IgM- or isotype-switched IgG- and IgE-BCR exhibits distinct mechanical force sensitivity and threshold. *eLife* **4**, e06925 (2015).

187. Shen, Z. *et al.* Conformational change within the extracellular domain of B cell receptor in B cell activation upon antigen binding. *eLife* **8**, e42271 (2019).

188. Yang, J. & Reth, M. The dissociation activation model of B cell antigen receptor triggering. *FEBS Lett.* **584**, 4872–4877 (2010).

189. Yang, J. & Reth, M. Oligomeric organization of the B-cell antigen receptor on resting cells. *Nature* **467**, 465–469 (2010).

190. Kläsener, K., Maity, P. C., Hobeika, E., Yang, J. & Reth, M. B cell activation involves nanoscale receptor reorganizations and inside-out signaling by Syk. *eLife* **3**, e02069 (2014).

191. Maity, P. C. *et al.* B cell antigen receptors of the IgM and IgD classes are clustered in different protein islands that are altered during B cell activation. *Sci. Signal.* **8**, ra93–ra93 (2015).

192. Mattila, P. K. *et al.* The Actin and Tetraspanin Networks Organize Receptor Nanoclusters to Regulate B Cell Receptor-Mediated Signaling. *Immunity* **38**, 461–474 (2013).

193. Treanor, B. *et al.* The Membrane Skeleton Controls Diffusion Dynamics and Signaling through the B Cell Receptor. *Immunity* **32**, 187–199 (2010).

194. Gasparrini, F. *et al.* Nanoscale organization and dynamics of the siglec CD 22 cooperate with the cytoskeleton in restraining BCR signalling. *EMBO J.* **35**, 258–280 (2016).

195. Davis, S. J. & van der Merwe, P. A. The kinetic-segregation model: TCR triggering and beyond. *Nat. Immunol.* **7**, 803–809 (2006).

196. Schmid, E. M. *et al.* Size-dependent protein segregation at membrane interfaces. *Nat. Phys.* **12**, 704–711 (2016).

197. Fernandes, R. A. *et al.* A cell topography-based mechanism for ligand discrimination by the T cell receptor. *Proc. Natl. Acad. Sci.* **116**, 14002–14010 (2019).

198. Carbone, C. B. *et al.* In vitro reconstitution of T cell receptor-mediated segregation of the CD45 phosphatase. *Proc. Natl. Acad. Sci.* **114**, E9338–E9345 (2017).

199. Sibener, L. V. *et al.* Isolation of a Structural Mechanism for Uncoupling T Cell Receptor Signaling from Peptide-MHC Binding. *Cell* **174**, 672-687.e27 (2018).

200. Al-Aghbar, M. A., Chu, Y.-S., Chen, B.-M. & Roffler, S. R. High-Affinity Ligands Can Trigger T Cell Receptor Signaling Without CD45 Segregation. *Front. Immunol.* **9**, 713 (2018).

201. Freeman, S. A. *et al.* Integrins Form an Expanding Diffusional Barrier that Coordinates Phagocytosis. *Cell* **164**, 128–140 (2016).

202. Bakalar, M. H. *et al.* Size-Dependent Segregation Controls Macrophage Phagocytosis of Antibody-Opsonized Targets. *Cell* **174**, 131-142.e13 (2018).

203. Felce, J. H. *et al.* CD45 exclusion– and cross-linking–based receptor signaling together broaden FceRI reactivity. *Sci. Signal.* 17 (2018).

204. Chen, K. Y. *et al.* Trapping or slowing the diffusion of T cell receptors at close contacts initiates T cell signaling. *Proc. Natl. Acad. Sci.* **118**, e2024250118 (2021).

205. Choudhuri, K., Wiseman, D., Brown, M. H., Gould, K. & van der Merwe, P. A. T-cell receptor triggering is critically dependent on the dimensions of its peptide-MHC ligand. *Nature* **436**, 578–582 (2005).

206. Chen, B.-M. *et al.* The Affinity of Elongated Membrane-Tethered Ligands Determines Potency of T Cell Receptor Triggering. *Front. Immunol.* **8**, 793 (2017).

207. Junghans, V. *et al.* Hydrodynamic trapping measures the interaction between membrane-associated molecules. *Sci. Rep.* **8**, 12479 (2018).

208. Son, S. *et al.* Molecular height measurement by cell surface optical profilometry (CSOP). *Proc. Natl. Acad. Sci.* **117**, 14209–14219 (2020).

209. Jimenez, A., Friedl, K. & Leterrier, C. About samples, giving examples: Optimized Single Molecule Localization Microscopy. *Methods* **174**, 100–114 (2020).

210. Cao, A. *et al.* Galectin-9 binds IgM-BCR to regulate B cell signaling. *Nat. Commun.* **9**, 3288 (2018).

211. Rossboth, B. *et al.* TCRs are randomly distributed on the plasma membrane of resting antigen-experienced T cells. *Nat. Immunol.* **19**, 821–827 (2018).

212. Baumgart, F. *et al.* Varying label density allows artifact-free analysis of membrane-protein nanoclusters. *Nat. Methods* **13**, 661–664 (2016).

213. Pageon, S. V. *et al.* Functional role of T-cell receptor nanoclusters in signal initiation and antigen discrimination. *Proc. Natl. Acad. Sci.* **113**, E5454–E5463 (2016).

214. Lillemeier, B. F. *et al.* TCR and Lat are expressed on separate protein islands on T cell membranes and concatenate during activation. *Nat. Immunol.* **11**, 90–96 (2010).

215. Burton, O. T. & Oettgen, H. C. Beyond immediate hypersensitivity: evolving roles for IgE antibodies in immune homeostasis and allergic diseases: IgE in immunity and allergy. *Immunol. Rev.* **242**, 128–143 (2011).

216. Gilfillan, A. M. & Tkaczyk, C. Integrated signalling pathways for mast-cell activation. *Nat. Rev. Immunol.* **6**, 218–230 (2006).

217. Metz, M. *et al.* Mast Cells Can Enhance Resistance to Snake and Honeybee Venoms. *Science* **313**, 526–530 (2006).

218. Gould, H. J. & Sutton, B. J. IgE in allergy and asthma today. *Nat. Rev. Immunol.* **8**, 205–217 (2008).

219. Kraft, S. & Kinet, J.-P. New developments in FcεRI regulation, function and inhibition. *Nat. Rev. Immunol.* **7**, 365–378 (2007).

220. Holdom, M. D. *et al.* Conformational changes in IgE contribute to its uniquely slow dissociation rate from receptor FcεRI. *Nat. Struct. Mol. Biol.* **18**, 571–576 (2011).

221. Stone, K. D., Prussin, C. & Metcalfe, D. D. IgE, mast cells, basophils, and eosinophils. *J. Allergy Clin. Immunol.* **125**, S73–S80 (2010).

222. Beck, L. A., Marcotte, G. V., MacGlashan Jr., D., Togias, A. & Saini, S. Omalizumab-induced reductions in mast cell FcεRI expression and function. *J. Allergy Clin. Immunol.* **114**, 527–530 (2004).

223. Boyce, J. A. Mast cells and eicosanoid mediators: a system of reciprocal paracrine and autocrine regulation. *Immunol. Rev.* **217**, 168–185 (2007).

224. Berger, S. A., Mak, T. W. & Paige, C. J. Leukocyte common antigen (CD45) is required for immunoglobulin E-mediated degranulation of mast cells. *J. Exp. Med.* **180**, 471–476 (1994).

225. Benhamou, M., Ryba, N. J., Kihara, H., Nishikata, H. & Siraganian, R. P. Protein-tyrosine kinase p72syk in high affinity IgE receptor signaling. Identification as a component of pp72 and association with the receptor gamma chain after receptor aggregation. *J. Biol. Chem.* **268**, 23318–23324 (1993).

226. Pullen, N. A., Falanga, Y. T., Morales, J. K. & Ryan, J. J. The Fyn-STAT5 Pathway: A New Frontier in IgE- and IgG-Mediated Mast Cell Signaling. *Front. Immunol.* **3**, (2012).

227. Wange, R. L. LAT, the Linker for Activation of T Cells: A Bridge Between T Cell-Specific and General Signaling Pathways. *Sci. Signal.* **2000**, (2000).

228. Turner, H. & Kinet, J.-P. Signalling through the high-affinity IgE receptor FcεRI. *Nature* **402**, 24–30 (1999).

229. Bell, K. S. *et al.* The role of individual protein kinase C isoforms in mouse mast cell function and their targeting by the immunomodulatory parasitic worm product, ES-62. *Immunol. Lett.* **168**, 31–40 (2015).

230. Metzger, H. Early Molecular Events in Antigen-Antibody Cell Activation. *Annu. Rev. Pharmacol. Toxicol.* **19**, 427–445 (1979).

231. Riske, F. *et al.* High affinity human IgE receptor (Fc epsilon RI). Analysis of functional domains of the alpha-subunit with monoclonal antibodies. *J. Biol. Chem.* **266**, 11245–11251 (1991).

232. Eckl-Dorna, J. *et al.* Allergen-Specific Antibodies Regulate Secondary Allergen-Specific Immune Responses. *Front. Immunol.* **9**, 3131 (2019).

233. Niemi, M. *et al.* Molecular Interactions between a Recombinant IgE Antibody and the β-Lactoglobulin Allergen. *Structure* **15**, 1413–1421 (2007).

234. Bax, H. J., Keeble, A. H. & Gould, H. J. Cytokinergic IgE Action in Mast Cell Activation. *Front. Immunol.* **3**, (2012).

235. Pandey, V., Mihara, S., Fensome-Green, A., Bolsover, S. & Cockcroft, S. Monomeric IgE Stimulates NFAT Translocation Into the Nucleus, a Rise in Cytosol Ca2+, Degranulation, and Membrane Ruffling in the Cultured Rat Basophilic Leukemia-2H3 Mast Cell Line. *J. Immunol.* **172**, 4048–4058 (2004).

236. Bax, H. J., Bowen, H., Dodev, T. S., Sutton, B. J. & Gould, H. J. Mechanism of the Antigen-Independent Cytokinergic SPE-7 IgE Activation of Human Mast Cells in Vitro. *Sci. Rep.* **5**, 9538 (2015).

237. Bax, H. J. *et al.* IgE Trimers Drive SPE-7 Cytokinergic Activity. *Sci. Rep.* **7**, 8164 (2017).

238. Balakrishnan, K., Hsu, F. J., Cooper, A. D. & McConnell, H. M. Lipid hapten containing membrane targets can trigger specific immunoglobulin E-dependent degranulation of rat basophil leukemia cells. *J. Biol. Chem.* **257**, 6427–6433 (1982).

239. Naldini, L. *et al.* In Vivo Gene Delivery and Stable Transduction of Nondividing Cells by a Lentiviral Vector. *Science* **272**, 263–267 (1996).

240. Sušac, L. *et al.* Structure of a fully assembled tumor-specific T cell receptor ligated by pMHC. *Cell* **185**, 3201-3213.e19 (2022).

241. The UniProt Consortium *et al.* UniProt: the Universal Protein Knowledgebase in 2023. *Nucleic Acids Res.* **51**, D523–D531 (2023).

242. Du, F. *et al.* Regulating the T7 RNA polymerase expression in E. coli BL21 (DE3) to provide more host options for recombinant protein production. *Microb. Cell Factories* **20**, 189 (2021).

243. Schmitt, J., Hess, H. & Stunnenberg, H. G. Affinity purification of histidine-tagged proteins. *Mol. Biol. Rep.* **18**, 223–230 (1993).

244. Taylor, F. B. *et al.* Protein C prevents the coagulopathic and lethal effects of Escherichia coli infusion in the baboon. *J. Clin. Invest.* **79**, 918–925 (1987).

245. Stearns, D. J., Kurosawa, S., Sims, P. J., Esmon, N. L. & Esmon, C. T. The interaction of a Ca2+-dependent monoclonal antibody with the protein C activation peptide region. Evidence for obligatory Ca2+ binding to both antigen and antibody. *J. Biol. Chem.* **263**, 826–832 (1988).

246. Schmidt, T. G. M. *et al.* The Role of Changing Loop Conformations in Streptavidin Versions Engineered for High-affinity Binding of the Strep-tag II Peptide. *J. Mol. Biol.* **433**, 166893 (2021).

247. Schmidt, T. G. & Skerra, A. The Strep-tag system for one-step purification and high-affinity detection or capturing of proteins. *Nat. Protoc.* **2**, 1528–1535 (2007).

248. Mekkaoui, L. *et al.* Lentiviral Vector Purification Using Genetically Encoded Biotin Mimic in Packaging Cell. *Mol. Ther. - Methods Clin. Dev.* **11**, 155–165 (2018).

249. Koniev, O. & Wagner, A. Developments and recent advancements in the field of endogenous amino acid selective bond forming reactions for bioconjugation. *Chem Soc Rev* **44**, 5495–5551 (2015).

250. Los, G. V. *et al.* HaloTag: A Novel Protein Labeling Technology for Cell Imaging and Protein Analysis. *ACS Chem. Biol.* **3**, 373–382 (2008).

251. Lee, J., Sengupta, P., Brzostowski, J., Lippincott-Schwartz, J. & Pierce, S. K. The nanoscale spatial organization of B-cell receptors on immunoglobulin M– and G–expressing human B-cells. *Mol. Biol. Cell* **28**, 511–523 (2017).

252. Veatch, S. L. *et al.* Correlation Functions Quantify Super-Resolution Images and Estimate Apparent Clustering Due to Over-Counting. *PLoS ONE* **7**, e31457 (2012).

253. Brameshuber, M. *et al.* Monomeric TCRs drive T cell antigen recognition. *Nat. Immunol.* **19**, 487–496 (2018).

254. Saltukoglu, D. *et al.* Plasma membrane topography governs the 3D dynamic localization of IgM B cell antigen receptor clusters. *EMBO J.* **42**, (2023).

255. Nahidiazar, L., Agronskaia, A. V., Broertjes, J., van den Broek, B. & Jalink, K. Optimizing Imaging Conditions for Demanding Multi-Color Super Resolution Localization Microscopy. *PLOS ONE* **11**, e0158884 (2016).

256. Sims, R. R. *et al.* Single molecule light field microscopy. *Optica* **7**, 1065 (2020).

257. Daly, S. *et al. High-density volumetric super-resolution microscopy*. http://biorxiv.org/lookup/doi/10.1101/2023.05.02.539032 (2023) doi:10.1101/2023.05.02.539032.

258. Beheiry, M. E. & Dahan, M. ViSP: representing single-particle localizations in three dimensions. *Nat. Methods* **10**, 689–690 (2013).

259. Takeda, A., Wu, J. J. & Maizel, A. L. Evidence for monomeric and dimeric forms of CD45 associated with a 30-kDa phosphorylated protein. *J. Biol. Chem.* **267**, 16651–16659 (1992).

260. James, J. R. *et al.* The T Cell Receptor Triggering Apparatus Is Composed of Monovalent or Monomeric Proteins. *J. Biol. Chem.* **286**, 31993–32001 (2011).

261. Sograte-Idrissi, S. *et al.* Circumvention of common labelling artefacts using secondary nanobodies. *Nanoscale* **12**, 10226–10239 (2020).

262. Haggart, R., Perera, J. & Huang, H. Cloning of a hamster anti-mouse CD79B antibody sequences and identification of a new hamster immunoglobulin lambda constant IGLC gene region. *Immunogenetics* **65**, 473–478 (2013).

263. Orozco, J. J. *et al.* Therapy of Myeloid Leukemia using Novel Bispecific Fusion Proteins Targeting CD45 and 90Y-DOTA. *Mol. Cancer Ther.* **19**, 2575–2584 (2020).

264. Mattheyses, A. L., Simon, S. M. & Rappoport, J. Z. Imaging with total internal reflection fluorescence microscopy for the cell biologist. *J. Cell Sci.* **123**, 3621–3628 (2010).

265. Ponjavic, A. *et al.* Single-Molecule Light-Sheet Imaging of Suspended T Cells. *Biophys. J.* **114**, 2200–2211 (2018).

266. Santos, A. M. *et al.* Capturing resting T cells: the perils of PLL. *Nat. Immunol.* **19**, 203–205 (2018).

267. Jung, Y. *et al.* Three-dimensional localization of T-cell receptors in relation to microvilli using a combination of superresolution microscopies. *Proc. Natl. Acad. Sci.* **113**, (2016).

268. Yoon, J. *et al.* Identification of non-activated lymphocytes using three-dimensional refractive index tomography and machine learning. *Sci. Rep.* **7**, 6654 (2017).

269. Oberdoerffer, P., Novobrantseva, T. I. & Rajewsky, K. Expression of a Targeted λ1 Light Chain Gene Is Developmentally Regulated and Independent of Igκ Rearrangements. *J. Exp. Med.* **197**, 1165–1172 (2003).

270. Kim, H.-R. *et al.* T cell microvilli constitute immunological synaptosomes that carry messages to antigen-presenting cells. *Nat. Commun.* **9**, 3630 (2018).

271. Tao, R. & Thill, J.-C. Flow Cross K-function: a bivariate flow analytical method. *Int. J. Geogr. Inf. Sci.* **33**, 2055–2071 (2019).

272. Kiskowski, M. A., Hancock, J. F. & Kenworthy, A. K. On the Use of Ripley's K-Function and Its Derivatives to Analyze Domain Size. *Biophys. J.* **97**, 1095–1103 (2009).

273. Ghosh, S. *et al.* ERM-Dependent Assembly of T Cell Receptor Signaling and Co-stimulatory Molecules on Microvilli prior to Activation. *Cell Rep.* **30**, 3434-3447.e6 (2020).

274. Dale, N. C., Johnstone, E. K. M., White, C. W. & Pfleger, K. D. G. NanoBRET: The Bright Future of Proximity-Based Assays. *Front. Bioeng. Biotechnol.* **7**, 56 (2019).

275. Broussard, J. A., Rappaz, B., Webb, D. J. & Brown, C. M. Fluorescence resonance energy transfer microscopy as demonstrated by measuring the activation of the serine/threonine kinase Akt. *Nat. Protoc.* **8**, 265–281 (2013).

276. Driscoll, M. K. *et al.* Robust and automated detection of subcellular morphological motifs in 3D microscopy images. *Nat. Methods* **16**, 1037–1044 (2019).

277. Heesters, B. A., Myers, R. C. & Carroll, M. C. Follicular dendritic cells: dynamic antigen libraries. *Nat. Rev. Immunol.* **14**, 495–504 (2014).

278. Jenkins, E. *et al.* Reconstitution of immune cell interactions in free-standing membranes. *J. Cell Sci.* jcs.219709 (2018) doi:10.1242/jcs.219709.

279. Kulenkampff, K. *et al.* The Costs of Close Contacts: Visualizing the Energy Landscape of Cell Contacts at the Nanoscale. *Biophys. J.* **118**, 1261–1269 (2020).

280. Lippert, A. H. *et al.* Soft Polydimethylsiloxane-Supported Lipid Bilayers for Studying T Cell Interactions. *Biophys. J.* **120**, 35–45 (2021).

281. Adams, C. L. *et al.* Complete analysis of the B-cell response to a protein antigen, from in vivo germinal centre formation to 3-D modelling of affinity maturation. *Immunology* **108**, 274–287 (2003).

282. van der Veen, J. N. *et al.* The critical role of phosphatidylcholine and phosphatidylethanolamine metabolism in health and disease. *Biochim. Biophys. Acta BBA - Biomembr.* **1859**, 1558–1572 (2017).

283. Müller, P., Schwille, P. & Weidemann, T. PyCorrFit—generic data evaluation for fluorescence correlation spectroscopy. *Bioinformatics* **30**, 2532–2533 (2014).

284. Politi, A. Z. *et al.* Quantitative mapping of fluorescently tagged cellular proteins using FCS-calibrated four-dimensional imaging. *Nat. Protoc.* **13**, 1445–1464 (2018).

285. Jung, C., Lee, J., Kang, M. & Kim, S. W. Measurement of the temperature-dependent diffusion properties of nanoparticles by using fluorescence correlation spectroscopy. *J. Korean Phys. Soc.* **65**, 1083–1089 (2014).

286. Mason, D. Y., Jones, M. & Goodnow, C. C. Development and follicular localization of tolerant B lymphocytes in lysozyme/anti-lysozyme lgM/lgD transgenic mice. *Int. Immunol.* **4**, 163–175 (1992).

287. Batista, F. D. & Neuberger, M. S. Affinity Dependence of the B Cell Response to Antigen: A Threshold, a Ceiling, and the Importance of Off-Rate. *Immunity* **8**, 751–759 (1998).

288. Abbott, R. K. *et al.* Precursor Frequency and Affinity Determine B Cell Competitive Fitness in Germinal Centers, Tested with Germline-Targeting HIV Vaccine Immunogens. *Immunity* **48**, 133-146.e6 (2018).

289. Keeble, A. H. *et al.* Approaching infinite affinity through engineering of peptide–protein interaction. *Proc. Natl. Acad. Sci.* **116**, 26523–26533 (2019).

290. Shelley, C. S. *et al.* Molecular characterization of sialophorin (CD43), the lymphocyte surface sialoglycoprotein defective in Wiskott-Aldrich syndrome. *Proc. Natl. Acad. Sci.* **86**, 2819–2823 (1989).

291. Cyster, J. G., Shotton, D. M. & Williams, A. F. The dimensions of the T lymphocyte glycoprotein leukosialin and identification of linear protein epitopes that can be modified by glycosylation. *EMBO J.* **10**, 893–902 (1991).

292. Lavoie, T. B. *et al.* Structural differences among monoclonal antibodies with distinct fine specicities and kinetic properties. *Mol. Immunol.* (1999).

293. Fitzpatrick, J. A. & Lillemeier, B. F. Fluorescence correlation spectroscopy: linking molecular dynamics to biological function in vitro and in situ. *Curr. Opin. Struct. Biol.* **21**, 650–660 (2011).

294. Muramatsu, N. & Minton, A. P. Tracer diffusion of globular proteins in concentrated protein solutions. *Proc. Natl. Acad. Sci.* **85**, 2984–2988 (1988).

295. Gurdap, C. O., Wedemann, L., Sych, T. & Sezgin, E. Influence of the extracellular domain size on the dynamic behavior of membrane proteins. *Biophys. J.* **121**, 3826–3836 (2022).

296. Dal Porto, J. M., Haberman, A. M., Shlomchik, M. J. & Kelsoe, G. Antigen Drives Very Low Affinity B Cells to Become Plasmacytes and Enter Germinal Centers. *J. Immunol.* **161**, 5373–5381 (1998).

297. Wilcock, M. J. DPhil Thesis: Characterisation of the Mechanism of B-Cell Receptor Triggering. (University of Oxford, 2018).

298. Junghans, V., Santos, A. M., Lui, Y., Davis, S. J. & Jönsson, P. Dimensions and Interactions of Large T-Cell Surface Proteins. *Front. Immunol.* **9**, 2215 (2018).

299. Calis, J. J. A. & Rosenberg, B. R. Characterizing immune repertoires by high throughput sequencing: strategies and applications. *Trends Immunol.* **35**, 581–590 (2014).

300. Hombach, J., Tsubata, T., Leclercq, L., Stappert, H. & Reth, M. Molecular components of the B-cell antigen receptor complex of the IgM class. *Nature* **343**, 760–762 (1990).

301. Schamel, W. W. A. & Reth, M. Stability of the B cell antigen receptor complex. *Mol. Immunol.* **37**, 253–259 (2000).

302. Gottwick, C. *et al.* A symmetric geometry of transmembrane domains inside the B cell antigen receptor complex. *Proc. Natl. Acad. Sci.* **116**, 13468–13473 (2019).

303. Lockey, C., Young, H., Brown, J. & Dixon, A. M. Characterization of interactions within the Igα/Igβ transmembrane domains of the human B-cell receptor provides insights into receptor assembly. *J. Biol. Chem.* **298**, 101843 (2022).

304. Ramesh, S., Park, S., Im, W., Call, M. J. & Call, M. E. T cell and B cell antigen receptors share a conserved core transmembrane structure. *Proc. Natl. Acad. Sci.* **119**, e2208058119 (2022).

305. Friess, M. D., Pluhackova, K. & Böckmann, R. A. Structural Model of the mIgM B-Cell Receptor Transmembrane Domain From Self-Association Molecular Dynamics Simulations. *Front. Immunol.* **9**, 2947 (2018).

306. Siegers, G. M. Identification of disulfide bonds in the Ig- /Ig- component of the B cell antigen receptor using the Drosophila S2 cell reconstitution system. *Int. Immunol.* **18**, 1385–1396 (2006).

307. Li, Y. *et al.* Structural insights into immunoglobulin M. *Science* **367**, 1014–1017 (2020).

308. Kumar, N., Arthur, C. P., Ciferri, C. & Matsumoto, M. L. Structure of the human secretory immunoglobulin M core. *Structure* **29**, 564-571.e3 (2021).

309. Chen, Q., Menon, R., Calder, L. J., Tolar, P. & Rosenthal, P. B. Cryomicroscopy reveals the structural basis for a flexible hinge motion in the immunoglobulin M pentamer. *Nat. Commun.* **13**, 6314 (2022).

310. Lee, H. J., Lee, H. S., Youn, T., Byrne, B. & Chae, P. S. Impact of novel detergents on membrane protein studies. *Chem* **8**, 980–1013 (2022).

311. Piper, S. J., Johnson, R. M., Wootten, D. & Sexton, P. M. Membranes under the Magnetic Lens: A Dive into the Diverse World of Membrane Protein Structures Using Cryo-EM. *Chem. Rev.* **122**, 13989–14017 (2022).

312. Chen, Y. *et al.* Cholesterol inhibits TCR signaling by directly restricting TCR-CD3 core tunnel motility. *Mol. Cell* **82**, 1278-1287.e5 (2022).

313. Jardine, J. G. *et al.* HIV-1 broadly neutralizing antibody precursor B cells revealed by germline-targeting immunogen. *Science* **351**, 1458–1463 (2016).

314. Umotoy, J. *et al.* Rapid and Focused Maturation of a VRC01-Class HIV Broadly Neutralizing Antibody Lineage Involves Both Binding and Accommodation of the N276-Glycan. *Immunity* **51**, 141-154.e6 (2019).

315. Liu, Z. *et al.* Systematic comparison of 2A peptides for cloning multi-genes in a polycistronic vector. *Sci. Rep.* **7**, 2193 (2017).

316. Zakeri, B. *et al.* Peptide tag forming a rapid covalent bond to a protein, through engineering a bacterial adhesin. *Proc. Natl. Acad. Sci.* **109**, (2012).

317. Liddy, N. *et al.* Monoclonal TCR-redirected tumor cell killing. *Nat. Med.* **18**, 980–987 (2012).

318. Liddy, N. Doctoral thesis: Molecular engineering of high affinity T-cell receptors for bispecific therapeutics. (Cardiff University, 2013).

319. Wu, S. *et al.* Fabs Enable Single Particle cryoEM Studies of Small Proteins. *Structure* **20**, 582–592 (2012).

320. Okazaki, M., Luo, Y., Han, T., Yoshida, M. & Seon, B. Three new monoclonal antibodies that define a unique antigen associated with prolymphocytic leukemia/non-Hodgkin·s lymphoma and are effectively internalized after binding to the cell surface antigen. *Blood* **81**, 84–94 (1993).

321. Tilly, H. *et al.* Polatuzumab Vedotin in Previously Untreated Diffuse Large B-Cell Lymphoma. *N. Engl. J. Med.* **386**, 351–363 (2022).

322. Polakis, P., Polson, A., Spencer, S. D. & Yu, S.-F. Immunoconjugates comprising anti-CD79B antibodies. WIPO Patent WO 2014/011519 A1. (2014).

323. Kampjut, D., Steiner, J. & Sazanov, L. A. Cryo-EM grid optimization for membrane proteins. *iScience* **24**, 102139 (2021).

324. Sevdali, E. *et al.* BAFFR activates PI3K/AKT signaling in human naive but not in switched memory B cells through direct interactions with B cell antigen receptors. *Cell Rep.* **39**, 111019 (2022).

325. Duan, H. *et al.* Glycan Masking Focuses Immune Responses to the HIV-1 CD4-Binding Site and Enhances Elicitation of VRC01-Class Precursor Antibodies. *Immunity* **49**, 301-311.e5 (2018).

326. Hauer, F. *et al.* GraDeR: Membrane Protein Complex Preparation for Single-Particle Cryo-EM. *Structure* **23**, 1769–1775 (2015).

327. Velazhahan, V., Ma, N., Vaidehi, N. & Tate, C. G. Activation mechanism of the class D fungal GPCR dimer Ste2. *Nature* **603**, 743–748 (2022).

328. Korepanova, A. & Matayoshi, E. D. HPLC-SEC Characterization of Membrane Protein-Detergent Complexes. *Curr. Protoc. Protein Sci.* **68**, (2012).

329. Sigworth, F. J. Principles of cryo-EM single-particle image processing. *Microscopy* **65**, 57–67 (2016).

330. Sutton, B., Davies, A., Bax, H. & Karagiannis, S. IgE Antibodies: From Structure to Function and Clinical Translation. *Antibodies* **8**, 19 (2019).

331. Galli, S. J. & Tsai, M. IgE and mast cells in allergic disease. *Nat. Med.* **18**, 693–704 (2012).

332. Blank, U., Ra, C. S. & Kinet, J. P. Characterization of truncated alpha chain products from human, rat, and mouse high affinity receptor for immunoglobulin E. *J. Biol. Chem.* **266**, 2639–2646 (1991).

333. Garman, S. C., Wurzburg, B. A., Tarchevskaya, S. S., Kinet, J.-P. & Jardetzky, T. S. Structure of the Fc fragment of human IgE bound to its high-affinity receptor FcεRIα. *Nature* **406**, 259–266 (2000).

334. Wurzburg, B. A., Garman, S. C. & Jardetzky, T. S. Structure of the Human IgE-Fc Cε3-Cε4 Reveals Conformational Flexibility in the Antibody Effector Domains. *Immunity* **13**, 375–385 (2000).

335. McDonnell, J. M. *et al.* The structure of the IgE Cε2 domain and its role in stabilizing the complex with its high-affinity receptor FcεRI. *Nat. Struct. Biol.* **8**, (2001).

336. Wan, T. *et al.* The crystal structure of IgE Fc reveals an asymmetrically bent conformation. *Nat. Immunol.* **3**, 681–686 (2002).

337. Drinkwater, N. *et al.* Human immunoglobulin E flexes between acutely bent and extended conformations. *Nat. Struct. Mol. Biol.* **21**, 397–404 (2014).

338. Blázquez-Moreno, A. *et al.* Transmembrane features governing Fc receptor CD16A assembly with CD16A signaling adaptor molecules. *Proc. Natl. Acad. Sci.* **114**, (2017).

339. Berman, H. M. The Protein Data Bank. *Nucleic Acids Res.* **28**, 235–242 (2000).

340. Lua, W.-H. *et al.* Role of the IgE variable heavy chain in FcεRIα and superantigen binding in allergy and immunotherapy. *J. Allergy Clin. Immunol.* **144**, 514-523.e5 (2019).

341. Wurzburg, B. A. *et al.* An Engineered Disulfide Bond Reversibly Traps the IgE-Fc3–4 in a Closed, Nonreceptor Binding Conformation. *J. Biol. Chem.* **287**, 36251–36257 (2012).

342. Pan, Y.-G., Yu, Y.-L., Lin, C.-C., Lanier, L. L. & Chu, C.-L. FcεRI γ-Chain Negatively Modulates Dectin-1 Responses in Dendritic Cells. *Front. Immunol.* **8**, 1424 (2017).

343. Song, C. P. *et al.* Purification of the Recombinant Green Fluorescent Protein Using Aqueous Two-Phase System Composed of Recyclable CO2-Based Alkyl Carbamate Ionic Liquid. *Front. Chem.* **6**, 529 (2018).

344. Zbären, N. *et al.* A novel functional mast cell assay for the detection of allergies. *J. Allergy Clin. Immunol.* **149**, 1018-1030.e11 (2022).

345. Bitting, K. *et al.* Identification of redundancy between human FcεRIβ and MS4A6A proteins points toward additional complex mechanisms for FcεRI trafficking and signaling. *Allergy* all.15595 (2022) doi:10.1111/all.15595.

346. Gounni, A. S. *et al.* Human neutrophils express the high-affinity receptor for immunoglobulin E (FcεRI): role in asthma. *FASEB J.* **15**, 940–949 (2001).

347. Letourneur, O., Sechi, S., Willette-Brown, J., Robertson, M. W. & Kinet, J.-P. Glycosylation of Human Truncated Fc∈RI α Chain Is Necessary for Efficient Folding in the Endoplasmic Reticulum. *J. Biol. Chem.* **270**, 8249–8256 (1995).

348. Shields, R., Mateo, S., Wu, L. & City, F. Anti-FcgammaRIIb receptor antibody and uses therefor. US Patent US2006/0073142A1. (2006).

349. Chizzonite, Richard Anthony, Hakimi, John & Kochan, Jarema Peter. Antibodies against an IgE receptor. EPO patent EP0499112A1. (1992).

350. Pierce, S. K. & Liu, W. The tipping points in the initiation of B cell signalling: how small changes make big differences. *Nat. Rev. Immunol.* **10**, 767–777 (2010).

351. Stone, M. B., Shelby, S. A., Núñez, M. F., Wisser, K. & Veatch, S. L. Protein sorting by lipid phase-like domains supports emergent signaling function in B lymphocyte plasma membranes. *eLife* **6**, e19891 (2017).

352. Pierce, S. K. Lipid rafts and B-cell activation. *Nat. Rev. Immunol.* **2**, 96–105 (2002).

353. Freeman, S. A. *et al.* Toll-like receptor ligands sensitize B-cell receptor signalling by reducing actin-dependent spatial confinement of the receptor. *Nat. Commun.* **6**, 6168 (2015).

354. Orbach, R. & Su, X. Surfing on Membrane Waves: Microvilli, Curved Membranes, and Immune Signaling. *Front. Immunol.* **11**, 2187 (2020).

355. Myers, D. R., Zikherman, J. & Roose, J. P. Tonic Signals: Why Do Lymphocytes Bother? *Trends Immunol.* **38**, 844–857 (2017).

356. Wilhelm, K. B. *et al.* Height, but not binding epitope, affects the potency of synthetic TCR agonists. *Biophys. J.* **120**, 3869–3880 (2021).

357. Milstein, O. *et al.* Nanoscale Increases in CD2-CD48-mediated Intermembrane Spacing Decrease Adhesion and Reorganize the Immunological Synapse. *J. Biol. Chem.* **283**, 34414–34422 (2008).

358. Moore, M. D., DiScipio, R. G., Cooper, N. R. & Nemerow, G. R. Hydrodynamic, Electron Microscopic, and Ligand-binding Analysis of the Epstein-Barr Virus/C3dg Receptor (CR2). *J. Biol. Chem.* **264**, 20576–20582 (1989).

359. Weisman, H. F. *et al.* Soluble Human Complement Receptor Type 1: In Vivo Inhibitor of Complement Suppressing Post-Ischemic Myocardial Inflammation and Necrosis. *Science* **249**, 146–151 (1990).

360. Koopman, G. *et al.* Adhesion of human B cells to follicular dendritic cells involves both the lymphocyte function-associated antigen 1/intercellular adhesion molecule 1 and very late antigen 4/vascular cell adhesion molecule 1 pathways. *J. Exp. Med.* **173**, 1297–1304 (1991).

361. Dustin, M. L. Complement Receptors in Myeloid Cell Adhesion and Phagocytosis. *Microbiol. Spectr.* **4**, 4.6.04 (2016).

362. Grönwall, C., Vas, J. & Silverman, G. J. Protective Roles of Natural IgM Antibodies. *Front. Immunol.* **3**, (2012).

363. Rodriguez-Zhurbenko, N., Quach, T. D., Hopkins, T. J., Rothstein, T. L. & Hernandez, A. M. Human B-1 Cells and B-1 Cell Antibodies Change With Advancing Age. *Front. Immunol.* **10**, 483 (2019).

364. Poljak, R. J. Structure of antibodies and their complexes with antigens. *Mol. Immunol.* **28**, 1341–1345 (1991).

365. Tolar, P. & Pierce, S. K. Unveiling the B cell receptor structure. *Science* **377**, 819–820 (2022).

366. Pan, S., Manabe, N. & Yamaguchi, Y. 3D Structures of IgA, IgM, and Components. *Int. J. Mol. Sci.* **22**, 12776 (2021).

367. Huang, C.-Y. *et al.* In situ structure and dynamics of an alphacoronavirus spike protein by cryo-ET and cryo-EM. *Nat. Commun.* **13**, 4877 (2022).

368. Garman, S. C., Kinet, J.-P. & Jardetzky, T. S. Crystal Structure of the Human High-Affinity IgE Receptor. *Cell* **95**, 951–961 (1998).

369. Pecht, I., Ortega, E. & Jovin, T. M. Rotational dynamics of the Fc.epsilon. receptor on mast cells monitored by specific monoclonal antibodies and IgE. *Biochemistry* **30**, 3450–3458 (1991).

370. Andrews, N. L. *et al.* Small, Mobile FcεRI Receptor Aggregates Are Signaling Competent. *Immunity* **31**, 469–479 (2009).

371. Schwartz, S. L. *et al.* Differential mast cell outcomes are sensitive to FcεRI-Syk binding kinetics. *Mol. Biol. Cell* **28**, 3397–3414 (2017).

372. Shelby, S. A., Holowka, D., Baird, B. & Veatch, S. L. Distinct Stages of Stimulated FcεRI Receptor Clustering and Immobilization Are Identified through Superresolution Imaging. *Biophys. J.* **105**, 2343–2354 (2013).

373. Andrews, N. L. *et al.* Actin restricts FcεRI diffusion and facilitates antigen-induced receptor immobilization. *Nat. Cell Biol.* **10**, 955–963 (2008).

374. Ikemizu, S. *et al.* Structure and Dimerization of a Soluble Form of B7-1. *Immunity* **12**, 51–60 (2000).

375. James, J. R., Oliveira, M. I., Carmo, A. M., Iaboni, A. & Davis, S. J. A rigorous experimental framework for detecting protein oligomerization using bioluminescence resonance energy transfer. *Nat. Methods* **3**, 1001–1006 (2006).

376. Zhao, Y. *et al.* PD-L1:CD80 Cis-Heterodimer Triggers the Co-stimulatory Receptor CD28 While Repressing the Inhibitory PD-1 and CTLA-4 Pathways. *Immunity* **51**, 1059-1073.e9 (2019).

377. Bhatia, S., Edidin, M., Almo, S. C. & Nathenson, S. G. Different cell surface oligomeric states of B7-1 and B7-2: Implications for signaling. *Proc. Natl. Acad. Sci.* **102**, 15569–15574 (2005).

378. Sondermann, P., Kaiser, J. & Jacob, U. Molecular Basis for Immune Complex Recognition: A Comparison of Fc-Receptor Structures. *J. Mol. Biol.* **309**, 737–749 (2001).

379. Ramsland, P. A. *et al.* Structural Basis for FcγRIIa Recognition of Human IgG and Formation of Inflammatory Signaling Complexes. *J. Immunol.* **187**, 3208–3217 (2011).

380. Maxwell, K. F. *et al.* Crystal structure of the human leukocyte Fc receptor, FcγRIIa. *Nat. Struct. Biol.* **6**, 437–442 (1999).

381. Dunne, P. D. *et al.* DySCo: Quantitating Associations of Membrane Proteins Using Two-Color Single-Molecule Tracking. *Biophys. J.* **97**, L5–L7 (2009).

382. Wilmes, S. *et al.* Mechanism of homodimeric cytokine receptor activation and dysregulation by oncogenic mutations. *Science* **367**, 643–652 (2020).

383. Mørch, A. M. *et al.* The kinase occupancy of T cell coreceptors reconsidered. *Proc. Natl. Acad. Sci.* **119**, e2213538119 (2022).

384. Paolini, R., Jouvin, M.-H. & Kinet, J.-P. Phosphorylation and dephosphorylation of the high-affinity receptor for immunoglobulin E immediately after receptor engagement and disengagement. *Nature* **353**, 855–858 (1991).

385. Castro-Dopico, T. & Clatworthy, M. R. IgG and Fcγ Receptors in Intestinal Immunity and Inflammation. *Front. Immunol.* **10**, 805 (2019).

386. Acchione, M. *et al.* Light chain somatic mutations change thermodynamics of binding and water coordination in the HyHEL-10 family of antibodies. *Mol. Immunol.* **47**, 457–464 (2009).